Numerical analysis of seeding process during Czochralski growth of oxide single crystals

Von der Fakultät für Mathematik, Naturwissenschaften und Informatik
der Brandenburgischen Technischen Universität Cottbus

zur Erlangung des akademischen Grades

Doktor der Naturwissenschaften
(Dr. rer. nat.)
genehmigte Dissertation
vorgelegt von

"Höheres Lizentiat" der Fachrichtung "Physik"

Mohammad Hossein Tavakoli

geboren am 30.12.1962 in Hamedan, Iran

Gutachter: Prof. Dr. rer. nat. habil. Dieter Schmeißer

Gutachter: Prof. Dr. rer. nat. habil. Arne Cröll

Gutachter: Prof. Dr. Roberto Fornari

Tag der mündlichen Prüfung: 24. Juli 2006

Acknowledgments

I would like to express my sincere gratitude, regards and thanks to my thesis advisor, Dr. Hermann Wilke, for his excellent guidance and support. His considerable involvement and encouragement are greatly appreciated. I am also indebted to Prof. Winfried Schroeder, former director of Institute for Crystal Growth (IKZ) - Berlin, for giving me the opportunity to find a Ph.D. position in IKZ, and his immense and unsparing help, support and assistance during my stay in Berlin. I would also like to thank Prof. Roberto Fornari, director of Institute for Crystal Growth, for his help and support.

I am specially thankful to the members of my research group (Group numerical modeling), Uwe Rehse, Klaus Boettcher and Wolfram Miller for their greatly aided my research efforts and professional development and also for their help and support.

I would like to specifically thank Dr. Anke Luedge for her innumerable and continuous help during the period of my research.

My sincere thanks to Dr. Reinhard Uecker, Dr. Peter Reiche and Steffen Ganschow, the Czochralski-dielectric lab for their nice company and discussion during my stay in IKZ.

I am grateful to other members of Institute for Crystal growth (IKZ), particularly Prof. Klaus Jacobs, Hans-Joachim Warneke (Personnel Assistant), Dr. Peggy Hofmann, Angelika Holland (secretary), and Peter Mehlhorn, Sven Heron and Sabine Bergmann (computer and network administrator) for their help and support.

Finally, I would like to thank my family members for their continuous support and encouragement. I am indebted to them for giving me happy and joyous environment at home.

Table of contents

Chapter 1: Introduction

Chapter 2: Induction heating

Chapter 3: Configuration contains only gas

Chapter 4: Configuration contains gas and melt

Chapter 5: Configuration contains gas, melt and seed

Chapter 6: Towards the three-dimensional calculation

Conclusions and outlook

Chapter 1

Introduction

1.1 Czochralski crystal growth

One of the most important methods of crystal growth has been associated from the very beginning with the name of *Jan Czochralski* (1885-1953).

The Czochralski method (CZ) is a *batch process* in which a single crystal is grown from the melt in a crucible, Fig. 1-1. This method is widely used in growing single crystals for several applications in the electronics and optics technology. The idea of the Czochralski method is based on pulling a crystal from the melt but it is certainly different from the other known methods like Bridgeman and Verneuil methods. The method was discovered in 1916 and the paper reporting the results was published in 1918. At that time Czochralski investigated the growth of metals and their velocities of growth, and obtained single crystals of a few *mm* in diameter and length up to 150 *mm*. The CZ method has been improved and cited from its very beginning. It is worth noting that up to the second world war scientists were mainly interested in the properties of metals and their alloys. However, after the war scientists became interested in the growth of various materials applied in electronics and optics technology. Initially, germanium and silicon were grown, but later semiconductors, oxides, fluorides and other binary and multicomponent compounds were also obtained as crystals. It should be noted that the CZ crystal growth technology is continuously being improved and developed even today [2-8,12,18,20].

The principle advantage of this technique is that the crystal is unconstrained as it cools, so a high degree of structural perfection can be obtained. The second major advantage of the technique is that crystal and crucible rotations can be used to modify the distribution of deliberately added solute.

The most important phenomenon in the CZ process is the flow in the melt. Several mechanisms are responsible for the melt flow as are shown in Fig. 1-2: (a) Because of the

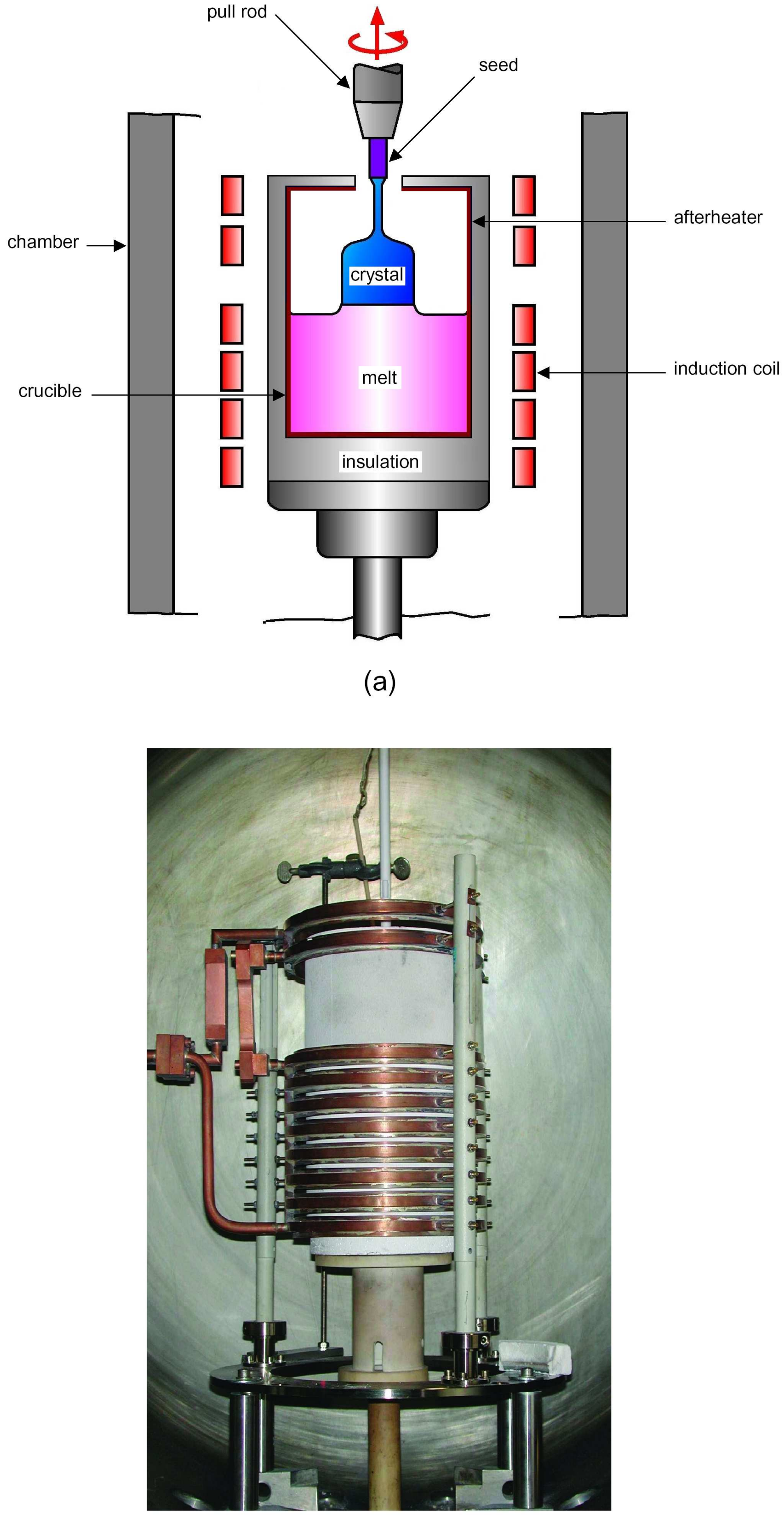

(a)

(b)

Fig. 1-1. Czochralski crystal growth system, (a) a schematic diagram and (b) a photo (from our Czochralski-dielectrics lab in *IKZ*).

fluid viscosity, the rotating crystal and crucible exert shear forces on the melt, so that the melt is driven to move in the azimuthal direction (azimuthal flow). Also, the centrifugal forces induced by crystal and crucible rotations drive the fluid near the crystal-melt interface and the crucible bottom outward. These meridional flows are called *forced convection*. The rotating crystal improves structural and stoichiometric uniformity in the melt and rotation of the crucible smooths out thermal symmetries that may arise from irregularities in heating. (b) The heating of the crucible causes temperature differences across the melt. Because of thermal expansion of material, hot melt is lighter than cold melt. Such a difference of densities leads to buoyancy in a certain part of the melt. Consequently, convection is induced (*free* or *natural convection*, or *buoyancy-driven flow*). (c) The variations of surface tension along the melt meniscus drives another flow called *Marangoni convection*. Since the coefficient of surface tension of most crystal materials in their molten form vary with temperature, a non-zero temperature gradient along the free surface causes a non-constant surface tracing, resulting in a finite shear at the free surface. The flow pattern is further complicated by the non-planar nature of gas-melt interface as well as the heat losses at this boundary.

The flow pattern caused by combinations of these mechanisms control the mass and heat transfer in the melt. Thus the quality, the size and the growth rate of the crystal are directly related to the characteristics of the flow patterns. This is why most studies on CZ crystal growth process have been concentrated on the flow patterns in the melt. It is worth noting that the flow patterns for semiconductors and those of oxides can be quite different because of their thermophysical parameters.

Another factor that influences the quality of the crystal is the shape of crystal-melt interface. The shape of crystal-melt interface can strongly affect the quality of the crystal grown from the CZ process. A strongly deflected interface (deep interface), which is common in many oxide CZ systems, induces thermal stresses in the crystal during cooling which lead to cracks, facets and dislocations. An inversion from a convex (toward the melt) to concave interface is a source of crystal defects. Finding conditions for a flat (or almost flat) crystal-melt interface is important to crystal growth.

1.1.1 Seeding process

The procedure of growing a crystal by the Czochralski method starts by filling the clean crucible with high purity polycrystalline material and often a small quantity of an impurity or dopant, which alters the physical properties of the grown crystal. The enclosure is filled with an inert atmosphere such as nitrogen or argon. Then the crucible is heated either by radio frequency induction heating or by resistive heating to melt the substrate. Resistive heating is typically used for semiconductor systems and induction

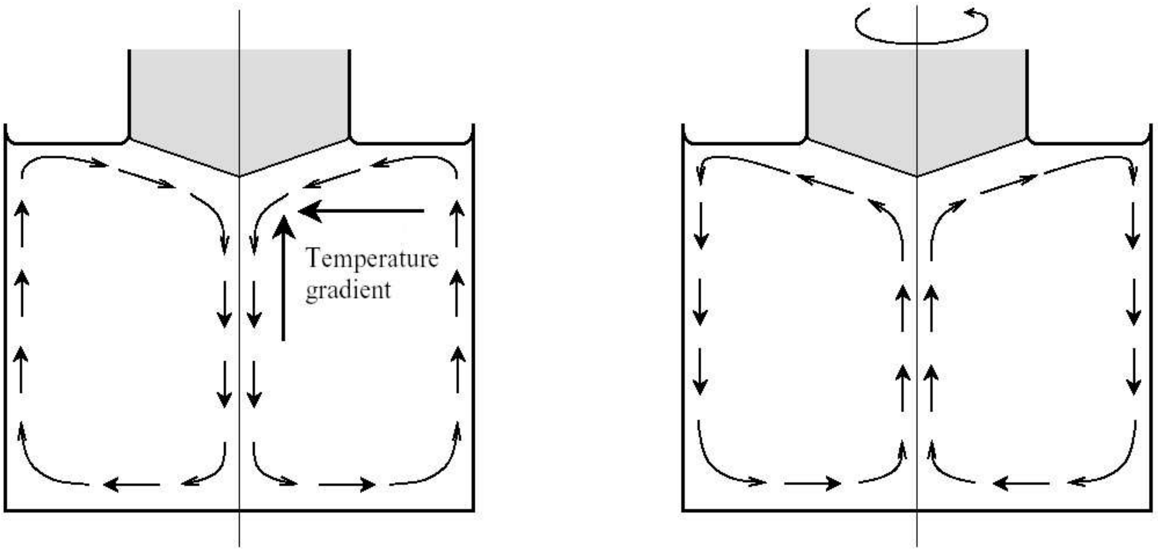

(a) Buoyancy−driven Flow

(b) Flow due to crystal rotation

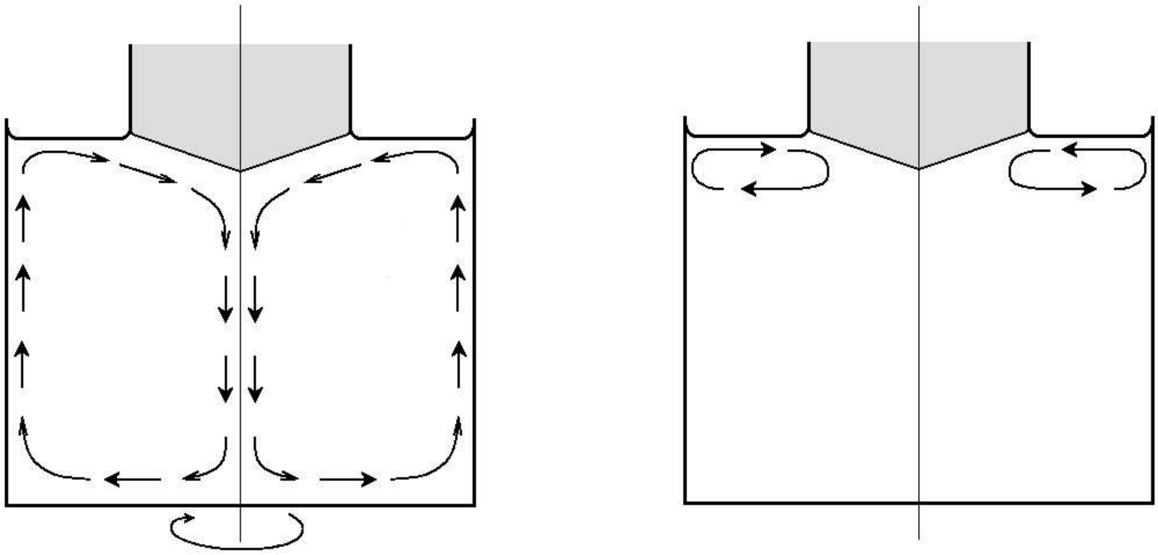

(c) Flow due to crucible rotation

(d) Marangoni Flow

Fig. 1-2. Different modes of fluid flow in a Czochralski melt.

heating is common for the higher-melting-point oxide materials. When the melt reached a certain temperature above its melting point, then a precisely-oriented single seed crystal attached to the pull rod is lowered by its vertical motion to the surface of the melt. After an appropriate start-up procedure and when the seed and melt have reached thermal equilibrium, the seed is slowly withdrawn from the melt. Under suitable thermal conditions, recrystallization in the form of a single crystal occurs around the original seed and as a result a single crystal is pulled upward. A meniscus forms about the edge of the crystal by surface tension as the melt is pulled upward. The shape of this meniscus is determined by the action of surface tension against the force of gravity.

Usually, after the seeding process the crystal is grown through a "necking" operation during the start up growth where a length of very small diameter crystal is solidified in an attempt to eliminate dislocations by forcing them to "grow out" to the surface of the crystal. After necking the crystal is grown to the desired diameter by reducing the power input of the induction coil, subsequently system parameters (usually growth rate and output) are adjusted to achieve constant-diameter growth. An active control mechanism is employed to keep the crystal diameter at the desired value. At the end of run, the crystal is withdrawn completely from the melt and is slowly cooled. The steps involved during the growth of single crystal in a Czochralski process are shown in Fig. 1-3.

1.1.2 Importance of numerical simulation

The quality and size of the crystal grown by the Czochralski process depend on complex physical phenomena taking place in the melt and, specially, in the vicinity of the solidification interface. So understanding of temperature distribution as well as heat and mass transport is a prerequisite to the optimization of Czochralski crystal growth systems. Control of crystal quality, as measured by the degree of crystallographic perfection of the lattice and spatial uniformity of solute in it depends on a well-organized flow and thermal field in the crystal growth apparatus. Fluid motion in a CZ system is of concern to crystal growers as it determines the transport of thermal energy, solute and impurities to the grown crystal. The magnitude of stresses in the grown crystal is governed by the temperature gradients in the melt and gas. It is not so easy to study transport phenomena experimentally during a real Czochralski process since it is carried out within a closed enclosure at high temperatures. Despite a large number of experiments carried out to understand transport phenomena, the knowledge of competing mechanisms during melt convection continues to be insufficient. An alternative possibility to the prediction and understanding of transport phenomena during the growth of crystals is *numerical simulation*.

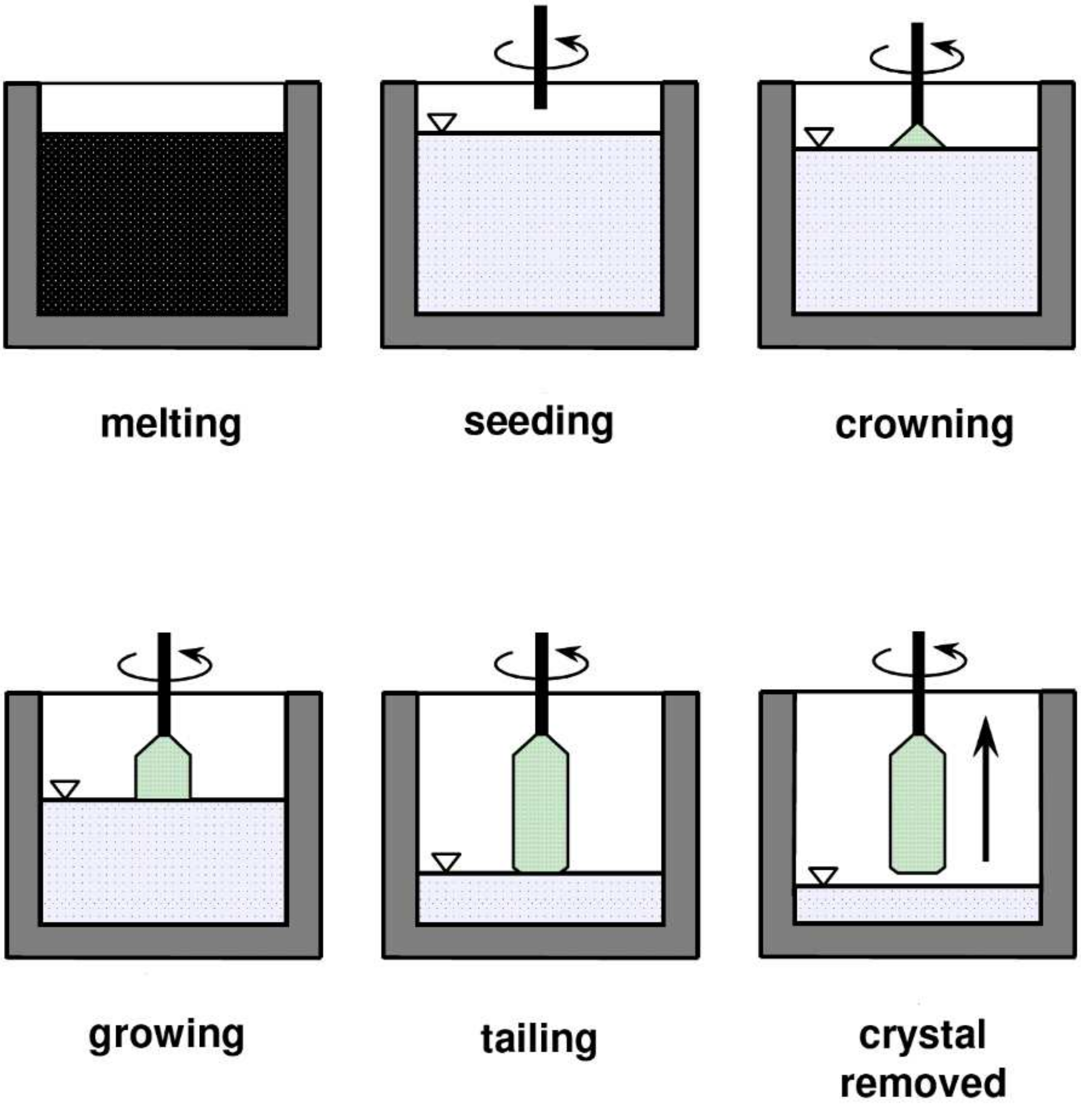

Fig. 1-3. Steps in the Czochralski crystal growth process.

Because of the difficulties and costs associated with doing experiments at high temperature, numerical simulation plays an important role in the understanding of Czochralski crystal growth systems. This approach has been developed systematically in the last two decades. Numerical simulation can provide detailed information of fluid flow, heat generation, heat and mass transfer, and lead to an improvement in the growth conditions of a Czochralski process. Accurate modeling of the Czochralski crystal growth has a large potential for impact on the bulk crystal industry because of the dominant use of this technology in the production of large diameter and perfect oxide and semiconductor crystals. The need for predictive modeling has become ever more acute as the demands have increased for growth of large diameter crystals and for the extension of the technology to the growth of new materials. However, the desire for an accurate mathematical analysis has been inhibited by the enormous complexity of the Czochralski system, which has made this analysis one of the most challenging problems in modeling of materials processing systems.

It is currently accepted that the transport properties in the CZ systems are primary factors affecting the quality of grown crystals. These transport properties of the CZ systems are themselves determined by a broad and inter-dependent matrix of variables that include crystal rotation, crucible rotation, pull velocity, heat generation, temperature gradient, gas convection, and system geometry and orientation. Thus, state-of-art crystal growth requires algorithms that model the physical phenomena by incorporating all parameters of interest. In addition, these simulations can form the basis of optimizing the process parameters and evolve guidelines for future designs.

Optimization of the design and control of a CZ crystal growth system center on enhancing the quality of the crystal, as measured by the perfection of its cylindrical shape, by the level of defects in the crystallography and by the uniformity and level of dopant and impurities in the crystal. Models of melt crystal growth systems focus either individually or collectively on these problems.

1.2 Fluid flow and heat transfer

1.2.1 Streamline and stream function

Streamlines are a family of curves showing the pattern of fluid flow, which are drawn in such manner that the velocity vectors for all points along the curves would meet them tangentially [9,16,17]. As illustrated in Fig. 1-4

$$\frac{v_y}{v_x} = \frac{\mathrm{d}y}{\mathrm{d}x} = \text{slope of streamline} \tag{1.1}$$

where v_x and v_y are the x component and y component of the velocity vector $\mathbf{v}$, respectively. As such, the velocity vector $\mathbf{v}$ is tangent to the streamline. In three dimensions the relation becomes

$$\frac{\mathrm{d}x}{v_x} = \frac{\mathrm{d}y}{v_y} = \frac{\mathrm{d}z}{v_z} \tag{1.2}$$

In steady state flow, a streamline is also a path line, which is a line describing the path or trajectory of a given fluid element. Streamlines can also reveal variations in the fluid velocity, and this is particularly obvious in two-dimensional flows. Convergence of streamlines represents acceleration, whereas divergence represents deceleration.

The *stream function* ψ can be defined as follows:

$$v_x = \frac{\partial \psi}{\partial y}, \ v_y = -\frac{\partial \psi}{\partial x} \tag{1.3}$$

Therefore

$$\mathrm{d}\psi = \frac{\partial \psi}{\partial x}\mathrm{d}x + \frac{\partial \psi}{\partial y}\mathrm{d}y = -v_y \mathrm{d}x + v_x \mathrm{d}y \tag{1.4}$$

Consider a path of constant ψ in the xy plane. Since $\mathrm{d}\psi = 0$ along the path, from Eq. (1.4)

$$\left.\frac{\mathrm{dy}}{\mathrm{dx}}\right|_{\psi=constant} = \frac{v_y}{v_x} \tag{1.5}$$

Substituting Eq. (1.a) into Eq. (1.e)

$$\left.\frac{\mathrm{dy}}{\mathrm{dx}}\right|_{\psi=constant} = \text{slope of streamline} \tag{1.6}$$

As such, a path of constant ψ is a streamline, and the tangent at every point on this path gives this direction of the velocity at that point.

In fluid dynamics, the stream function is defined for two-dimensional flows. The difference between the values of the stream function at any two points gives the volumetric flow rate (or flux) through a line connecting the two points. Note that since streamlines are tangent to the flow, the value of the stream function must be the same along a streamline. If there were a flux across a line, it would necessarily not be tangent to the flow, hence would not be a streamline.

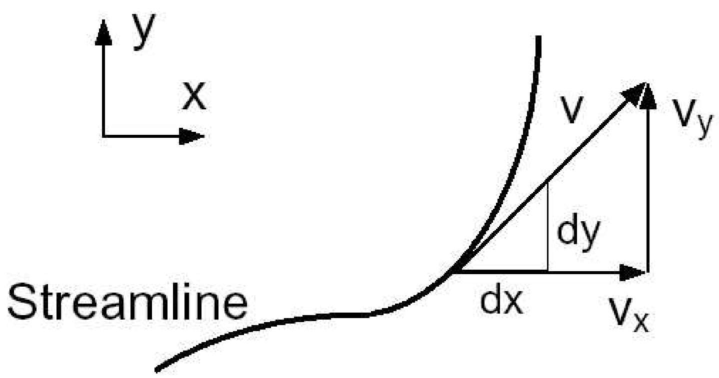

Fig. 1-4. A velocity vector **v** along a streamline.

1.2.2 Continuity equation

In fluid dynamics, a continuity equation is an equation of conservation of mass. Its differential form is

$$\frac{\partial \rho}{\partial t} + \nabla \cdot (\rho \mathbf{v}) = 0 \tag{1.7}$$

where ρ is density, t is time, and $\mathbf{v}$ is fluid velocity. For an incompressible fluid $\rho = const.$ and the equation of continuity simplifies to

$$\nabla \cdot \mathbf{v} = 0 \qquad (\rho = const.) \tag{1.8}$$

1.2.3 Navier-Stokes equations

The equations of motion for an element of fluid are given by the Navier-Stokes equations [16,17]

$$\rho \left(\frac{\partial \mathbf{v}}{\partial t} + \mathbf{v} \cdot \nabla \mathbf{v} \right) = \rho \mathbf{f} - \nabla p + \nabla \left(\mu \nabla \mathbf{v} \right) \tag{1.9}$$

Here, the left hand side comprises the product of the unit mass and its acceleration while the right hand side represents the sum of the external forces acting on the unit.

The term $\nabla(\mu\nabla\mathbf{v})$, where μ is the viscosity of the fluid, accounts for the effect of viscous forces. The internal friction due to the viscous nature of the fluid is manifested only when one region of fluid moves relative to another. Faster moving layers entrain slower moving ones so that momentum is transferred from the faster to the slower layers.

This unique value of volume force arises in those fluids where the transfer obeys *Newton's laws of motion*. Such fluids are called *Newtonian fluids*.

The negative of the pressure gradient is that volume force which acts on the fluid element when the pressure changes from point to point. It is not the pressure itself but only its gradient which is required in the equation of motion (since we want the net force on an element of volume) while the local pressure may be taken in an arbitrary way.

The vector **f** represents the volume force exerted on the element of fluid. Gravity is one example of a volume force while the electromagnetic Lorentz force due to induced currents is another. In general, any gradient of extended chemical potential can be considered as such a body force. The gravity effect is of great importance in natural convection which is driven by buoyancy density difference and impeded by the viscous inertia of the fluid. The viscosity dissipates kinetic energy while the buoyancy force releases internal energy.

One example of **f** due to spatial temperature is

$$\mathbf{f} = -\mathbf{g}\rho\beta_T\left(T - T_0\right) \tag{1.10}$$

where T_0 refers to a reference temperature, $\beta_T = -\left(\partial\ell n\rho/\partial T\right)$ and g is the gravitational constant. The above equation is called *the Boussinesq approximation*. Boussinesq approximation means that the density of the fluid is assumed to be constant except in the buoyancy term in Navier-Stokes equations (1% variation or less throughout the fluid).

In fluid dynamics, the Boussinesq approximation is used in the field of buoyancy-driven flow. The essence of the Boussinesq approximation is that the difference in inertia is negligible but gravity is sufficiently strong to make the specific weight appreciably different between the two fluids.

Boussinesq flows are common in nature, industry and the public buildings (natural ventilation, central heating). The approximation is extremely accurate for many such flows, and makes the mathematics and physics simpler.

1.2.4 Marangoni convection

Marangoni convection occurs when the surface tension of an interface (generally liquid-air) depends on the concentration of a species or on the temperature distribution [10]. In the case of temperature dependence, the Marangoni effect is also called *thermocapillary convection*. The basic consideration which introduces *Marangoni convection* is the shear stress balance at the interface between fluid phase 1 and 2,

$$\mu_1\frac{\partial v_{x1}}{\partial z} - \mu_2\frac{\partial v_{x2}}{\partial z} = \frac{\partial\gamma}{\partial x} = \frac{\partial\gamma}{\partial T}\frac{\partial T}{\partial x} \tag{1.11}$$

where γ is the surface tension at the interface. For the majority of pure liquids $\partial\gamma/\partial T < 0$ and, since surface atoms move from positions of high chemical potential to lower chemical potential, we should expect the surface motion to occur from regions of high γ (low T) to regions of lower γ (high T). Thus, the compensating surface flow to maintain a flat interface will be from hot (low γ) to cold (high γ).

1.2.5 Heat transfer

Heat transfer is the transfer of heat due to a temperature difference. Heat transfer can occur by three different mechanisms: conduction, convection and radiation [9,16,17].

Conduction refers to heat transfer that occurs across a stationary solid or fluid in which a temperature gradient exists. In contrast, convection refers to the heat transfer that occurs across a moving fluid in which a temperature gradient exists. Radiation, specially thermal radiation, refers to the heat transfer between two surfaces at different temperatures separated by a medium transparent to the electromagnetic waves emitted by surfaces.

Conduction heat transfer

When there exists a temperature gradient within a body, heat energy will flow from the region of high temperature to the region of low temperature. This phenomenon is known as conduction heat transfer, and is described by *Fourier's Law* (named after the French physicist *Joseph Fourier*),

$$\mathbf{q} = -k\nabla T \tag{1.12}$$

This equation determines the heat flux vector $\mathbf{q}$ for a given temperature profile T and thermal conductivity k. A heat flux is defined as the amount of heat transferred per unit area per unit time. The minus sign ensures that heat flows down the temperature gradient. The thermal diffusivity α is related to the thermal conductivity k, the specific heat C, and the density ρ by,

$$\alpha = \frac{k}{\rho C} \tag{1.13}$$

Convection heat transfer

For a steady state fluid at constant pressure or for fluids with a density independent of temperature, the heat transfer equation is given by

$$\alpha\nabla^2 T - \mathbf{v}\cdot\nabla T = 0 \tag{1.14}$$

Convection is usually the dominant form of heat transfer in liquids and gases. This is a term used to characterize the combined effects of conduction and fluid flow. In convection, heat transfer occurs by the movement of hot or cold portions of the fluid together with heat transfer by conduction. As this happens, cooler liquid or gas takes the place of the warmer areas which have risen higher. This cycle results in a continuous circulation pattern and heat is transfered to cooler areas. Two types of convection are commonly distinguished, free convection, in which gravity and buoyancy forces drive the fluid movement, and forced convection, where a fan, stirrer, or other means are used to move the fluid. Buoyant convection is due to the effects of gravity, and absent in microgravity environments.

Radiation heat transfer

Radiation is heat transfer by the emission of electromagnetic waves which carry energy away from the emitting object. The relationship governing radiation from hot objects is called the *Stefan-Boltzmann law*:

$$\mathbf{q} = \sigma\varepsilon\left(T^4 - T_a^4\right) \tag{1.15}$$

where ε is the emissivity, $\sigma = 5.6703 \times 10^{-8}\ Watt/m^2K^4$ the Stefan-Boltzmann constant and T_a the surrounding temperature. Radiation is the only form of heat transfer that can occur in the absence of any form of medium and as such is the only type of heat transfer through a vacuum. Thermal radiation is a direct result of the movements of atoms and molecules in a material. Since these atoms and molecules are composed of charged particles (protons and electrons), their movements result in the emission of electromagnetic radiation, which carries energy away from the surface. At the same time, the surface is constantly bombarded by radiation from the surroundings, resulting in the transfer of energy to the surface. Since the amount of emitted radiation increases with increasing temperature, a net transfer of energy from higher temperatures to lower temperatures results.

1.3 Numerical analysis

Numerical analysis is the study of problems using discrete mathematics. Some of the problems it deals with arise directly from the study of calculus; other areas of interest are real variable or complex variable questions, numerical linear algebra in real or complex fields, the solution of differential equations, and other related problems arising in physical sciences and engineering [11,12,16,17].

Many problems in mathematics do not possess an analytical solution. In these situations, one has two options: either one tries to find an approximate solution using asymptotic analysis or one seeks for a numerical solution. The latter choice describes the field of numerical analysis. Furthermore, problems must sometimes be replaced by a discrete problem whose solution is can be determined approximately; this process is called *discretization*. For example, the solution of a differential equation is a function. This function must be represented by a finite amount of data, for instance by its value at a finite number of points at its domain, even though this domain is a continuum.

The algorithms of numerical analysis are applied to solve many problems in science and engineering, e.g., in computational physics and computational fluid dynamics. In fact, almost all supercomputers are continually running numerical analysis algorithms. Numerical analysis is also concerned with computing (in an approximate way) the solution of differential equations, both ordinary differential equations and partial differential equations. Partial differential equations are solved by first discretizing the equation, bringing it into a finite-dimensional subspace. This can be done by a *finite element method*, a *finite difference method*, or (particularly in engineering) a *finite volume method*. The theoretical justification of these methods often involves theorems of functional analysis. The accuracy of these methods can be estimated a priory because of internal nonlinearities.

1.3.1 Finite element method

In numerical analysis, the finite element method (FEM) is used for solving partial differential equations (PDE) approximately. Solutions are approximated by either eliminating the differential equation completely (steady state problems), or rendering the PDE into an equivalent ordinary differential equation, which is then solved using standard techniques such as finite differences, etc. Finite element methods are used in a wide variety of engineering disciplines, e.g., electromagnetics and fluid dynamics.

In solving partial differential equations, the primary challenge is to create an equation which approximates the equation to be studied, but which is numerically stable, meaning that errors in the input data and intermediate calculations do not accumulate and cause the resulting output to be garbage. Finite element methods have also been developed to approximately solve integral equations such as the heat transport equation.

Several approximate numerical analysis methods have evolved over the years; a commonly used method is the finite difference scheme. The familiar finite difference model of a problem gives a pointwise approximation to the governing equations. This model (formed by writing difference equations for an array of grid points) is improved as more points are used. With finite difference techniques we can treat some fairly difficult problems; but, for example, when we encounter irregular geometries or an unusual specification of boundary conditions, we find that finite difference techniques become hard to use. Unlike the finite difference method, which envisions the solution region as an array of grid points, the finite element method envisions the solution region as built up of many small, interconnected subregions or elements. A finite element model of a problem gives a piecewise approximation to the governing equations. The basic premise of the finite element method is that a solution region can be analytically modeled or approximated by replacing it with an assemblage of discrete elements. Since these elements can be put together in a variety of ways, they can be used to represent exceedingly complex shapes. As an example of how a finite difference model and a finite element model might be used to represent a complex geometrical shape, consider the turbine blade cross section in Fig. 1.5. For this device we may want to find the distribution of displacements and stresses for a given force loading or the distribution of temperature for a given thermal loading. The interior coolant passage of the blade, along with its exterior shape, gives it a nonsimple geometry. A uniform finite difference mesh would reasonably cover the blade (the solution region), but the boundaries must be approximated by a series of horizontal and vertical lines (or "stair steps"). On the other hand, the finite element model (using the simplest two-dimensional element-the triangle) gives a better approximation to the region. Also, a better approximation to the boundary shape results because the curved boundary is represented by straight lines of any inclination. This example is not intended to suggest that finite element models are decidedly better than finite difference models for all problems. The only purpose of the example is to demonstrate that the finite element method is particularly well suited for problems with complex geometries [11,16,17,22].

In a continuum problem of any dimension, i.e. a body of matter (solid, liquid, or gas) or simply a region of space in which a particular phenomenon is occurring, the field variable (whether it is pressure, temperature, displacement, stress, or some other quantity) possesses infinitely many values. Because it is a function of each generic point in the body or solution region. Consequently, the problem is one with an infinite number of unknowns. The finite element discretization procedures reduce the problem to one of a finite number of unknowns by dividing the solution region into elements and by expressing the unknown field variable in terms of assumed approximating functions within each element. The approximating functions (sometimes called *interpolation functions*) are defined in terms of the values of the field variables at specified points called *nodes* or *nodal points*. Nodes usually lie on the element boundaries where adjacent elements are connected. In addition to boundary nodes, an element may also have a few interior nodes. The nodal values of the field variable and the interpolation functions for the

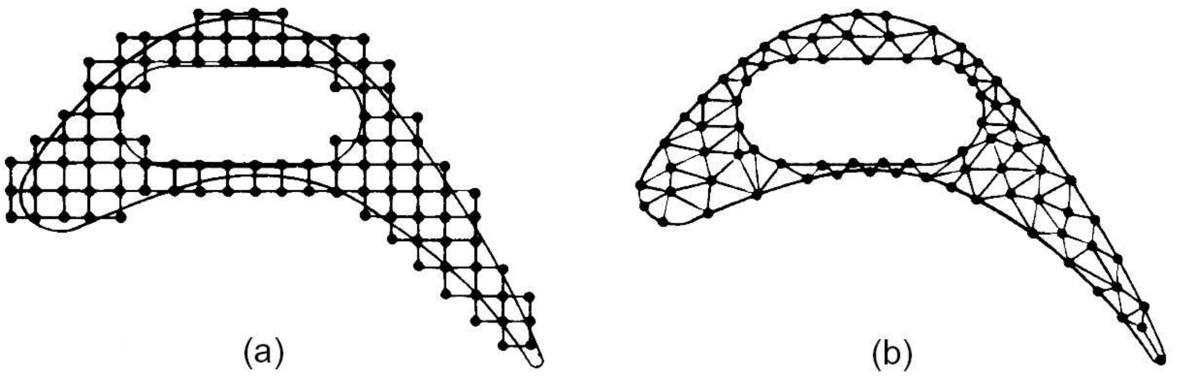

Fig. 1-5. (a) Finite difference and (b) finite element discretization of a turbine blade profile.

elements completely define the behavior of the field variable within the elements.

For the finite element representation of a problem the nodal values of the field variable become the unknowns. Once these unknowns are found, the interpolation functions define the field variable throughout the assemblage of elements. Clearly, the nature of the solution and the degree of approximation depend not only on the size and number of the elements used but also on the interpolation functions selected. As one would expect, we cannot choose functions arbitrarily, because certain compatibility conditions should be satisfied. Often functions are chosen so that the field variable or its derivatives are continuous across adjoining element boundaries. These are applied to the formulation of different kinds of elements.

A third and even more versatile approach to deriving element properties has its basis in mathematics and is known as the *weighted residuals approach.* The weighted residuals approach begins with the governing equations of the problem and proceeds without relying on a variational statement. This approach is advantageous because it thereby becomes possible to extend the finite element method to problems where no functional is available. The method of weighted residuals is widely used to derive element properties for nonstructural applications such as heat transfer and fluid mechanics. Regardless of the approach used to find the element properties, the solution of a continuum problem by the finite element method always follows an orderly step-by-step process. To summarize in general terms how the finite element method works we will succinctly list these steps as follow,

1. *Discretize the Continuum.* The first step is to divide the continuum or solution region into elements. In the example of Figure 1.5 the turbine blade has been divided

into triangular elements that might be used to find the temperature distribution or stress distribution in the blade. A variety of element shapes may be used, and different element shapes may be employed in the same solution region. Indeed, when analyzing an elastic structure that has different types of components such as plates and beams, it is not only desirable but also necessary to use different elements in the same solution. Although the number and the type of elements in a given problem are matters of engineering judgment, the analyst can rely on the experience of others for guidelines.

2. *Select Interpolation Functions.* The next step is to assign nodes to each element and then choose the interpolation function to represent the variation of the field variable over the element. The field variable may be a scalar, a vector, or a higher-order tensor. Often, polynomials are selected as interpolation functions for the field variable because they are easy to integrate and differentiate. The degree of the polynomial chosen depends on the number of nodes assigned to the element, the nature and number of unknowns at each node, and certain continuity requirements imposed at the nodes and along the element boundaries. The magnitude of the field variable as well as the magnitude of its derivatives may be the unknowns at the nodes.

3. *Find the Element Properties.* Once the finite element model has been established (that is, once the elements and their interpolation functions have been selected), we are ready to determine the matrix equations expressing the properties of the individual elements. For this task we may use one of the three approaches just mentioned: the direct approach, the variational approach, or the weighted residuals approach.

4. *Assemble the Element Properties to Obtain the System Equations.* To find the properties of the overall system modeled by the network of elements we must "assemble" all the element properties. In other words, we combine the matrix equations expressing the behavior of the elements and form the matrix equations expressing the behavior of the entire system. The matrix equations for the system have the same form as the equations for an individual element except that they contain many more terms because they include all nodes. The basis for the assembly procedure stems from the fact that at a node, where elements are interconnected, the value of the field variable is the same for each element sharing that node. A unique feature of the finite element method is that the system equations are generated by assembly of the individual element equations. In contrast, in the finite difference method the system equations are generated by writing nodal equations.

5. *Impose the Boundary Conditions.* Before the system equations are ready for solution they must be modified to account for the boundary conditions of the problem. At this stage we impose known nodal values of the dependent variables or nodal loads.

6. *Solve the System Equations.* The assembly process gives a set of simultaneous

equations that we solve to obtain the unknown nodal values of the problem. If the problem describes steady or equilibrium behavior, then we must solve a set of linear or nonlinear algebraic equations. If the problem is unsteady, the nodal unknowns are a function of time, and we must solve a set of linear or nonlinear ordinary differential equations.

7. *Make Additional Computations if Desired.* Many times we use the solution of the system equations to calculate other important parameters. For example, in a structural problem the nodal unknowns are displacement components. From these displacements we calculate element strains and stresses. Similarly, in a heat-conduction problem the nodal unknowns are temperatures, and from these we calculate element heat fluxes.

The seven steps mentioned above have to be carried out before any meaningful information can be obtained regardless of the size and complexity of the problem to be solved.

It is worth making one final comment on the finite element method. It can be shown readily that the finite element solution is often the best approximation to the analytic answer, in terms of minimizing some integral norm of the difference between the answer and its approximation. This is often used as an alternative approach to derive the finite element equations. It is also perhaps the easiest way to see the following important fact:

If the solution is rapidly varying in some region of space then it is necessary to have relatively more elements in that region to model the behavior of the solution accurately in that region.

1.3.2 Galerkin Method

A general boundary value problem (BVP) consists of an ordinary differential equation (ODE) with side conditions specified at more than one point. This module illustrates the solution of second-order scalar ODEs of the form

$$u'' = f\left(t, u, u'\right) \tag{1.16}$$

on an interval $[a, b]$ with boundary conditions $u(a) = \alpha$ and $u(b) = \beta$. The *Galerkin method* approximates the solution to the BVP by a linear combination of basis functions determined by requiring that the residual be orthogonal to each of the homogeneous basis functions, i.e., those that vanish on the boundary, and that the boundary conditions be satisfied.

Let $\varphi_1, \ldots, \varphi_n$ be a set of basis functions. We will approximate the solution to the boundary value problem by a linear combination $v(t, \mathbf{x}) = x_1\varphi_1(t) + ... + x_n\varphi_n(t)$ of the basis functions, where the vector $\mathbf{x}$ of coefficients is to be determined. The coefficients of the homogeneous basis functions (i.e., $\varphi_i(a) = \varphi_i(b) = 0$) are determined by an orthogonality condition, while the coefficients of the inhomogeneous basis functions are chosen to satisfy the boundary conditions. The orthogonality condition requires that for each homogeneous basis function φ_i,

$$\int_a^b v''(t,x)\,\varphi_i(t)\,\mathrm{d}t = \int_a^b f\left(t, v(t,x), v'(t,x)\right)\varphi_i(t)\,\mathrm{d}t \tag{1.17}$$

Integrating the left side by parts and using homogeneity, we can replace $v''(t,\mathbf{x})\varphi_i(t)$ by $-v'(t,\mathbf{x})\varphi_i'(t)$, which lowers the differentiability requirements on the basis functions:

$$-\int_a^b v'(t,x)\,\varphi_i'(t)\,\mathrm{d}t = \int_a^b f\left(t, v(t,x), v'(t,x)\right)\varphi_i(t)\,\mathrm{d}t \tag{1.18}$$

The result is a system of equations that can be solved for the coefficients $\mathbf{x}$ of the approximate solution $v(t,\mathbf{x})$. This system of equations will be nonlinear if the function f is nonlinear. The necessary integrals can be evaluated by numerical quadrature, and the accuracy of the solution will be affected by the accuracy of this numerical integration. The equation (1.16) along with the natural and essential boundary conditions is called the *strong form* of the equations and the equation (1.18) is often called the *weak form*. Note that the weak form implicitly contains the natural boundary condition while the essential boundary condition must be stated separately.

1.3.3 Green's theorem

In physics and mathematics, *Green's theorem* gives the relationship between a line integral around a simple closed curve $\mathcal{C}$ and a double integral over the plane region $\mathcal{D}$ bounded by $\mathcal{C}$. Green's theorem was named after British scientist George Green and is a special case of the more general *Stokes' theorem*.

The theorem statement is the following. Let $\mathcal{C}$ be a positively oriented, piecewise smooth, simple closed curve in the plane and let $\mathcal{D}$ be the region bounded by $\mathcal{C}$. If $L(x,y)$ and $M(x,y)$ have continuous partial derivatives on an open region containing $\mathcal{D}$, then

$$\oint_{\mathcal{C}} L\,\mathrm{d}x + M\,\mathrm{d}y = \iint_{\mathcal{D}} \left(\frac{\partial M}{\partial x} - \frac{\partial L}{\partial y}\right)\mathrm{d}x\,\mathrm{d}y \tag{1.19}$$

where the left hand side is a line integral and the right hand side is an area integral.

1.3.4 ENTWIFE package

ENTWIFE is a finite-element computer program for solving systems of partial differential equations [21-22]. ENTWIFE has extensive capabilities for analysing nonlinear problems that may exhibit bifurcation phenomena. The program can be used to compute solution branches, various bifurcation points, and paths of bifurcation points. It can also be used to examine the stability of previously computed solutions using eigenvalue techniques. The package is based on an efficient implementation of the finite element method that provides many options for modeling the behavior of complex physical, chemical and biological systems. The ENTWIFE code provides the facility for automatically generating finite element computer code from a model specification in the form of the model equations. This allows different models to be easily explored. In addition of a build-in library of equations relating to fluid flow and heat transfer processes, ENTWIFE has a special and important feature called *user equation.* This useful facility, in particular, allows the user to define the set of equations to be analyzed, i.e. it provides the possibility of solving any set of user equations which may be not previously defined within ENTWIFE. This prominent part may be contrasted with similar packages which can only solve the prearranged equations and boundary conditions and so they can not accept any new equation or boundary condition. This special attraction makes the ENTWIFE to be more powerful and flexible than other similar packages. In addition, a pre-processor, called ENTCODE, provides an interface to computer algebra packages (Mathematica, Maple and REDUCE) that can be used to generate the required FORTRAN subroutines which calculate the Jacobian and derivatives of the nonlinear system under study. This pre-processor, makes ENTWIFE an extremely powerful tool for investigating new physical models. ENTWIFE will run on most Unix workstations, including machines running Linux, Fig. 1-6.

The software is written in FORTRAN. Problems are defined using a simple -to-use high level Command Language. ENTWIFE has been extensively verified and is widely used in the analysis of practical problems. The code has also several other features as:

- modeling of non-linear systems in one, two and three spatial dimensions, or a mixture of these;
- modeling of *mixed physics* where different physical equations apply in different subregions;
- many options for grid generation, including local refinement, deletion, redistribution and re-numbering of elements, and matching to complex boundaries;
- a wide range of finite-element types (i.e. more than 50) is available. It is easy to change the element and the interpolation scheme being used for the variables in a problem;
- a number of different time-stepping algorithms;

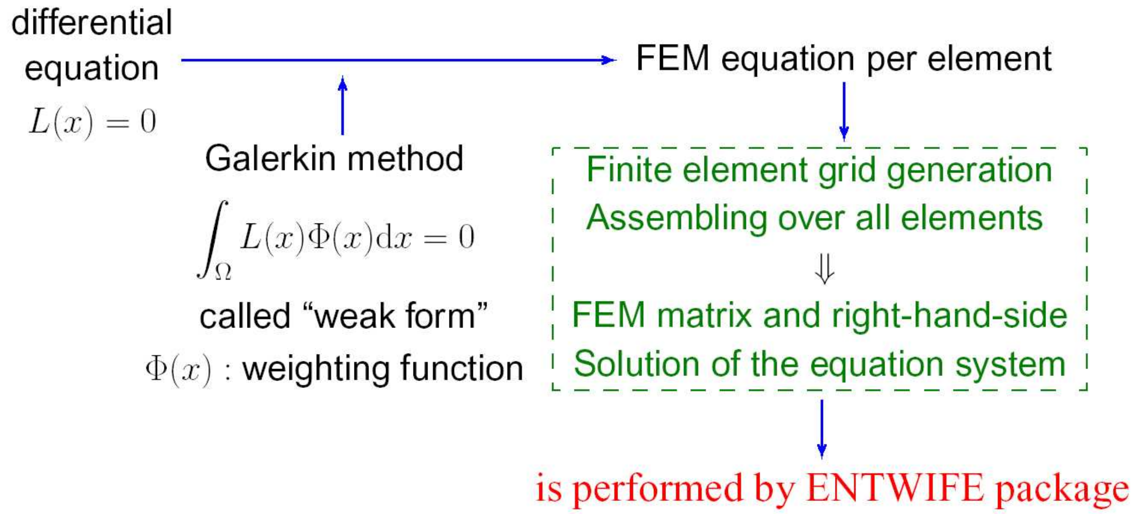

Fig. 1-6. The role of ENTWIFE package for solving partial differential equations using finite element method.

- the Gauss scheme used to evaluate the integrals appearing in the weak form can be changed. ENTWIFE has a number of Gauss schemes available, and it is easy to implement new schemes;
- a wide range of output options including plots of contours, vectors, tensors, streamlines and pathlines in 2D and 3D.

In the work presented here, we use ENTWIFE to find the solutions of the governing equations. The distribution and number of elements used in every case was chosen after careful studies of mesh refinement using the element bisect concept. The discrete equations are solved using a *Newton-Raphson method* combined with the frontal solver MUMPS (*MUltifrontal Massively Parallel sparse direct Solver*) for the linear system arising from this method.

1.4 Scope of the present work

The motivation behind the present work is to explore in detail the induction heating and the basic transport process during the seeding process of the Czochralski crystal growth method, the interaction among the transport processes and their influence on the growth of high quality oxide crystals in particular sapphire crystal. With this objective, a two-dimensional and three-dimensional quasi-steady state mathematical model incorporating all of the important phenomena of the Czochralski environment are developed. The model incorporates induction heating, fluid flow and heat transfer mechanisms in the melt, the seed and the gas phase, the metal crucible and afterheater, and insulation in the enclosure. Transport mechanisms considered are conduction and convection in the melt as well as in the gas, conduction within the seed crystal, the crucible, afterheater and the insulation, and radiative exchange from the melt-gas interface as well as the outer surfaces of the system. Since sapphire seed crystals are semi-transparent and small in radius, absorption, emission and scattering in the crystal and melt have been neglected.The geometry and orientation of coil-crucible-afterheater-insulation, and the seed-melt interface shape and its changes during the seeding process are important factors that determine the quality of grown crystal. Special emphasizes have been given to understand the influence of system design on the final temperature and flow field and interface movement throughout the work. The presence of an active afterheater, its location and geometry due to various transport mechanisms are carefully analyzed. In addition, the influence of an open observation window located in the afterheater and its insulation is investigated using a three-dimensional calculation.

1.5 Thesis organization

The present thesis has been organized in the following manner:

▶ Chapter 2 describes the mathematical formulation used in the present work for modeling the induction heating in the Czochralski system, including electromagnetic field and heat generation, and shows results for some different geometries and orientations of metallic parts, i.e. crucible, afterheater and RF coil.

▶ Chapter 3 presents the two-dimensional quasi-steady state mathematical model and results for some different configurations of oxide Czochralski furnace containing only gas, by application of the internal heat generation in the crucible and afterheater. The goal of these calculation is to study and investigate the influence of geometry and orientation of crucible, afterheater and insulation on the overall heat transport in the CZ system.

▶ Chapter 4 describes the two-dimensional quasi-steady state mathematical formulation and results for some different Czochralski systems containing the oxide melt and gas, by means of induction heating as heat source term. The aim of the work in this chapter is to develop a global analysis of an inductively heated CZ furnace for real oxide crystal growth systems just before the seeding process, and to reveal the effect of an active afterheater and a gap (closed and open) between the crucible and afterheater, the melt level, and the crucible with different bottom shapes (flat and round) on the heat transport mechanism of the system.

▶ Chapter 5 explains the two-dimensional quasi-steady state mathematical model and results for different steps of the seeding process of oxide Czochralski crystal growth, and helps to reveal the effect of an active afterheater, a crucible with different bottom shapes (flat and round), and different positions of the seed crystal with respect to the melt surface on the heat transport mechanisms of the seed, melt and gas. Different seed rotation rates and their influences on the heat transfer mechanism as well as seed-melt interface shape are carefully studied.

► Chapter 6 explains the mathematical description and results of three-dimensional calculations of heat generation, temperature and flow field in a CZ system. This three-dimensional quasi-steady state numerical modeling has been performed to investigate and reveal the influence of an observation window on the heat transfer mechanism of the Czochralski furnace containing only gas.

► Conclusions drawn from the present study are summarized.

Chapter 2

Induction heating

2.1 Introduction

The Czochralski (CZ) crystal growth technique frequently utilizes the principle of induction heating to supply the required thermal power to the melt. This power is generated by induction heater coils that surround the metal crucible. An alternating current is passed through the coils. This azimuthal current produces an approximately orthogonal time-varying magnetic field outside the coils (Amperes law) which in turn generates (induces) an oscillating azimuthal electric field (Faraday's law). Both fields penetrate the metal crucible, to an extent that depends on the electrical conductivity of the metal. The electric field within the metal walls causes a parallel current flow (Ohm's law) and the product of the electric field strength with the current describes the rate of energy dissipation in the metal - the familiar I^2R heating - in the form of temporal and spatial volumetric heating. This internal heat generation is partly conducted into the melt - at the inner wall and bottom of the crucible - and partly lost to the surroundings [1,19].

In order to gain a better understanding of the entire CZ process as applied to the growth of oxide crystals (e.g., YAG, sapphire, GGG), which includes various modes of heat transfer and a complex range of fluid dynamic phenomena, the simulation of the CZ growth is necessary. The simulation can not be complete without a proper description of the source term for crystal growth - power supplied to the melt. Indeed one could argue that no thermal modeling should begin until the induction heating process is properly simulated.

2.2 Mathematical model

2.2.1 Governing equations

Assuming that media are stationary, isotropic, and linear in their electromagnetic properties (e.g. no iron is permitted), the governing *E&M* equations are the so-colled Maxwell equations, written here in the "rmks" units (rationalized meter-kilogram-second-coulomb) [1,13]:

$$\nabla \cdot (\epsilon \mathbf{E}) = \rho \tag{2.1}$$

$$\nabla \cdot \mathbf{B} = 0 \tag{2.2}$$

$$\nabla \times \left(\frac{1}{\mu} \mathbf{B} \right) = \mathbf{J} + \frac{\partial (\epsilon \mathbf{E})}{\partial t} \tag{2.3}$$

$$\nabla \times \mathbf{E} = -\frac{\partial \mathbf{B}}{\partial t} \tag{2.4}$$

where $\mathbf{E}$ is the electric field intensity vector ($volts/meter = newton/coulomb$), ϵ is the permittivity ($coulomb/volt{\cdot}meter$), ρ is the density of free charge ($coulomb/m^3$), $\mathbf{B}$ is the magnetic flux density vector ($Weber/m^2 = volt{\cdot}sec/m^2$), μ is the magnetic permeability ($volts \cdot sec/ampere$), and $\mathbf{J}$ is the free charge current density vector ($ampere/m^2$). $\mathbf{J}$ will be a specified quantity in the induction coil (the "*source*" term) and will be given by Ohm's law,

$$\mathbf{J} = \sigma_e \mathbf{E} \tag{2.5}$$

elsewhere, where σ_e is the electrical conductivity ($amperes/volt\ meter \equiv mho/m$) of the medium.

The first simplification to these equations is, $\partial (\epsilon \mathbf{E}) / \partial t$, so-called displacement current term, is completely negligible in our context since it is important only when the wavelength is of comparable (or shorter) size to that of the system in question. At the 10 kHz frequency of the induction heating system, this length ($\lambda = c/f$) is $\sim 30\ km$.

We now state quantitatively the objective of this analysis: compute the power dissipated in the metal crucible, which power is given by

$$P = \mathbf{J} \cdot \mathbf{E} = \sigma_e E^2 \tag{2.6}$$

in $Watt/m^3$ and is generally a function of space and time.

In our system, we have no charges $\rho = 0$ and in our model we assume constant ϵ, μ, and σ_e; the latter being thus far taken as zero in all materials except the conductors. Also, we have no magnetic materials, μ is everywhere the same constant - the permeability of free space (i.e. $\mu = \mu_0 = 4\pi \times 10^{-7} wb/A \cdot m$).

Introducing the vector potential, $\mathbf{A}$, via

$$\mathbf{B} = \nabla \times \mathbf{A} \tag{2.7}$$

along with the convenient "*gauge condition*" that $\nabla \cdot \mathbf{A} = 0$, it follows that

$$\mathbf{E} = -\frac{\partial \mathbf{A}}{\partial t} \tag{2.8}$$

$$\nabla^2 \mathbf{A} = -\mu \mathbf{J} \tag{2.9}$$

so that the problem is reduced to one of finding $\mathbf{A}$ - assuming $\mathbf{J}$ is known. In our model, we assume that $\mathbf{J}$ is in fact known in the induction heater coil, is related to $\mathbf{E}$ via Ohm's law (2.5) in the conductors, and is zero in the non-conductors. But (2.9) is still a three-dimensional vector equation, whose solution is intractable. On the other hand, the goal of a CZ experiment and a guiding feature in its design, is to attain axisymmetric behavior in all relevant quantities, and this must include the $E\&M$ fields. Hence we now invoke the assumption of axisymmetry so that all quantities are independent of the azimuthal coordinate, ϕ. One further modeling assumption, that is physically reasonable and computationally very cost-effective, is to ignore the helicity (pitch) of the heater coils and thus assume that $\mathbf{J} = \mathbf{e}_\phi J_\phi$; i.e., the current flows only in the azimuthal direction - both in the coil and (via induction) in the conductors. This leads to the simplification that $A_r = A_z = 0$ and $B_\phi = E_r = E_z = 0$, the only non-zero field variables are thus A_ϕ, E_ϕ, B_r, and B_z. Thus the (scalar) governing equation is now simply

$$\frac{\partial}{\partial r}\left[\frac{1}{r}\frac{\partial}{\partial r}\left(rA_\phi\right)\right] + \frac{\partial^2 A_\phi}{\partial z^2} = -\mu J_\phi \tag{2.10}$$

from which

$$E_\phi = -\frac{\partial A_\phi}{\partial t}$$

$$B_r = -\frac{\partial A_\phi}{\partial z}$$

$$B_z = \frac{1}{r}\frac{\partial \left(rA_\phi\right)}{\partial r}$$

While (2.10) is ostensibly in a form useful for numerical approximation, it is somewhat more useful to introduce a *" magnetic stream function"*, $\psi_B\left(r, z, t\right) \equiv rA_\phi\left(r, z, t\right)$, to give [35,37,38]

$$\frac{\partial}{\partial r}\left(\frac{1}{r}\frac{\partial \psi_B}{\partial r}\right)+\frac{\partial}{\partial z}\left(\frac{1}{r}\frac{\partial \psi_B}{\partial z}\right)=-\mu J_\phi \tag{2.11}$$

which is the equation that will be solved numerically - once J_ϕ and boundary conditions are specified (the magnetic field "*flows*" along lines of constant ψ_B; $B \cdot \nabla \psi_B = 0$).

Setting

$$J_\phi = J_0 \cos \omega t$$

as the driving current in the coil, and

$$J_\phi = \sigma_e E_\phi = -\sigma_e \frac{\partial A_\phi}{\partial t} = -\sigma_e \frac{1}{r}\frac{\partial \psi_B}{\partial t}$$

in the conductors, leads to a solution of the form

$$\psi_B\left(r,z,t\right) = C\left(r,z\right)\cos \omega t + S\left(r,z\right)\sin \omega t \tag{2.12}$$

where $C\left(r,z\right)$ is the in-phase component and $S\left(r,z\right)$ is the out-of-phase component of the solution. The final coupled second-order elliptic equations are thus

$$\frac{\partial}{\partial r}\left(\frac{1}{r}\frac{\partial C}{\partial r}\right)+\frac{\partial}{\partial z}\left(\frac{1}{r}\frac{\partial C}{\partial z}\right) = \begin{cases} -\mu J_0 & \text{in the coil} \\ \dfrac{\mu\sigma_e\omega}{r}S & \text{in the conductors} \\ 0 & \text{elsewhere} \end{cases} \tag{2.13}$$

$$\frac{\partial}{\partial r}\left(\frac{1}{r}\frac{\partial S}{\partial r}\right)+\frac{\partial}{\partial z}\left(\frac{1}{r}\frac{\partial S}{\partial z}\right) = \begin{cases} 0 & \text{in the coil} \\ -\dfrac{\mu\sigma_e\omega}{r}C & \text{in the conductors} \\ 0 & \text{elsewhere} \end{cases} \tag{2.14}$$

The quantity $\sqrt{\mu\sigma_e\omega}$ has the dimensional of inverse meters and $\delta = \sqrt{2/\mu\sigma_e\omega}$ is called the *skin depth* and is a measure of the field penetration depth into the conductors.

For the boundary conditions, in the limit of $r \longrightarrow \infty$, there are no fields and herein we take the pragmatic approach that ψ_B (i.e. C and S goes to zero far from the coil and the only remaining issue is to define "*far*". We shall define "*far*" as the outer region of our computational domain (i.e. out of the CZ furnace) because the presence of a conducting chamber wall reduces strongly the $E\&M$ fields. Also, symmetry conditions for equation (2.13) and (2.14) require that each component vanish at the centerline. Thus, the boundary conditions are

$$C = S = 0 \begin{cases} for \quad r = 0 \\ \\ as \quad (r, z) \longrightarrow \infty \end{cases} \tag{2.15}$$

Upon solving (2.13) and (2.14) for $C\,(r, z)$ and $S\,(r, z)$, the energy dissipation rate can be computed via

$$\begin{aligned} P\,(r, z, t) &= \sigma_e E_\phi^2 = \sigma_e \left(\frac{\partial A_\phi}{\partial t}\right)^2 = \frac{\sigma_e}{r^2}\left(\frac{\partial \psi_B}{\partial t}\right)^2 \\ &= \frac{\sigma_e \omega^2}{r^2}\,(S\cos\omega t - C\sin\omega t)^2 \\ &= \frac{\sigma_e \omega^2}{r^2}\left(C^2 + S^2 - CS\sin 2\omega t\right) \end{aligned}$$

Power is deposited into the crucible as a time-harmonic spatial function with twice the frequency of the driving current. The period for this time-dependence is $2\pi/\omega = 10^{-4}s$ for a 10 kHz induction system. Since the time-harmonic function is so short, we represent the heat generation by the time averaged quantity, which we average over one period to obtain the volumetric heat generation rate,

$$\begin{aligned} q\,(r, z) &= \frac{\omega}{2\pi}\int_0^{2\pi/\omega} P\,(r, z, t)\ \mathrm{d}t \\ &= \frac{\sigma_e \omega^2}{2r^2}\left(C^2 + S^2\right) \end{aligned} \tag{2.16}$$

This is the function that will be used as a source term in the heat transport equation.

The above induction heating model incorporates RF coil and metallic parts configuration into the numerical simulations of Czochralski crystal growth system, making it possible to numerically study the effects of setup geometry on the heat generation and heat transfer mechanism in the system. An important and useful feature of this model is that the governing equations for the components of the magnetic stream function, equations (2.13) and (2.14), are linear with respect to the applied coil current density J_0, therefore the magnitudes of $C\,(r, z)$ and $S\,(r, z)$ scale linearly with the coil current. It therefore follows from equation (2.15) that the heat generation in the crucible q scales with J_0^2. The induction generator power to the coil is $R_{coil}\langle I_0\rangle^2$, where R_{coil} is the resistivity of the coil circuit and $\langle I_0\rangle$ is the rms current to the coil ($R_{coil} = I_0 \mathrm{A}_{\mathrm{coil}}/\sqrt{2}$, where A$_{\text{coil}}$ is the cross-sectional area of the coil turn). This leads to the simple relation that the power delivered to the crucible is linearly proportional to the power measured at the coil.

2.2.2 Weak form calculation

The weak form of the equations (2.13) and (2.14) for $C\left(r,z\right)$ and $S\left(r,z\right)$ are

$$\iint\left[\frac{\partial}{\partial r}\left(\frac{1}{r}\frac{\partial C}{\partial r}\right)+\frac{\partial}{\partial z}\left(\frac{1}{r}\frac{\partial C}{\partial z}\right)\right]\Phi_c\; r\,\mathrm{d}r\,\mathrm{d}z$$

$$=\begin{cases}-\mu J_0\iint\Phi_c\; r\,\mathrm{d}r\,\mathrm{d}z & \text{in the coil}\\ \mu\sigma_e\omega\iint S\Phi_c\; r\,\mathrm{d}r\,\mathrm{d}z & \text{in the conductors}\\ 0 & \text{elsewhere}\end{cases}\tag{2.17}$$

$$\iint\left[\frac{\partial}{\partial r}\left(\frac{1}{r}\frac{\partial S}{\partial r}\right)+\frac{\partial}{\partial z}\left(\frac{1}{r}\frac{\partial S}{\partial z}\right)\right]\Phi_s\; r\,\mathrm{d}r\,\mathrm{d}z$$

$$=\begin{cases}0 & \text{in the coil}\\ -\mu\sigma_e\omega\iint C\Phi_s\; r\,\mathrm{d}r\,\mathrm{d}z & \text{in the conductors}\\ 0 & \text{elsewhere}\end{cases}\tag{2.18}$$

respectively, where Φ is an appropriate test function. By using Green's theorem and integral by parts, the final weak form equations for C and S are

$$\iint\left(\frac{\partial C}{\partial r}\frac{\Phi_c}{r}+\frac{\partial C}{\partial r}\frac{\partial\Phi_c}{\partial r}+\frac{\partial C}{\partial z}\frac{\partial\Phi_c}{\partial z}\right)\,\mathrm{d}r\,\mathrm{d}z$$

$$=\begin{cases}-\mu J_0\iint\Phi_c\; r\,\mathrm{d}r\,\mathrm{d}z & \text{in the coil}\\ \mu\sigma_e\omega\iint S\Phi_c\; r\,\mathrm{d}r\,\mathrm{d}z & \text{in the conductors}\\ 0 & \text{elsewhere}\end{cases}\tag{2.19}$$

$$\iint \left(\frac{\partial S}{\partial r} \frac{\Phi_s}{r} + \frac{\partial S}{\partial r} \frac{\partial \Phi_s}{\partial r} + \frac{\partial S}{\partial z} \frac{\partial \Phi_s}{\partial z} \right) \, \mathrm{d}r \, \mathrm{d}z$$

$$= \begin{cases} 0 & \text{in the coil} \\ -\mu \sigma_e \omega \iint C \Phi_s \, r \, \mathrm{d}r \, \mathrm{d}z & \text{in the conductors} \\ 0 & \text{elsewhere} \end{cases} \tag{2.20}$$

For the volumetric heat generation rate $q\,(r, z)$ (equation (2.16)), the weak form is simply

$$\iint \left[q - \frac{\sigma_e \omega^2}{2r^2} \left(C^2 + S^2 \right) \right] \Phi_q \; r \, \mathrm{d}r \, \mathrm{d}z = 0 \tag{2.21}$$

Thus, the equations (2.19) – (2.21) are the equations to be solved by finite element method and, for our purposes using ENTWIFE.

2.2.3 Numerical method

We employed the finite element method (ENTWIFE package[21-22]), using the standard Galerkin formulation for solution of the governing equations. The distribution and number of used elements were chosen after a careful study in order to obtain a sufficiently accurate approximation of the solution. The discrete equations are solved using a Newton-Raphson method combined with the frontal solver MUMPS (*MUltifrontal Massively Parallel sparse direct Solver*[23]) for the linear system arising from this method. Since the equations are linear, only one iteration is necessary.

2.2.4 The calculation conditions

Values of electrical conductivity employed for our calculations are presented in Table 2-1 [14,15,19] and operating parameters are listed in Table 2-2. The induction coil has two parts with 6 and 1 hollow rectangular- shaped copper turns, respectively. In a real growth system this coil is usually cooled very efficiently by water flowing inside the coil turns. Therefore it is realistic to assume that the coil is always at room temperature. For the calculations we have assumed an electrical current in the coil of 1000 A with a frequency of 10 kHz. For the magnetic permeability (μ) we assume that it is everywhere the constant value of free space $\mu = \mu_r \mu_0 \simeq \mu_0$ (i.e. $\mu_r \simeq 1$) where μ_r is the relative magnetic permeability. The results based on this set of parameters will be presented in

Symbel	Value	Reference
σ_e^{co}	5.9×10^5	[3]
σ_e^{cr}	1.72×10^4	[2]
σ_e^{ch}	4.0×10^4	[1]

Table 2-1. Values of electrical conductivity (mho/cm) used in our calculations; the subscripts co, cr and ch denote coil (*copper*), crucible (*iridium*) and chamber (*stainless steel*), respectively.

the next part of this chapter.

2.3 Results and discussion

For the employed frequency of 10 kHz, the skin depth $\left(\delta = \sqrt{2/\mu\sigma_e\omega}\right)$ is 1.6 mm for Iridium crucible and afterheater and 2.5 mm for stainless steel chamber, which is neither "very small" nor " very large" compared to the wall thickness of crucible (2 mm) and chamber ($\sim$ 1 cm).

In order to find a good information of the induction heating in the CZ system, we have considered these cases:

case a: crucible, no afterheater,
case b: crucible and afterheater, no gap,
case c: crucible and afterheater, no gap, change in the radius of the RF coil,
case d: crucible and afterheater, no gap, separate turns of RF coil (N=6),
case e: crucible and afterheater, no gap, separate turns of RF coil (N=3),
case f: crucible and afterheater, no gap, round crucible edge,
case g: crucible and afterheater, with a gap,
case h: crucible and afterheater, with a gap, separate turns of RF coil (N=6),
case i: crucible and afterheater, with a gap, separate turns of RF coil (N=3),

In all cases the induction coil and chamber have been taken into account.

2.3.1 case a: Crucible, no afterheater

In the first case, there are crucible, RF coil and chamber in the CZ system. The simplest "equivalent cylinder" model of the 6-turn coil was employed for the simulation, i.e. rather than model each individual coil, the total current was assumed to flow uniformly through a single right cylindrical annulus.

Description (units)	Symbel	Value
Crucible inner radius (mm)	r_c	49
Crucible thickness (mm)	l_c	2
Crucible inner height (mm)	h_c	98
Afterheater inner height (mm)	h_{af}	100
Afterheater hole (mm)	r_{af}	10
Gap between crucible and afterheater (mm)	D_{ca}	0, 20
Coil inner radius (mm)	r_{co}	85, 95
Coil thickness (mm)	l_{co}	10
Coil wall thickness (mm)	s_{co}	1
Height of coil turns (mm)	h_{co}	20
Distance between coil turns (mm)	d_{co}	3, 37.5
Distance between two coils (mm)	D_{co}	55
Current frequency of RF coil (kHz)	f	10
Electrical current in RF coil (A)	I_d	1000

Table 2-2. Operating parameters used for calculations.

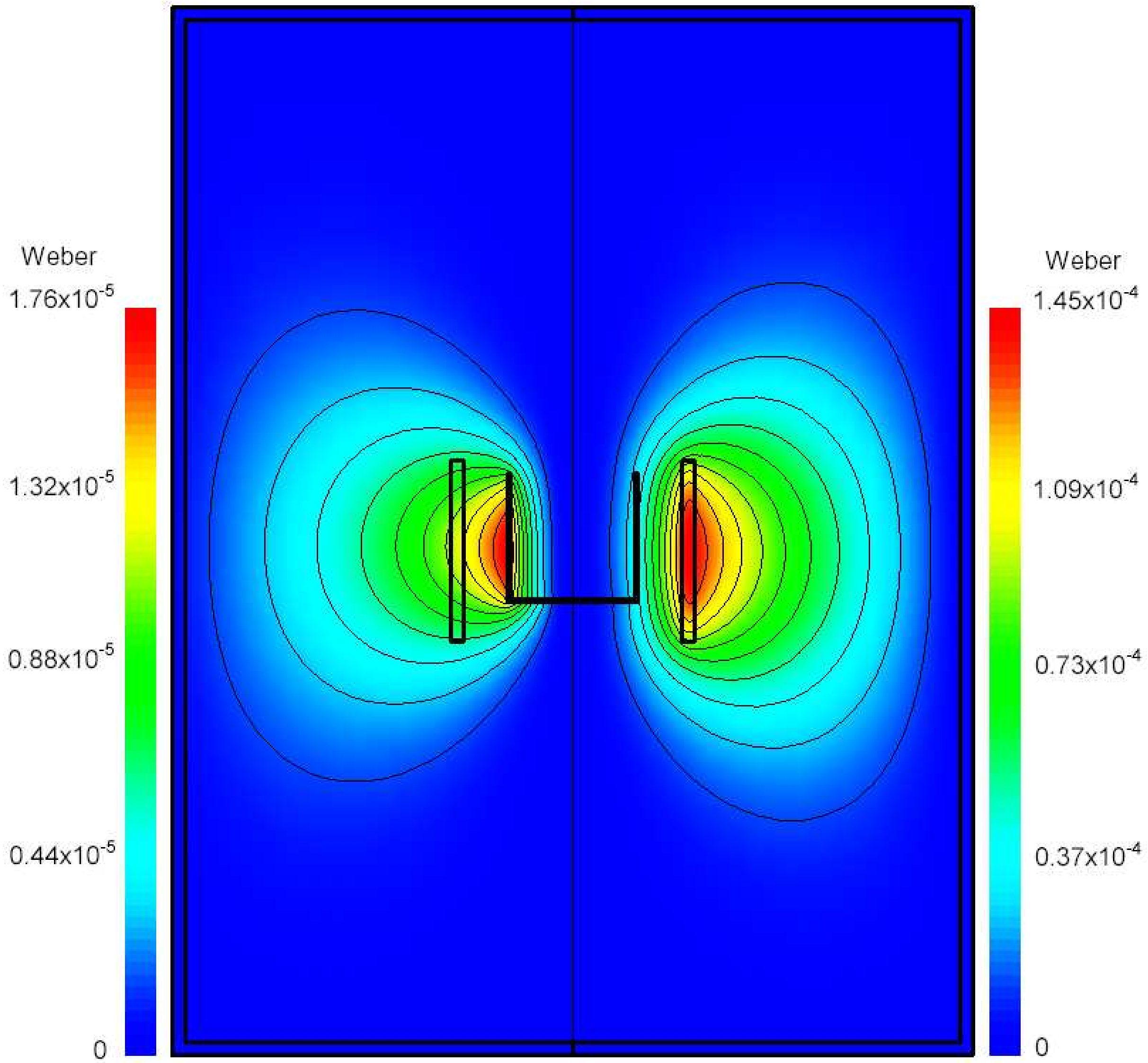

Fig. 2-1. Components of the magnetic stream function (ψ_B) calculated for *case a*. The right hand side shows the in-phase component (C), with $C_{max} = 1.45 \times 10^{-4}$ $Weber$ located in the coil and the left hand side shows the out-of-phase component (S), with $S_{max} = 1.76 \times 10^{-5}$ $Weber$ located at the crucible wall.

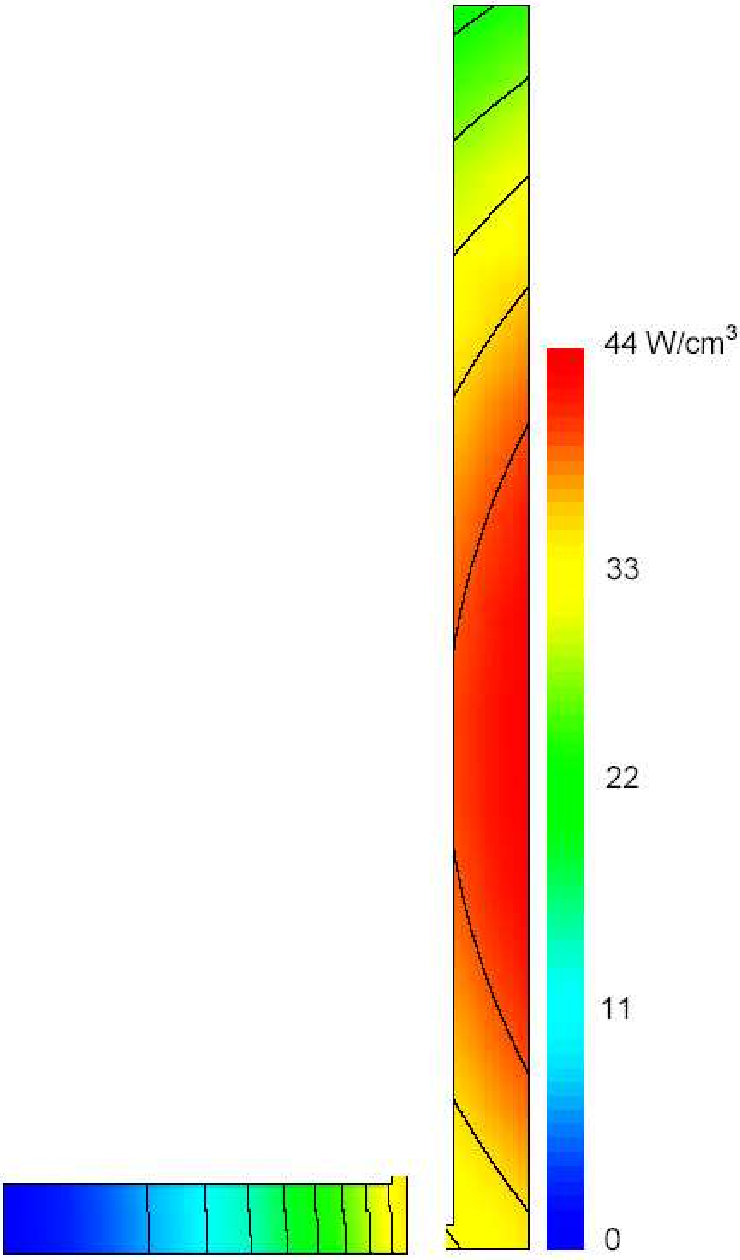

Fig. 2-2. Contours of the volumetric power distribution (q) in the bottom and side wall of crucible, computed for *case a* (for a better demonstration the wall and bottom part are separately magnified). The maximum value of energy deposition is $q_{max} = 44\ Watt/cm^3$ and it is located at the outer surface of crucible wall.

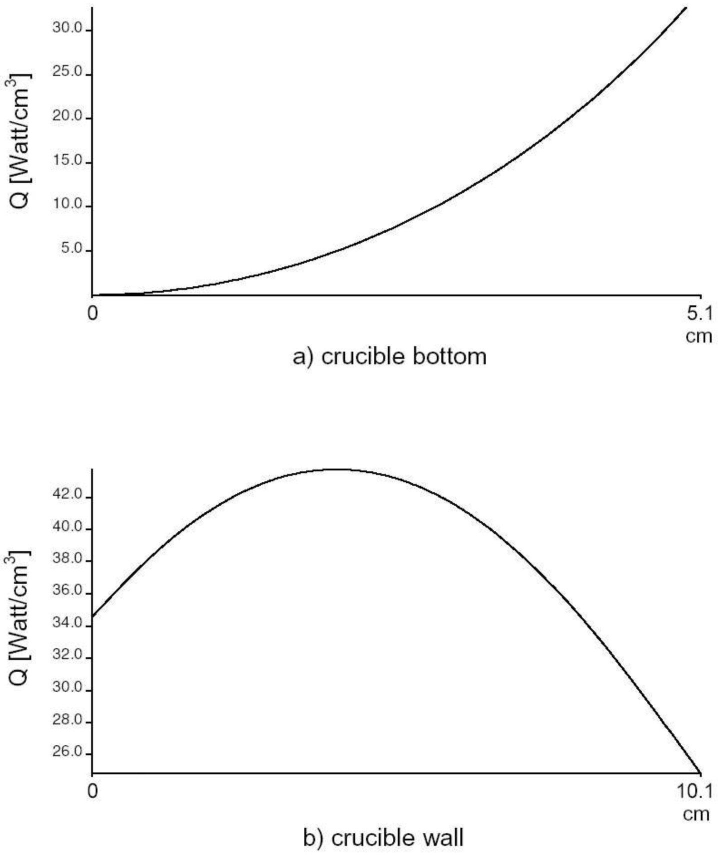

Fig. 2-3. Profiles of the heat generated along the outer surface of crucible bottom and side wall calculated for *case a*, (a) crucible bottom and (b) crucible wall.

Fig. 2-1 shows the contours of in-phase component (right hand side) and out-of-phase component (left hand side) of the magnetic stream function for the CZ system. The maximum value of in-phase component ($C_{max} = 1.45 \times 10^{-4}\ Weber$) is located in the middle part of the coil and its value rapidly decreases toward the crucible wall, while the maximum value of the out-of-phase component ($S_{max} = 1.76 \times 10^{-5}\ Weber$) is located on the middle part of crucible wall and its value rapidly reduces toward the centerline. Although C_{max} is about 8.3 times greater than S_{max}, the magnitudes of C and S are similar within the crucible and afterheater and also chamber wherein the phase shift occurs and the required heat generation is produced. It means that within the conductors both components (C and S) contribute to the heat generation about equally. In the chamber the maximum values of in-phase and out-of-phase components are $C_{max}^{chamber} = 7.06 \times 10^{-7}\ Weber$ and $S_{max}^{chamber} = 8.07 \times 10^{-7}\ Weber$, respectively and in the middle part of its side wall.

The volumetric heat generation rate (q) in the crucible wall and bottom has been

Part	Heat generated ($Watt$)	Percentage (%)
Crucible bottom	188	9
Crucible wall	1850	88
Chamber	72	3
Total	2110	100

Table 2-3. Detail information about the heat generated in the different parts of the CZ system, calculated for the *case a*.

shown in Fig. 2-2 (for a better demonstration the wall and bottom part are separately magnified). The maximum value of energy deposition in the crucible is $q_{max}^{crucible} = 44\ Watt/cm^3$ and it is found at the outer surface of crucible wall. Fig. 2-3 shows the profiles of the generated heat along the outer surfaces of the crucible. Figs. 2-2 and 2-3 indicate that the heat is mostly generated in the crucible wall and less in the bottom. The total energy deposition rate in the system (crucible and chamber) is $Q_{total}^{system} = 2.11\ kWatt$ by using integral over their volume. More details of heat generated in the different parts have been shown in the table 2-3.

2.3.2 case b: Crucible and afterheater, no gap

In this case, the configuration contains crucible and active afterheater without any gap between them. Also the RF coil has an additional turn for afterheater. In this case we can not assume the simplest "equivalent cylinder" model for whole RF coil including this additional turn because the distance between the main coil and this single turn is $D_{co} = 5.5\ cm$ and it is so larger than the distance between the turns in the main coil ($d_{co} = 3\ mm$), i.e. we have considered an "equivalent cylinder" plus a single turn.

Fig. 2-4 shows the contours of in-phase component (right hand side) and out-of-phase component (left hand side) of the magnetic stream function for this configuration. The maximum value of in-phase component is $C_{max} = 1.47 \times 10^{-4}\ Weber$ located in the middle part of the main coil and the maximum value of the out-of-phase component is $S_{max} = 1.86 \times 10^{-5}\ Weber$ located in the middle part of crucible wall. The magnitude of C_{max} is about 7.9 times greater than S_{max}. Also, there is a local maximum of in-phase-component ($C_{max}^{second\ coil} = 6.46 \times 10^{-5}\ Weber$) in the second coil which comes from the driving current in it.

The volumetric heat generation rate (q) in the crucible and afterheater has been shown in Fig. 2-5. The maximum value of energy deposition in the crucible and af-

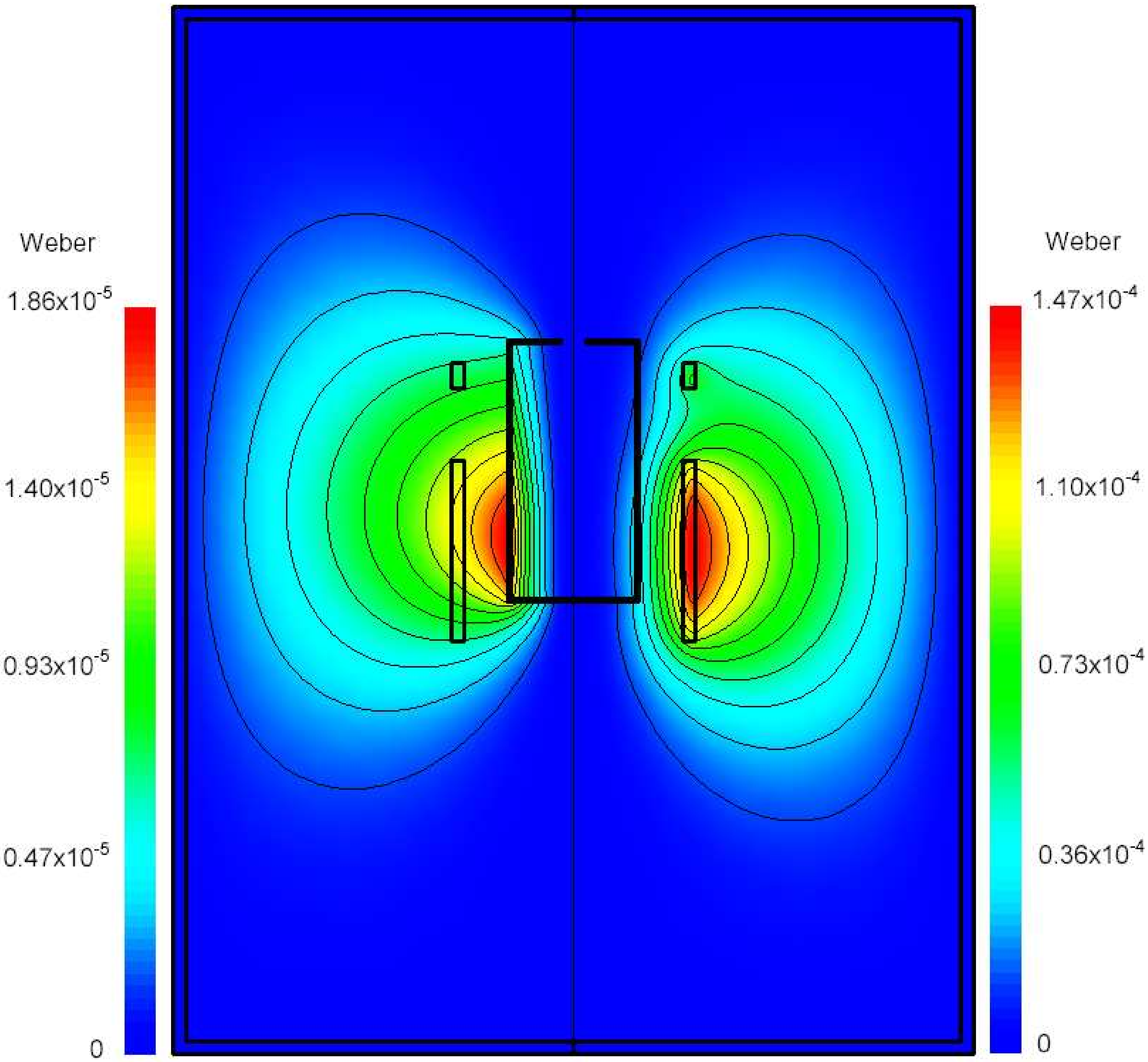

Fig. 2-4. Components of the magnetic stream function (ψ_B) calculated for *case b*. The right hand side shows the in-phase component (C), with $C_{max} = 1.47 \times 10^{-4}$ $Weber$ located in the coil and the left hand side shows the out-of-phase component (S), with $S_{max} = 1.86 \times 10^{-5}$ $Weber$ located on the crucible wall. There is a local maximum of in-phase-component ($C_{max}^{second\ coil} = 6.46 \times 10^{-5}$ $Weber$) in the second coil.

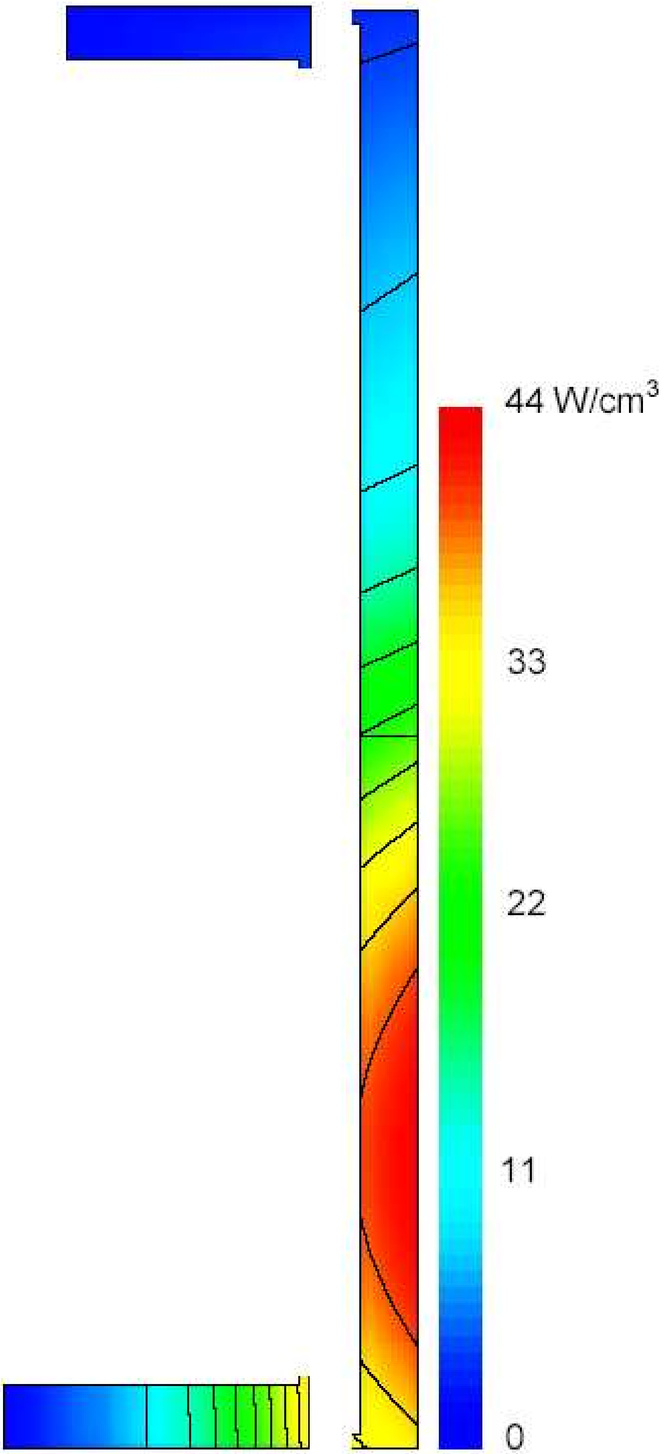

Fig. 2-5. Contours of the volumetric power distribution (q) in the crucible and afterheater, computed for *case b*. The maximum value of energy deposition is $q_{max} = 44\ Watt/cm^3$ and it is located at the outer surface of crucible wall.

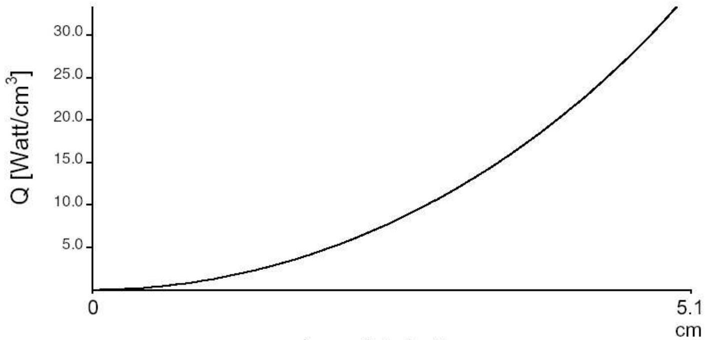

a) crucible bottom

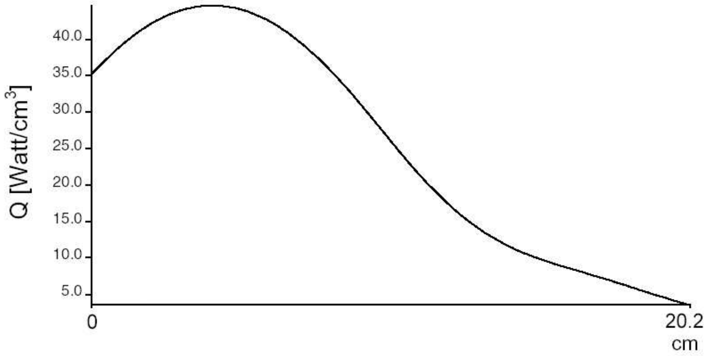

b) crucible & afterheater wall

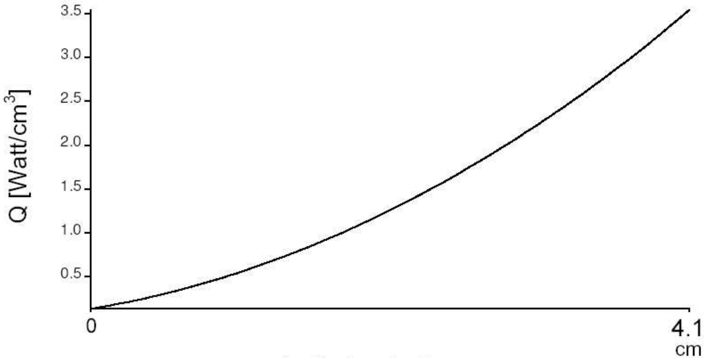

c) afterheater top cover

Fig. 2-6. Profiles of the heat generated along the outer surfaces of crucible and afterheater calculated for *case b*, (a) crucible bottom, (b) crucible wall, and (c) afterheater top cover.

Part	Heat generated ($Watt$)	Percentage (%)
Crucible bottom	191	7
Crucible wall	1900	72
Afterheater wall	438	17
Afterheater top cover	27	1
Chamber	88	3
Total	2644	100

Table 2-4. Detail information about the heat generated in the different parts of the CZ system, calculated for the *case b*.

terheater is $q_{max}^{crucible} = 44.6\ Watt/cm^3$ and it is placed at the outer surface of crucible side wall. Fig. 2-6 shows the profiles of the generated heat along the outer surfaces of the crucible (bottom and side wall) and afterheater (side wall and top cover). It indicates that the heat is mostly produced in the crucible wall and less in the afterheater. The total energy deposition rate in the crucible, afterheater and chamber is $Q_{total}^{system} = 2.64\ kWatt$. More details of the heat generation in the different parts have been shown in the table 2-4.

It should be mention that although the values of C_{max} is the same in both *cases a* and *b*, but the value of S_{max} has been increased about 6% in *case b* and as a result $q_{max}^{crucible}$ has been increased about 2%. Consequently, $Q_{total}^{crucible}$ has an increase of 2.2% (45 $Watt$). Because by placing the active afterheater, the domain of the out-of-phase component (S) is extended to include this active afterheater too. Also noteworthy is the position of the $q_{max}^{crucible}$ does not change.

2.3.3 case c: Crucible and afterheater, no gap, change in the radius of the RF coil

In this case the inner radius of the RF coil is increased from $r_{co} = 8.5\ cm$ (*case b*) to $r_{co} = 9.5\ cm$ (i.e. $\triangle r_{coil} = 12\%$), on the other hand the distance between crucible and coil is increased about 30%. Fig. 2-7 shows the contours of in-phase component (right hand hand side) and out-of-phase component (left hand side) of the magnetic stream function for this configuration. The maximum value of in-phase component ($C_{max} = 1.74 \times 10^{-4}\ Weber$) is located in the middle part of the main coil and the maximum value of the out-of-phase component ($S_{max} = 1.73 \times 10^{-5}\ Weber$) is placed on the middle part of crucible wall. The magnitude of C_{max} is about 10 times greater

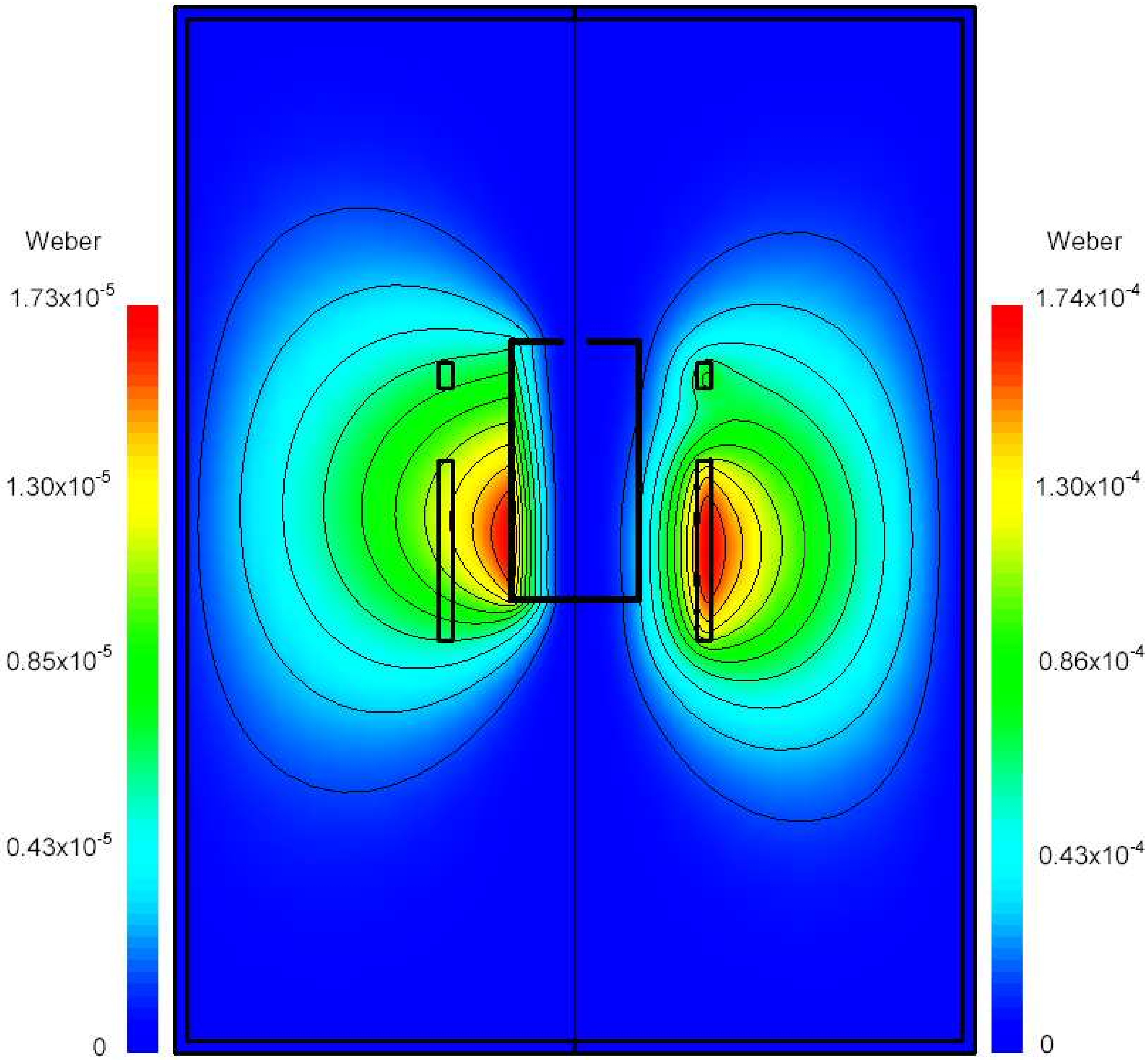

Fig. 2-7. Components of the magnetic stream function (ψ_B) calculated for *case c*. The right hand side shows the in-phase component (C), with $C_{max} = 1.74 \times 10^{-4}$ $Weber$ located in the coil and the left hand side shows the out-of-phase component (S), with $S_{max} = 1.73 \times 10^{-5}$ $Weber$ located on the crucible wall.

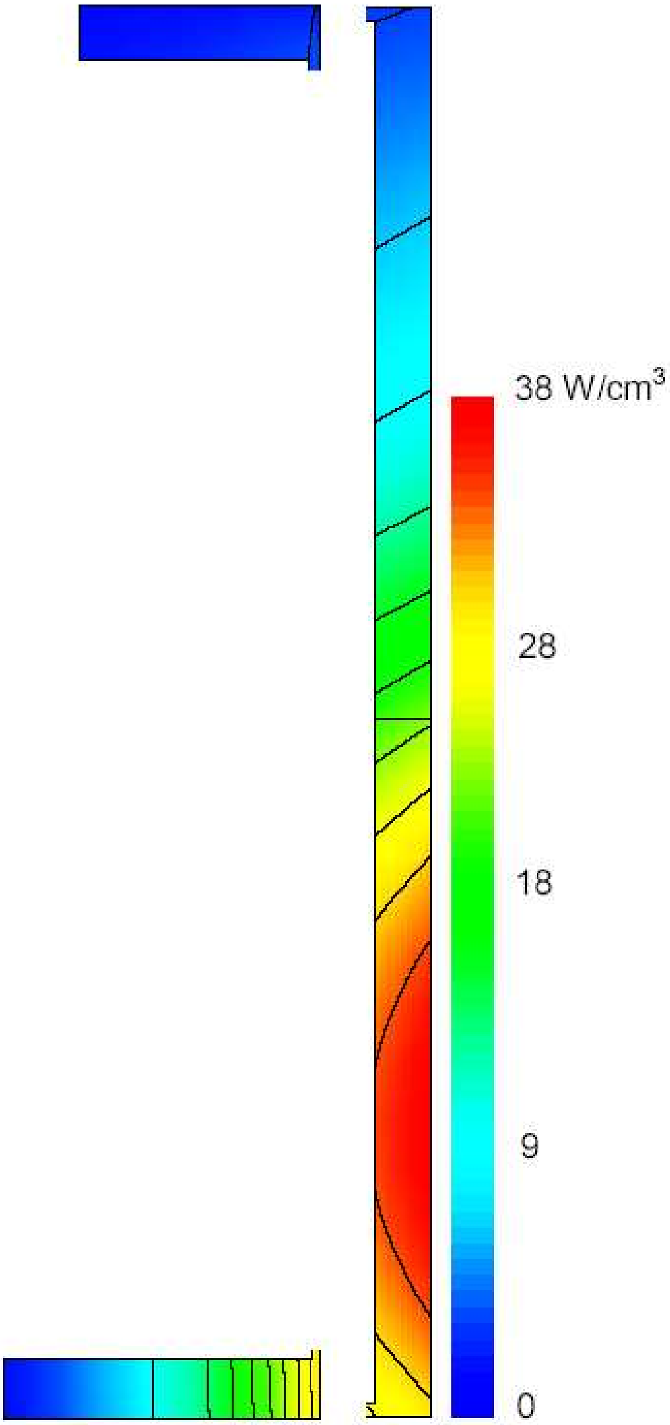

Fig. 2-8. Contours of the volumetric power distribution (q) in the crucible and afterheater, computed for *case c*. The maximum value of energy deposition is q_{max} = 38.3 $Watt/cm^3$ and it is located at the outer surface of crucible wall.

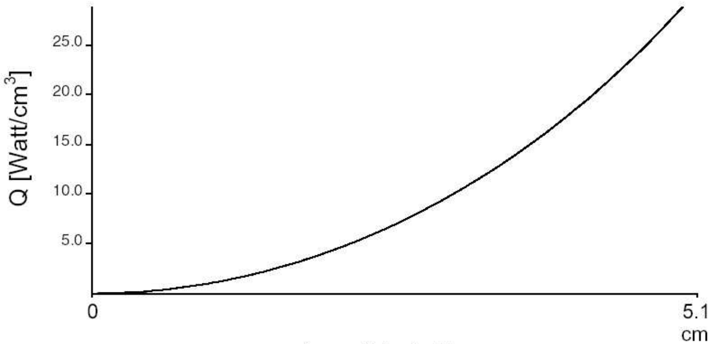

a) crucible bottom

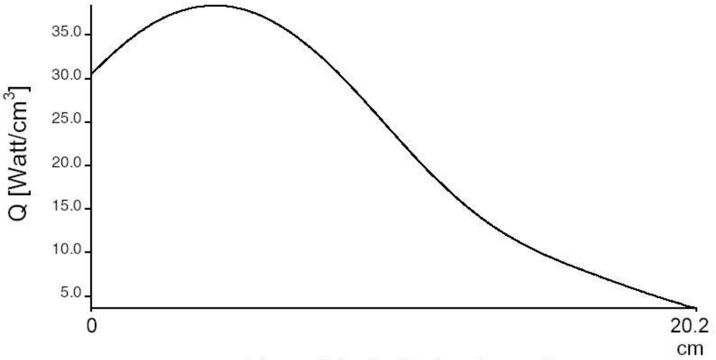

b) crucible & afterheater wall

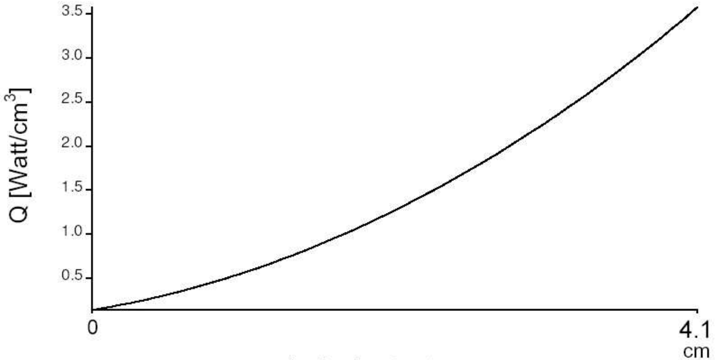

c) afterheater top cover

Fig. 2-9. Profiles of the heat generated along the outer surfaces of crucible and afterheater calculated for *case c*, (a) crucible bottom, (b) crucible wall, and (c) afterheater top cover.

Part	Heat generated ($Watt$)	Percentage (%)
Crucible bottom	136	7
Crucible wall	1436	70
Afterheater wall	373	18
Afterheater top cover	24	1
Chamber	70	4
Total	2039	100

Table 2-5. Detail information about the heat generated in the different parts of the CZ system, calculated for the *case c*.

than S_{max}. By comparison with the *case b*, we can find that the in-phase component is less "compressed" between crucible and the RF coil because the distance between them has been increased. Also C_{max} has an increase of 19% but S_{max} has been reduced about 7%. The reason is that by increasing the distance between conductors (crucible and afterheater) and induction coil, the influence of their interaction becomes less effective and as a result there is an increase in the component C and a decrease in the component S.

The volumetric heat generation rate (q) in the crucible and afterheater has been shown in Fig. 2-8. The maximum value of energy deposition in the crucible and afterheater is $q_{max}^{crucible} = 38.3\ Watt/cm^3$ and at the outer surface of crucible wall. Fig. 2-9 shows the profiles of the generated heat at the outer surface of the crucible and afterheater. The total energy deposition rate in the crucible, afterheater and chamber is $Q_{total}^{system} = 2.04\ kWatt$. More details of the energy generation in the different parts have been presented in the table 2-5.

The decrease in total power generation of the crucible is 13% (278 $Watt$) and in contrast, the power dissipated in the chamber is markedly increased 58% (51 $Watt$) and so the total heat generation in the system is reduced about 9.2% (244 $Watt$). Also noteworthy is that the change in the coil diameter has not any effective influence on the spatial distribution of heat generation in the crucible and afterheater.

2.3.4 case d: Crucible and afterheater, no gap, separate turns of RF coil (N=6)

In this case we employ the real configuration of the induction coil (i.e. 6-turn induction coil), in which J_0 is the actual current density. To do it we need to apply a fine mesh

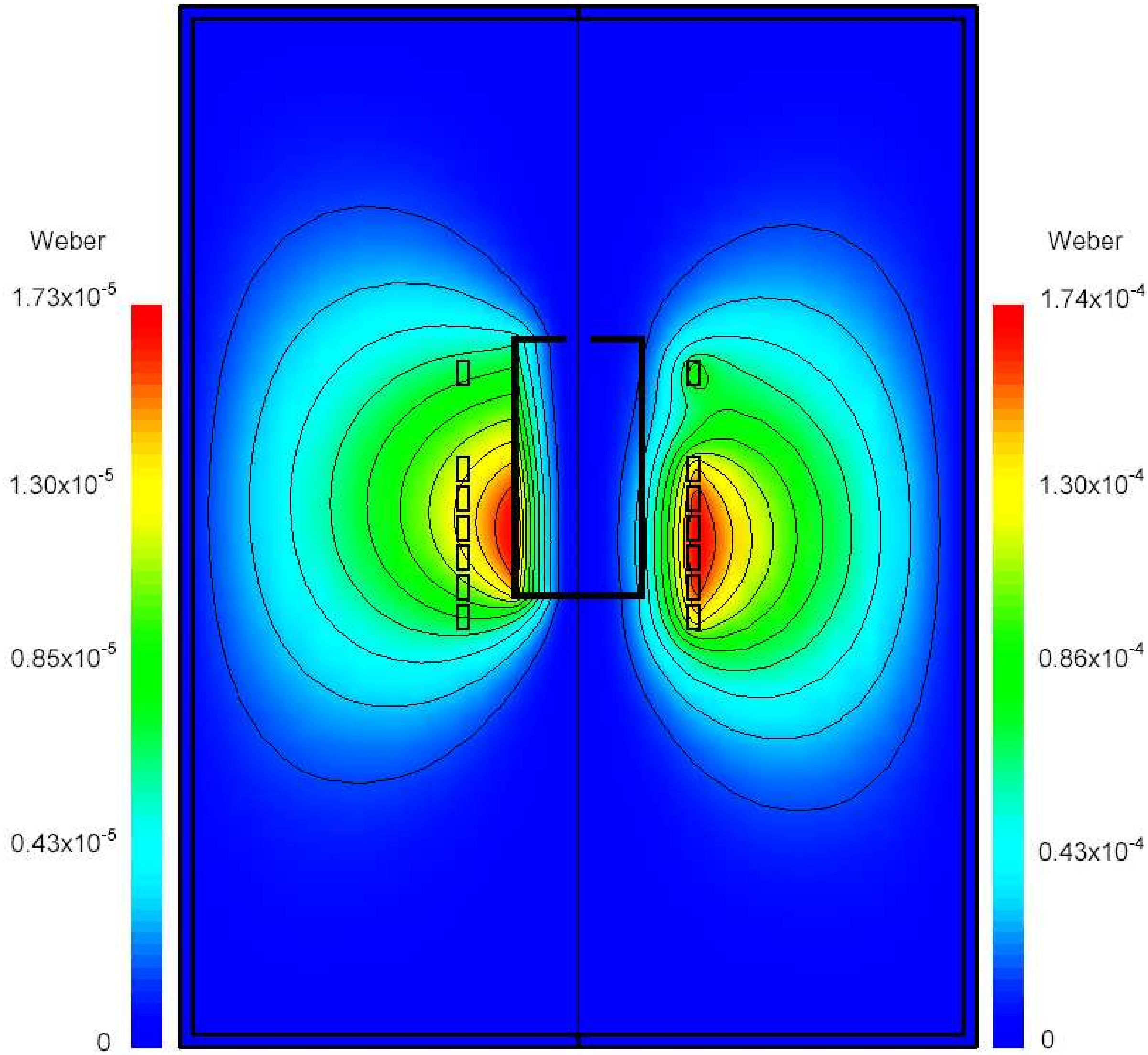

Fig. 2-10. Components of the magnetic stream function (ψ_B) calculated for *case d*. The right hand hand side shows the in-phase component (C), with $C_{max} = 1.74\times10^{-4}$ $Weber$ located in the coil and the left side shows the out-of-phase component (S), with $S_{max} = 1.73 \times 10^{-5}$ $Weber$ located on the crucible wall.

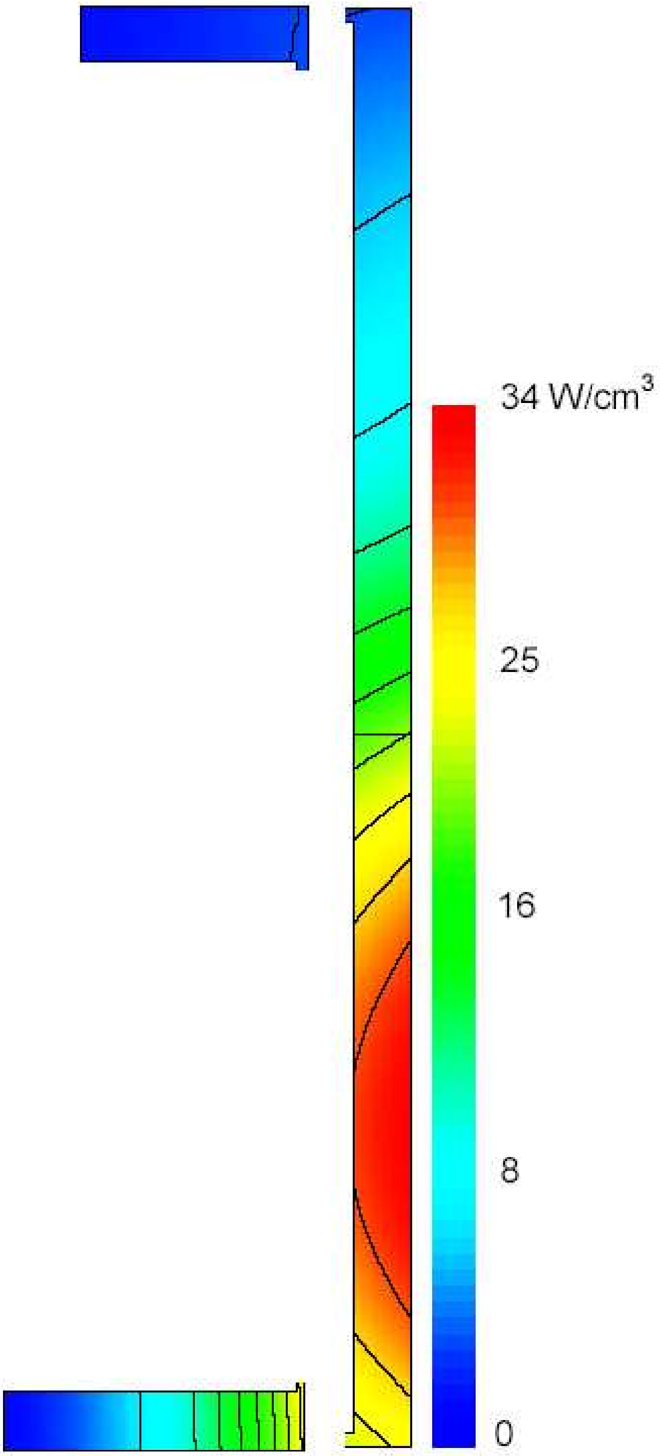

Fig. 2-11. Contours of the volumetric power distribution (q) in the crucible and afterheater, computed for *case d*. The maximum value of energy deposition is $q_{max} = 33.6\ Watt/cm^3$ and it is located at the outer surface of crucible wall.

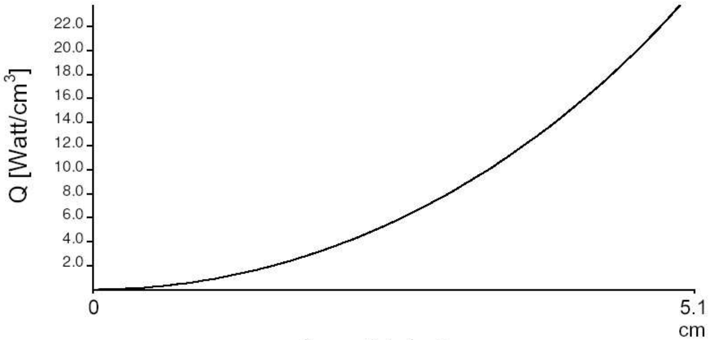

a) crucible bottom

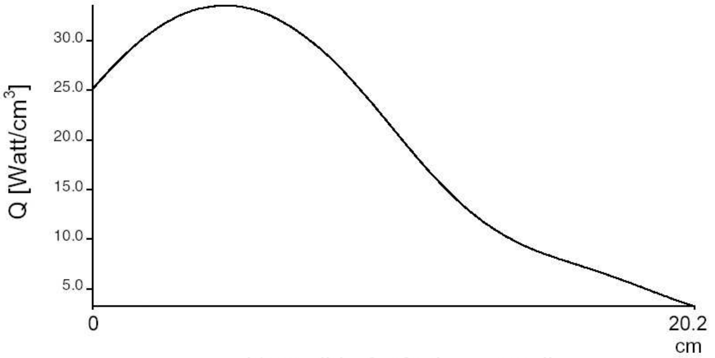

b) crucible & afterheater wall

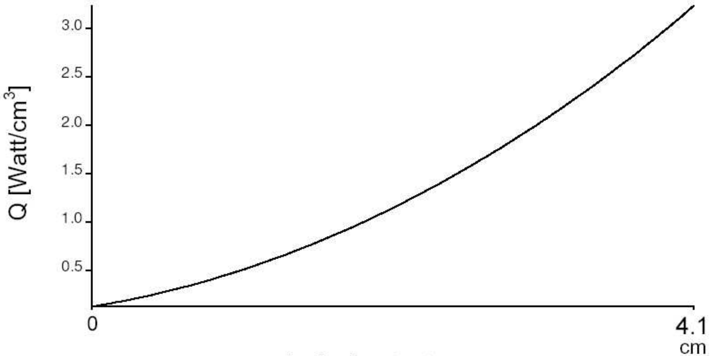

c) afterheater top cover

Fig. 2-12. Profiles of the heat generated along the outer surfaces of crucible and afterheater calculated for *case d*, (a) crucible bottom, (b) crucible wall, and (c) afterheater top cover.

Part	Heat generated ($Watt$)	Percentage (%)
Crucible bottom	166	7
Crucible wall	1647	69
Afterheater wall	421	17
Afterheater top cover	27	1
Chamber	139	6
Total	2400	100

Table 2-6. Detail information about the heat generated in the different parts of the CZ system, calculated for the *case d*.

in and near the RF coil in order to detect the boundaries of this multi-turn coil and to find an accurate result and so it increases the time of calculation effectively ($\sim 100\%$). Our aim is to investigate the influence of individual turns on the distribution of C and S components and also heat generation. In this case the gap between turns in the main coil is $d_{co} = 3\ mm$, that is very small than the height of every turn ($h_{co} = 20\ mm$ and $h_{co}/d_{co} = 6.7$).

Fig. 2-10 shows the contours of in-phase component (right hand hand side) and out-of-phase component (left side) of the magnetic stream function for this configuration. The maximum value of in-phase component is $C_{max} = 1.74 \times 10^{-4}\ Weber$ and the maximum value of the out-of-phase component is $S_{max} = 1.73 \times 10^{-5}\ Weber$ and $C_{max}/S_{max} = 7.9$.

The volumetric heat generation rate (q) in the crucible and afterheater has been shown in Fig. 2-11. The maximum value of energy deposition in the crucible and afterheater is $q_{max}^{crucible} = 33.55\ Watt/cm^3$ and it is located at the outer surface of crucible wall. Fig. 2-12 shows the profiles of the generated heat along the outer surfaces of the crucible and afterheater. The total energy deposition rate in the system is $Q_{total}^{system} = 2.4\ kWatt$. More details of the heat generation in the different conductor parts have been presented in the table 2-6.

Although both components C and S have been reduced by 13% compared to the *case b*, but the spatial distribution of both components in and near the crucible and afterheater is the same. The difference is only significant in and near the RF coil itself, on the other hand the crucible and afterheater is too far from the coil to detect the difference. Also the total heat generation in the crucible and afterheater has been decreased by 25% (519 $Watt$), but the spatial distribution of the heat generation has not been changed. As the results show, in this case the “single equivalent cylinder” model of induction coil (*case b*) is a good approximation instead of a "multi-turn coil" and decreases the spending time for calculations effectively.

2.3.5 case e: Crucible and afterheater, no gap, separate turns of RF coil (N=3)

In this case we continue the calculation of influence of the separate turns, by reduction of turns in the main coil from 6 to 3. So, the distance between turns will be increased from $d_{co} = 3\ mm$ (*case d*) to $d_{co} = 37.5\ mm$, that is comparable to the turn height ($h_{co} = 20\ mm$). It should be mention that the position of the first and last turns of the main coil and also the second coil do not change. Also similar to the previous case, it is necessary to employ a fine mesh near and in the coil.

Fig. 2-13 shows the contours of in-phase component (right hand side) and out-of-phase component (left hand side) of the magnetic stream function for this configuration. The maximum value of in-phase component is $C_{max} = 6.81 \times 10^{-5}\ Weber$ on the middle turn of main coil and the maximum value of the out-of-phase component is $S_{max} = 7.91 \times 10^{-6}\ Weber$ on the crucible wall and $C_{max}/S_{max} = 8.6$. In fact there is a local maximum for in-phase component on every turn in the range of $5.5 - 6.8 \times 10^{-5}\ Weber$. So because of long distance between coil turns, the interaction of them is too week to produce a continuous field (C) similar to the *case d* around itself.

The volumetric heat generation rate (q) in the crucible and afterheater has been shown in Fig. 2-14. The maximum value of energy deposition in the crucible and afterheater is $q_{max}^{crucible} = 7.14\ Watt/cm^3$ and at the outer surface of crucible wall. Fig. 2-15 shows the profiles of the generated heat along the outer surfaces of the crucible and afterheater. The total energy deposition rate in the crucible, afterheater and chamber is $Q_{total}^{system} = 0.58\ kWatt$. More details of the heat generated in the different parts have been presented in the table 2-7.

At first it is clear that the magnitude of both components of electromagnetic field and heat generation reduces proportional to the reduction of the number of turns. Secondly the distribution of in-phase component (C) has been changed strongly in and between the RF coil and crucible. The contours of this component have been shown in the Fig. 2-16 for the space between crucible and afterheater, and for two *cases d* and *e*. In the *case d*, the shape of the contours is about straight line parallel to the crucible wall which illuminates the uniform gradient of component (C) in that area. In the *case e*, the contours have a wavy shape that indicates a non-uniform gradient of this component. This non-uniform gradient makes a non-uniform distribution of heat production in the crucible and afterheater which is shown in the Figs 2-14 and 2-15. There are two maxima in the crucible side wall and that influences directly the temperature and flow field of

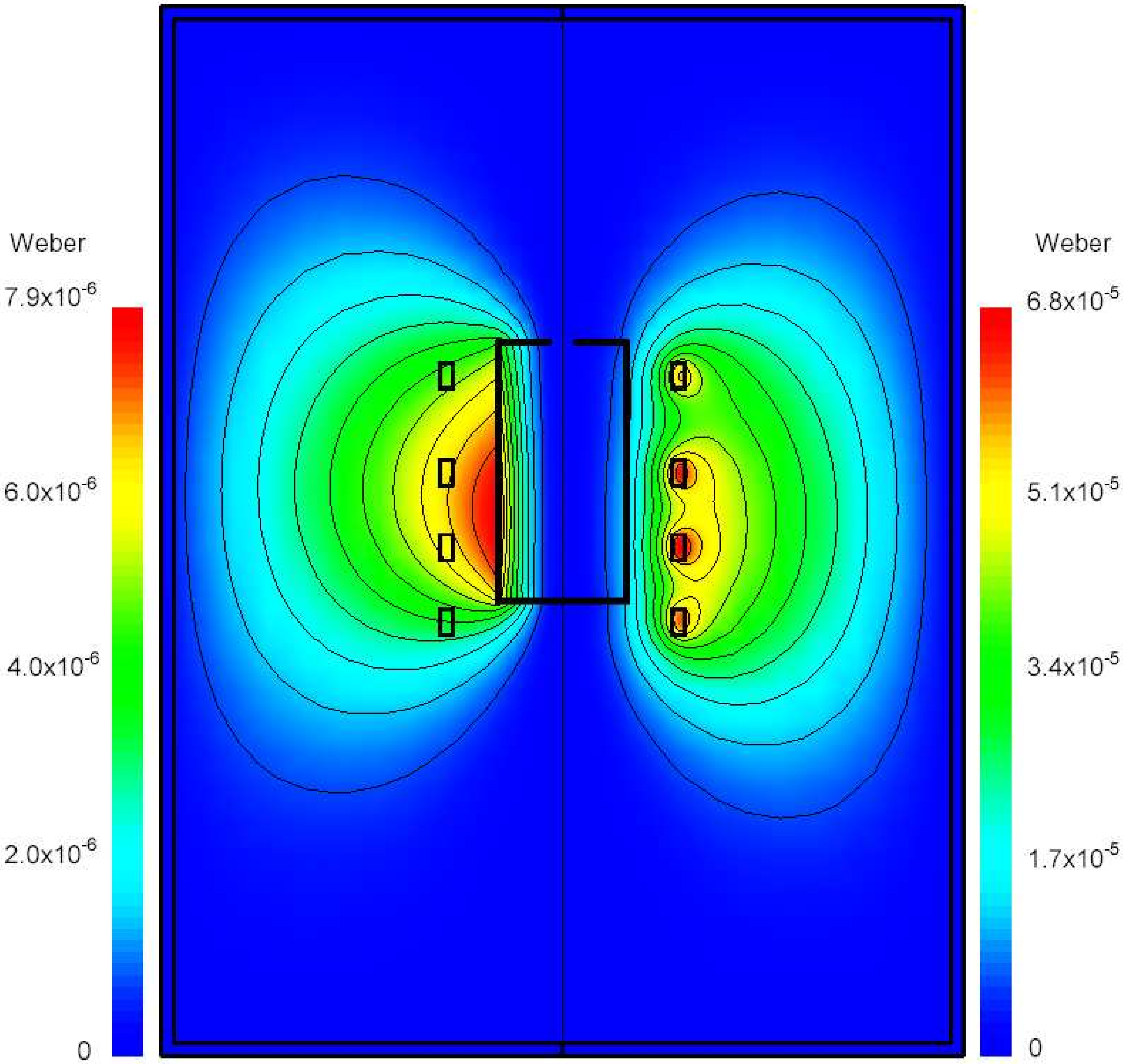

Fig. 2-13. Components of the magnetic stream function (ψ_B) calculated for *case e*. The right hand hand side shows the in-phase component (C), with $C_{max} = 6.81 \times 10^{-5}\ Weber$ located in the coil and the left side shows the out-of-phase component (S), with $S_{max} = 7.91 \times 10^{-6}\ Weber$ located on the crucible wall.

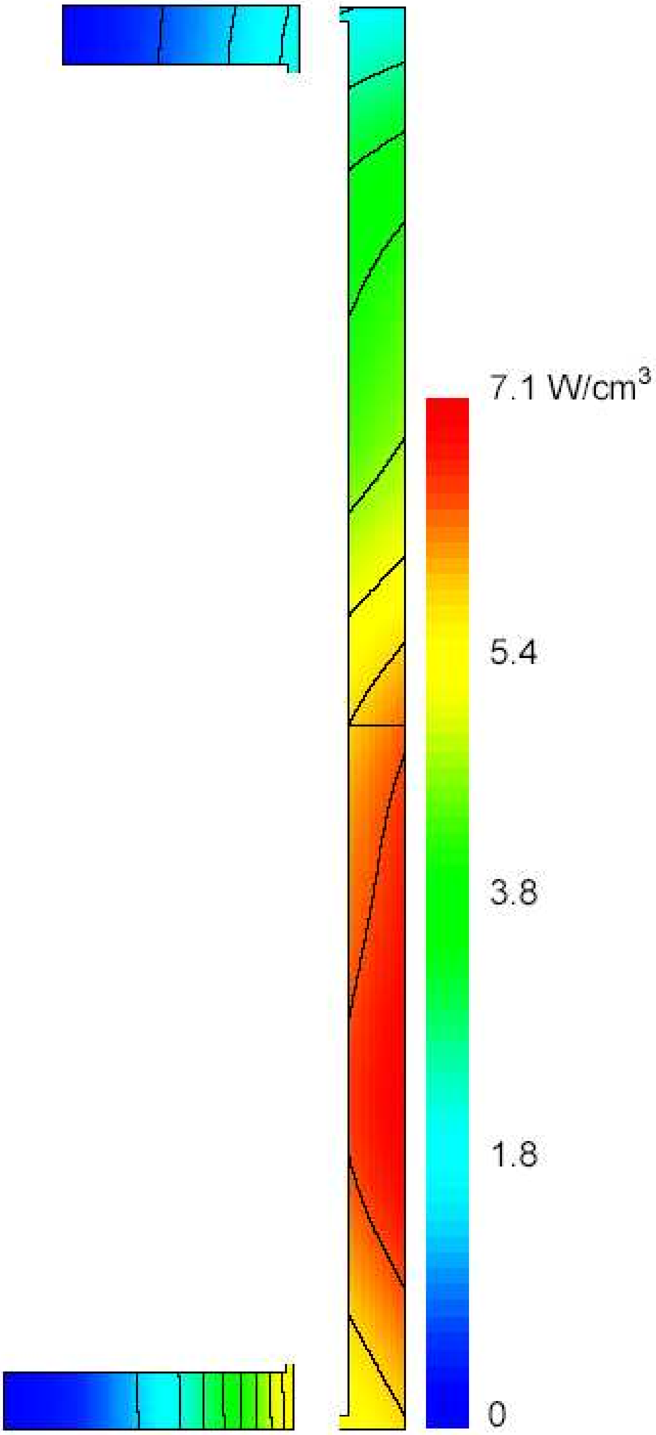

Fig. 2-14. Contours of the volumetric power distribution (q) in the crucible and afterheater, computed for *case e*. The maximum value of energy deposition is $q_{max} = 7.14\ Watt/cm^3$ and it is located at the outer surface of crucible wall.

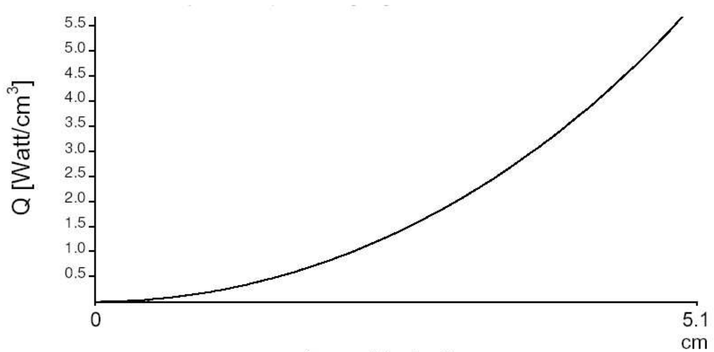

a) crucible bottom

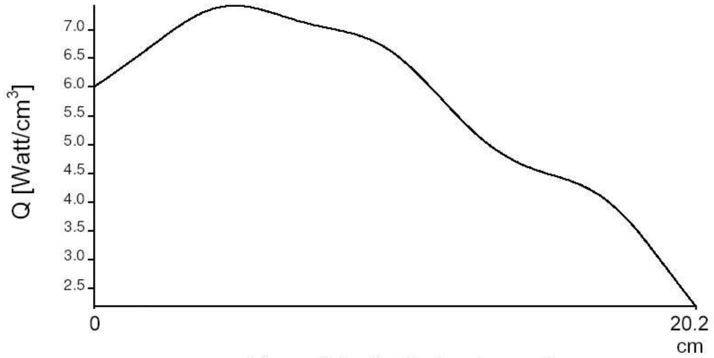

b) crucible & afterheater wall

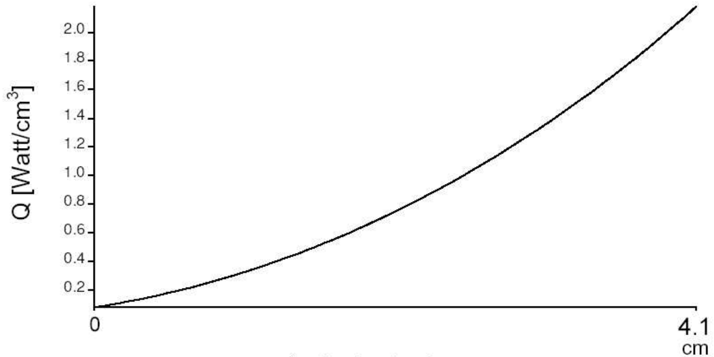

c) afterheater top cover

Fig. 2-15. Profiles of the heat generated along the outer surfaces of crucible and afterheater calculated for *case e*, (a) crucible bottom, (b) crucible wall, and (c) afterheater top cover.

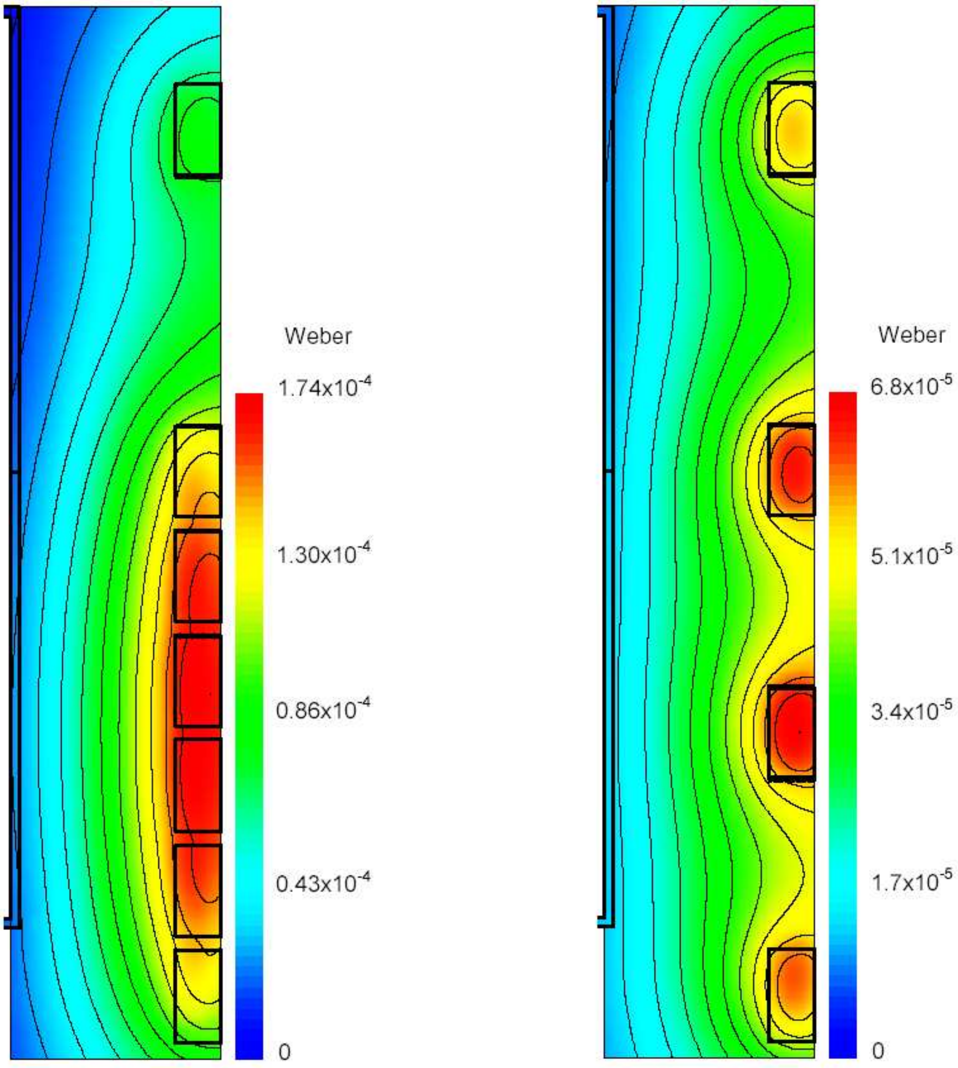

(a) (b)

Fig. 2-16. Contours of the in-phase-component (C) in space between crucible and afterheater, for two *cases* d (left side) and e (right hand side). In the *case* d, the shape of the contours is about straight line parallel to the crucible wall which illuminates the uniform gradient of this component in that area. In the *case* e, the contours have a wavy shape that indicates a non-uniform gradient of this component.

Part	Heat generated ($Watt$)	Percentage (%)
Crucible bottom	32	5
Crucible wall	335	58
Afterheater wall	170	30
Afterheater top cover	16	3
Chamber	22	4
Total	576	100

Table 2-7. Detail information about the heat generated in the different parts of the CZ system, calculated for the *case e*.

the system. Also in this case the induction coil can not deposit enough power into the crucible to get the job done, i.e. to melt oxide materials such as sapphire (melting point $\sim 2000\ ^oC$). Also the heat generation in the afterheater is considerable compared to the crucible and that is not convenient for the growing crystal.

2.3.6 case f: Crucible and afterheater, no gap, flat and rounded crucible bottom

In this case we consider a crucible with a rounded bottom ($r_{cb} = 10\ mm$) instead of a flat bottom (Fig. 2-17). Contours of the in-phase and out-of-phase components of the magnetic stream function for this configuration have been shown in the Fig. 2-18. The maximum value of in-phase component is $C_{max} = 1.47 \times 10^{-4}\ Weber$ on the middle of main coil and the maximum value of the out-of-phase component is $S_{max} = 1.87 \times 10^{-5}\ Weber$ on the crucible wall. Comparison of these results with those of *case b*, demonstrates that they are the same and this means the round edge of the crucible has not any effective influence on the distribution and values of these component except of the area near to the round edge. Fig. 2-19 shows a close up of the contours of the both components, in space between crucible and afterheater.

The volumetric heat generation rate (q) in the crucible and afterheater has been shown in Fig. 2-20. The maximum value of energy generation in the crucible and afterheater is $q_{max}^{crucible} = 44.9\ Watt/cm^3$ and at the outer surface of crucible wall. Fig. 2-21 shows the profiles of the generated heat along the outer surfaces of the crucible and afterheater. The total energy deposition rate in the crucible, afterheater and chamber is $Q_{total}^{system} = 2.61\ kWatt$. More details of the heat generated in the different parts have been presented in the table 2-8. At first the change in total heat generation in the

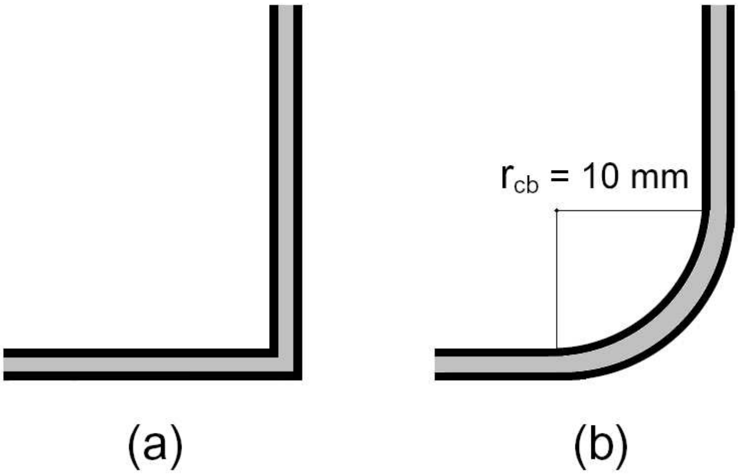

Fig. 2-17. Shapes of the crucible bottom with the (a) flat, and rounded of radius $r_{cb} = 10\ mm$ (b).

Part	Heat generated ($Watt$)	Percentage (%)
Crucible bottom	260	10
Crucible wall	1800	69
Afterheater wall	437	17
Afterheater top cover	27	1
Chamber	88	3
Total	2612	100

Table 2-8. Detail information about the heat generated in the different parts of the CZ system, calculated for the *case f*. The round part is included to the crucible bottom.

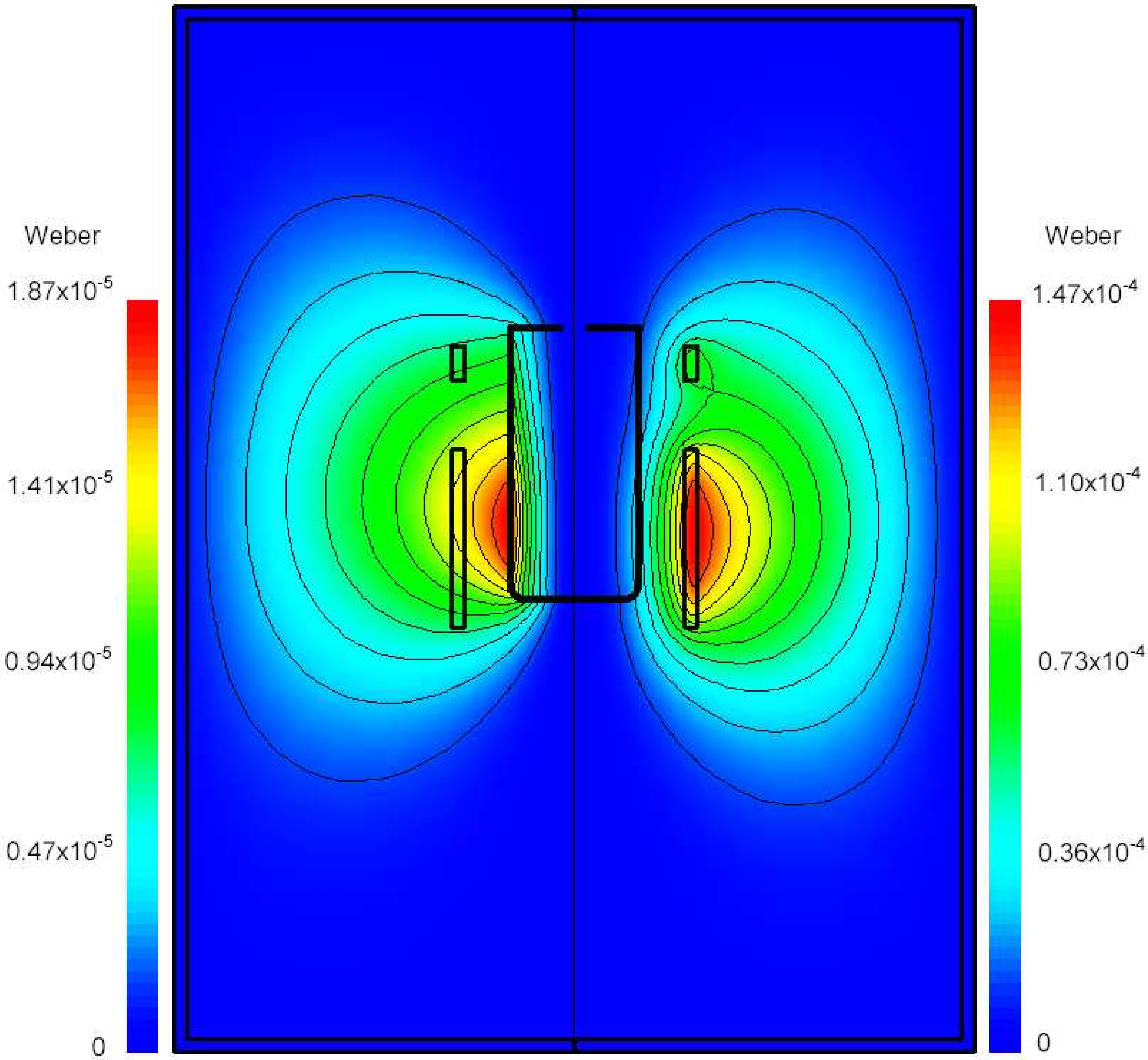

Fig. 2-18. Components of the magnetic stream function (ψ_B) calculated for *case f*. The right hand side shows the in-phase component (C), with $C_{max} = 1.47 \times 10^{-4}$ $Weber$ located in the coil and the left hand side shows the out-of-phase component (S), with $S_{max} = 1.87 \times 10^{-5}$ $Weber$ located on the crucible wall.

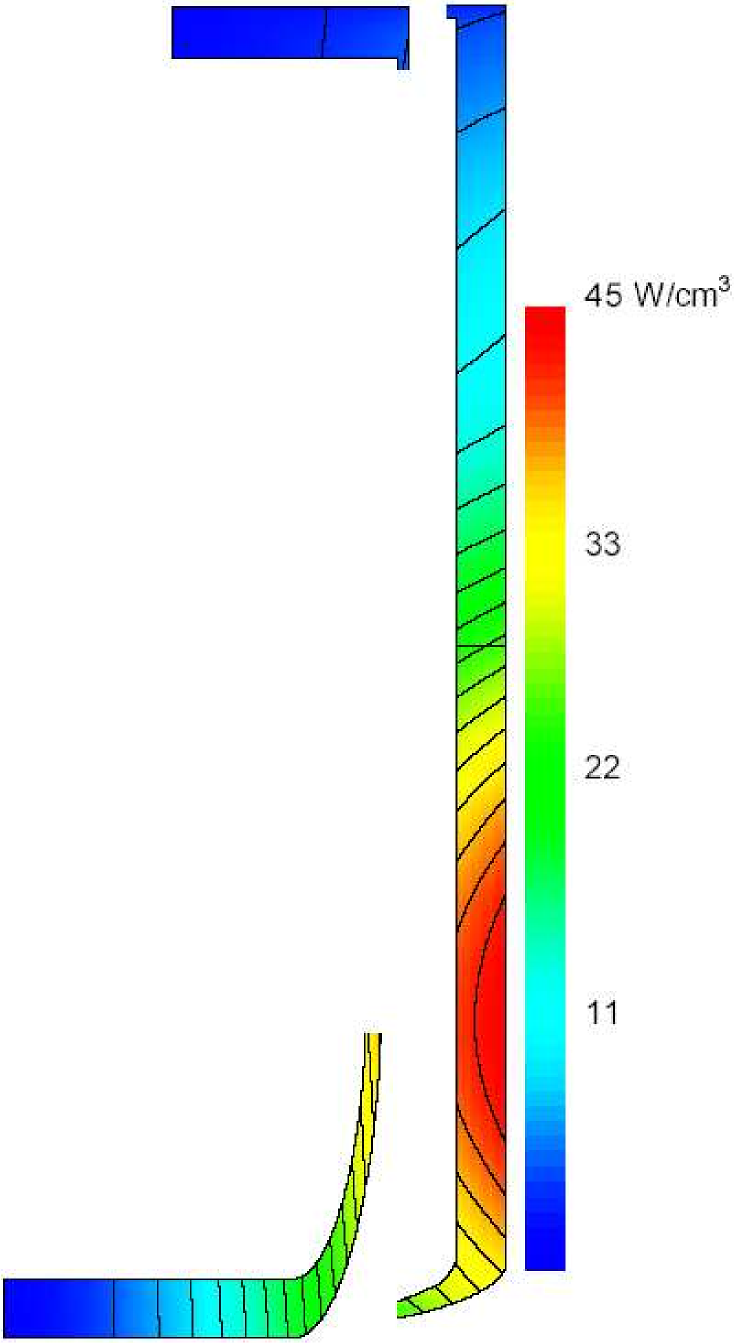

Fig. 2-19. Contours of the volumetric power distribution (q) in the crucible and afterheater, computed for *case f*. The maximum value of energy deposition is $q_{max} = 44.9\ Watt/cm^3$ and it is located at the outer surface of crucible wall.

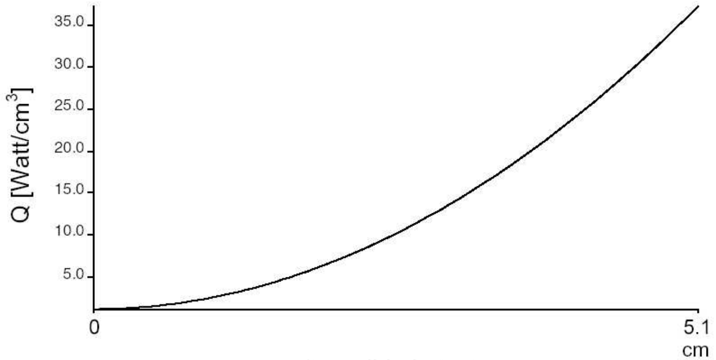

a) crucible bottom

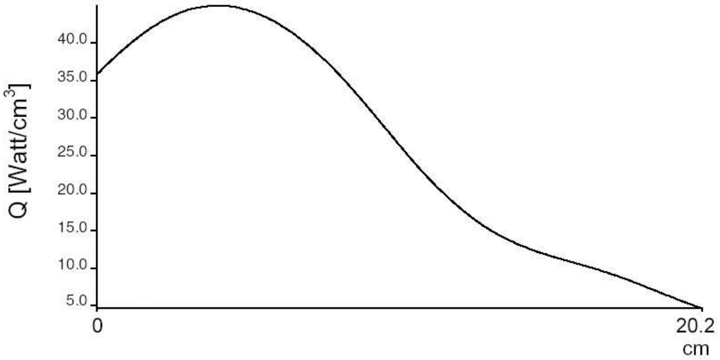

b) crucible & afterheater wall

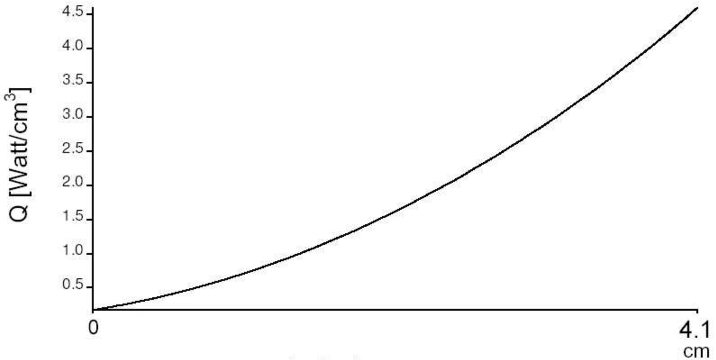

c) afterheater top cover

Fig. 2-20. Profiles of the heat generated along the outer surfaces of crucible and afterheater calculated for *case f*, (a) crucible bottom (round edge is included), (b) crucible wall, and (c) afterheater top cover.

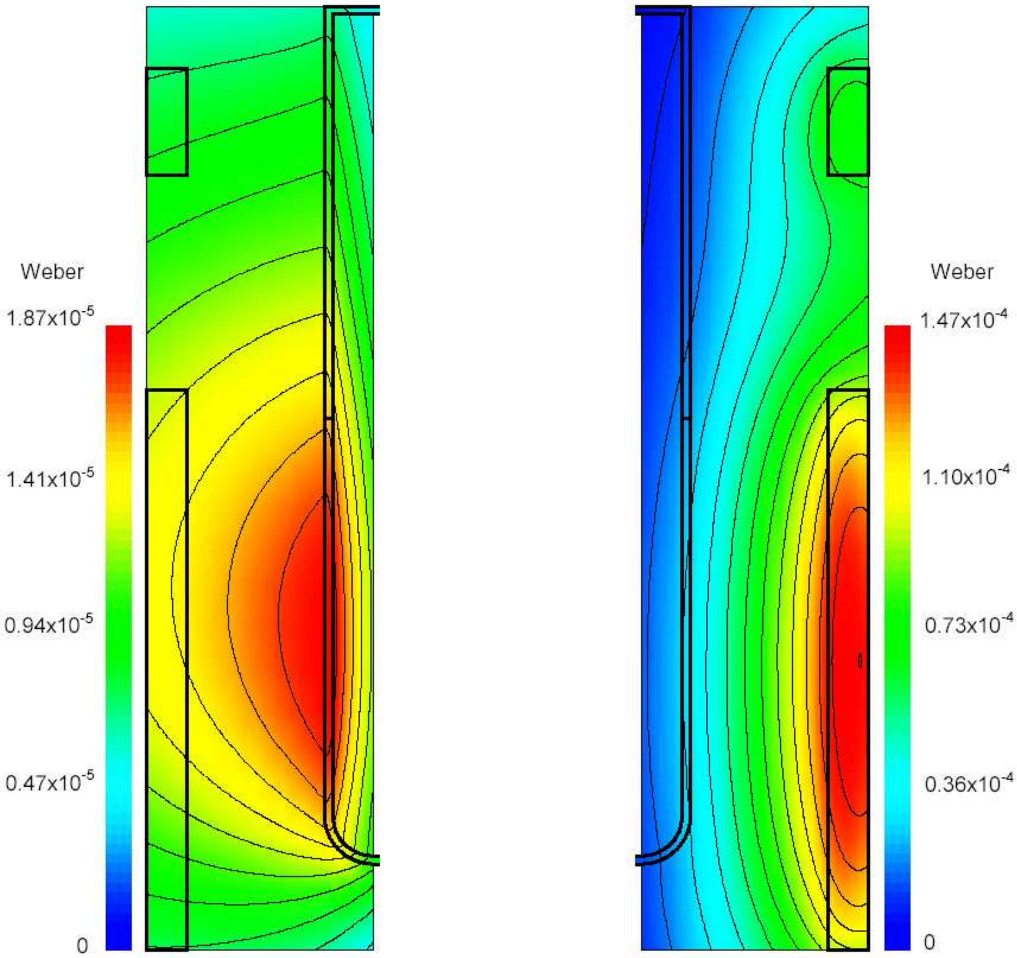

(a) (b)

Fig. 2-21. Contours of the in-phase (a) and out-of-phase (b) components in space between crucible and afterheater for *case f*.

Part	Heat generated ($Watt$)	Percentage (%)
Crucible bottom	201	7
Crucible wall	1988	76
Afterheater wall	303	12
Afterheater top cover	14	1
Chamber	91	4
Total	2598	100

Table 2-9. Detail information about the heat generated in the different parts of the CZ system, calculated for the *case g*.

system is -1.2% ($-32\ Watt$). The reason for this reduction is that in the round edge the distance between crucible and RF coil increases from the side wall toward its bottom. Second the position of the $q_{max}^{crucible}$ is $\sim 5\ mm$ higher than *case b*. This condition directly influences the temperature and flow field and will change the position of temperature maximum in the system.

2.3.7 case g: Crucible and afterheater, with a gap

In this case, there is a gap ($D_{ca} = 20\ mm$) between crucible and afterheater without any change in the position of coil turns. On the other hand, the configuration of the RF coil is the same as *case b* with the "equivalent cylinder" model for it.

Contours of the in-phase and out-of-phase components of the magnetic stream function are shown in Fig. 2-22, with the $C_{max} = 1.49 \times 10^{-4}\ Weber$ located in the coil and $S_{max} = 1.86 \times 10^{-5}\ Weber$ located on the crucible wall and also $C_{max}/S_{max} = 8$. It is clear that C_{max} has been increased 1.1% while S_{max} is the same. It indicates that the orientation of the afterheater is not very effective on the distribution of in-phase component (C), Because it is too far from the main coil to have any effective influence on the coil (in the second coil, the variation of component C is about 1.%).

The distribution of the heat generation in the crucible and afterheater is shown in Fig. 2-23 with $q_{max} = 45.4\ Watt/cm^3$, and its profiles along the outer surfaces of the crucible and afterheater are presented in Fig. 2-24. These two figures demonstrate that the distribution of the heat generation in the crucible is the same as *case b* and in the afterheater is less $\triangle Q_{total}^{afterheater} = 148\ Watt$ (32%). It should be mentioned the total heat generation in the afterheater top cover is reduced 50% ($\triangle Q^{afterheater\ top\ cover} = 148\ Watt$), compared to the *case b* and this affects significantly the temperature and

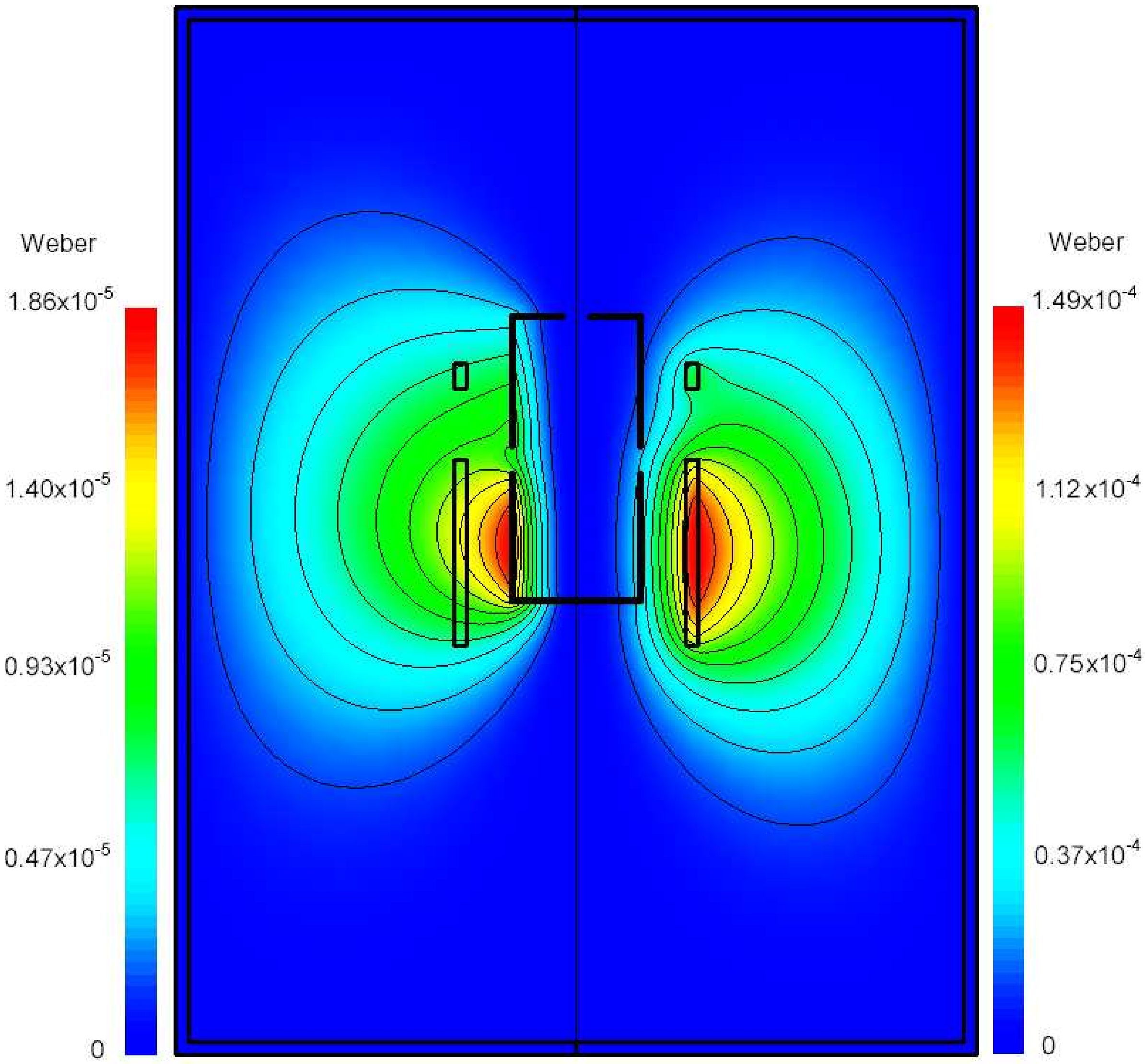

Fig. 2-22. Components of the magnetic stream function (ψ_B) calculated for *case g*. The right hand side shows the in-phase component (C), with $C_{max} = 1.49 \times 10^{-4}$ $Weber$ located in the coil and the left hand side shows the out-of-phase component (S), with $S_{max} = 1.86 \times 10^{-5}$ $Weber$ located on the crucible wall.

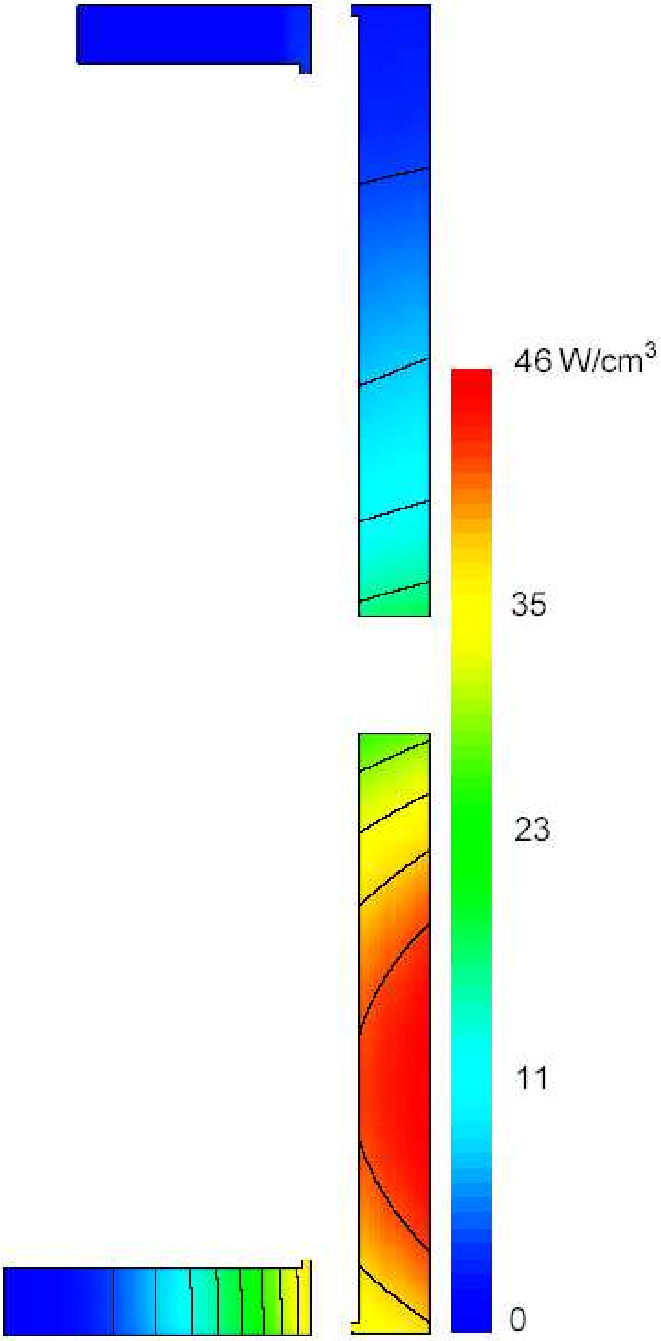

Fig. 2-23. Contours of the volumetric power distribution (q) in the crucible and afterheater, computed for *case g*. The maximum value of energy deposition is $q_{max} = 46.4\ Watt/cm^3$ and it is located at the outer surface of crucible wall.

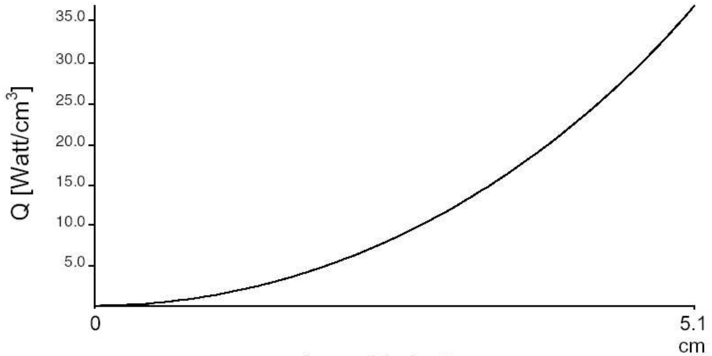

a) crucible bottom

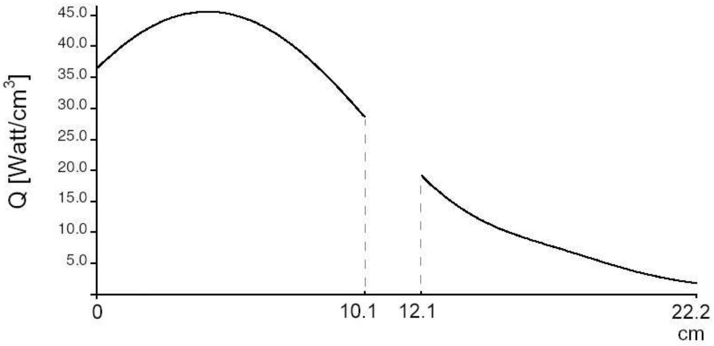

b) crucible & afterheater wall

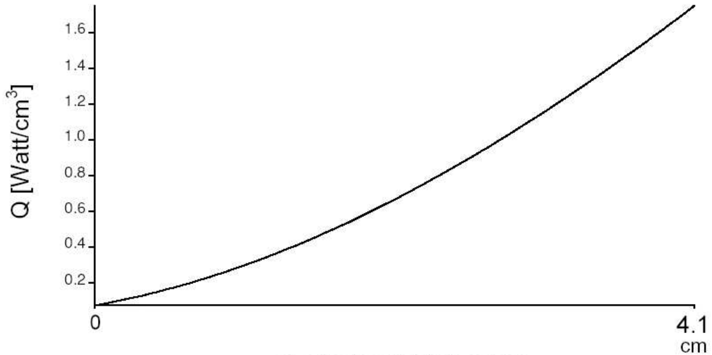

c) afterheater top cover

Fig. 2-24. Profiles of the heat generated along the outer surfaces of crucible and afterheater calculated for *case g*, (a) crucible bottom, (b) crucible wall, and (c) afterheater top cover.

Part	Heat generated ($Watt$)	Percentage (%)
Crucible bottom	137	7
Crucible wall	1465	75
Afterheater wall	267	13
Afterheater top cover	13	1
Chamber	70	4
Total	1952	100

Table 2-10. Detail information about the heat generated in the different parts of the CZ system, calculated for the *case h*.

flow field in the system. More details of the heat generated in the different parts have been presented in the table 2-9.

2.3.8 case h: Crucible and afterheater, with a gap, separate turns of RF coil (N=6)

In this case we use again the real multi-turn coil similar to *case d*, i.e. the number of turns in the main coil is 6 and the gap between turns is $d_{co} = 3\ mm$.

Fig. 2-25 shows the distribution of the in-phase component (right hand side) and out-of-phase (left hand side) of the magnetic stream function (ψ_B), computed for this configuration. The maximum values of the in-phase and out-of-phase components are $C_{max} = 1.28 \times 10^{-4}\ Weber$ and $S_{max} = 1.6 \times 10^{-5}\ Weber$, respectively and $C_{max}/S_{max} = 7.9$. Similar to cases no gap between crucible and afterheater, both components (C and S) have been reduced by 13%, compared to the *case g* and without any change in the spatial distribution of them in and near the crucible and afterheater.

Fig. 2-26 shows the distribution of volumetric heat generation (q) in the crucible and afterheater with $q_{max}^{crucible} = 34.1\ Watt/cm^3$ and Fig. 2-27 represents the profiles of heat generated along the outer surfaces of crucible and afterheater. The total energy production in the system is $Q_{total}^{system} = 1.95\ kWatt$ and the details have been shown in the table 2.10.

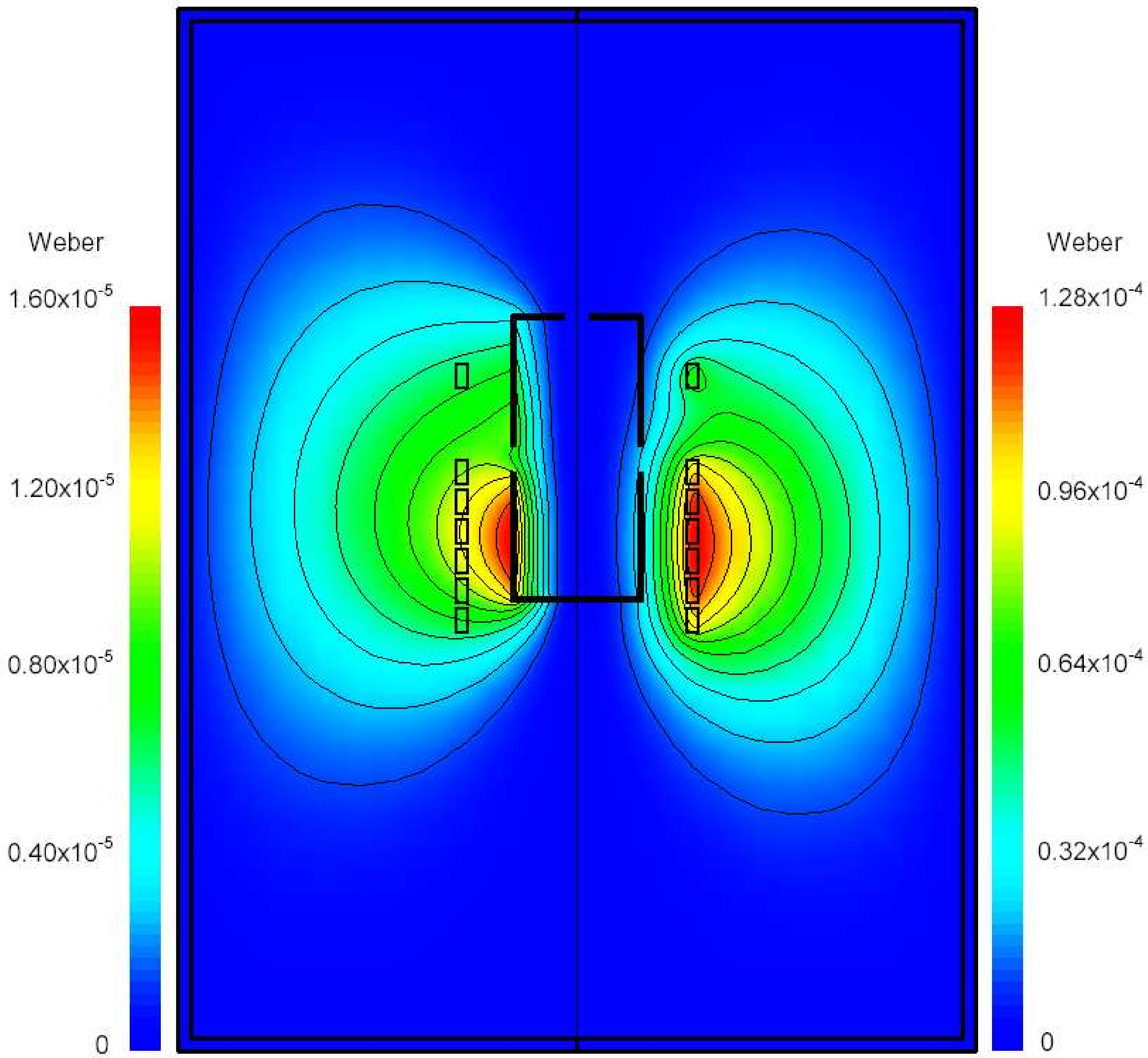

Fig. 2-25. Components of the magnetic stream function (ψ_B) calculated for *case h*. The right hand side shows the in-phase component (C), with $C_{max} = 1.28 \times 10^{-4}$ $Weber$ located in the coil and the left hand side shows the out-of-phase component (S), with $S_{max} = 1.60 \times 10^{-5}$ $Weber$ located on the crucible wall.

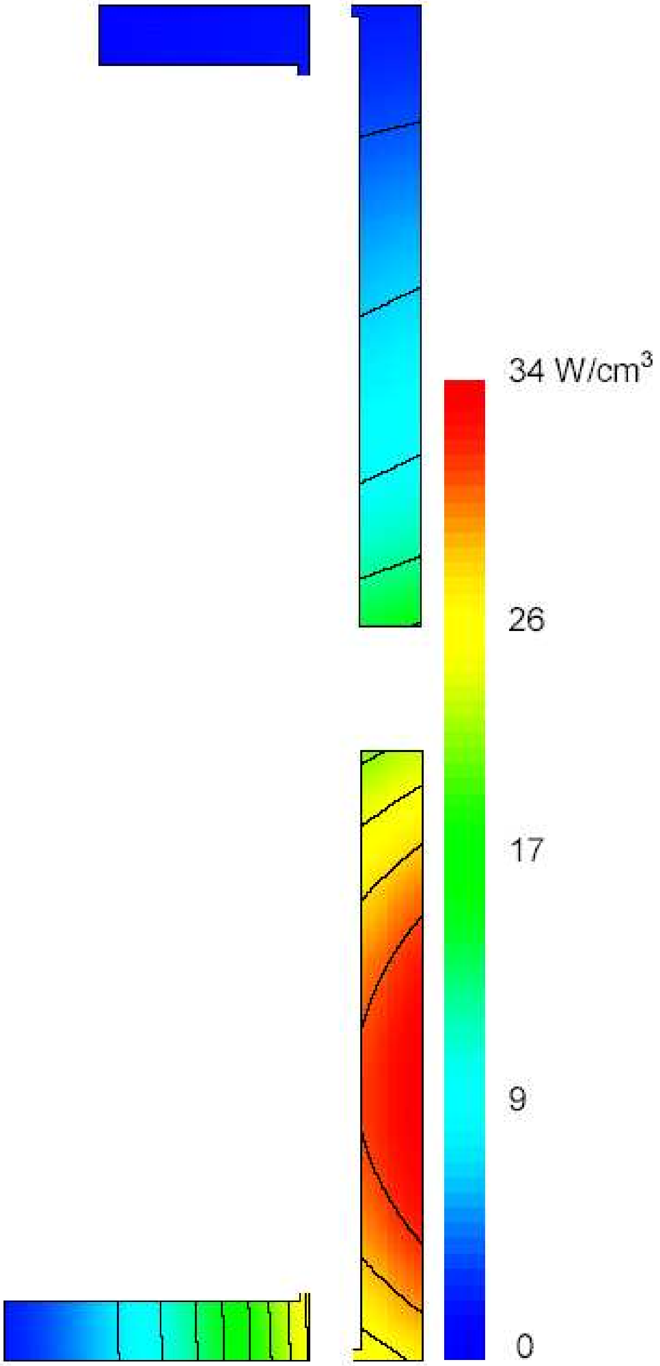

Fig. 2-26. Contours of the volumetric power distribution (q) in the crucible and afterheater, computed for *case h*. The maximum value of energy deposition is $q_{max} = 34.1\ Watt/cm^3$ and it is located at the outer surface of crucible wall.

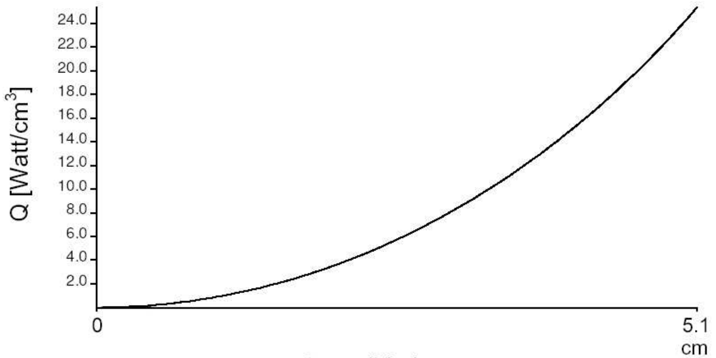

a) crucible bottom

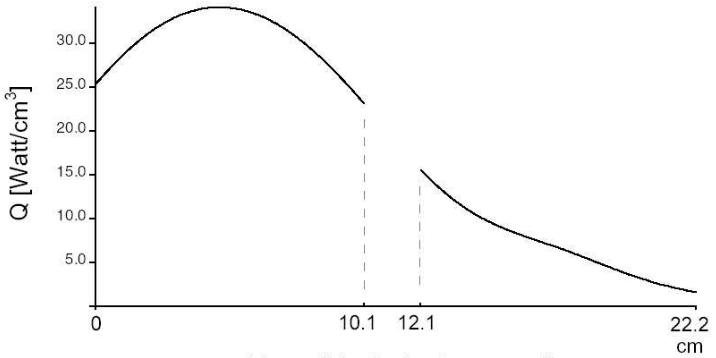

b) crucible & afterheater wall

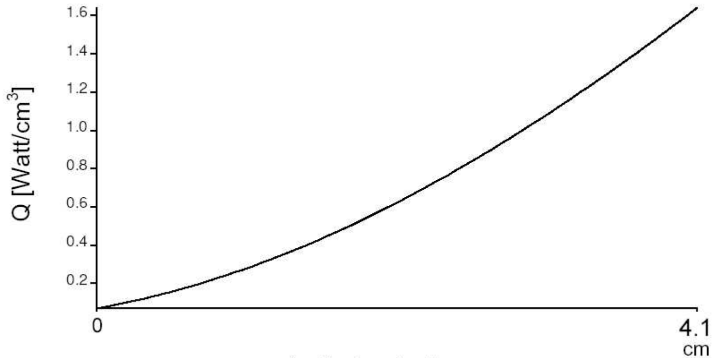

c) afterheater top cover

Fig. 2-27. Profiles of the heat generated along the outer surfaces of crucible and afterheater calculated for *case h*, (a) crucible bottom, (b) crucible wall, and (c) afterheater top cover.

Part	Heat generated ($Watt$)	Percentage (%)
Crucible bottom	33	6
Crucible wall	342	63
Afterheater wall	138	25
Afterheater top cover	9	2
Chamber	22	4
Total	544	100

Table 2-11. Detail information about the heat generated in the different parts of the CZ system, calculated for the *case i.*

2.3.9 case i: Crucible and afterheater, with a gap, separate turns of RF coil (N=3)

For the configuration with a gap between crucible and afterheater, we delete three turns of the main coil. Consequently, the distance between turns is $d_{co} = 37.5\ mm$, without any change in the position of the first and the last turn of the coil (similar to *case e.*

Fig. 2-28 shows the contours of in-phase component right hand side) and out-of-phase component (left hand side) of the magnetic stream function for this configuration. The maximum value of in-phase component is $C_{max} = 6.84 \times 10^{-5}\ Weber$ on the middle turn of main coil and the maximum value of the out-of-phase component is $S_{max} = 7.73 \times 10^{-6}\ Weber$ on the crucible wall and $C_{max}/S_{max} = 8.8$. There are local maxima for in-phase component on every turn in the range of $4.0 - 6.84 \times 10^{-5}\ Weber$.

The volumetric energy generation rate (q) in the crucible and afterheater has been shown in Fig. 2-29. The maximum value of energy deposition in the crucible and afterheater is $q_{max}^{crucible} = 7.14\ Watt/cm^3$. Fig. 2-30 shows the profiles of the generated heat along the outer surfaces of the crucible and afterheater. The total energy deposition rate in the crucible, afterheater and chamber is $Q_{total}^{system} = 0.54\ kWatt$. More details of the heat generated in the different parts have been presented in the table 2-11.

The distribution of in-phase component is markedly different in and between crucible and induction coil, in comparison with *case h*, as the Fig. 2-31 shows. In the *case h* the contours have approximately a straight line shape parallel to the crucible side wall but in the present case, they have a wavy shape that represent a non-uniform variation of this component in that aria. Also as indicated in Figs. 2-29 and 2-30, the energy distribution in the crucible and afterheater side wall is not uniform and also the heat production in the afterheater is comparable to the crucible.

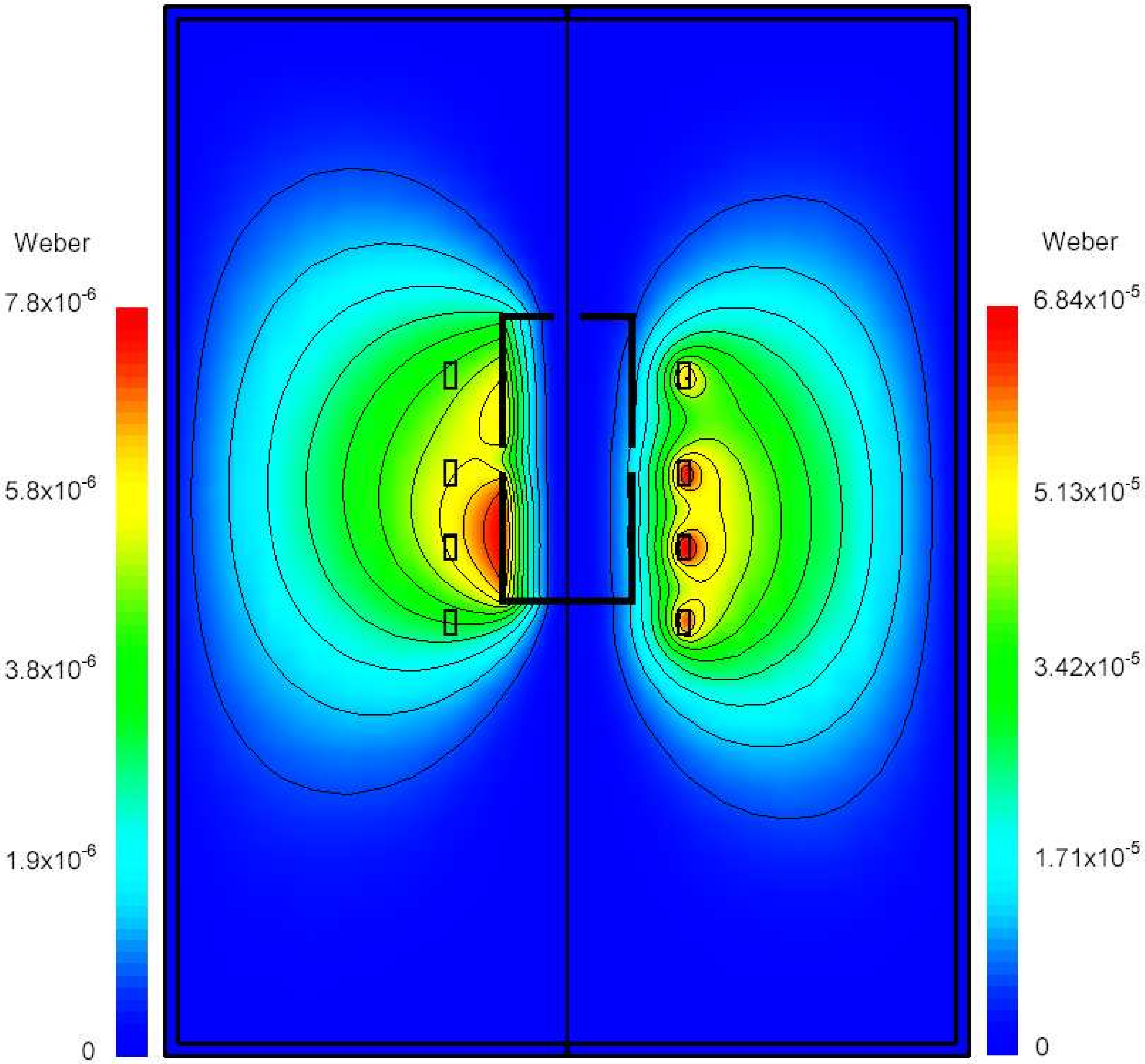

Fig. 2-28. Components of the magnetic stream function (ψ_B) calculated for *case i*. The right hand side shows the in-phase component (C), with $C_{max} = 6.84 \times 10^{-5}$ $Weber$ located in the coil and the left hand side shows the out-of-phase component (S), with $S_{max} = 7.73 \times 10^{-6}$ $Weber$ located on the crucible wall.

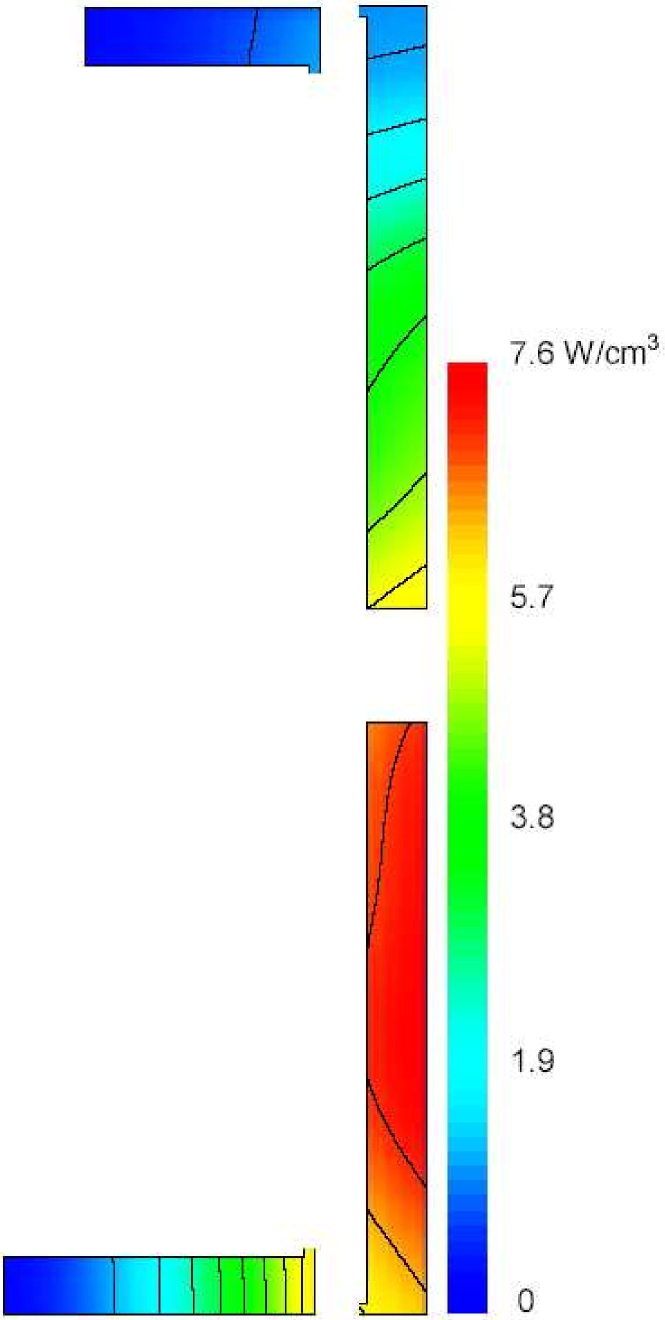

Fig. 2-29. Contours of the volumetric power distribution (q) in the crucible and afterheater, computed for *case i*. The maximum value of energy deposition is $q_{max} = 7.6\ Watt/cm^3$ and it is located at the outer surface of crucible wall.

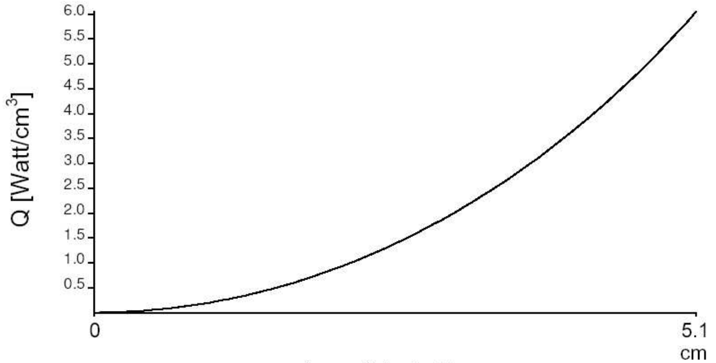

a) crucible bottom

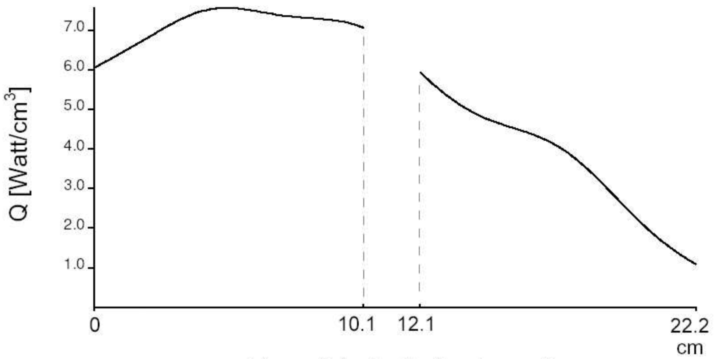

b) crucible & afterheater wall

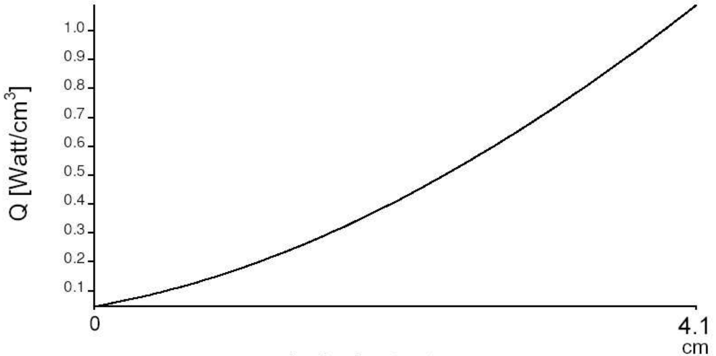

c) afterheater top cover

Fig. 2-30. Profiles of the heat generated along the outer surfaces of crucible and afterheater calculated for *case i*, (a) crucible bottom, (b) crucible wall, and (c) afterheater top cover.

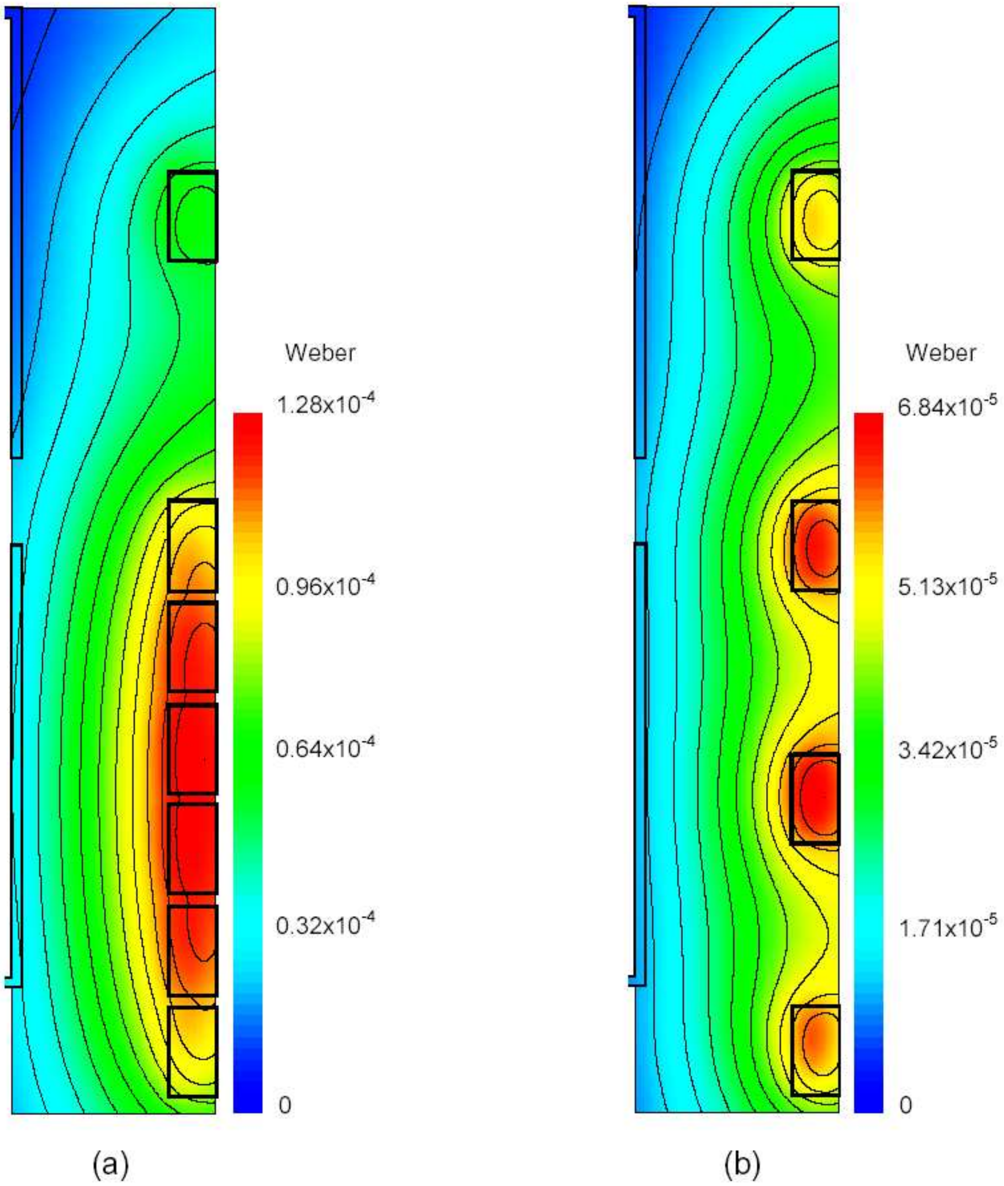

Fig. 2-31. Contours of the in-phase-component (C) in space between crucible and afterheater, for two *cases* d (left hand side) and e (right hand side). In the *case* d, the shape of the contours is about straight line parallel to the crucible wall which illuminates the uniform gradient of this component in that area. In the *case* e, the contours have a wavy shape that indicates a non-uniform gradient of this component.

2.4 Conclusions

We have presented and demonstrated some results of induction heating for an oxide Czochralski crystal growth system using a finite element method. The following conclusions were obtained:

1) The maximum value of in-phase component (C_{max}) is located in the induction coil and the maximum value of the out-of-phase component (S_{max}) is placed on the crucible side wall.

2) Distribution of the in-phase component depends on the coil geometry and for the out-of-phase component depends on the crucible-afterheater orientation.

3) Although C_{max} is much greater than S_{max} ($C_{max}/S_{max} \sim 9$), the magnitudes of C and S are similar within the crucible and afterheater and also chamber wherein the phase shift occurs and the required heat generation is produced. It means that within the conductors both components (C and S) contribute to the heat generation about equally.

4) The major portion of the heat generation is in the crucible side wall.

5) By including an active afterheater, the total heat generation in the crucible will be increased.

6) Change in the coil diameter has not any effective influence on the spatial distribution of heat generation in the crucible and afterheater.

7) When the gap between coil turns is very small than turn height, the "equivalent cylinder" model is a good approximation instead of multi-turn coil and it reduces the calculation time effectively.

8) When the gap between coil turns is comparable to the turn height, the variation of in-phase component (C) in and between induction coil and crucible is not uniform and its contours have a wavy shape. Also, the distribution of the heat generation in the crucible and afterheater side wall is non-uniform.

9) By using a rounded crucible bottom, the position of the $q_{max}^{crucible}$ at the crucible side wall goes upward, compared to the flat bottom shape.

10) By placing a gap between crucible and afterheater, the distribution and magnitude of the heat generation in the crucible does not change but in the afterheater is different. The energy production in the afterheater is smaller specially in the top cover.

Chapter 3

Configuration contains only gas

3.1 Introduction

In this chapter, the temperature distribution and flow field are computed for some Czochralski systems contain only *gas*, by application of the internal heat generation in the crucible and afterheater. The goal of these calculation is to study and investigate the influence of geometry and orientation of crucible, afterheater and insulation on the overall heat transport in the CZ system.

3.2 Mathematical model

We consider CZ systems usually used in dielectric crystal growth, which consist of a crucible and afterheater (*iridium*), insulation (ZrO_2) and chamber (*stainless steel*). Our model involves the following basic assumption: (1) The system is axisymmetric, (2) The system is in quasi-steady state, (3) Internal radiation is not included, (4) There is no melt and crystal in the system. (5) Gas is incompressible Newtonian fluid satisfying the Boussinesq approximation. Thus the fundamental equations are,
(a) Fluid flow in gas:

$$\rho \mathbf{v} \cdot \nabla \mathbf{v} = -\nabla p + \mu \nabla^2 \mathbf{v} + \rho \beta g (T - T_0) \vec{e}_z \tag{3.1}$$

which is the Navier-Stokes equation with Boussinesq approximation.
(b) continuity equation:

$$\nabla \cdot \mathbf{v} = 0 \tag{3.2}$$

(c) Heat transport by conduction and convection (energy equation):

$$\alpha\nabla^2 T_g - \mathbf{v}\cdot\nabla T_g = 0 \qquad \text{convection and conduction in the gas} \tag{3.3}$$

$$\nabla^2 T_c + q = 0 \qquad \text{conduction in the crucible \& afterheater} \tag{3.4}$$

$$\nabla^2 T_i = 0 \qquad \text{conduction in the insulation} \tag{3.5}$$

where the subscripts g, c and i denote gas, conductors (crucible and afterheater) and insulation, respectively. The boundary conditions are,
a) at bottom and wall of the crucible, afterheater wall and top cover:

$$\mathbf{v} = 0 \tag{3.6}$$

b) at the outer surfaces of insulation:

$$-k_i\frac{\partial T_i}{\partial \hat{n}} = h_i\left(T_i - T_a\right) + \sigma\varepsilon_i\left(T_i^4 - T_a^4\right) \tag{3.7}$$

which denotes the heat dissipation via radiation and convection from those surfaces.
c) at the afterheater hole:

$$T = T_{ah} \tag{3.8}$$

where $\mathbf{v} = (u, v, w)$ is the fluid velocity vector, p the pressure, T the temperature, $\vec{e}_z$ the z-directional unit vector, g the acceleration due to gravity, β the thermal expansion coefficient, μ the dynamic viscosity, α the thermal diffusivity, q the heat source density, ε the emissivity, k the thermal conductivity, ρ the density, h the Newtonian heat transfer coefficient, $\hat{n}$ the unit normal vector, σ the Stefan-Boltzmann constant, T_a the ambient temperature and T_{ah} the temperature at the afterheater hole.

3.3 Weak form calculation

In axisymmetric condition all variables are independent of the azimuthal coordinate (ϕ), i.e.

$$F = F(r, z), \qquad F = \mathbf{v}, T, p \tag{3.9}$$

In order to use numerical computation and apply finite element method, at first we write the components of the governing equations and BCs in the cylindrical coordinates (r, ϕ, z), then we calculate their weak form and finally the non-dimensional form of the weak form.

3.3.1 Fluid flow

Components of the Navier-Stokes equation with Boussinesq approximation (Eq. 3.1) in the cylindrical coordinates are as:

$$\begin{cases} u\dfrac{\partial u}{\partial r} + w\dfrac{\partial u}{\partial z} - \dfrac{v^2}{r} = -\dfrac{1}{\rho}\dfrac{\partial p}{\partial r} + \nu\left(\nabla^2 u - \dfrac{u}{r^2}\right) \\[2ex] u\dfrac{\partial v}{\partial r} + w\dfrac{\partial v}{\partial z} + \dfrac{uv}{r} = \nu\left(\nabla^2 v - \dfrac{v}{r^2}\right) \\[2ex] u\dfrac{\partial w}{\partial r} + w\dfrac{\partial w}{\partial z} = -\dfrac{1}{\rho}\dfrac{\partial p}{\partial z} + \nu\nabla^2 w + g\beta\left(T - T_0\right) \end{cases} \tag{3.10}$$

where $\nabla^2 \equiv \frac{1}{r}\frac{\partial}{\partial r}\left(r\frac{\partial}{\partial r}\right) + \frac{1}{r^2}\frac{\partial^2}{\partial \varphi^2} + \frac{\partial}{\partial z^2}$ is the *Laplacian operator*. We have $\nu = \mu/\rho$ where ν is the kinematic viscosity and assume $T_0 = 0$.

Weak form

The weak form of the set of equations (3-10) is as:

$$\begin{aligned} & \iint \left[u\frac{\partial u}{\partial r} + w\frac{\partial u}{\partial z} - \frac{v^2}{r} + \frac{1}{\rho}\frac{\partial p}{\partial r} - \nu\left(\nabla^2 u - \frac{u}{r^2}\right)\right] \Phi_u \; r\,\mathrm{d}r\,\mathrm{d}z \\ + & \iint \left[u\frac{\partial v}{\partial r} + w\frac{\partial v}{\partial z} + \frac{uv}{r} - \nu\left(\nabla^2 v - \frac{v}{r^2}\right)\right] \Phi_v \; r\,\mathrm{d}r\,\mathrm{d}z \\ + & \iint \left[u\frac{\partial w}{\partial r} + w\frac{\partial w}{\partial z} + \frac{1}{\rho}\frac{\partial p}{\partial z} - \nu\nabla^2 w - g\beta\left(T - T_0\right)\right] \Phi_w \; r\,\mathrm{d}r\,\mathrm{d}z \\ = & \;\; 0 \end{aligned} \tag{3.11}$$

where Φ is the weighting function. By using the Green's theorem,

$$
\begin{aligned}
& \iint \left[\left(u\frac{\partial u}{\partial r} + w\frac{\partial u}{\partial z} - \frac{v^2}{r} + \nu\frac{u}{r^2} \right) \Phi_u - \frac{p}{\rho}\left(\frac{\partial \Phi_u}{\partial r} + \frac{\Phi_u}{r} \right) \right. \\
& \left. + \, \nu \left(\frac{\partial u}{\partial r}\frac{\partial \Phi_u}{\partial r} + \frac{\partial u}{\partial z}\frac{\partial \Phi_u}{\partial z} \right) \right] \; r \,\mathrm{d}r \,\mathrm{d}z \\
+ \quad & \iint \left[\left(u\frac{\partial v}{\partial r} + w\frac{\partial v}{\partial z} + \frac{uv}{r} + \nu\frac{v}{r^2} \right) \Phi_v + \nu \left(\frac{\partial v}{\partial r}\frac{\partial \Phi_v}{\partial r} + \frac{\partial v}{\partial z}\frac{\partial \Phi_v}{\partial z} \right) \right] \; r \,\mathrm{d}r \,\mathrm{d}z \\
+ \quad & \iint \left[\left(u\frac{\partial w}{\partial r} + w\frac{\partial w}{\partial z} - g\beta T \right) \Phi_w - \frac{p}{\rho}\frac{\partial \Phi_w}{\partial z} + \nu \left(\frac{\partial w}{\partial r}\frac{\partial \Phi_w}{\partial r} + \frac{\partial w}{\partial z}\frac{\partial \Phi_w}{\partial z} \right) \right] \; r \,\mathrm{d}r \,\mathrm{d}z \\
= \quad & 0
\end{aligned}
\tag{3.12}
$$

Non-dimensional form

By using $(R, Z) = (r, z)/L_c$, $(U, V, W) = (u, v, w)/U_c$, $\Theta = T/T_c$, $P = p/\rho U_c^2$ and $U_c = \nu/L_c$, where L_c is the characteristic length, U_c the characteristic velocity and T_c the characteristic temperature, the non-dimensional form is as follow,

$$
\begin{aligned}
& \iint \left[\left(U\frac{\partial U}{\partial R} + W\frac{\partial U}{\partial Z} - \frac{V^2}{R} + \frac{U}{R^2} \right) \Phi_u - P\left(\frac{\partial \Phi_u}{\partial R} + \frac{\Phi_u}{R} \right) \right. \\
& \left. + \left(\frac{\partial U}{\partial R}\frac{\partial \Phi_u}{\partial R} + \frac{\partial U}{\partial Z}\frac{\partial \Phi_u}{\partial Z} \right) \right] \; R \,\mathrm{d}R \,\mathrm{d}Z \\
+ \quad & \iint \left[\left(U\frac{\partial V}{\partial R} + W\frac{\partial V}{\partial Z} + \frac{UV}{R} + \frac{V}{R^2} \right) \Phi_v + \left(\frac{\partial V}{\partial R}\frac{\partial \Phi_v}{\partial R} + \frac{\partial V}{\partial Z}\frac{\partial \Phi_v}{\partial Z} \right) \right] \; R \,\mathrm{d}R \,\mathrm{d}Z \\
+ \quad & \iint \left[\left(U\frac{\partial W}{\partial R} + W\frac{\partial W}{\partial Z} - Gr \cdot \Theta \right) \Phi_w - P\frac{\partial \Phi_w}{\partial Z} \right. \\
& \left. + \left(\frac{\partial W}{\partial R}\frac{\partial \Phi_w}{\partial R} + \frac{\partial W}{\partial Z}\frac{\partial \Phi_w}{\partial Z} \right) \right] \; R \,\mathrm{d}R \,\mathrm{d}Z \\
= \quad & 0
\end{aligned}
\tag{3.13}
$$

where $Gr = g\beta T_c L_c^3/\nu^2$ is the *Grashof number.*

3.3.2 Continuity equation

From Eq. (3-2) we have

$$\nabla.\mathbf{v} = 0 \;\longrightarrow\; \frac{1}{r}\frac{\partial}{\partial r}(ru) + \frac{\partial w}{\partial z} = 0 \;\longrightarrow\; \frac{\partial u}{\partial r} + \frac{u}{r} + \frac{\partial w}{\partial z} = 0 \tag{3.14}$$

So the weak form is as:

$$\iint \left(\frac{\partial u}{\partial r} + \frac{u}{r} + \frac{\partial w}{\partial z}\right) \Phi_c \; r \,\mathrm{d}r \,\mathrm{d}z = 0 \tag{3.15}$$

and the non-dimensional form:

$$\iint \left(\frac{\partial U}{\partial R} + \frac{U}{R} + \frac{\partial W}{\partial Z}\right) \Phi_c \; R \,\mathrm{d}R \,\mathrm{d}Z = 0 \tag{3.16}$$

3.3.3 Energy equation

From Eq.s (3-3)-(3-5) and $\alpha = k/\rho c_p$, where α is the thermal diffusivity and c_p the specific heat in constant pressure, we can calculate the weak form of the energy equations.

Weak form

$$\begin{aligned}
& k_c \iint\limits_{\textit{crucible}} \left(\nabla T_c \cdot \nabla \Phi_{ce} - \frac{q}{k_c}\Phi_{ce}\right) \; r \,\mathrm{d}r \,\mathrm{d}z \\
+ \;& k_i \iint\limits_{\textit{insulation}} \nabla T_i \cdot \nabla \Phi_{ie} \; r \,\mathrm{d}r \,\mathrm{d}z \;+\; k_i \int\limits_{\substack{\textit{outer surfaces}\\ \textit{of insulation}}} \frac{\partial T_i}{\partial \hat{n}} \Phi_{ie} \; r \,\mathrm{d}r \\
+ \;& \iint\limits_{\textit{gas}} \left[k_g \left(\nabla T_g \cdot \nabla \Phi_{ge}\right) + \rho_g c_p \mathbf{v} \cdot \nabla T_g \Phi_{ge}\right] \; r \,\mathrm{d}r \,\mathrm{d}z \\
= \;& 0
\end{aligned} \tag{3.17}$$

and dividing by k_g, we will find

$$\begin{aligned}
& k_{cg} \iint\limits_{crucible} \left(\nabla T_c \cdot \nabla \Phi_{ce} - \frac{q}{k_c} \Phi_{ce} \right) \, r \, \mathrm{d}r \, \mathrm{d}z \\
+ \; & k_{ig} \iint\limits_{insulation} \nabla T_i \cdot \nabla \Phi_{ie} \, r \, \mathrm{d}r \, \mathrm{d}z \; + \; k_{ig} \int\limits_{\substack{outer\ surfaces \\ of\ insulation}} \frac{\partial T_i}{\partial \hat{n}} \Phi_{ie} \, rdr \\
+ \; & \iint\limits_{gas} \left[(\nabla T_g \cdot \nabla \Phi_{ge}) + \rho_g c_p \mathbf{v} \cdot \nabla T_g \Phi_{ge} \right] \, r \, \mathrm{d}r \, \mathrm{d}z \\
= \; & 0 \qquad (3.18)
\end{aligned}$$

where $k_{cg} = k_c/k_g$ and, $k_{ig} = k_i/k_g$. Finally by using the Green's theorem,

$$\begin{aligned}
& k_{cg} \iint\limits_{crucible} \left(\frac{\partial T_c}{\partial r} \frac{\partial \Phi_{ce}}{\partial r} + \frac{\partial T_c}{\partial z} \frac{\partial \Phi_{ce}}{\partial z} - \frac{q}{k_c} \Phi_{ce} \right) \, r \, \mathrm{d}r \, \mathrm{d}z \\
+ \; & k_{ig} \iint\limits_{insulation} \left(\frac{\partial T_i}{\partial r} \frac{\partial \Phi_{ie}}{\partial r} + \frac{\partial T_i}{\partial z} \frac{\partial \Phi_{ie}}{\partial z} \right) \, r \, \mathrm{d}r \, \mathrm{d}z \; + \; k_{ig} \int\limits_{\substack{outer\ surfaces \\ of\ insulation}} \frac{\partial T_i}{\partial \hat{n}} \Phi_{ie} \, r \, \mathrm{d}r \\
+ \; & \iint\limits_{gas} \left(\frac{\partial T_g}{\partial r} \frac{\partial \Phi_{ge}}{\partial r} + \frac{\partial T_g}{\partial z} \frac{\partial \Phi_{ge}}{\partial z} \right) \, r \, \mathrm{d}r \, \mathrm{d}z \; + \; \frac{1}{\alpha} \iint\limits_{gas} \left(u \frac{\partial T_g}{\partial r} + w \frac{\partial T_g}{\partial z} \right) \Phi_{ge} \, r \, \mathrm{d}r \, \mathrm{d}z \\
= \; & 0 \qquad (3.19)
\end{aligned}$$

Non-dimensional form

The non-dimensional form is

$$
\begin{aligned}
& \frac{k_{cg}}{Pr} \iint\limits_{crucible} \left[\frac{\partial \Theta_c}{\partial R}\frac{\partial \Phi_{ce}}{\partial R} + \frac{\partial \Theta_c}{\partial Z}\frac{\partial \Phi_{ce}}{\partial Z} - \left(\frac{L_c^2}{T_c k_c}\right) q \Phi_{ce} \right] R \,\mathrm{d}R \,\mathrm{d}Z \\
+ & \frac{k_{ig}}{Pr} \iint\limits_{insulation} \left(\frac{\partial \Theta_i}{\partial R}\frac{\partial \Phi_{ie}}{\partial R} + \frac{\partial \Theta_i}{\partial Z}\frac{\partial \Phi_{ie}}{\partial Z} \right) R \,\mathrm{d}R \,\mathrm{d}Z + \frac{k_{ig}}{Pr} \int\limits_{\substack{outer\ surfaces \\ of\ insulation}} \frac{\partial \Theta_i}{\partial \hat{N}} \Phi_{ie} \, R \,\mathrm{d}R \\
+ & \frac{1}{Pr} \iint\limits_{gas} \left(\frac{\partial \Theta_g}{\partial R}\frac{\partial \Phi_{ge}}{\partial R} + \frac{\partial \Theta_g}{\partial Z}\frac{\partial \Phi_{ge}}{\partial Z} \right) R \,\mathrm{d}R \,\mathrm{d}Z + \iint\limits_{gas} \left(U\frac{\partial \Theta_g}{\partial R} + W\frac{\partial \Theta_g}{\partial Z} \right) \Phi_{ge} \, R \,\mathrm{d}R \,\mathrm{d}Z \\
= & \ 0
\end{aligned}
\tag{3.20}
$$

where $Pr = \nu/\alpha$ is the *Prandtl number.*

The non-dimensional form of the boundary condition at the outer surfaces of insulation is as follow:

$$
-\frac{\partial \Theta_i}{\partial \hat{N}} = Bio\left(\Theta_i - \Theta_a\right) + Rad\left(\Theta_i^4 - \Theta_a^4\right) \tag{3.21}
$$

where $Bio = hL_c/k_i$ is the *Biot number* and $Rad = \sigma \epsilon_i L_c T_c^3/k_i$ is the *Radiation number.*

3.3.4 Stream function

It is useful to introduce the fluid stream function (ψ), which its relation to the velocity is

$$
U = \frac{1}{R}\frac{\partial \psi}{\partial Z}, \qquad V = -\frac{1}{R}\frac{\partial \psi}{\partial R} \tag{3.22}
$$

Differentiating the above equations and subtracting gives

$$
-\left(\frac{\partial^2 \psi}{\partial R^2} + \frac{\partial^2 \psi}{\partial Z^2}\right) + \frac{1}{R}\frac{\partial \psi}{\partial R} + R\left(\frac{\partial U}{\partial Z} - \frac{\partial V}{\partial R}\right) = 0 \tag{3.23}
$$

This leads to the weak form

$$
\iint \left\{ \frac{\partial \psi}{\partial R}\frac{\partial \Phi_p}{\partial R} + \frac{\partial \psi}{\partial Z}\frac{\partial \Phi_p}{\partial Z} + \left[\frac{1}{R}\frac{\partial \psi}{\partial Z} + R\left(\frac{\partial U}{\partial Z} - \frac{\partial V}{\partial R}\right)\right] \Phi_p \right\} R \,\mathrm{d}R \,\mathrm{d}Z = 0 \tag{3.24}
$$

Description (units)	Symbel	Value
Density (kg/m^3)	ρ_g	0.35
Dynamic viscosity ($kg/m \cdot s$)	μ_g	$4. \times 10^{-5}$
Kinematic viscosity (m^2/s)	ν_g	1.14×10^{-4}
Thermal expansion coefficient ($1/K$)	β_g	2.7×10^{-3}
Specific heat ($kJ/kg \cdot K$)	c_p	1.14
Thermal diffusivity (m^2/s)	α_g	2.7×10^{-4}
Thermal conductivity ($W/m \cdot k$)	k_g	0.11
	k_c	147
	k_i	2.14
Emissivity	ε_i	0.2
Heat transfer coefficient ($W/m^2 \cdot K$)	h_i	20

Table 3-1. Physical properties used for calculations; the subscripts g, c and i denote gas (air), crucible ($iridium$) and insulation (ZrO_2), respectively.

3.3.5 The calculation conditions

Values of physical properties employed for our calculations are presented in Table 3-1 [9,14,15]. In all calculations the ambient temperature is set to be 25^oC and the frequency of input electrical current is 10 kHz. We have selected the crucible inner radius (r_c) as the characteristic length (L_c) and temperature at a special position (for example afterheater hole) as the characteristic temperature (T_c). It should be mentioned that the all values of temperature at those special positions are from measurement in our Czochralski-dielectric lab in IKZ and we have used them as a boundary condition. In all configurations, the afterheater has a top cover and the crucible has a baffle in some cases.

Once a solution is obtained for $q\,(r, z)$ in every configuration, the nodal values of this variable in the crucible and afterheater, are saved for later use in the temperature and flow field calculation. Since the electromagnetic field components (C and S) scale linearly with the electric current of the RF coil (chapter 2), so only one induction computation need to be performed for a given configuration. This greatly simplifies solution and also decreases the time for heat transfer calculations efficiently. The results for different configurations will be presented hereafter.

3.4 Results and discussion

3.4.1 case a: crucible and afterheater, with and without a gap

Fig. 3-a-1 shows a sketch of these two systems and the operating parameters are listed in Table 3-2. Boundary condition for temperature at the afterheater hole is set to be 1188 ^oC and 1120 ^oC for the configuration without and with a gap, respectively. Then the non-dimensional numbers are $Gr = 3.5 \times 10^5$ (configuration without a gap) and $Gr = 3.3 \times 10^5$ (configuration with a gap), $Pr = 0.7$, $Rad_i = 0.8$ (configuration without a gap), $Rad_i = 0.7$ (configuration with a gap) and $Bio_i = 0.45$.

The aim of these calculations was to investigate the effect of the insulation and a closed gap (filled out by insulation) between crucible and afterheater on the gas flow and temperature field.

Induction heating

Fig. 3-a-2 represents the distribution of heat generation in the crucible and afterheater for these two configurations. The maximum value of energy deposition is $q_{max} = 25\ W/cm^3$ for configuration without a gap and $q_{max} = 22\ W/cm^3$ for configuration with a gap, and at the outer surface of crucible wall for both systems. The total energy production in the crucible and afterheater is $Q_{total} = 1.5\ kW$ and $Q_{total} = 1.3\ kW$ for configuration without and with a gap, respectively.

Configuration without a gap between crucible and afterheater

Fig. 3-a-3(a) shows the gas flow pattern and temperature distribution for the whole system. There are two separate eddies of gas convection in the crucible and afterheater. In the crucible buoyancy drives a flow, which moves upward along the crucible wall, radially toward the centerline and down along the axis of symmetry. The maximum value of the streamfunction for this vortex is $\psi^c_{max} = -24$ and located in the center of the crucible. This vortex occupies not only the whole volume of the crucible but also a part of the afterheater. This flow transfers the heat from the crucible wall to the bulk of gas. On the other hand, there is a counterclockwise rotating vortex in the afterheater with a maximum value of $\psi^a_{max} = 11$. It moves up the fluid along the centerline and down along the afterheater wall. Also there is a small clockwise and weak rotating vortex in the lower part of the afterheater wall (not visible).

For the temperature field, the maximum temperature $T_{max} = 1410\ ^oC$ is in the middle of the crucible wall and the minimum $T_{min} = 950\ ^oC$ at the bottom corner of the insulation. The temperature profiles along the axis of symmetry from crucible bottom

Description (units)	Symbel	Value
Crucible inner radius (mm)	r_c	49
Crucible thickness (mm)	l_c	2
Crucible inner height (mm)	h_c	98
Afterheater inner height (mm)	h_{af}	100
Afterheater top cover hole (mm)	r_{af}	10
Distance between crucible and afterheater (mm)	D_{ca}	0, 30
Coil inner radius (mm)	r_{co}	85
Coil thickness (mm)	l_{co}	13
Height of coil turns (mm)	h_{co}	27
Distance between coil turns (mm)	d_{co}	5
Distance between two coils (mm)	D_{co}	25
Thickness of crucible insulation at the bottom (mm)	h_{ci}	50
Thickness of crucible insulation at the wall (mm)	d_{ci}	24
Thickness of afterheater insulation (mm)	d_{ai}	6
Ambient temperature (^oC)	T_a	25

Table 3-2. Operating parameters used for the configuration *case a*.

to the afterheater hole ($r = 0$), from the calculation and measurement are shown in Fig. 3-a-4(a). These profiles both demonstrate that in the crucible the temperature is approximately constant and then drops close to the afterheater hole. It means the temperature gradient in the crucible and afterheater is low but close to the afterheater hole it is extremely high (i.e. the heat flux is high in this aria).

Configuration with a gap between crucible and afterheater

Fig. 3-a-3(b) shows the effect of a gap between crucible and afterheater on the gas flow and temperature distribution. There are two vortexes with opposite direction and also with about equal strength ($\psi^c_{max} = -29$, $\psi^a_{max} = 34$). The first occupies the crucible and the second is located in the afterheater and also gap insulation. In this case the flow is intense near to the crucible bottom and afterheater top cover.

In the temperature field, we found the maximum value $T_{max} = 1360\ ^oC$ in the upper half of the crucible wall and the minimum value $T_{min} = 950\ ^oC$ at the bottom corner of the insulation. This maximum value is smaller than in the previous case ($\simeq 50\ ^oC$)

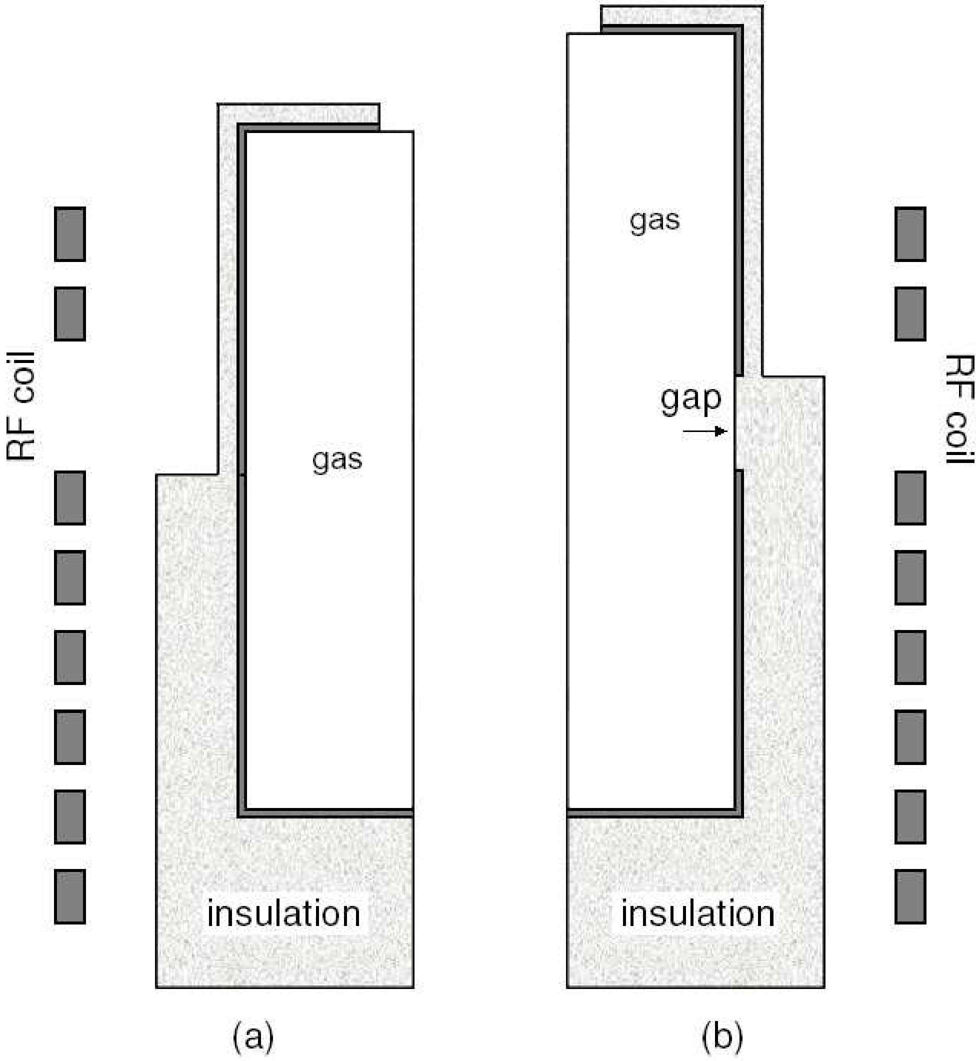

Fig. 3-a-1. Schematic diagram of two cases of Czochralski growth furnace, (a) without and (b) with a gap between crucible and afterheater.

but the position and value of minimum is the same. The calculated and measured temperature profiles along the axis of symmetry are presented in Fig. 3-a-4(b). It shows that the temperature in the crucible is approximately constant, decreases in the gap and is constant again in the afterheater until it drops close to its hole.

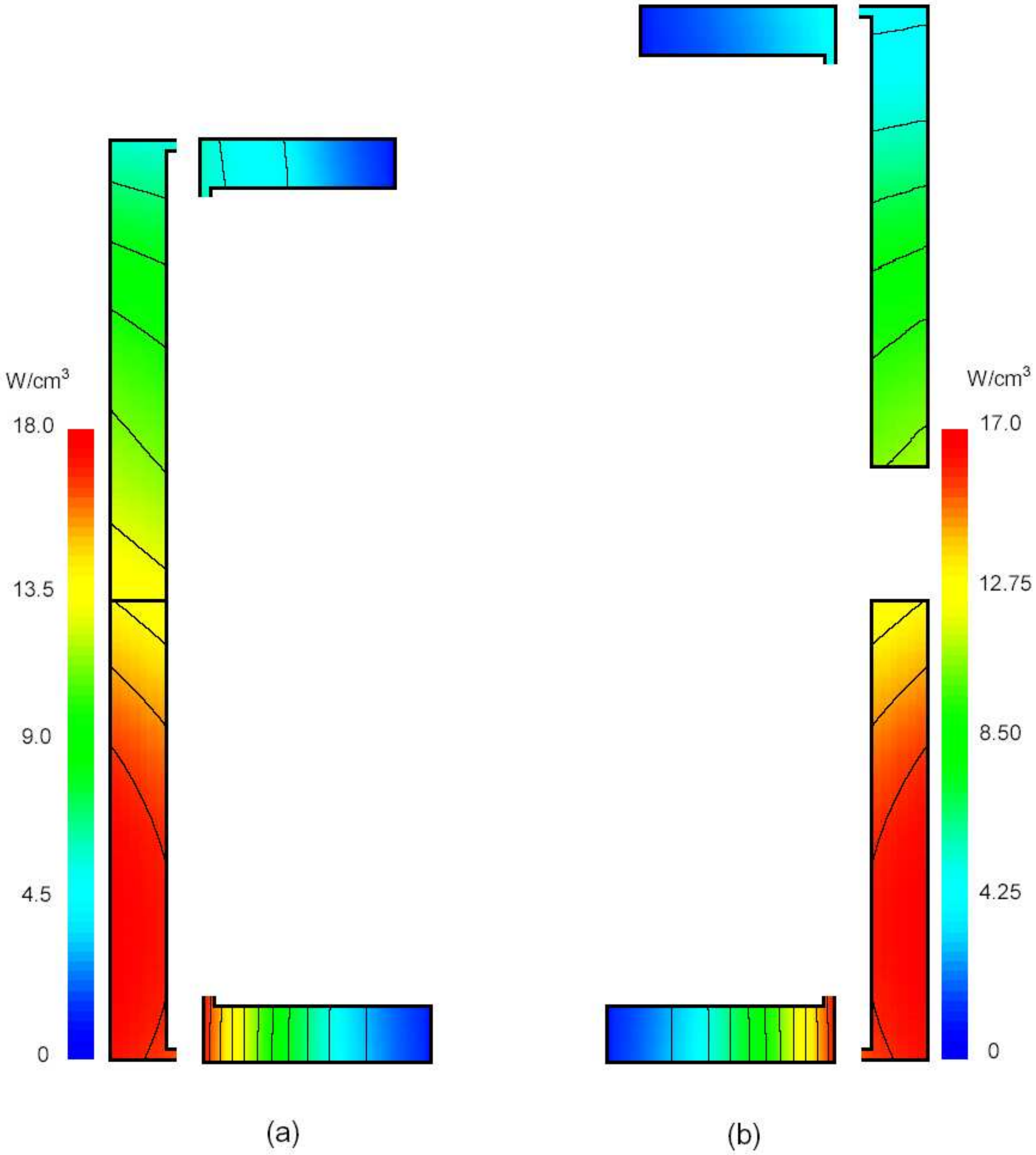

(a) (b)

Fig. 3-a-2. contours of the volumetric power distribution (q) in the crucible and afterheater. The maximum value of energy deposition is $q_{max}^{without} = 18\ W/cm^3$ for configuration without a gap (a), and $q_{max}^{with} = 17\ W/cm^3$ for configuration with a gap (b), and at the outer surface of crucible wall.

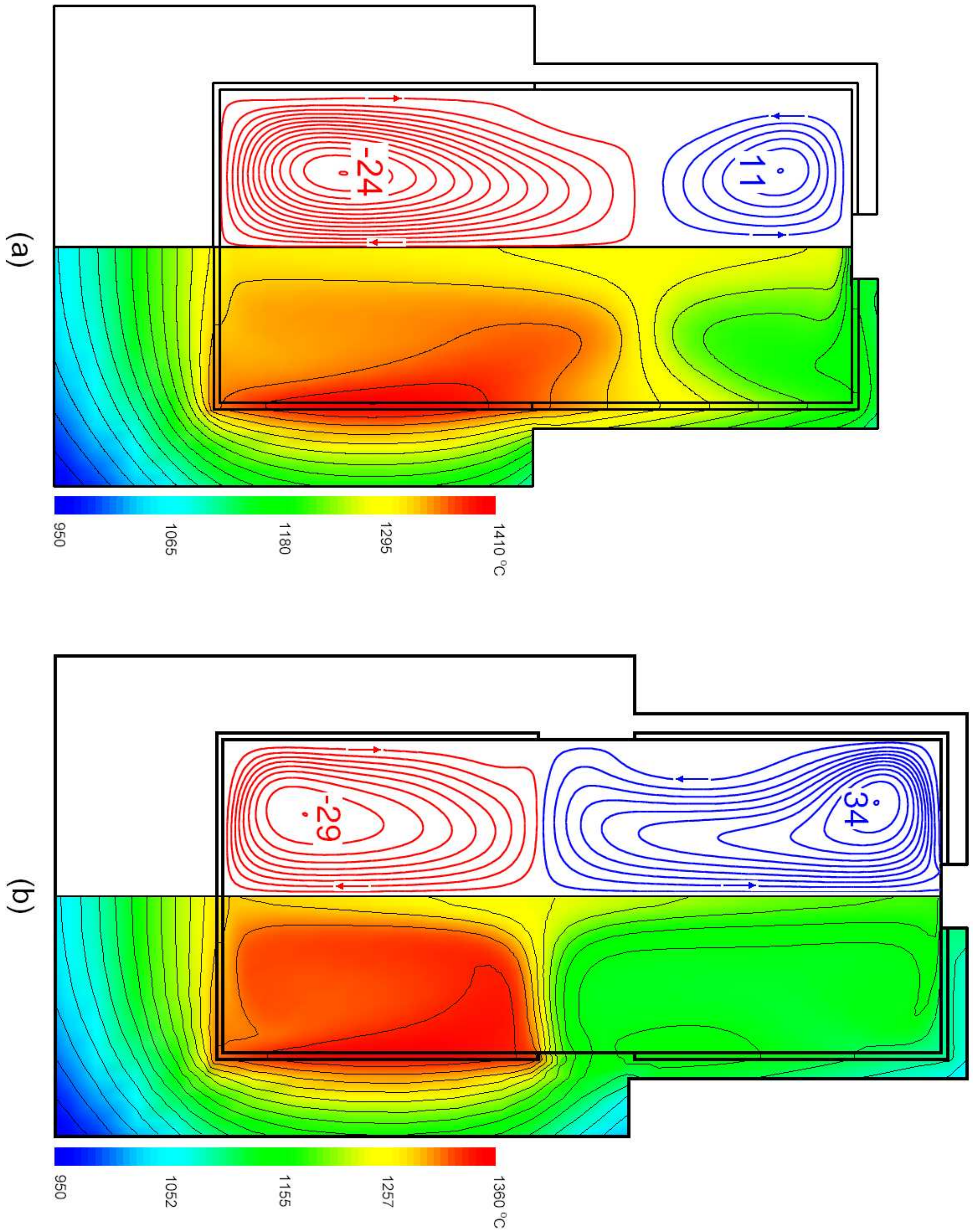

Fig. 3-a-3. contours of the temperature (right hand side) and the stream function (left hand side) for configuration (a) without, and (b) with a gap between crucible and afterheater.

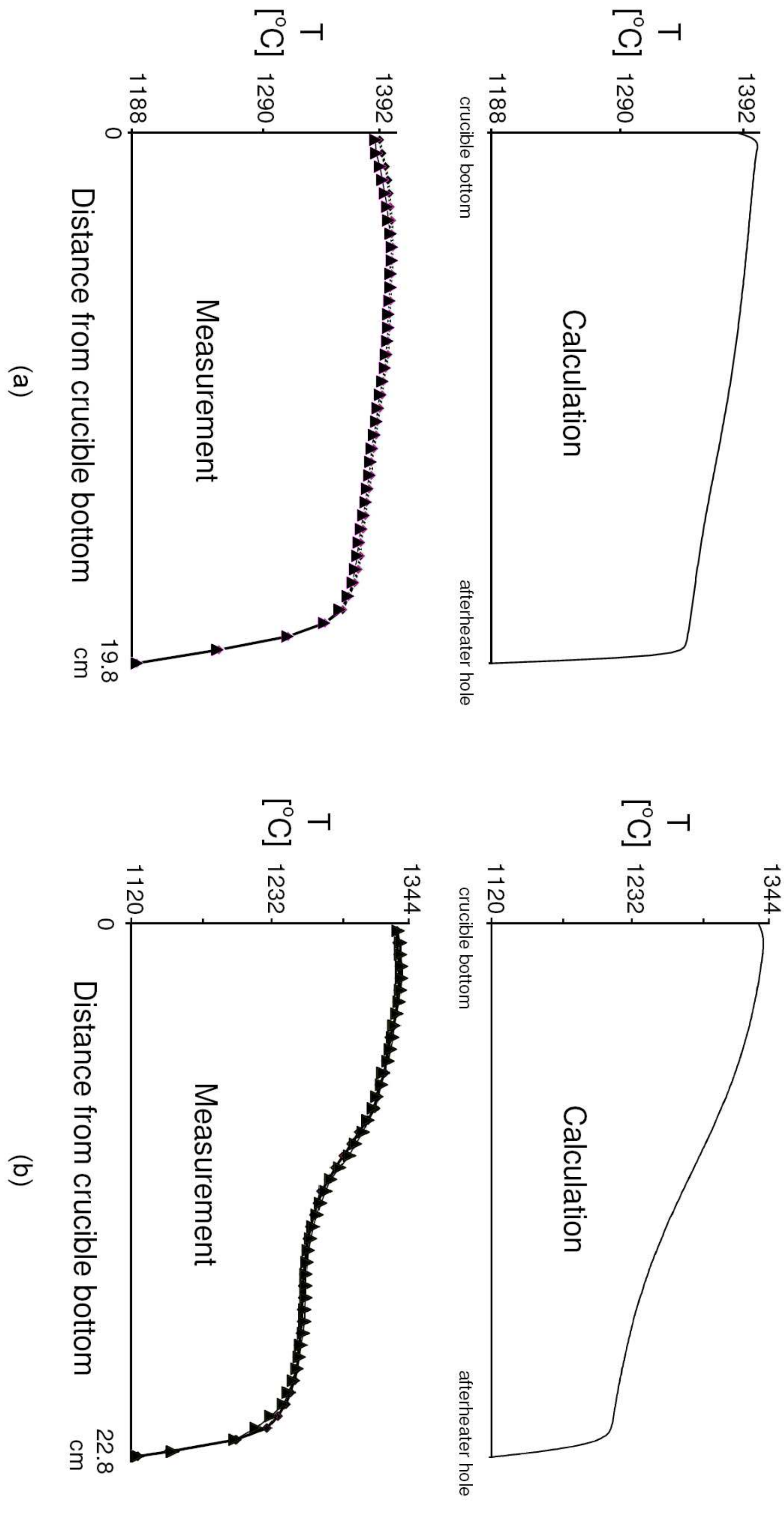

Fig. 3-a-4. Vertical temperature profiles along the axis of symmetry from crucible bottom to the afterheater hole for the configuration (a) without, and (b) with a gap between crucible and afterheater.

Description (units)	Symbel	Value
Crucible inner radius (*mm*)	r_c	50
Crucible thickness (*mm*)	l_c	2
Crucible inner height (*mm*)	h_c	100
Crucible baffle hole (*mm*)	r_{ch}	31
Afterheater inner height (*mm*)	h_{af}	100
Afterheater top cover hole (*mm*)	r_{af}	10-40
Afterheater insulation hole (*mm*)	r_{afi}	10-45
Distance between crucible and afterheater (*mm*)	D_{ca}	10
Coil inner radius (*mm*)	r_{co}	92.5
Coil thickness (*mm*)	l_{co}	10
Height of coil 1 (*mm*)	H_{co}^1	181
Height of coil 2 (*mm*)	H_{co}^2	57
Height of coil turns (*mm*)	h_{co}^2	26
Distance between coil turns (*mm*)	d_{co}	5
Distance between two coils (*mm*)	D_{co}	25
Thickness of crucible insulation at the bottom (*mm*)	h_{ci}	50
Thickness of crucible insulation at the wall (*mm*)	d_{ci}	12
Thickness of afterheater insulation (*mm*)	d_{ai}	12
Insulation inner height above the afterheater (*mm*)	h_i	50

Table 3-3. Operating parameters used for the configuration *case b*.

3.4.2 case b: crucible and afterheater, with an open gap

Designation (Fig. 3-b-1):

G: Gap between crucible and afterheater,
AH: Afterheater top cover Hole,
AIH: Afterheater top cover Insulation Hole,
T_{AIH}: Temperature at the centerline and close to the AIH

Fig. 3-b-1 shows a sketch of these systems and the operating parameters are listed in Table 3-3. In these configurations, crucible always has a baffle and G is an open gap that gas flows into the system. The aim of these set of calculations was to investigate the influence of radiuses of AH and AIH on the temperature and flow field of the system and

specially on the T_{AIH}. To do it, the radius of AH ($10-40\ mm$) and AIH ($10-45\ mm$) have been changed and temperature and velocity field have been calculated.

For the boundary condition of the temperature, there are two BCs:

- at G: $T_G = 1510\ ^oC$
- at AIH: T_{AIH} = 950 - 1550 ^oC with linear variation from corner to the centerline

that both of them are from measurement. The temperature at G (i.e. T_G) is selected as the characteristic temperature (T_c). So the Grashof number is $Gr = 2.9 \times 10^5$ and the other non-dimensional numbers are the same as *case a*.

Induction heating

Fig. 3-b-2 shows the volumetric distribution of heat generation in the crucible and afterheater for two cases: $AH = 10\ mm$ (left hand side) and $AH = 40\ mm$ (right hand side). For all configurations, $q_{max} = 43 - 53\ W/cm^3$ and $Q_{total} = 2.7 - 3.3\ kW$ corresponding to the different geometry of AH and AIH.

Temperature and velocity field

1. There is a gas flow in the system that enters from G (maximum velocity value $10-60\ cm/s$) and goes out via AH and AIH. Its velocity is increased gradually from G to AH and is high in the space above the afterheater. The maximum value of velocity is $\text{v}_{max} = 70 - 90\ cm/s$ and in AIH. Also a small part of this gas flow exits immediately from the upper part of G. In the cases that $AIH \geq AH$, a second incoming gas flow exists which comes into the system from AIH and adjacent of the insulation roof with the maximum velocity value $0 - 10\ cm/s$. There is a vortex in the crucible too that occupies it completely, Fig. 3-b-3.

2. Temperature gradient in the G space both in the horizontal and vertical direction is high ($50 - 70\ ^oC/cm$), and close to AIH in vertical direction is very high. In the axis of symmetry and from crucible bottom, temperature decreases gradually ($\triangle T = 65-105\ ^oC$ and $\delta T = 2.5-4.0\ ^oC/cm$) until drops close to AIH ($\Delta T = 120-160\ ^oC$), Fig. 3-b-4. The maximum value for temperature in system, i.e. $T_{max} = 1750-1950\ ^oC$ and in the middle part of crucible wall.

3. For $AIH = 10\ mm$, T_{AIH} is almost the same for all cases ($\simeq 1700^oC$). In this state AIH controls and limits the gas flow and so this flow is not very powerful. As a result the heat generated by RF-coil remains in the system and T_{AIH} is high. By increasing the radius of AIH from 10 to 20 mm, the intensity of gas flow is increased and so T_{AIH} decreases ($\triangle T_{AIH} \approx 10\ ^oC$). In the axis of symmetry and from crucible bottom, temperature is approximately constant in the crucible space ($\triangle T \approx 8\ ^oC$ and

$\delta T \approx 0.8\ ^{o}C/cm$) and then decreases gradually ($\triangle T \approx 75\ ^{o}C$ and $\delta T \approx 4.7\ ^{o}C/cm$ until drops near to the AIH ($\triangle T \approx 130\ ^{o}C$), Fig3. 3-b-5 and 3-b-6.

4.In the cases $AIH > 20\ mm$, there are two different behaviors in the system:

a) $AH < 25\ mm$: T_{AIH} is nearly constant or reduces few for every case. As has been already mentioned, there is a second incoming gas flow from the AIH and also there is a vortex above the afterheater top cover and close to the insulation wall. The velocity profile of the incoming gas flow from G is constant (with the maximum value 15 cm/s) and does not depend on the AIH. The maximum velocity value (v_{max}) is always in the central part of AH and AIH and is constant ($\mathrm{v}_{max} \approx 75\ cm/s$).

b) $AH \geq 25\ mm$: At first T_{AIH} is increased ($\delta T \approx 22\ ^{o}C/cm$) and then remains nearly constant, i.e. there is a minimum value for it in the $AIH = 20\ mm$. By increasing the radius of the AIH, the velocity of gas flow both in G and AIH increases ($\triangle v \approx 30$ and 20 cm/s, respectively) and the maximum velocity value is moved to the middle part of radius of AIH from the its center and so the gas flow in the system becomes more powerful. As a result this strong gas flow transfers the inducted heat outside. So the temperature decreases in the system and we should increase the input power. In this case the T_{max} that is located at the crucible wall, is increased ($\triangle T \approx 200\ ^{o}C$) and so T_{AIH} increases. On the other hand, this strong gas flow affects the temperature field in the crucible space and increases its temperature gradient. Also the temperature in the axis of symmetry and from the crucible bottom decreases almost linear ($\delta T \approx 2\ ^{o}C/cm$. These are different from the cases $AH < 25\ mm$.

5. For the cases $AIH < 25\ mm$, by increasing the radius of AH then T_{AIH} does not change very much and approximately is constant. Because essentially in these cases the AIH controls the gas flow and so its velocity is not very high inside the system. Also the temperature field is similar for all cases and temperature gradient in the crucible is low. In the axis of symmetry and from the crucible bottom, the temperature profile is similar to the section 2. But for cases $AIH \geq 25\ mm$, T_{AIH} is increased as its rate is almost the same for different values of AH ($\delta T_{AIH} \approx 1\ ^{o}C/mm$). The gas flow and temperature field both depend on the radius of AH. In crucible the temperature gradient is low for $AH < 25\ mm$ and is increased proportional with radius of AH for $AH \geq 25\ mm$. Also in this case, the velocity of gas flow inside the system becomes high ($60 - 80\ cm/s$).

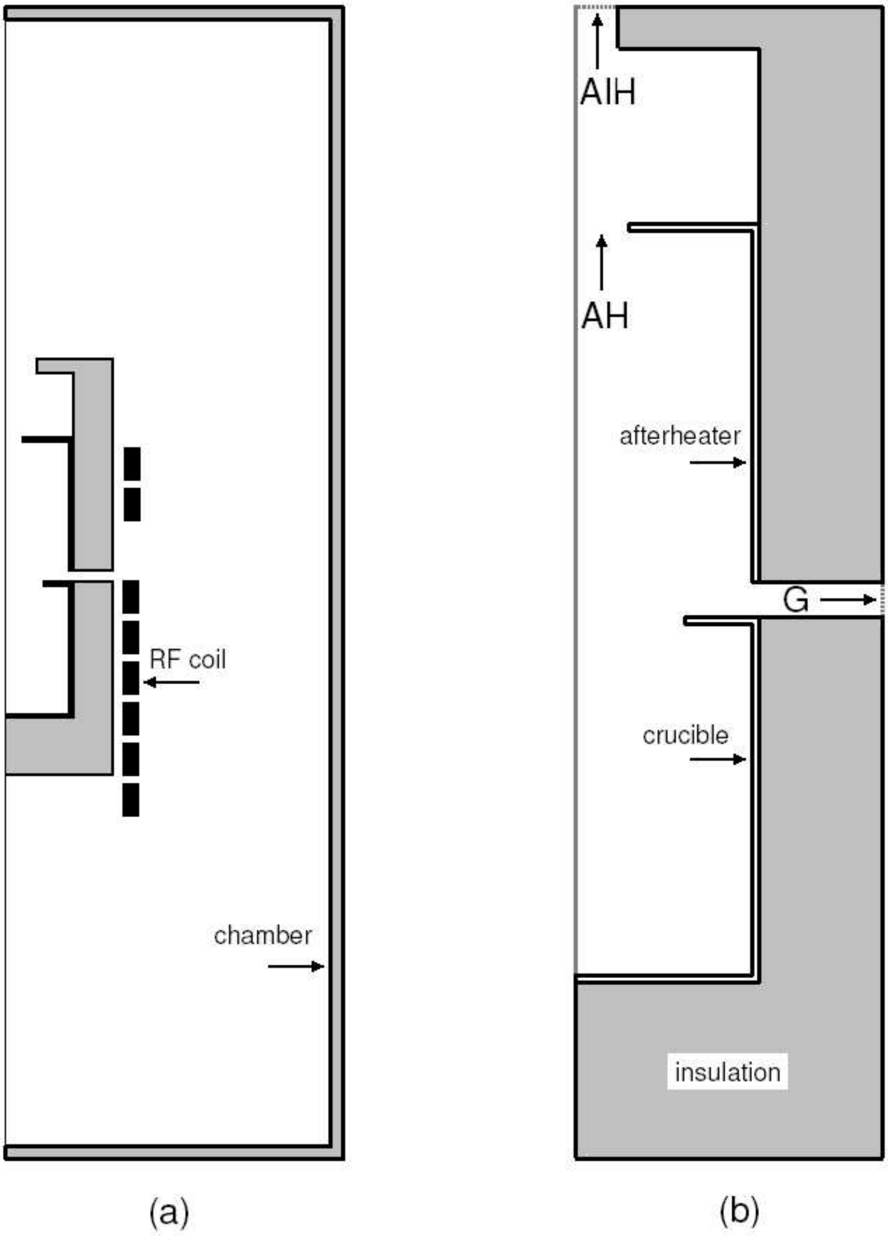

Fig. 3-b-1. A sketch for the configurations with an open gap between crucible and afterheater. Afterheater insulation has a top cover too.

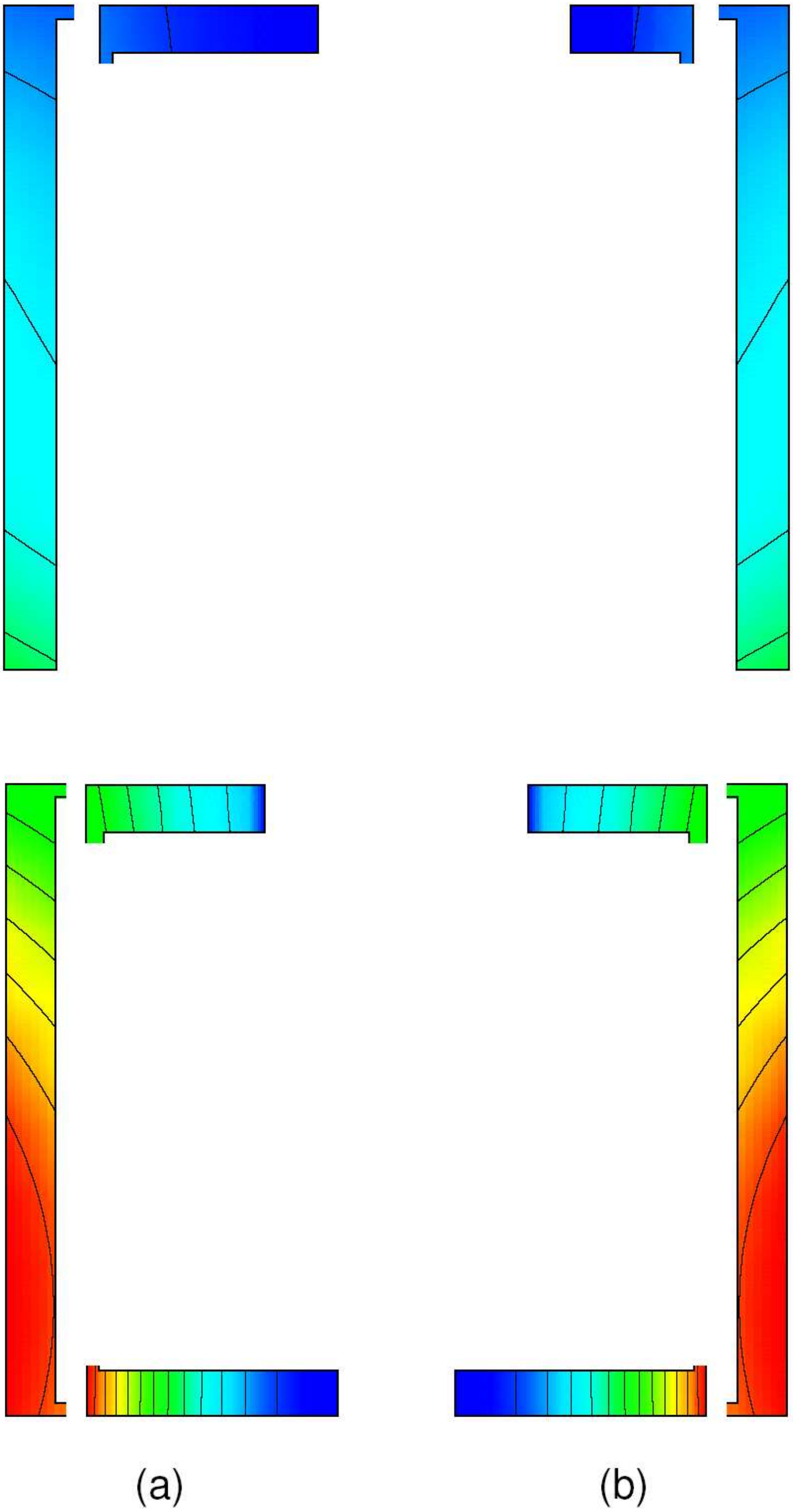

Fig. 3-b-2. contours of the volumetric power distribution (q) in the crucible and after-heater, (a) $AH = 10\ mm$ and (b) $AH = 40\ mm$.

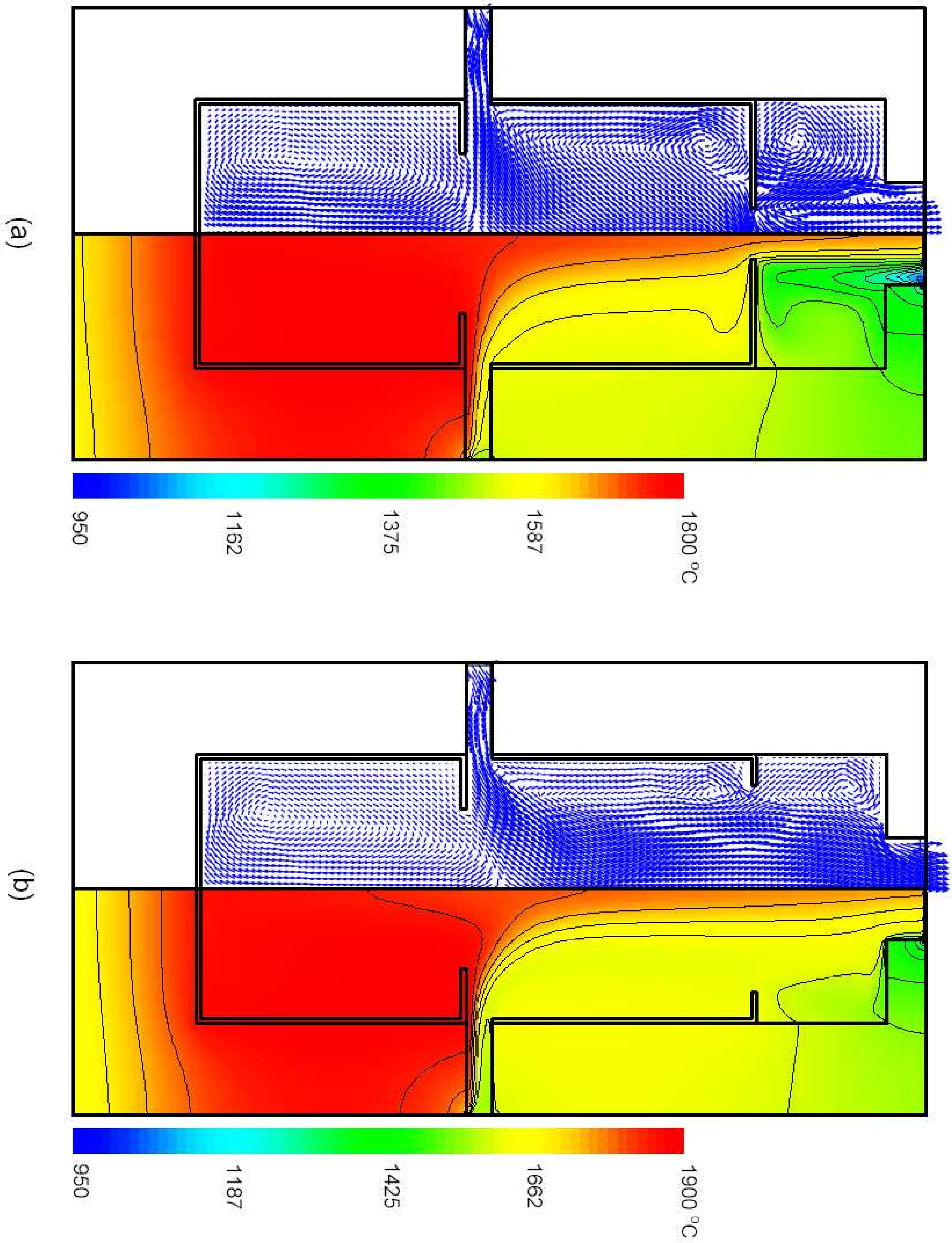

Fig. 3-b-3. Temperature distribution (right hand side) and gas flow (left hand side) for $AIH = 20\ mm$, (a) $AH = 10\ mm$ and (b) $AH = 40\ mm$.

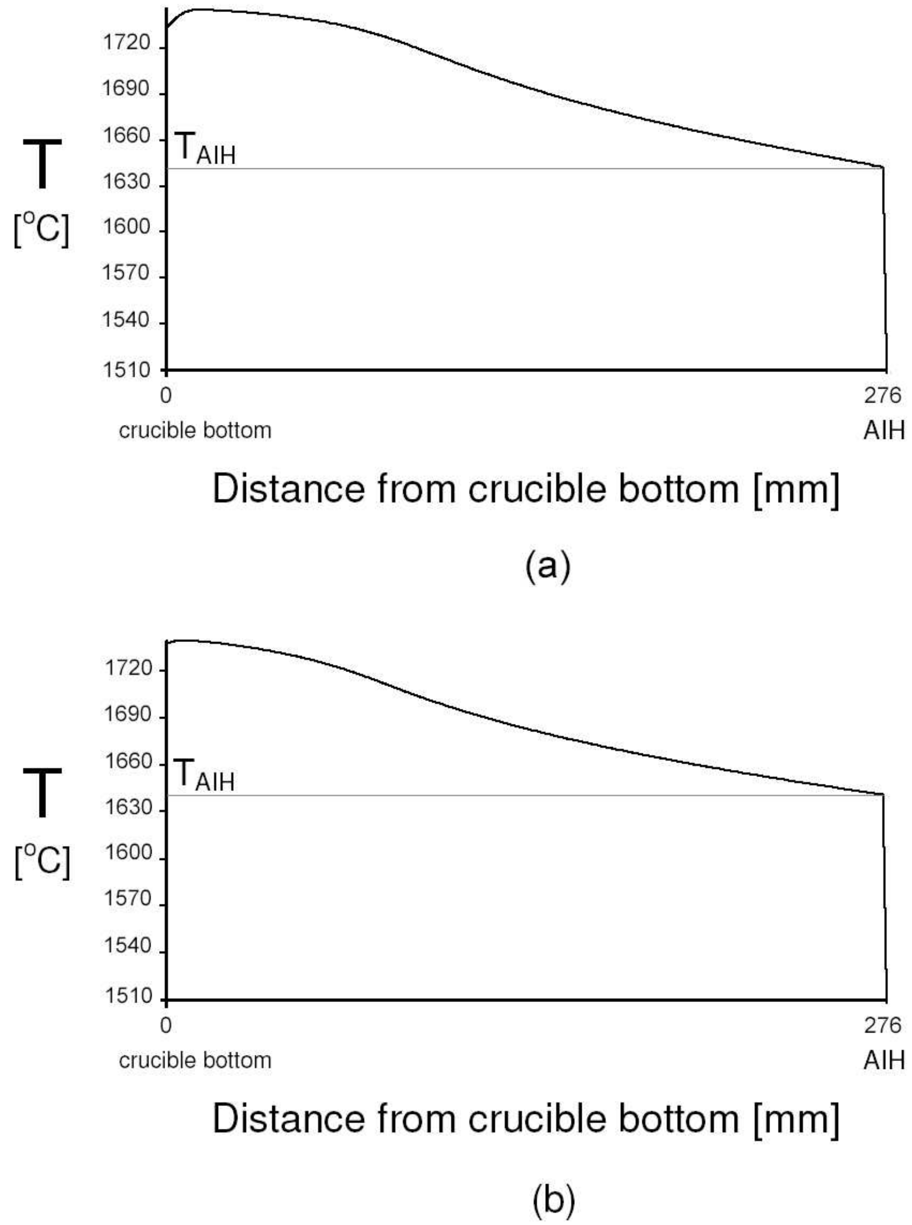

Fig. 3-b-4. Vertical temperature profiles along the axis of symmetry from crucible bottom to the afterheater insulation hole (AIH) for $AIH = 20\ mm$, (a) $AH = 10\ mm$ and (b) $AH = 40\ mm$.

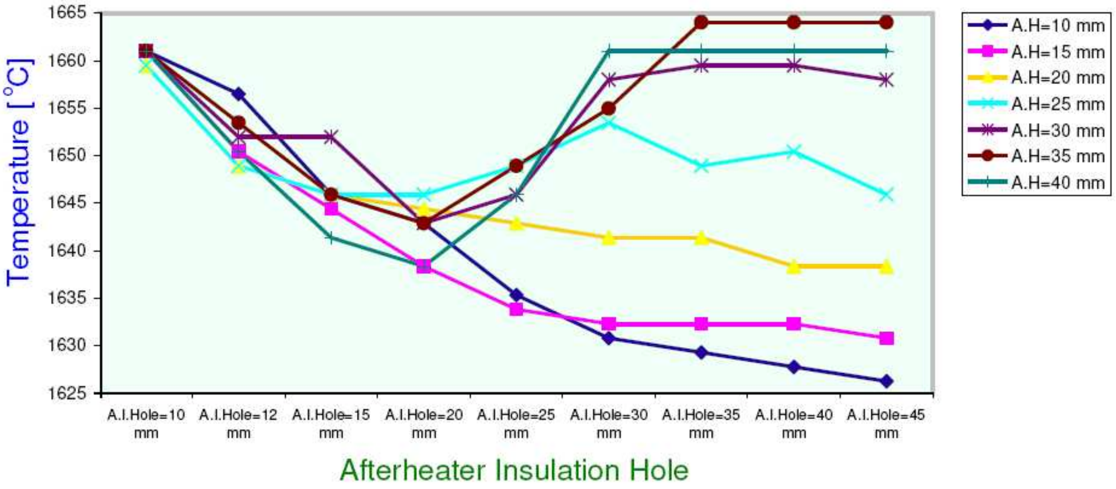

Fig. 3-b-5. Variation of the temperature at the centerline and close to the afterheater insulation hole T_{AIH}, in base of the radius of afterheater insulation hole (AIH).

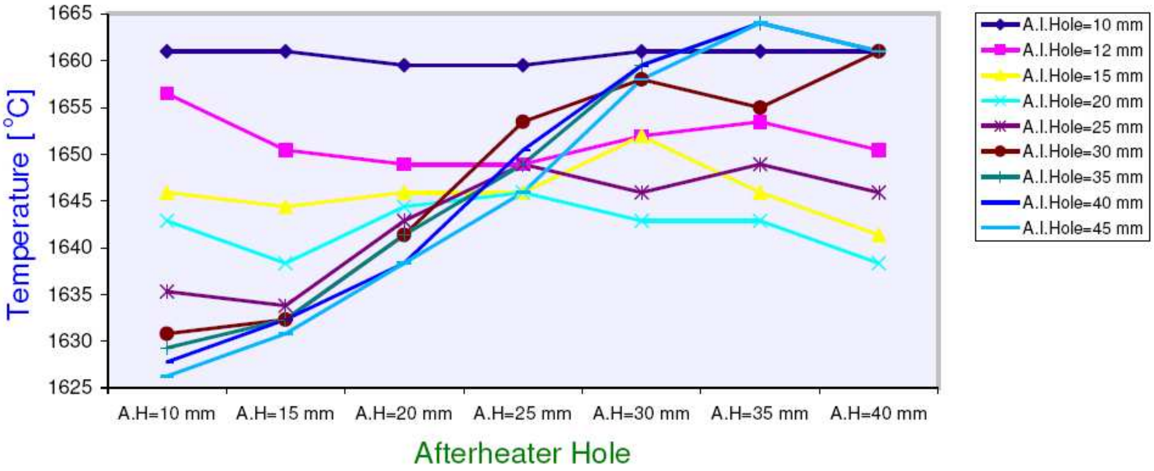

Fig. 3-b-6. Variation of the temperature at the centerline and close to the afterheater insulation hole T_{AIH}, in base of the radius of afterheater hole (AH).

Description (units)	Symbel	Value
Crucible inner radius (mm)	r_c	50
Crucible thickness (mm)	l_c	2
Crucible inner height (mm)	h_c	100
Crucible baffle hole (mm)	r_{ch}	31
Afterheater inner height (mm)	h_{af}	100
Afterheater top cover hole (mm)	r_{af}	10-40
Slot between afterheater and insulation (mm)	d_s	20
Distance between crucible and afterheater (mm)	D_{ca}	0, 10, 20
Coil inner radius (mm)	r_{co}	92.5
Coil thickness (mm)	l_{co}	10
Height of coil 1 (mm)	H^1_{co}	181
Height of coil 2 (mm)	H^2_{co}	57
Height of coil turns (mm)	h_{co}	26
Distance between coil turns (mm)	d_{co}	5
Distance between two coils (mm)	D_{co}	25
Thickness of crucible insulation at the bottom (mm)	h_{ci}	50
Thickness of crucible insulation at the wall (mm)	d_{ci}	35
Thickness of afterheater insulation (mm)	d_{ai}	15

Table 3-4. Operating parameters used for the configuration *case c*.

3.4.3 case c: crucible and afterheater, with a slot between afterheater and insulation

Designation (Fig. 3-c-1):

G:	Gap between insulations of crucible and afterheater,
AH:	Afterheater top cover Hole,
S:	Slot between the afterheater top cover and insulation,

Fig. 3-c-1 shows a sketch of these systems and the operating parameters are listed in Table 3-4. In these configurations, crucible always has a baffle and there is a slot between afterheater and insulation. In the configuration without a gap $G = 0$, there is no gas flow from G but for the configurations with an open gap ($G = 10,\ 20\ mm$), a gas flow

exists that enters the system via this gap. The aim of these set of calculations was to investigate the influence of a slot between afterheater and insulation on the temperature and flow field of the system. To do it, the distance between crucible and afterheater (equal to the distance between their insulations) has been changed ($G = 0, 10,\ 20\ mm$) and temperature and velocity field have been calculated.

For the boundary conditions of the temperature, there are three BCs:

- at G: $T_G = 1110\ ^oC$
- at AH: $T_{AH} = 1180\ ^oC$
- at S: $T_S = 1180\ ^oC$

that all of them are from measurement in the lab. The temperature at AH (i.e. T_{AH}) is selected as the characteristic temperature (T_c) for our calculations. So the Grashof number is $Gr = 3.3 \times 10^5$ and the other non-dimensional numbers are the same as in *case a* and *b*.

Induction heating

Fig. 3-c-2 shows the volumetric distribution of heat generation in the crucible and afterheater for these three cases. For the configuration without a gap ($G = 0$), the maximum of heat generation is $q^{G=0}_{max} = 30\ W/cm^3$ and the total heat generation in the crucible and afterheater is $Q^{G=0}_{total} = 1.86\ kW$. For the configuration with an open gap ($G = 10,\ 20\ mm$), the maximum of heat generation is $q^{G=10}_{max} = 33\ W/cm^3$ and $q^{G=20}_{max} = 35\ W/cm^3$, and the total heat generation is $Q^{G=10}_{total} = 2.05\ kW$ and $Q^{G=20}_{total} = 2.17\ kW$.

Temperature and velocity field

Fig. 3-c-3 shows the gas flow and temperature distribution for these three systems. For the case without a gap (i.e. $G = 0$), there is a strong gas flow in the system. The buoyancy moves the gas upward along the crucible & afterehater side wall and then it goes down along the centerline. Inside this big vortex, there are also two separate eddies of convection in the crucible and afterheater with the same direction of main vortex. In the slot, there is a vortex that is upwards along the afterheater wall and downwards along the insulation. These two upward gas flows inside and outside the afterheater and adjacent to its wall, transfers the heat outside via AH and S effectively. The maximum value of velocity is $\mathrm{v}^{G=0}_{max} = 5\ cm/s$ and at the centerline of crucible. The maximum of temperature for this case is $T^{G=0}_{max} = 1480\ ^oC$ and at the middle of the crucible wall. At the centerline, temperature is approximately constant and then decreases in the afterheater linearly, Fig. 3-c-4. In this case the upper part of the system is the coldest part.

For the cases with an open gap between crucible and afterheater (i.e. $G = 10$ and $20\ mm$), there is a gas flow in the system that enters from G (maximum velocity value $\mathrm{v}_G^{G=10} = 8.5\ cm/s$ and $\mathrm{v}_G^{G=20} = 9.5\ cm/s$) and goes out via AH and S. The velocity is increased gradually from G to AH and is high in the afterheater. The maximum values of velocity are $\mathrm{v}_{max}^{G=10} = 13\ cm/s$ and $\mathrm{v}_{max}^{G=20} = 27\ cm/s$, both at AH. In the slot the velocity of gas is nearly constant and the values at S are $\mathrm{v}_S^{G=10} = 3.2\ cm/s$ and $\mathrm{v}_G^{G=20} = 7.5\ cm/s$. Also in the crucible there is an eddy of gas convection, in which gas flows upward along the crucible wall and downward along the axis of symmetry. The center of this vortex is located in the upper part of the crucible and close to its baffle. For the case $G = 10\ mm$, there is a weak and thin vortex in the afterheater and close to its side wall but for the case $G = 20\ mm$, that is very small, weaker and is located in the top cover corner.

For the temperature field, the maximum values are $T_{max}^{G=10} = 1450\ ^oC$ and $T_{max}^{G=20} = 1420\ ^oC$. They are located at the crucible wall, 1 cm and 1.5 cm below the position of $T_{max}^{G=0}$, respectively. The reason for this displacement of T_{max} is the gas flow from the open gap. Because it transfers the heat from the crucible baffle to AH and as a result the position of T_{max} is moved down. Also the required heat generation in the system has been increases. In these two cases, the coldest part of the system is the afterheater insulation, contrary to the case $G = 0$. The temperature profiles along the axis of symmetry, Fig. 3-c-4, indicate that the temperature is nearly constant in the crucible and its magnitude is reduced after the crucible baffle and drops close to AH. This temperature gradient close to AH, is higher in the case $G = 20\ mm$. It comes from the stronger gas flow in this case than the case $G = 10\ mm$.

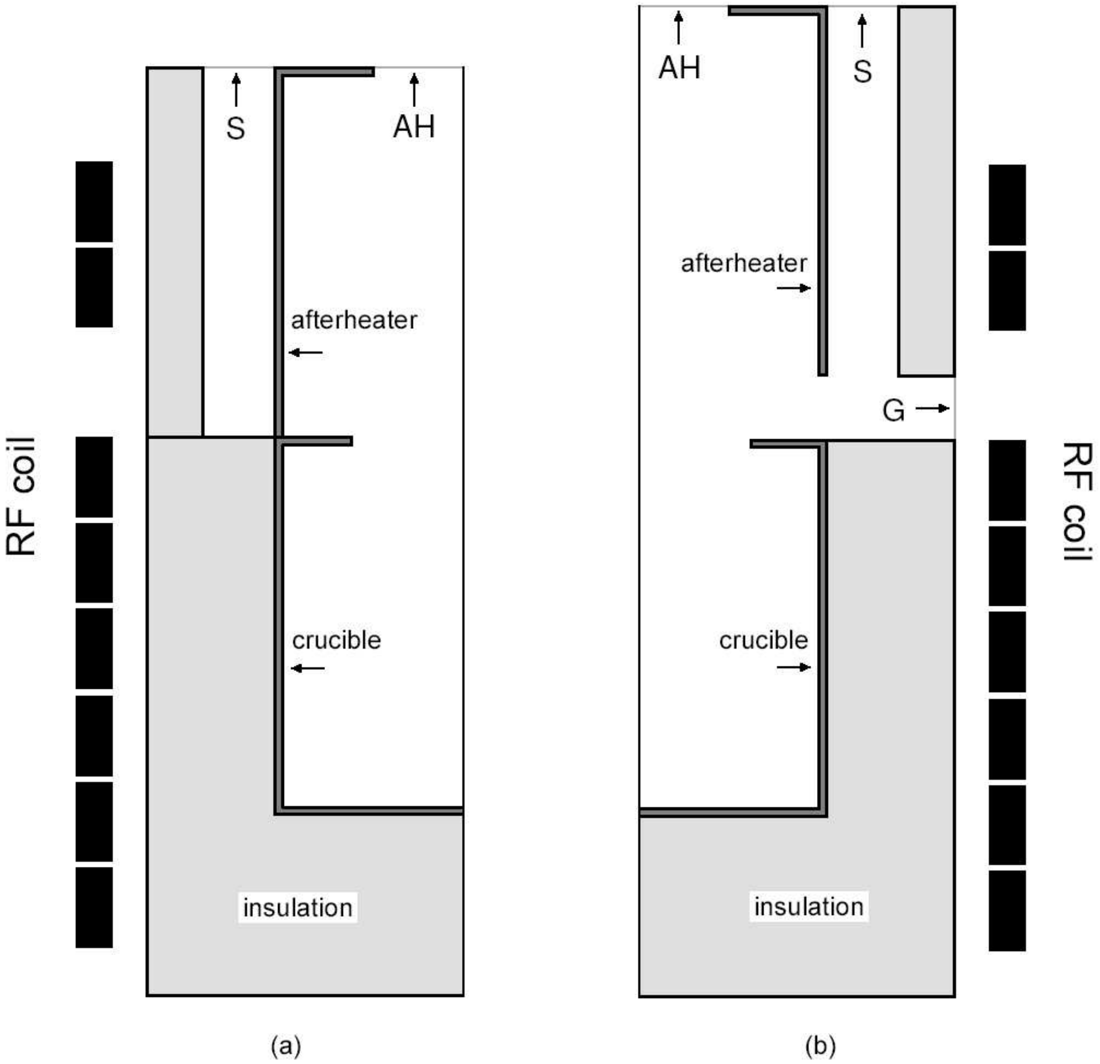

Fig. 3-c-1. A sketch for the configurations with a slot between afterheater and insulation, (a) without a gap ($G = 0\ mm$) and (b) with a gap between crucible and afterheater ($G = 10,\ 20\ mm$).

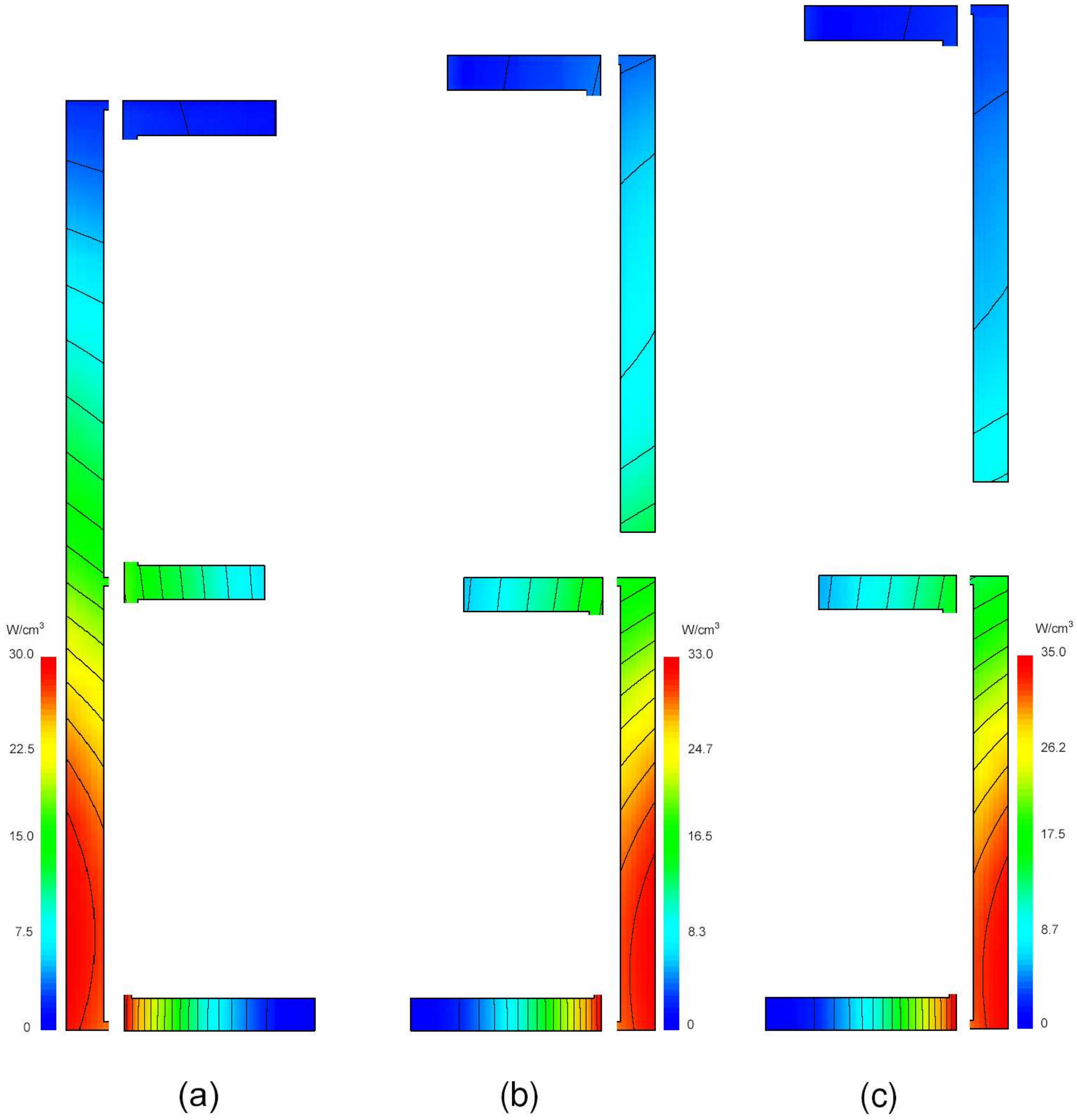

Fig. 3-c-2. contours of the volumetric heat distribution (q) in the crucible and after-heater, (a) $G = 0\ mm$, (b) $G = 10\ mm$ and (c) $G = 20\ mm$.

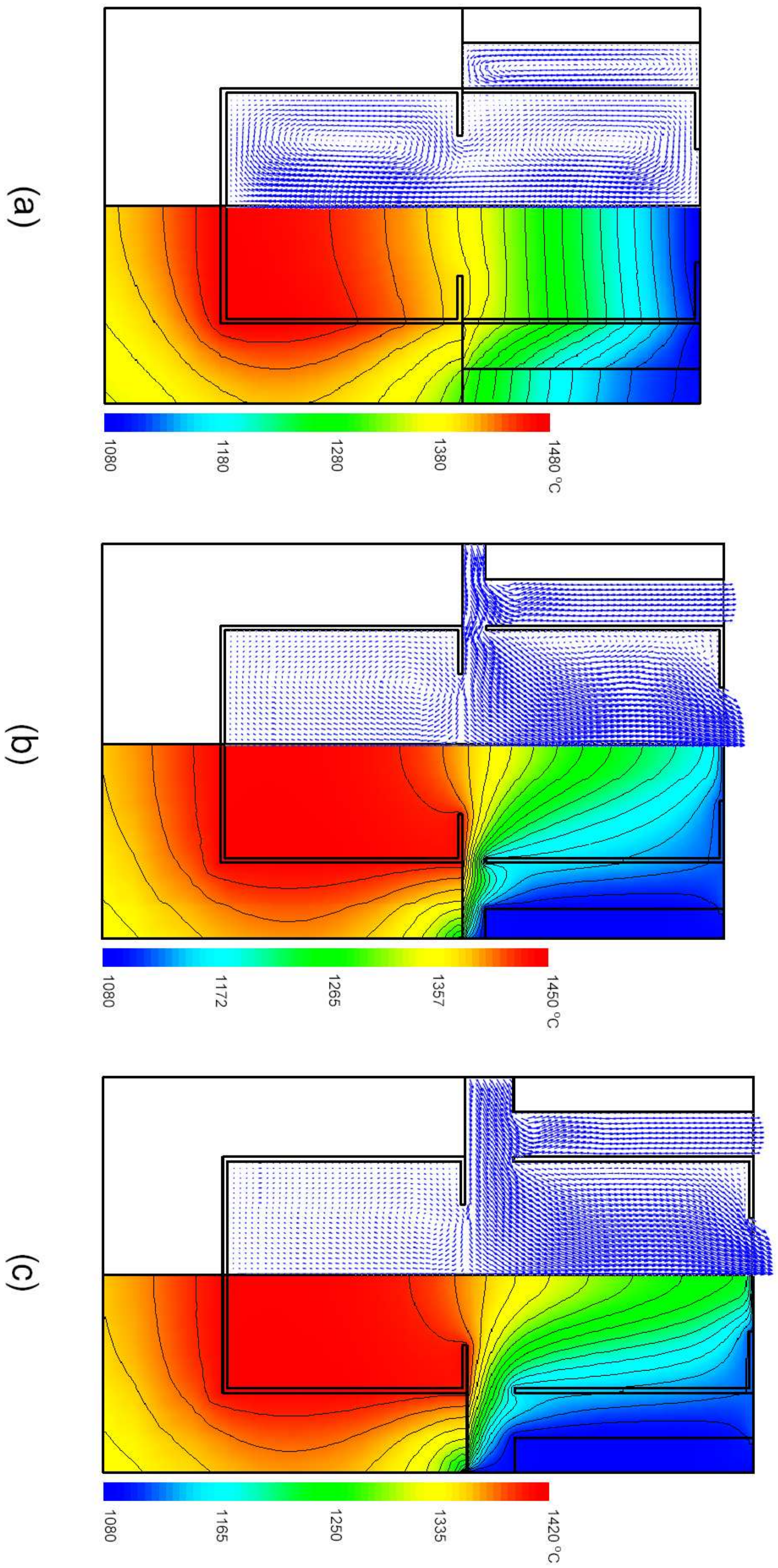

Fig. 3-c-3. Temperature distribution (right hand side) and gas flow (left hand side) for (a) $G = 0\ mm$, (b) $G = 10\ mm$ and (c) $G = 20\ mm$.

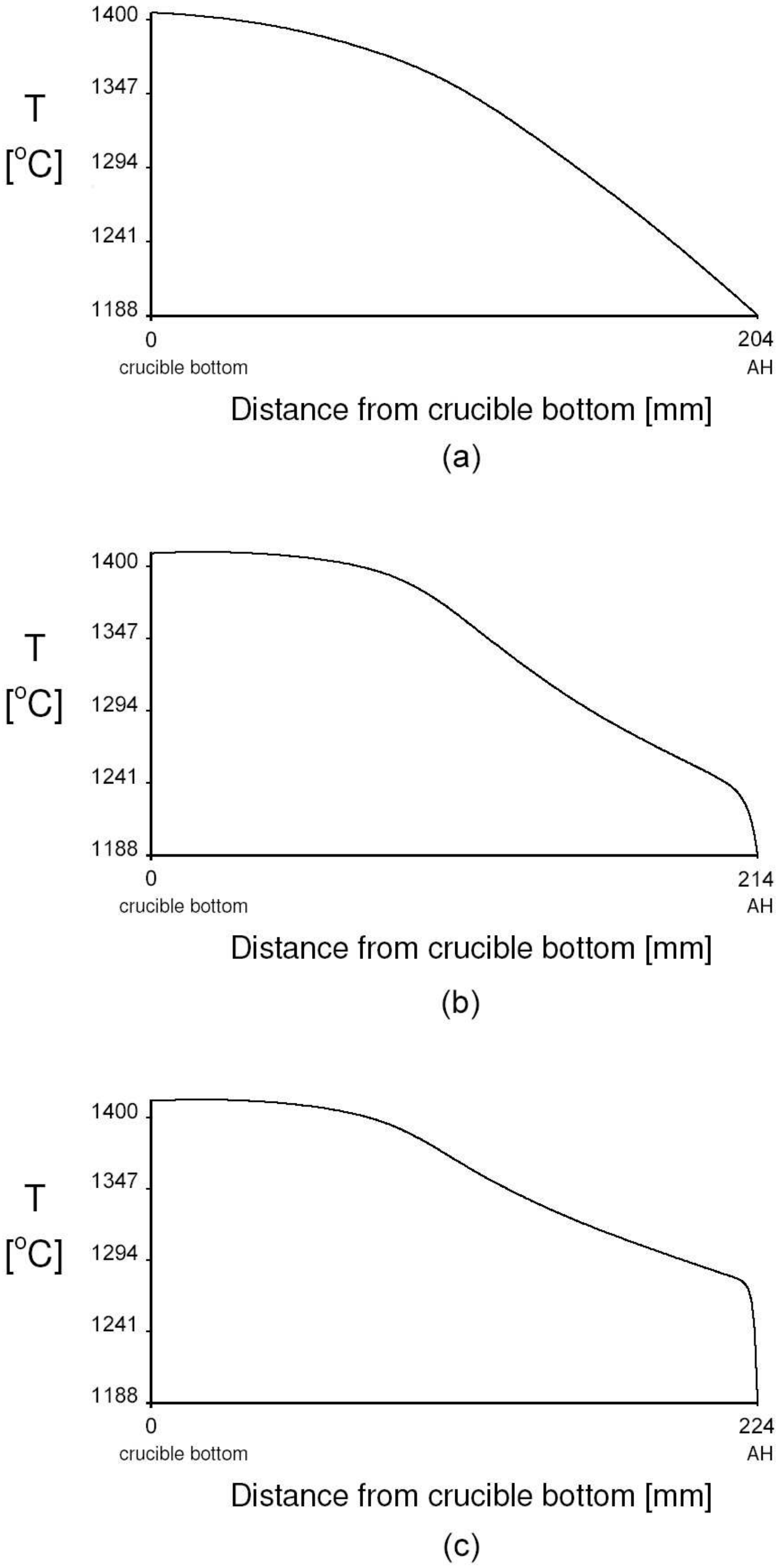

Fig. 3-c-4. Vertical temperature profiles along the axis of symmetry from crucible bottom to the afterheater top cover hole for (a) $G = 0\ mm$, (b) $G = 10\ mm$ and (c) $G = 20\ mm$.

3.5 Conclusions

From these calculations of some different configurations for Czochralski crystal growth containing only gas, we can conclude:

1) There is a good agreement between our results and those of measurement.

2) In all cases which were studied here, buoyancy drives a gas flow in the crucible which flows upwards along the side wall and downwards along the axis of symmetry.

3) By using a closed gap between crucible and afterheater, the temperature and fluid flow change dramatically in the system.

4) By placing an open gap between crucible and afterheater, there is a gas flow in the system which enters from this gap and goes outside via the top cover hole.

5) By using an open gap and a separate top cover for the insulation, when the afterheater top cover hole is smaller than the insulation top cover hole, there is a second incoming gas flow which enters from insulation top cover hole.

6) The position of T_{max} at the crucible side wall is lower in the systems with an open gap than without a gap.

7) Using a slot between afterheater and insulation produces a high and linear temperature gradient at the centerline of afterheater.

Chapter 4

Configuration contains melt and gas

4.1 Introduction

In this chapter, temperature distribution and flow field are computed for some Czochralski systems contain the *melt* and *gas*, by application of the internal heat generation in the crucible and afterheater. The goal of these calculations is to study and investigate the influence of the geometry and orientation of crucible, afterheater and a gap on the overall heat transport of the CZ system.

The procedure of growing a crystal by the CZ method starts by filling the crucible with polycrystalline material of high purity and often a small fraction of a dopant which alters the physical properties of the grown crystal. Then the crucible is heated by RF to melt these materials. After the melt has reached thermal equiblirium, a single-crystal seed attached to a pull rod is lowered to the surface of the melt, where a stable solid-liquid interface is established. Then the seed is slowly withdrawn from the melt and a single crystal is pulled upwards.

The aim of the work in this chapter is to develop a global analysis of an inductively heated CZ furnace for real oxide crystal growth systems during the seeding process, and to reveal the effect of an active afterheater between crucible and afterheater (i.e. metallic material and heated by RF) and a gap (closed and open) on the heat transport mechanisms of melt and gas. In chapter 3 our attention was paid to the effects of thermal insulation, a gap between crucible and afterheater and a slot between afterheater and insulation on the gas flow and temperature field of some systems without any seed and melt. But in the analysis presented here, the molten material was included in the calculations. A seed crystal was not taken into account corresponding to the situation just before the seed touches the melt.

4.2 Mathematical model

We consider CZ systems usually used in dielectric crystal growth, which consist of a crucible and afterheater (*iridium*), insulation (ZrO_2) and chamber (*stainless steel*). Our model involves the following basic assumption: (1) The system is axisymmetric, (2) The system is in steady state, (3) Internal radiation is not included, (4) There is no seed crystal in the system, (5) Melt and gas are incompressible Newtonian fluids satisfying the Boussinesq approximation. Thus the fundamental equations are,
(a) Fluid flow in the melt and gas:

$$\rho \mathbf{v} \cdot \nabla \mathbf{v} = -\nabla p + \mu \nabla^2 \mathbf{v} + \rho \beta g (T - T_0) \vec{e_z} \tag{4.1}$$

which is the Navier-Stokes equation with Boussinesq approximation.
(b) Continuity equation:

$$\nabla \cdot \mathbf{v} = 0 \tag{4.2}$$

(c) Heat transport by conduction and convection (energy equation):

$$\alpha \nabla^2 T_f - \mathbf{v} \cdot \nabla T_f = 0 \quad \text{convection and conduction in the melt and gas} \tag{4.3}$$

$$\nabla^2 T_c + q = 0 \quad \text{conduction in the crucible and afterheater} \tag{4.4}$$

$$\nabla^2 T_i = 0 \quad \text{conduction in the insulation} \tag{4.5}$$

where the subscripts f, c and i denote fluids (gas and melt), conductors (crucible and afterheater) and insulation, respectively. The boundary conditions are,
a) at the bottom and wall of the crucible, afterheater wall and top cover:

$$\mathbf{v} = 0 \tag{4.6}$$

a) at the melt-gas interface:

$$-k_l \frac{\partial T_l}{\partial z} = \sigma \varepsilon_l \left(T_l^4 - T_{eff}^4 \right) \tag{4.7}$$

$$\mu_l \frac{\partial u_l}{\partial z} - \mu_g \frac{\partial u_g}{\partial z} = \frac{\partial \gamma}{\partial r} = \frac{\partial \gamma}{\partial T} \frac{\partial T}{\partial r} \tag{4.8}$$

$$v_z = 0 \tag{4.9}$$

where the subscripts g and l denote gas and melt, respectively. The Eqs. (4.7) and (4.8) represent the heat radiation and the thermal Marangoni effect at this interface, respectively. In the Eq. (4.7), T_{eff} is the corresponding effective ambient temperature with respect to the melt surface. In our calculation, T_{eff} is assumed to be a known constant. Considering the importance of the thermal radiation at high temperature and sensitivity of this radiative heat flux to T_{eff}, a realistic approximation for T_{eff} is necessary. We believe the temperature at the afterheater hole (T_{ah}) is a good approximation for T_{eff} since it depends on the operating parameters, overall heat transfer of the configuration and system design (especially the afterheater geometry and its insulation) and also it can be measured easily in the lab. Therefore, the ambient effective temperature (T_{eff}) is set to be afterheater hole temperature (T_{ah}) in our calculation.

c) at the outer surfaces of insulation:

$$-k_i \frac{\partial T_i}{\partial \hat{n}} = h_i \left(T_i - T_a\right) + \sigma \varepsilon_i \left(T_i^4 - T_a^4\right) \tag{4.10}$$

which denotes the heat dissipation via radiation and convection from those surfaces.
d) at the afterheater hole:

$$T = T_{ah} \tag{4.11}$$

where $\mathbf{v} = (u, v, w)$ is the fluid velocity vector, p the pressure, T the temperature, $\vec{e}_z$ the z-directional unit vector, g the acceleration due to gravity, β the thermal expansion coefficient, μ the dynamic viscosity, α the thermal diffusivity, γ the surface tension, q the heat source density, ε the emissivity, k the thermal conductivity, ρ the density, h the Newtonian heat transfer coefficient, $\hat{n}$ the unit normal vector, σ the Stefan-Boltzmann constant and T_a the ambient temperature for the system.

4.3 Weak form calculation

Similar to the chapter 2, at first we write the components of the governing equations and BCs in the cylindrical coordinates (r, ϕ, z), then we calculate their weak form and finally the non-dimensional form of the weak form.

4.3.1 Fluid flow

Components of the Navier-Stokes equation with Boussinesq approximation (Eq. 4.1) in the cylindrical coordinates for the melt are as:

$$\begin{cases} \rho_l\left(u_l\dfrac{\partial u_l}{\partial r}+w_l\dfrac{\partial u_l}{\partial z}-\dfrac{v_l^2}{r}+\nu_l\dfrac{u_l}{r^2}\right)+\dfrac{\partial p_l}{\partial r}-\mu_l\nabla^2u_l=0 \\ \rho_l\left(u_l\dfrac{\partial v_l}{\partial r}+w_l\dfrac{\partial v_l}{\partial z}+\dfrac{u_lv_l}{r}+\nu_l\dfrac{v_l}{r^2}\right)-\mu_l\nabla^2v_l=0 \\ \rho_l\left(u_l\dfrac{\partial w_l}{\partial r}+w_l\dfrac{\partial w_l}{\partial z}-g\beta_lT_l\right)+\dfrac{\partial p_l}{\partial z}-\mu_l\nabla^2w_l=0 \end{cases} \tag{4.12}$$

and the gas,

$$\begin{cases} \rho_g\left(u_g\dfrac{\partial u_g}{\partial r}+w_g\dfrac{\partial u_g}{\partial z}-\dfrac{v_g^2}{r}+\nu_g\dfrac{u_g}{r^2}\right)+\dfrac{\partial p_g}{\partial r}-\mu_g\nabla^2u_g=0 \\ \rho_g\left(u_g\dfrac{\partial v_g}{\partial r}+w_g\dfrac{\partial v_g}{\partial z}+\dfrac{u_gv_g}{r}+\nu_g\dfrac{v_g}{r^2}\right)-\mu_g\nabla^2v_g=0 \\ \rho_g\left(u_g\dfrac{\partial w_g}{\partial r}+w_g\dfrac{\partial w_g}{\partial z}-g\beta_gT_g\right)+\dfrac{\partial p_g}{\partial z}-\mu_g\nabla^2w_g=0 \end{cases} \tag{4.13}$$

Weak form

In axisymmetric condition $\vec{v}=\vec{v}\,(r,z)$ and the weak form of the Eqs. (4.12), (4.13) and BC (Eq. 4.8) is:

$$
\begin{aligned}
& \iint\limits_{melt} \Bigg[\rho_l \left(u_l \frac{\partial u_l}{\partial r} + w_l \frac{\partial u_l}{\partial z} - \frac{v_l^2}{r} + \nu_l \frac{u_l}{r^2}\right) \Phi_{lu} - p_l \left(\frac{\partial \Phi_{lu}}{\partial r} + \frac{\Phi_{lu}}{r}\right) \\
& + \; \mu_l \left(\frac{\partial u_l}{\partial r}\frac{\partial \Phi_{lu}}{\partial r} + \frac{\partial u_l}{\partial z}\frac{\partial \Phi_{lu}}{\partial z}\right)\Bigg] \; r \, \mathrm{d}r \, \mathrm{d}z \\
+ \; & \iint\limits_{melt} \Bigg[\rho_l \left(u_l \frac{\partial v_l}{\partial r} + w_l \frac{\partial v_l}{\partial z} + \frac{u_l v_l}{r} + \nu_l \frac{v_l}{r^2}\right) \Phi_{lv} \\
& + \mu_l \left(\frac{\partial v_l}{\partial r}\frac{\partial \Phi_{lv}}{\partial r} + \frac{\partial v_l}{\partial z}\frac{\partial \Phi_{lv}}{\partial z}\right)\Bigg] \; r \, \mathrm{d}r \, \mathrm{d}z \\
+ \; & \iint\limits_{melt} \Bigg[\rho_l \left(u_l \frac{\partial w_l}{\partial r} + w_l \frac{\partial w_l}{\partial z} - g \beta_l T_l\right) \Phi_{lw} - p_l \frac{\partial \Phi_{lw}}{\partial z} \\
& + \; \mu_l \left(\frac{\partial w_l}{\partial r}\frac{\partial \Phi_{lw}}{\partial r} + \frac{\partial w_l}{\partial z}\frac{\partial \Phi_{lw}}{\partial z}\right)\Bigg] \; r \, \mathrm{d}r \, \mathrm{d}z \\
- \; & \iint\limits_{gas} \Bigg[\rho_g \left(u_g \frac{\partial u_g}{\partial r} + w_g \frac{\partial u_g}{\partial z} - \frac{v_g^2}{r} + \nu_g \frac{u_g}{r^2}\right) \Phi_{gu} - p_g \left(\frac{\partial \Phi_{gu}}{\partial r} + \frac{\Phi_{gu}}{r}\right) \qquad (4.14) \\
& + \; \mu_g \left(\frac{\partial u_g}{\partial r}\frac{\partial \Phi_{gu}}{\partial r} + \frac{\partial u_g}{\partial z}\frac{\partial \Phi_{gu}}{\partial z}\right)\Bigg] \; r \, \mathrm{d}r \, \mathrm{d}z \\
- \; & \iint\limits_{gas} \Bigg[\rho_g \left(u_g \frac{\partial v_g}{\partial r} + w_g \frac{\partial v_g}{\partial z} + \frac{u_g v_g}{r} + \nu_g \frac{v_g}{r^2}\right) \Phi_{gv} \\
& + \mu_g \left(\frac{\partial v_g}{\partial r}\frac{\partial \Phi_{gv}}{\partial r} + \frac{\partial v_g}{\partial z}\frac{\partial \Phi_{gv}}{\partial z}\right)\Bigg] \; r \, \mathrm{d}r \, \mathrm{d}z \\
- \; & \iint\limits_{gas} \Bigg[\rho_g \left(u_g \frac{\partial w_g}{\partial r} + w_g \frac{\partial w_g}{\partial z} - g \beta_g T_g\right) \Phi_{gw} - p_g \frac{\partial \Phi_{gw}}{\partial z} \\
& + \mu_g \left(\frac{\partial w_g}{\partial r}\frac{\partial \Phi_{gw}}{\partial r} + \frac{\partial w_g}{\partial z}\frac{\partial \Phi_{gw}}{\partial z}\right)\Bigg] \; r \, \mathrm{d}r \, \mathrm{d}z \\
= \; & \mu_l \int\limits_{\substack{\textit{melt-gas} \\ \textit{interface}}} \frac{\partial u_l}{\partial z} \; \Phi_{lu} \; r \, \mathrm{d}r \; - \; \mu_g \int\limits_{\substack{\textit{melt-gas} \\ \textit{interface}}} \frac{\partial u_g}{\partial z} \; \Phi_{gu} \; r \, \mathrm{d}r
\end{aligned}
$$

Non-Dimensional form

By using $(R, Z) = (r, z)/L_c$, $(U, V, W) = (u, v, w)/U_c$, $\Theta = T/T_c$, $P = p/\rho_l U_c^2$ and $U_c = \nu_l/L_c$, the non-dimensional form of the Eq. (4.14) is as follow

$$
\begin{aligned}
& \iint\limits_{melt} \Bigg[\left(U_l \frac{\partial U_l}{\partial R} + W_l \frac{\partial U_l}{\partial Z} - \frac{V_l^2}{R} + \nu_l \frac{U_l}{R^2} \right) \Phi_{lu} - P_l \left(\frac{\partial \Phi_{lu}}{\partial R} + \frac{\Phi_{lu}}{R} \right) \\
& \quad + \left(\frac{\partial U_l}{\partial R} \frac{\partial \Phi_{lu}}{\partial R} + \frac{\partial U_l}{\partial Z} \frac{\partial \Phi_{lu}}{\partial Z} \right) \Bigg] \; R \, \mathrm{d}R \, \mathrm{d}Z \\
+ & \iint\limits_{melt} \Bigg[\left(U_l \frac{\partial V_l}{\partial R} + W_l \frac{\partial V_l}{\partial Z} + \frac{U_l V_l}{R} + \frac{V_l}{R^2} \right) \Phi_{lv} \\
& \quad + \left(\frac{\partial V_l}{\partial R} \frac{\partial \Phi_{lv}}{\partial R} + \frac{\partial V_l}{\partial Z} \frac{\partial \Phi_{lv}}{\partial Z} \right) \Bigg] \; R \, \mathrm{d}R \, \mathrm{d}Z \\
+ & \iint\limits_{melt} \Bigg[\left(U_l \frac{\partial W_l}{\partial R} + W_l \frac{\partial W_l}{\partial Z} - Gr \; \Theta_l \right) \Phi_{lw} - P_l \frac{\partial \Phi_{lw}}{\partial Z} \\
& \quad + \left(\frac{\partial W_l}{\partial R} \frac{\partial \Phi_{lw}}{\partial R} + \frac{\partial W_l}{\partial Z} \frac{\partial \Phi_{lw}}{\partial Z} \right) \Bigg] \; R \, \mathrm{d}R \, \mathrm{d}Z \\
- & \; \rho_{gl} \iint\limits_{gas} \Bigg[\left(U_g \frac{\partial U_g}{\partial R} + W_g \frac{\partial U_g}{\partial Z} - \frac{V_g^2}{R} + \nu_{lg} \frac{U_g}{R^2} \right) \Phi_{gu} - \rho_{lg} P_g \left(\frac{\partial \Phi_{gu}}{\partial R} + \frac{\Phi_{gu}}{R} \right) \\
& \quad + \nu_{gl} \left(\frac{\partial U_g}{\partial R} \frac{\partial \Phi_{gu}}{\partial R} + \frac{\partial U_g}{\partial Z} \frac{\partial \Phi_{gu}}{\partial Z} \right) \Bigg] \; R \, \mathrm{d}R \, \mathrm{d}Z \\
- & \; \rho_{gl} \iint\limits_{gas} \Bigg[\rho_g \left(U_g \frac{\partial V_g}{\partial R} + W_g \frac{\partial V_g}{\partial Z} + \frac{U_g V_g}{R} + \nu_{gl} \frac{V_g}{R^2} \right) \Phi_{gv} \\
& \quad + \nu_{gl} \left(\frac{\partial V_g}{\partial R} \frac{\partial \Phi_{gv}}{\partial R} + \frac{\partial V_g}{\partial Z} \frac{\partial \Phi_{gv}}{\partial Z} \right) \Bigg] \; R \, \mathrm{d}R \, \mathrm{d}Z \\
- & \; \rho_{gl} \iint\limits_{gas} \Bigg[\left(U_g \frac{\partial W_g}{\partial R} + W_g \frac{\partial W_g}{\partial Z} - \beta_{gl} \; Gr \; \Theta_g \right) \Phi_{gw} - \rho_{lg} P_g \frac{\partial \Phi_{gw}}{\partial Z} \\
& \quad + \nu_{gl} \left(\frac{\partial W_g}{\partial R} \frac{\partial \Phi_{gw}}{\partial R} + \frac{\partial W_g}{\partial Z} \frac{\partial \Phi_{gw}}{\partial Z} \right) \Bigg] \; R \, \mathrm{d}R \, \mathrm{d}Z \\
= & \int\limits_{\substack{melt\text{-}gas \\ interface}} \frac{\partial U_l}{\partial Z} \; \Phi_{lu} \; R \, \mathrm{d}R \; - \; \mu_{gl} \int\limits_{\substack{melt\text{-}gas \\ interface}} \frac{\partial U_g}{\partial Z} \; \Phi_{gu} \; R \, \mathrm{d}R
\end{aligned}
\tag{4.15}
$$

where $\rho_{lg} = \rho_l/\rho_g$, $\nu_{gl} = \nu_g/\nu_l$ and $Gr = g\beta_l T_c L_c^3/\nu_l^2$ is the Grashof number.

For the boundary condition on the melt free surface:

$$\frac{\partial U_l}{\partial Z} - \mu_{gl}\frac{\partial U_g}{\partial Z} = Ma\frac{\partial \theta}{\partial R} \tag{4.16}$$

where $Ma = |\partial\gamma/\partial T| T_c L_c/\mu_l \nu_l$ is the Marangoni number.

4.3.2 Continuity equation

From the Eq. (4.2) the continuity equations for the melt and gas are,

$$\frac{\partial u_l}{\partial r} + \frac{u_l}{r} + \frac{\partial w_l}{\partial z} = 0 \tag{4.17}$$

$$\frac{\partial u_g}{\partial r} + \frac{u_g}{r} + \frac{\partial w_g}{\partial z} = 0 \tag{4.18}$$

The weak form is

$$\iint\limits_{melt} \left(\frac{\partial u_l}{\partial r} + \frac{u_l}{r} + \frac{\partial w_l}{\partial z}\right) \Phi_{lc} \;\; r\,\mathrm{d}r\,\mathrm{d}z \;\; - \iint\limits_{gas} \left(\frac{\partial u_g}{\partial r} + \frac{u_g}{r} + \frac{\partial w_g}{\partial z}\right) \Phi_{gc} \;\; r\,\mathrm{d}r\,\mathrm{d}z = 0 \tag{4.19}$$

and the non-dimensional form

$$\iint\limits_{melt} \left(\frac{\partial U_l}{\partial R} + \frac{U_l}{R} + \frac{\partial W_l}{\partial Z}\right) \Phi_{lc} \; R\,\mathrm{d}R\,\mathrm{d}Z$$

$$- \iint\limits_{gas} \left(\frac{\partial U_g}{\partial R} + \frac{U_g}{R} + \frac{\partial W_g}{\partial Z}\right) \Phi_{gc} \; R\,\mathrm{d}R\,\mathrm{d}Z = 0 \tag{4.20}$$

4.3.3 Energy equation

The energy equations for media are as follow:

$k_c \nabla^2 T_c + q = 0$ conduction in the crucible and afterheater (4.21)

$k_i \nabla^2 T_i = 0$ conduction in the insulation (4.22)

$\alpha_l \nabla^2 T_l - \mathbf{v}_l \cdot \nabla T_l = 0$ conduction and convection in the melt (4.23)

$\alpha_g \nabla^2 T_g - \mathbf{v}_g \cdot \nabla T_g = 0$ conduction and convection in the gas (4.24) where k is thermal conductivity, $\alpha = k/\rho c_p$ thermal diffusivity, $\mathbf{v} = (u, v, w)$ velocity, ρ density and c_p specific heat in constant pressure, T temperature and q heat source density.

Weak form

The weak form of the above equations and the BCs (Eqs. 4.7 and 4.10) is

$$
\begin{aligned}
& k_c \underset{\textit{crucible}}{\iint} \left(\nabla T_c \cdot \nabla \Phi_{ce} - \frac{q}{k_c} \Phi_{ce} \right) \, r \, \mathrm{d}r \, \mathrm{d}z \; + \; k_i \underset{\textit{insulation}}{\iint} \nabla T_i \cdot \nabla \Phi_{ie} \; r \, \mathrm{d}r \, \mathrm{d}z \\
+ \; & \underset{\textit{melt}}{\iint} \left[k_l \left(\nabla T_l \cdot \nabla \Phi_{le} \right) + \rho_l c_{pl} \mathbf{v}_l \cdot \nabla T_l \Phi_{le} \right] \; r \, \mathrm{d}r \, \mathrm{d}z \\
+ \; & \underset{\textit{gas}}{\iint} \left[k_g \left(\nabla T_g \cdot \nabla \Phi_{ge} \right) + \rho_g c_{pg} \mathbf{v}_g \cdot \nabla T_g \Phi_{ge} \right] \; r \, \mathrm{d}r \, \mathrm{d}z \\
= \; & k_i \underset{\substack{\textit{outer surfaces} \\ \textit{of insulation}}}{\int} \frac{\partial T_i}{\partial \hat{n}} \Phi_{ie} \; r \, \mathrm{d}r \; + \; k_l \underset{\textit{melt surface}}{\int} \frac{\partial T_l}{\partial z} \Phi_{le} \; r \, \mathrm{d}r
\end{aligned}
\tag{4.25}
$$

and dividing by k_l, we will find

$$
\begin{aligned}
& k_{cl} \underset{\textit{crucible}}{\iint} \left(\nabla T_c \cdot \nabla \Phi_{ce} - \frac{q}{k_c} \Phi_{ce} \right) \, r \, \mathrm{d}r \, \mathrm{d}z \; + \; k_{il} \underset{\textit{insulation}}{\iint} \nabla T_i \cdot \nabla \Phi_{ie} \; r \, \mathrm{d}r \, \mathrm{d}z \\
+ \; & \underset{\textit{melt}}{\iint} \nabla T_l \cdot \nabla \Phi_{le} \; r \, \mathrm{d}r \, \mathrm{d}z \; + \; \frac{1}{\alpha_l} \underset{\textit{melt}}{\iint} \mathbf{v}_l \cdot \nabla T_l \Phi_{le} \; r \, \mathrm{d}r \, \mathrm{d}z \\
+ \; & k_{gl} \underset{\textit{gas}}{\iint} \nabla T_g \cdot \nabla \Phi_{ge} \; r \, \mathrm{d}r \, \mathrm{d}z \; + \; \frac{k_{gl}}{\alpha_g} \underset{\textit{gas}}{\iint} \mathbf{v}_g \cdot \nabla T_g \Phi_{ge} \; r \, \mathrm{d}r \, \mathrm{d}z \\
= \; & k_{il} \underset{\substack{\textit{outer surfaces} \\ \textit{of insulation}}}{\int} \frac{\partial T_i}{\partial \hat{n}} \Phi_{ie} \; r \, \mathrm{d}r \; + \underset{\textit{melt surface}}{\int} \frac{\partial T_l}{\partial z} \Phi_{le} \; r \, \mathrm{d}r
\end{aligned}
\tag{4.26}
$$

where $k_{cl} = k_c/k_l$, $k_{il} = k_i/k_l$ and $k_{gl} = k_g/k_l$. Finally,

$$\begin{aligned} & k_{cl} \iint\limits_{crucible} \left(\frac{\partial T_c}{\partial r}\frac{\partial \Phi_{ce}}{\partial r} + \frac{\partial T_c}{\partial z}\frac{\partial \Phi_{ce}}{\partial z} - \frac{q}{k_c}\Phi_{ce} \right) r\,\mathrm{d}r\,\mathrm{d}z \\ + \quad & k_{il} \iint\limits_{insulation} \left(\frac{\partial T_i}{\partial r}\frac{\partial \Phi_{ie}}{\partial r} + \frac{\partial T_i}{\partial z}\frac{\partial \Phi_{ie}}{\partial z} \right) r\,\mathrm{d}r\,\mathrm{d}z \\ + \quad & \iint\limits_{melt} \left(\frac{\partial T_l}{\partial r}\frac{\partial \Phi_{le}}{\partial r} + \frac{\partial T_l}{\partial z}\frac{\partial \Phi_{le}}{\partial z} \right) r\,\mathrm{d}r\,\mathrm{d}z + \frac{1}{\alpha_l} \iint\limits_{melt} \left(u_l \frac{\partial T_l}{\partial r} + w_l \frac{\partial T_l}{\partial z} \right) \Phi_{le}\; r\,\mathrm{d}r\,\mathrm{d}z \\ + \quad & k_{gl} \iint\limits_{gas} \left(\frac{\partial T_g}{\partial r}\frac{\partial \Phi_{ge}}{\partial r} + \frac{\partial T_g}{\partial z}\frac{\partial \Phi_{ge}}{\partial z} \right) r\,\mathrm{d}r\,\mathrm{d}z + \frac{k_{gl}}{\alpha_g} \iint\limits_{gas} \left(u_g \frac{\partial T_g}{\partial r} + w_g \frac{\partial T_g}{\partial z} \right) \Phi_{ge}\; r\,\mathrm{d}r\,\mathrm{d}z \\ = \quad & k_{il} \int\limits_{\substack{outer\ surfaces\\ of\ insulation}} \frac{\partial T_i}{\partial \hat{n}} \Phi_{ie}\; r\,\mathrm{d}r + \int\limits_{melt\ surface} \frac{\partial T_l}{\partial z} \Phi_{le}\; r\,\mathrm{d}r \end{aligned} \tag{4.27}$$

Non-dimensional form

The non-dimensional form is

$$
\begin{aligned}
& k_{cl} \iint\limits_{crucible} \left[\frac{\partial \Theta_c}{\partial R} \frac{\partial \Phi_{ce}}{\partial R} + \frac{\partial \Theta_c}{\partial Z} \frac{\partial \Phi_{ce}}{\partial Z} - \left(\frac{L_c^2}{T_c k_c} \right) q \Phi_{ce} \right] \, R \, \mathrm{d}R \, \mathrm{d}Z \\
+ \; & k_{il} \iint\limits_{insulation} \left(\frac{\partial \Theta_i}{\partial R} \frac{\partial \Phi_{ie}}{\partial R} + \frac{\partial \Theta_i}{\partial Z} \frac{\partial \Phi_{ie}}{\partial Z} \right) \, R \, \mathrm{d}R \, \mathrm{d}Z \\
+ \; & \iint\limits_{melt} \left(\frac{\partial \Theta_l}{\partial R} \frac{\partial \Phi_{le}}{\partial R} + \frac{\partial \Theta_l}{\partial Z} \frac{\partial \Phi_{le}}{\partial Z} \right) \, R \, \mathrm{d}R \, \mathrm{d}Z \\
+ \; & Pr \iint\limits_{melt} \left(U_l \frac{\partial \Theta_l}{\partial R} + W_l \frac{\partial \Theta_l}{\partial Z} \right) \Phi_{le} \; R \, \mathrm{d}R \, \mathrm{d}Z \\
+ \; & k_{gl} \iint\limits_{gas} \left(\frac{\partial \Theta_g}{\partial R} \frac{\partial \Phi_{ge}}{\partial R} + \frac{\partial \Theta_g}{\partial Z} \frac{\partial \Phi_{ge}}{\partial Z} \right) \, R \, \mathrm{d}R \, \mathrm{d}Z \\
+ \; & \frac{\nu_l k_{gl}}{\alpha_g} \iint\limits_{gas} \left(U_g \frac{\partial \Theta_g}{\partial R} + W_g \frac{\partial \Theta_g}{\partial Z} \right) \Phi_{ge} \; R \, \mathrm{d}R \, \mathrm{d}Z \\
= \; & k_{il} \int\limits_{\substack{outer\ surfaces \\ of\ insulation}} \frac{\partial \Theta_i}{\partial \hat{N}} \Phi_{ie} \; R \, \mathrm{d}R + \int\limits_{melt\ surface} \frac{\partial \Theta_l}{\partial Z} \Phi_{le} \; R \, \mathrm{d}R \qquad (4.28)
\end{aligned}
$$

where $Pr = \nu_l / \alpha_l$ is the Prandtl number of the melt. Finally, from dividing by Pr, we will have

$$
\begin{aligned}
& \frac{k_{cl}}{Pr} \iint\limits_{crucible} \left[\frac{\partial \Theta_c}{\partial R} \frac{\partial \Phi_{ce}}{\partial R} + \frac{\partial \Theta_c}{\partial Z} \frac{\partial \Phi_{ce}}{\partial Z} \; - \; \left(\frac{L_c^2}{T_c k_c} \right) q \Phi_{ce} \right] \; R \,\mathrm{d}R \,\mathrm{d}Z \\
+ \; & \frac{k_{il}}{Pr} \iint\limits_{insulation} \left(\frac{\partial \Theta_i}{\partial R} \frac{\partial \Phi_{ie}}{\partial R} + \frac{\partial \Theta_i}{\partial Z} \frac{\partial \Phi_{ie}}{\partial Z} \right) \; R \,\mathrm{d}R \,\mathrm{d}Z \\
+ \; & \frac{1}{Pr} \iint\limits_{melt} \left(\frac{\partial \Theta_l}{\partial R} \frac{\partial \Phi_{le}}{\partial R} + \frac{\partial \Theta_l}{\partial Z} \frac{\partial \Phi_{le}}{\partial Z} \right) \; R \,\mathrm{d}R \,\mathrm{d}Z \\
+ \; & \iint\limits_{melt} \left(U_l \frac{\partial \Theta_l}{\partial R} + W_l \frac{\partial \Theta_l}{\partial Z} \right) \Phi_{le} \; R \,\mathrm{d}R \,\mathrm{d}Z \\
+ \; & \frac{k_{gl}}{Pr} \iint\limits_{gas} \left(\frac{\partial \Theta_g}{\partial R} \frac{\partial \Phi_{ge}}{\partial R} + \frac{\partial \Theta_g}{\partial Z} \frac{\partial \Phi_{ge}}{\partial Z} \right) \; R \,\mathrm{d}R \,\mathrm{d}Z \\
+ \; & \frac{k_{gl}}{\alpha_{gl}} \iint\limits_{gas} \left(U_g \frac{\partial \Theta_g}{\partial R} + W_g \frac{\partial \Theta_g}{\partial Z} \right) \Phi_{ge} \; R \,\mathrm{d}R \,\mathrm{d}Z \\
= \; & \frac{k_{il}}{Pr} \int\limits_{\substack{outer\ surfaces \\ of\ insulation}} \frac{\partial \Theta_i}{\partial \hat{N}} \Phi_{ie} \; R \,\mathrm{d}R \; + \; \frac{1}{Pr} \int\limits_{melt\ surface} \frac{\partial \Theta_l}{\partial Z} \Phi_{le} \; R \,\mathrm{d}R \qquad (4.29)
\end{aligned}
$$

where $\alpha_{gl} = \alpha_g / \alpha_l$.

The non-dimensional form of the boundary conditions (Eqs. 4.7 and 4.10) are as follow

$$
-\frac{\partial \Theta_i}{\partial \hat{N}} = Bio_i \left(\Theta_i - \Theta_a \right) + Rad_i \left(\Theta_i^4 - \Theta_a^4 \right) \qquad (4.30)
$$

$$
-\frac{\partial \Theta_l}{\partial Z} = Rad_l \left(\Theta_l^4 - \Theta_{ah}^4 \right) \qquad (4.31)
$$

where $Bio_i = h_i L_c / k_i$ and $Rad_i = \sigma \epsilon_i L_c T_c^3 / k_i$ are the Biot number and the Radiation number of the insulation, respectively and $Rad_l = \sigma \epsilon_l L_c T_c^3 / k_l$ is the Radiation number of the melt.

4.3.4 Stream function

Similar to the chapter 2, the equations for the fluid stream function (ψ) are,

$$U_l = \frac{1}{R}\frac{\partial \psi_l}{\partial Z}, \qquad V_l = -\frac{1}{R}\frac{\partial \psi_l}{\partial R} \tag{4.32}$$

$$U_g = \frac{1}{R}\frac{\partial \psi_g}{\partial Z}, \qquad V_g = -\frac{1}{R}\frac{\partial \psi_g}{\partial R} \tag{4.33}$$

This leads to the weak form

$$\begin{aligned} &\iint\limits_{melt} \left\{ \frac{\partial \psi_l}{\partial R}\frac{\partial \Phi_{lp}}{\partial R} + \frac{\partial \psi_l}{\partial Z}\frac{\partial \Phi_{lp}}{\partial Z} + \left[\frac{1}{R}\frac{\partial \psi_l}{\partial Z} + R\left(\frac{\partial U_l}{\partial R} - \frac{\partial V_l}{\partial Z} \right) \right] \Phi_{lp} \right\} \; R \, \mathrm{d}R \, \mathrm{d}Z \\ + &\iint\limits_{gas} \left\{ \frac{\partial \psi_g}{\partial R}\frac{\partial \Phi_{gp}}{\partial R} + \frac{\partial \psi_g}{\partial Z}\frac{\partial \Phi_{gp}}{\partial Z} + \left[\frac{1}{R}\frac{\partial \psi_g}{\partial Z} + R\left(\frac{\partial U_g}{\partial R} - \frac{\partial V_g}{\partial Z} \right) \right] \Phi_{gp} \right\} \; R \, \mathrm{d}R \, \mathrm{d}Z = 0 \end{aligned} \tag{4.34}$$

4.3.5 The calculation conditions

Values of physical properties employed for our calculations are presented in Table 4-1 [9,14,15] and so $Pr = 21.2$. In all calculations the ambient temperature is set to be 25 ^oC and the frequency of input electrical current is 10 kHz. We have selected the crucible inner radius (r_c) as the characteristic length (L_c) and the melting point (T_m) as the characteristic temperature (T_c). The temperature at the centerline of the melt free surface (where the seed crystal will be placed) is 2070 ^oC, i.e. 20 ^oC above the melting point of sapphire (corresponding to the real condition of the seeding process). This is not a boundary condition but it should be a result from the calculations.

The shape of melt-gas interface is considered as an analytical function taken from experimental growth results. We expect that this assumption, which simplifies our numerical calculations considerably, is a good approximation for this interface shape.

It should be mentioned that the inductive coupling with a molten oxide contained in a metal crucible is insignificant for the frequency considered (10 kHz), therefore heat generation in these crystal growth melts can be neglected.

Description (units)	Symbel	Value
Density (kg/m^3)	ρ_l	3500
	ρ_g	0.35
Dynamic viscosity ($kg/m \cdot s$)	μ_l	4.75×10^{-2}
	μ_g	$4. \times 10^{-5}$
Kinematic viscosity (m^2/s)	ν_l	1.36×10^{-5}
	ν_g	1.14×10^{-4}
Thermal expansion coefficient ($1/K$)	β_l	1.8×10^{-5}
	β_g	2.7×10^{-3}
Specific heat ($kJ/kg \cdot K$)	c_{pl}	1.56
	c_{pg}	1.14
Thermal diffusivity (m^2/s)	α_l	6.4×10^{-7}
	α_g	2.7×10^{-4}
Thermal conductivity ($W/m \cdot k$)	k_l	3.5
	k_g	0.11
	k_c	147
	k_i	2.14
Emissivity	ε_l	0.3
	ε_i	0.2
Thermocapillary coefficient ($dyn/cm \cdot K$)	$\partial\gamma_l/\partial T$	-3.5×10^{-2}
Heat transfer coefficient ($W/m^2 \cdot K$)	h_i	20
Contact angle of the melt	θ	18

Table 4-1. Physical properties used for calculations; the subscripts l, g, c and i denote melt (*sapphire*), gas (*air*), crucible (*iridium*) and insulation (ZrO_2), respectively.

Description (units)	Symbel	Value
Crucible inner radius (mm)	r_c	49
Crucible thickness (mm)	l_c	2
Crucible inner height (mm)	h_c	98
Afterheater inner height (mm)	h_{af}	100
Afterheater hole (mm)	r_{af}	10
Distance between crucible and afterheater (mm)	D_{ca}	0, 30
Coil inner radius (mm)	r_{co}	85
Coil thickness (mm)	l_{co}	13
Height of coil turns (mm)	h_{co}	27
Distance between coil turns (mm)	d_{co}	5
Distance between the two coils (mm)	D_{co}	25
Thickness of crucible insulation at the bottom (mm)	h_{ci}	50
Thickness of crucible insulation at the wall (mm)	d_{ci}	24
Thickness of afterheater insulation (mm)	d_{ai}	6
Melt depth (mm)	d_{melt}	93
Ambient temperature (^oC)	T_a	25
Temperature at the afterheater hole (^oC)	T_{ah}	1700, 1600

Table 4-2. Operating parameters used for calculations of *case a.*

4.4 Results and discussion

4.4.1 case a: crucible and afterheater, with and without a gap

Fig. 4-a-1 shows a sketch of these two systems and the operating parameters are listed in Table 4-2. The non-dimensional numbers are $Gr = 2.6 \times 10^5$, $Ma = 6167$, $Rad_l = 3$, $Rad_i = 3.25$ and $Bio_i = 0.23$.

The temperature at the afterheater top cover hole is set to be 1700 ^oC and 1600 ^oC for the configuration without and with a gap between crucible and afterheater, respectively. These values are taken from measurements in our Czochralski-dielectrics lab and they are used as boundary conditions.

The contact angle and deflection height of the crucible meniscus is set to be 18^0

(Table 4-1) and 4 mm, respectively, taken from observation in the lab during the seeding process of sapphire growth. The calculation results based on this set of parameters will be presented hereafter.

The aim of these calculations was to investigate the effect of the insulation and a closed gap (covered outside by insulation) between crucible and afterheater on the fluid flow and temperature field of the system just before the seeding process.

Induction heating

The geometry and orientation of the coil-crucible-afterheater setup for both configurations is the same as *case a* in chapter 2. So we do not discuss about the spatial distribution of heat generation in these two systems again. In the present case including melt and gas, the maximum value of energy deposition is $q_{max}^{without} = q_{max}^{with} \simeq 50\ W/cm^3$ for both cases and the total energy production in the crucible and afterheater is $Q_{total}^{without} = 2.94\ kW$ and $Q_{total}^{with} = 2.86\ kW$ for the configuration without and with a gap, respectively.

Temperature and flow field

Fig. 4-a-2 shows the contours of the stream function in melt and gas (left hand side), and isotherms in the melt, gas, crucible, afterheater and insulation (right hand side) for both configurations. In the melt of both configurations, a clockwise vortex caused by free convection (buoyancy driven) and thermal Marangoni convection (surface tension driven) exists and occupies the entire volume. This flow transfers the heat from the crucible wall to the central part (where the seed crystal will be located). Also, there is a weak and small counterclockwise vortex in the crucible meniscus (visible in Fig. 4-a-3 by the opposite sign of the velocity v at the right hand side). Fig. 4-a-3 shows the velocity profile along the melt free surface from the centerline to the crucible wall with a maximum value of $\mathrm{v}_{max(melt\ surface)}^{without} \simeq 0.28\ cm/s$ and $\mathrm{v}_{max(melt\ surface)}^{with} \simeq 0.27\ cm/s$ for the configuration without and with a gap, respectively, at the position $\sim 1.5\ cm$ distance to the symmetry axis. In the bulk melt, the maximum value of velocity in both configurations is $\mathrm{v}_{max}^{melt} \simeq 0.75\ cm/s$, downwards and at the axis of symmetry, Fig. 4-a-4.

In the gas part of both configurations, there are two separate vortices with opposite direction of rotation, a strong vortex and a weak one. In the configuration without a gap, the first gas vortex rotates clockwise, is located above the melt surface and is extended to the afterheater hole while the second vortex rotates counterclockwise and is placed close to the afterheater corner. In the configuration with a gap, the small and weak clockwise vortex is placed above the melt surface close to the gap while the strong counterclockwise vortex occupies almost the whole volume of the afterheater. The center of this vortex is located close to the afterheater corner and as a result the gas flow is

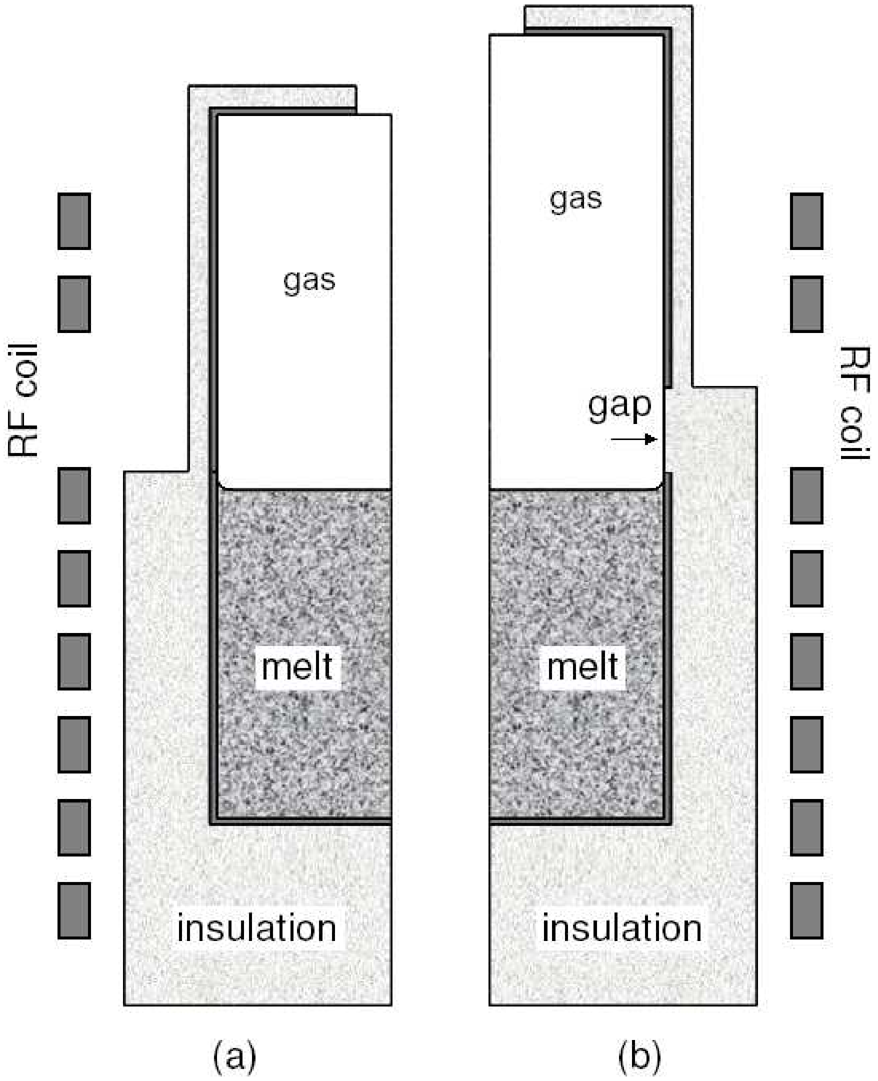

Fig. 4-a-1. Schematic diagram of two cases of Czochralski growth furnace containing the melt and gas, (a) without and (b) with a gap between crucible and afterheater.

more intense in this area. Also, there is a very tiny and weak counterclockwise vortex just above the melt-gas interface (not visible) in both configurations, which is extended from the crucible wall to the symmetry axis. It is a result of the continuous tangential velocity at the melt-gas interface and the high difference between the viscosity of melt and gas ($\nu_{melt}/\nu_{gas} \sim 10^3$). The fluid flow in this eddy is directed from the crucible wall towards the axis of symmetry along the melt-gas interface (i.e. the same as the melt flow at this interface) and returns towards the crucible wall in a very small distance above the melt surface.

The maximum value of velocity in the gas is $\mathrm{v}^{without}_{max(gas)} = 38\ cm/s$, downwards and located at the axis of symmetry for the configuration without a gap, and $\mathrm{v}^{with}_{max(gas)} =$

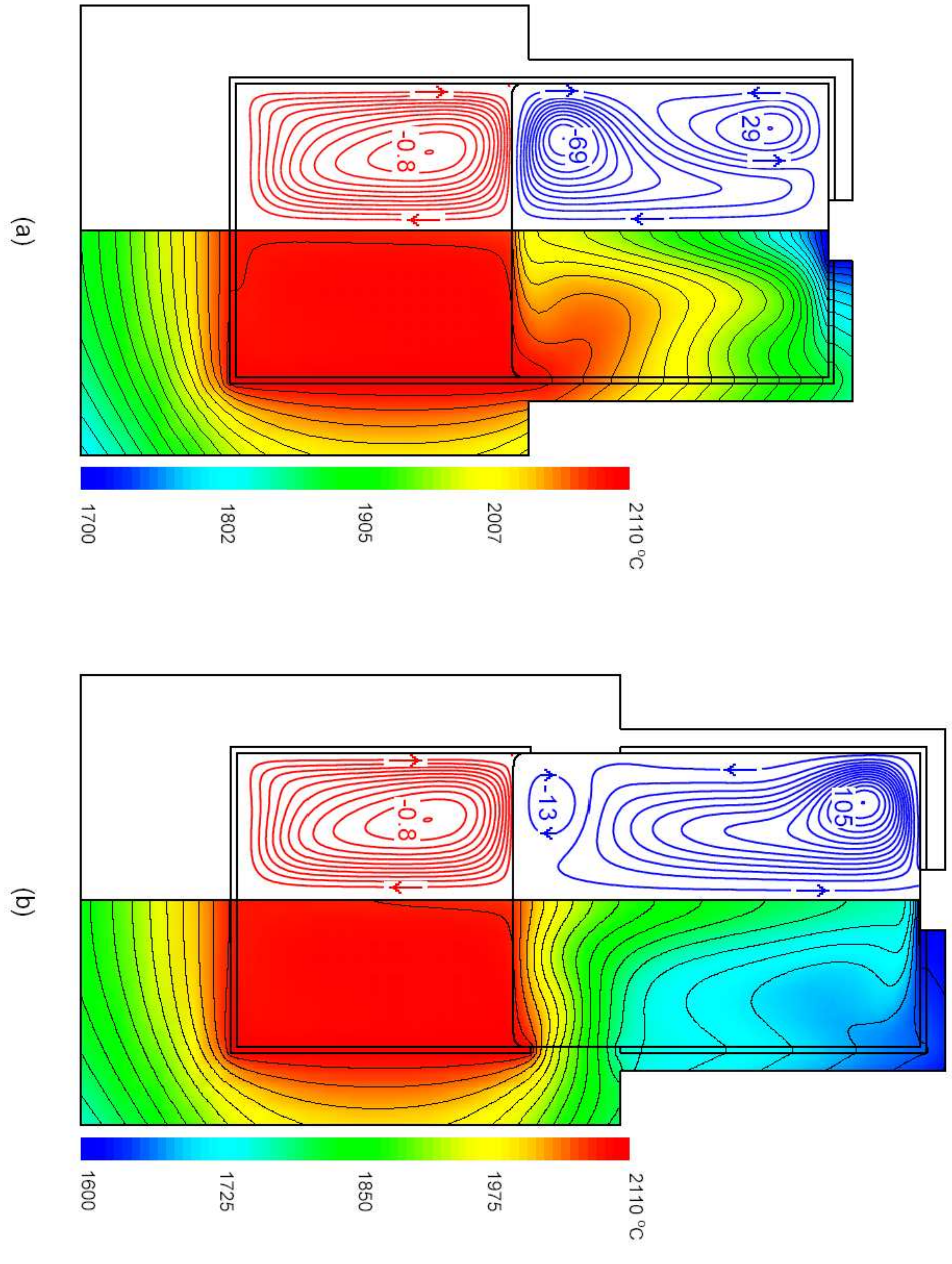

Fig. 4-a-2. Isotherms (right hand side) and the stream function (left hand side) for (a) configuration without a gap and (b) configuration with a gap between crucible and afterheater.

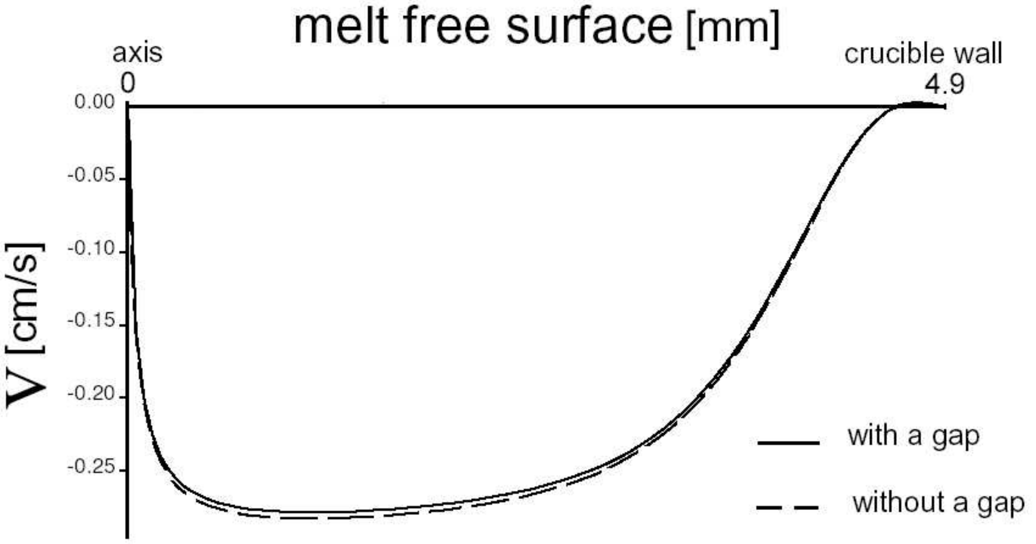

Fig. 4-a-3. Profile of the velocity along the melt-gas interface taken from the symmetry axis to the crucible wall for both configurations. The maximum is $v_{max}^{melt\ surface} \simeq 0.28$ and 0.27 cm/s for the configuration without and with a gap, respectively and its position is ~ 1.5 cm distance from the centerline.

45 cm/s, upwards and also at the symmetry axis in the configuration with a gap between crucible and afterheater.

The temperature field in the melt part of both configurations is markedly influenced by the strong buoyant and Marangoni flow which is normal for high Prandtl number materials such as molten oxides. In the oxide melts (such as sapphire, YAG and lithium aluminate), the role of convection is more important than conduction in the heat transfer mechanism and consequently the isotherm shapes have a deflection proportional to the convection mode and flow structure. The isotherms in the melt are pushed up along the crucible sides, deflected towards the symmetry axis close to the melt surface and deformed downwards in the vicinity of the centerline.

There is a relatively considerable difference between the melt temperature field of both configurations which is shown by the displacement of the isotherms in the configuration with a gap compared to the other one. This is a result of different heat loss from the melt surface and is also caused by a different gas flow pattern especially above the melt-gas interface. The effect of the first factor (i.e. heat dissipation from the melt surface) is more important than the second (gas flow pattern). In the configuration with a gap the heat radiation exchange from the melt surface is stronger than in the other configuration since the temperature at the afterheater hole in this configuration

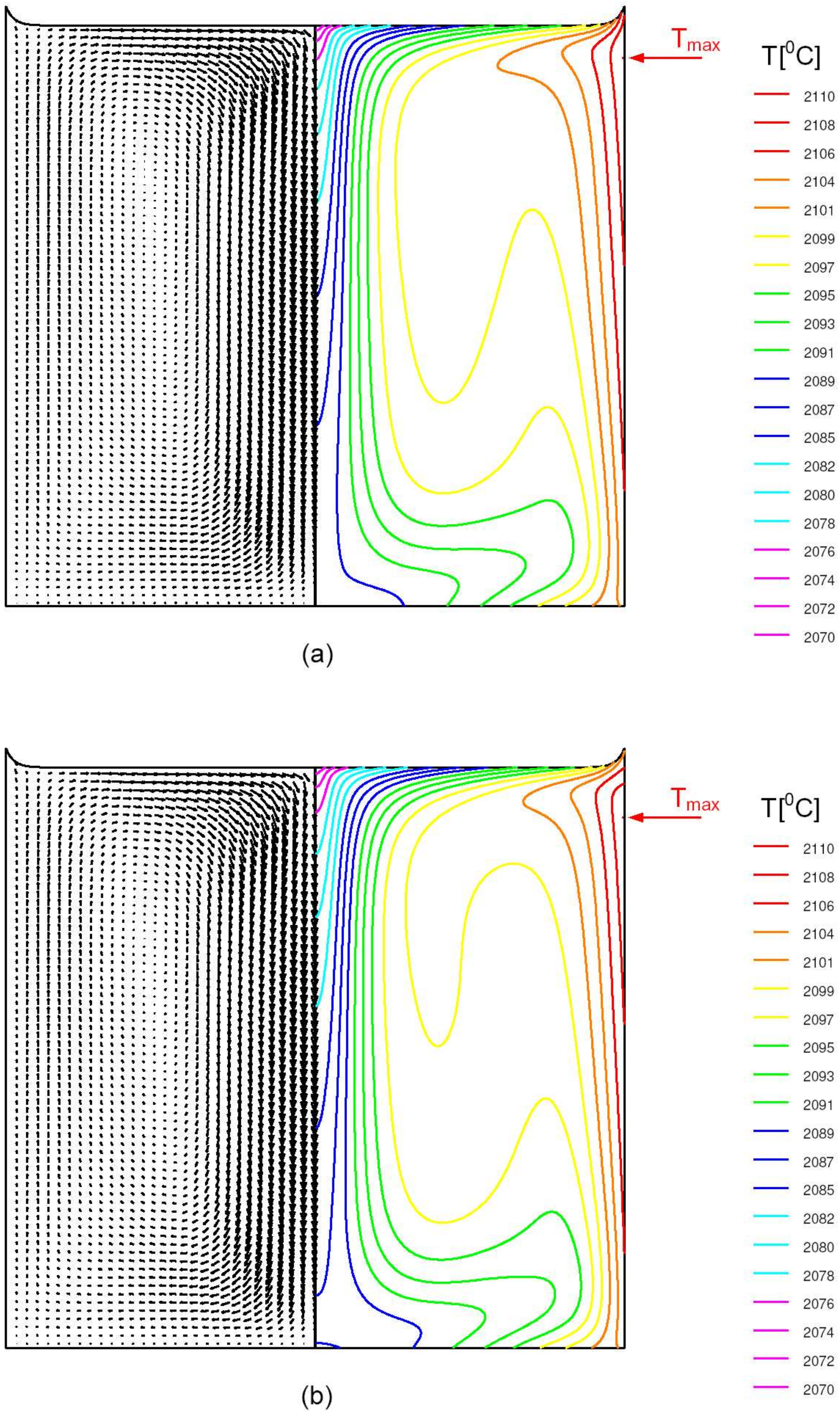

Fig. 4-a-4. Temperature and velocity vector field of the melt for (a) configuration without a gap and (b) configuration with a gap between crucible and afterheater.

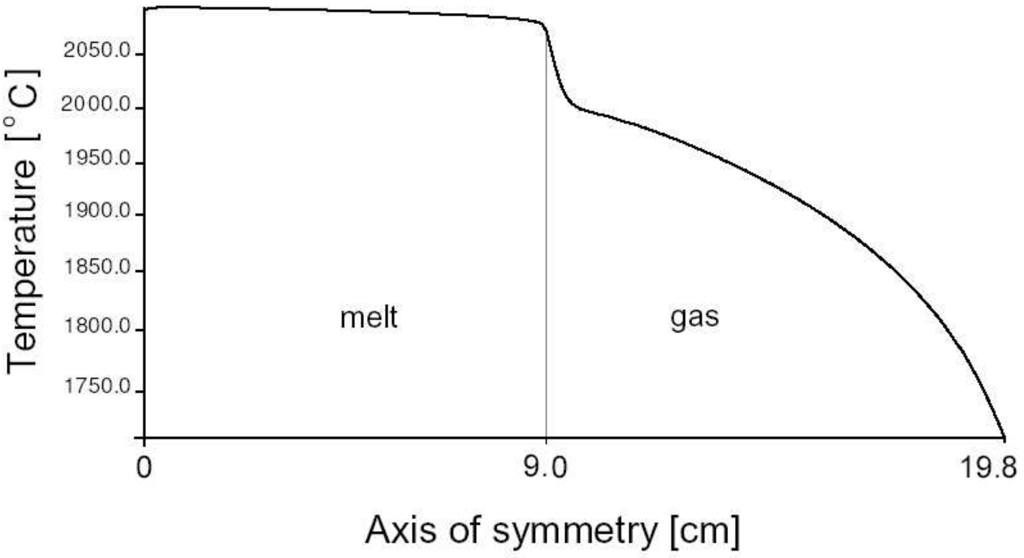

(a)

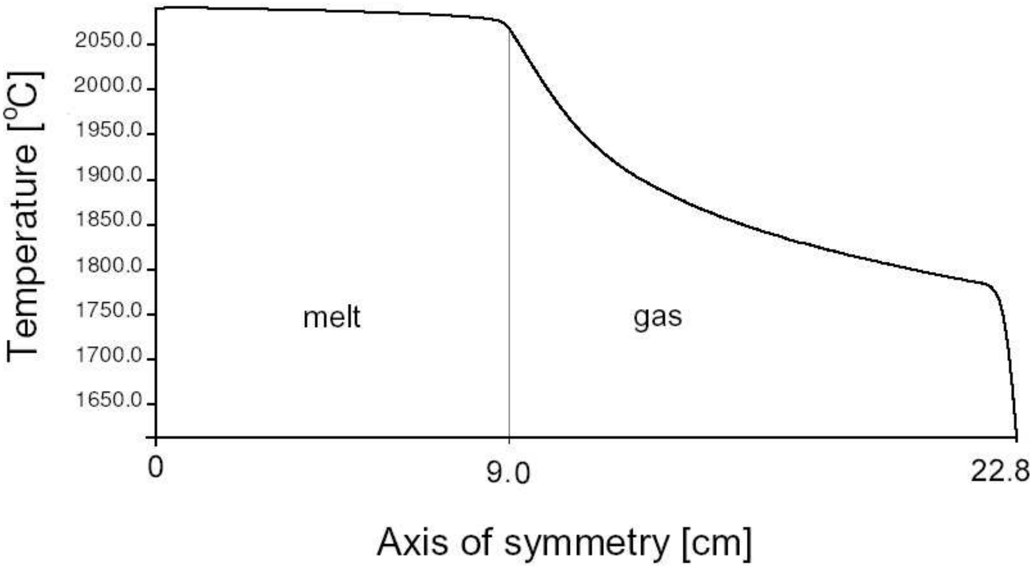

(b)

Fig. 4-a-5. Vertical temperature profiles along the axis of symmetry taken from the crucible bottom to the afterheater hole for (a) configuration without a gap and (b) configuration with a gap between crucible and afterheater. The melt height is $9cm$ at the centerline. The temperature profile in (a) is appropriate for growing crystals with evaporation problems.

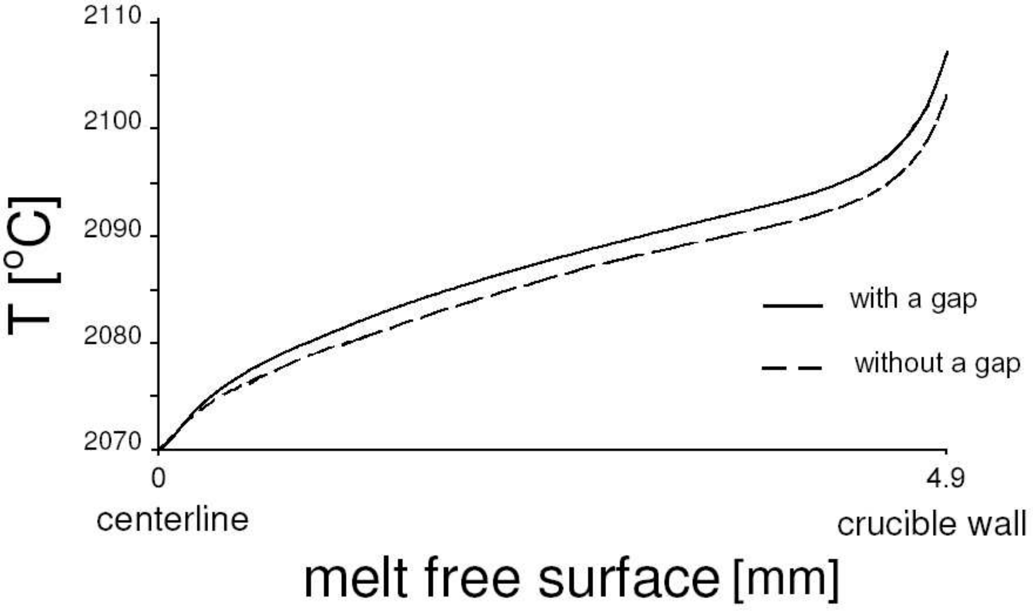

Fig. 4-a-6. Radial temperature profile along the melt-gas interface for both configurations.

is 100 ^{o}C less than in the configuration without a gap between crucible and afterheater (Eq. 4-a-4).

The temperature field in the gas domain is also moderately affected by the strong thermal flow in both configurations which is a result of the intensive gas flow in this part of the system. In the configuration without a gap, the isotherms are pushed towards the afterheater top cover hole in the vicinity of the afterheater wall and are deflected downwards along the symmetry axis. This structure of gas isotherm shapes indicates that the overall heat transfer in the gas part is influenced by the melt surface and lower part of the afterheater wall (which is hot) towards the afterheater hole. On the other hand in the configuration with a gap, the isotherms have a horizontal shape above the melt surface in the gap. They have also been pushed upwards along the centerline and downwards close to the afterheater side wall. This gas isotherm distribution indicates that the overall heat transfer in the afterheater is caused by the melt surface towards the afterheater top cover as well as its hole. Also, there is a high vertical temperature gradient in the gap region close to the side wall caused by the upwards directed heat flux from the melt surface in that part.

Fig. 4-a-5 represents the temperature profile of both configurations along the axis of symmetry ($r = 0$), where it is plotted from the crucible bottom to the afterheater top cover. This figure shows that at the symmetry axis of both configurations, the temperature gradient is high and about linear close to the melt-gas interface on both

sides. This figure also shows two different temperature gradients along the symmetry axis in the gas domain, which is a result of different gas flow structure in that part of the system. In the configuration without a gap, the temperature variation is quite high just above the melt surface and then it decreases but it is still relatively high because of the downward gas flow along the axis of symmetry. This kind of temperature variation is appropriate for materials that need a relatively high temperature gradient along the axis of symmetry. For some grown crystals such as lithium aluminate ($LiAlO_2$), the surface evaporation is a crucial problem during the growth process. To prevent this problem, such a high tempearture variation in the gas domain is necessary. It should be mentioned that the sharp conversion in the temperature gradient above the melt surface can originate thermal stress (related to $\partial^2 T/\partial z^2$) within the grown crystal which may promote cracking by a thermal stress mechanisms [6,8,10,28]. In the configuration with a gap, the temperature gradient is not as high as in the first configuration except close to the afterheater hole where it is extremely high. It arises from the upwards gas flow in the afterheater and a slow gas motion in the gap along the symmetry axis. This type of temperature variation is suitable for the most grown crystals such as sapphire because they are sensitive to thermal stress, crack, defect and dislocation. By using this kind of temperature profile along the symmetry axis, control of thermal stress in the grown crystal is possible [66].

Fig. 4-a-6 represents the temperature variation at the melt-gas interface for both configurations. It shows that the temperature variation along the melt surface is about linear with the rate $\delta\overline{T} \sim 3\ ^oC/mm$ except in the crucible meniscus as well as close to the symmetry axis. As has already been mentioned, there is a small and weak melt convection in the crucible meniscus and its circulation is in opposite direction compared to the main thermal flow in the melt (Fig. 4-a-3). This second melt vortex modifies the temperature distribution in that area and so the temperature gradient at the melt surface of the crucible meniscus is higher than $\delta\overline{T}$. On the other hand, there is a typical temperature boundary layer in the vicinity of the axis of symmetry where the direction of the melt flow changes from the radial direction (towards the axis) to the axial direction (downwards) and so the temperature gradient is relatively high. It is important to note that the melt surface temperature in the configuration with a gap is lower than in the configuration whitout a gap ($\simeq 5\ ^oC$ at the crucible wall) which is a result of different heat loss from the melt surface by radiation, as we have already discussed before.

The temperature maximum value is $T_{max} = 2110\ ^oC$ at the inner crucible wall for both configurations. It is located at 1 cm and 1.3 cm distance below the melt surface in the configuration without and with a gap, respectively. The minimum value of the temperature is located at the afterheater hole in both configurations. The maximum value of temperature difference for the melt is $\triangle T^{melt}_{max} = 40\ ^{o}C$ for both configurations, while in the whole system $\triangle T^{without}_{max(system)} = 410\ ^{o}C$ for the configuration without a gap, and $\triangle T^{with}_{max(system)} = 510\ ^{o}C$ for the configuration with a gap.

There are significant differences between the flow structure and temperature field in the gas part of both configurations, which is a direct result of the different position of the active afterheater with respect to the crucible. The presence of multiple eddies gas flow in the afterheater of both configurations indicates a more complicated heat transfer mechanism in this part of the system rather than in the melt. The temperature field of both fluid parts (melt and gas) is markedly influenced by their strong thermal flow. Although the melt motion is much slower than the gas flow ($\mathrm{v}^{gas}_{max}/\mathrm{v}^{melt}_{max} \sim 50$) the thermal flow in both fluid parts is quite strong and modifies the temperature field in the melt as well as in the gas part (because of a high difference between their viscosities $\nu_{melt}/\nu_{gas} \sim 10^{3}$). On the other hand, different positions of the afterheater with respect to the crucible influences the radiation heat exchange from the melt surface which directly modifies the thermal field of the melt especially close to the melt surface. In the work presented here, a lifted upwards afterheater leads to shifting downwards the T_{max} position at the crucible wall and the temperature difference at the free surface as well as the melt motion there decreases.

4.4.2 case b: crucible and afterheater, with an open gap

Designation (Fig. 4-b-1):

G: Gap between crucible and afterheater,

AH: Afterheater top cover Hole,

For the boundary condition of the temperature, there are two BCs:

- at G: $T_G = 1190\ ^oC$
- at AIH: $T_{AIH} = 1600$ - $1680\ ^oC$ with linear variation from the corner to the symmetry axis

Fig. 4-b-1 shows a sketch of this system and the operating parameters are listed in Table 4-3. Then the non-dimensional numbers are $Gr = 1.2 \times 10^4$, $Ma = 2340$, $Rad_l = 1.17$, $Rad_i = 1.27$ and $Bio_i = 0.09$.

The contact angle and deflection height of the meniscus with the crucible side wall is set to be 18^0 (Table 4-1) and 2 mm, respectively, taken from observations in the lab. The calculation results based on this set of parameters will be presented hereafter.

The aim of these calculations was to investigate the effect of an open gap with gas inflow and the influence of melt depth on the fluid flow and temperature field of the system just before the seeding process. Accordingly, the melt depth has been changed $d^1_{melt} = 26\ mm$ (deep melt) and $d^2_{melt} = 13\ mm$ (shallow melt), and then temperature and velocity field have been calculated.

Induction heating

Fig. 4-b-2 shows the volumetric distribution of heat generation in the crucible and afterheater. The maximum of heat generation is $q^1_{max} = 43\ W/cm^3$ and $q^2_{max} = 40\ W/cm^3$, and the total energy production is $Q^1_{total} = 650\ W$ and $Q^2_{total} = 620\ W$ for the melt depth of $d^1_{melt} = 26\ mm$ and $d^2_{melt} = 13\ mm$, respectively. Although in the second case of shallow melt $d^2_{melt} = (1/2)\ d^1_{melt}$ and the amount of heat entering the melt from the crucible walls is decreased, but the difference in the total heat generation is not high, i.e. $\triangle Q_{total} = 30\ W \simeq 0.05\ Q^1_{total}$. The reason is a strong gas flow that transfers the heat from the crucible wall to the afterheater and then outside via the afterheater hole.

Temperature and velocity field

Fig. 4-b-3 shows the fluid flow in the melt and gas (left hand side), and isotherms in the whole system (right hand side) for two different melt depths (a) $d^1_{melt} = 26\ mm$ and (b) $d^2_{melt} = 13\ mm$. In the melt, a clockwise vortex caused by free convection (buoyancy driven) and thermal Marangoni convection (surface tension driven) exists and occupies

Description (units)	Symbel	Value
Crucible inner radius (mm)	r_c	19
Crucible thickness (mm)	l_c	2
Crucible inner height (mm)	h_c	38
Afterheater inner height (mm)	h_{af}	58
Afterheater hole (mm)	r_{af}	8
Distance between crucible and afterheater (mm)	D_{ca}	10
Coil inner radius (mm)	r_{co}	52
Coil thickness (mm)	l_{co}	10
Height of coil turns (mm)	h_{co}	10
Distance between coil turns (mm)	d_{co}	2
Distance between the two coils (mm)	D_{co}	35
Thickness of crucible insulation at the bottom (mm)	h_{ci}	35
Thickness of crucible insulation at the wall (mm)	d_{ci}	10
Thickness of afterheater insulation (mm)	d_{ai}	10
Melt depth (mm)	d_{melt}	26, 13
Ambient temperature (^oC)	T_a	25

Table 4-3. Operating parameters used for calculations of *case b*.

the entire volume. In the case of deep melt $d^1_{melt} = 26\ mm$, the maximum value of the velocity in the melt is $\mathrm{v}^1_{max(melt)} = 0.25\ cm/s$ at the melt-gas interface and axis of symmetry too. For the case of shallow melt (i.e. $d^2_{melt} = 13\ mm$), the maximum value of the velocity is $\mathrm{v}^2_{max(melt)} = 0.18\ cm/s$ at the melt-gas interface.

In the gas, the flow enters the system from G (maximum velocity value $\mathrm{v}_G = 4.5\ cm/s$) and goes out via AH. The velocity is increased gradually from G to AH and is high in the afterheater. The maximum value of the gas velocity is $\mathrm{v}^{gas}_{max} = 18\ cm/s$ at AH in both cases. There is also an eddy of gas convection in the crucible above the melt, in which gas flows upwards along the crucible wall and downwards along the axis of symmetry. This gas flow is stronger in the case of shallow melt, because of a long distance between melt surface and gap.

For the temperature field, the maximum of temperature is $T_{max} = 2100\ ^oC$ at the crucible side wall and the minimum $T_{min} = 1190\ ^oC$ at G for both cases (i.e. $\triangle T^{melt}_{max} =$

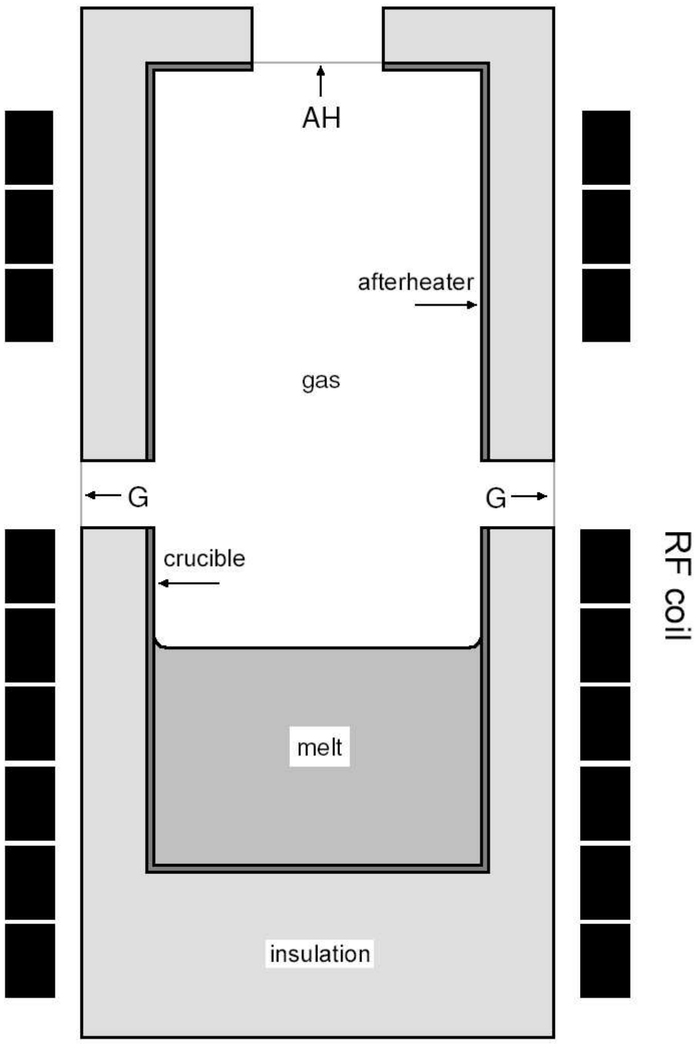

Fig. 4-b-1. A sketch of the configuration with an open gap between crucible and afterheater containing the melt.

40 ^oC and $\triangle T_{max}^{system} = 910\ ^oC$). In the case $d_{melt}^1 = 26\ mm$ the location of T_{max} is below the melt surface ($\sim 6\ mm$) but in the second case (i.e. $d_{melt}^2 = 13\ mm$), it is located close to the melt free surface (i.e. at the crucible meniscus). Although the displacement of the melt level is $\triangle H_{melt} = 13\ mm$ but the movement of T_{max} location is not the same and is $\triangle H_{Tmax} \simeq 7\ mm$. For this reason the thermal flow in the second case is more intense close to the melt surface and crucible wall, i.e. the position of the streamfunction center has been shifted towards the crucible meniscus, Fig. 4-b-4.

The shape of isotherms are deflected towards the centerline in the gap, upwards in the afterheater and downwards in the gas domain of the crucible, proportional to the gas flow structure in these parts of the system. The temperature profiles along the axis of symmetry from crucible bottom to the afterheater hole ($r = 0$) for both cases, are

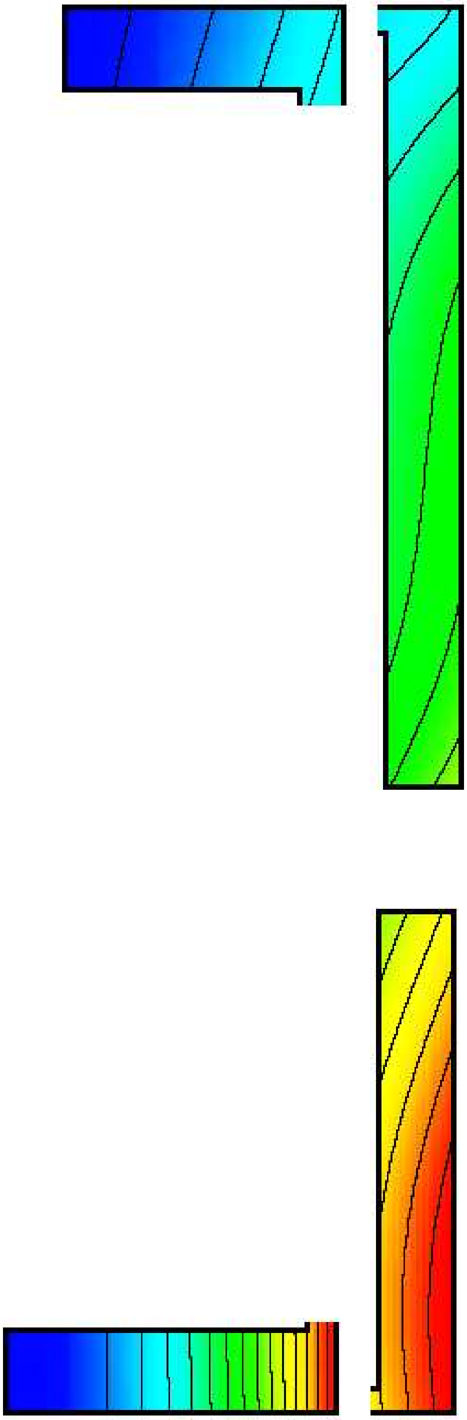

Fig. 4-b-2. Volumetric power distribution (q) in the crucible and afterheater.

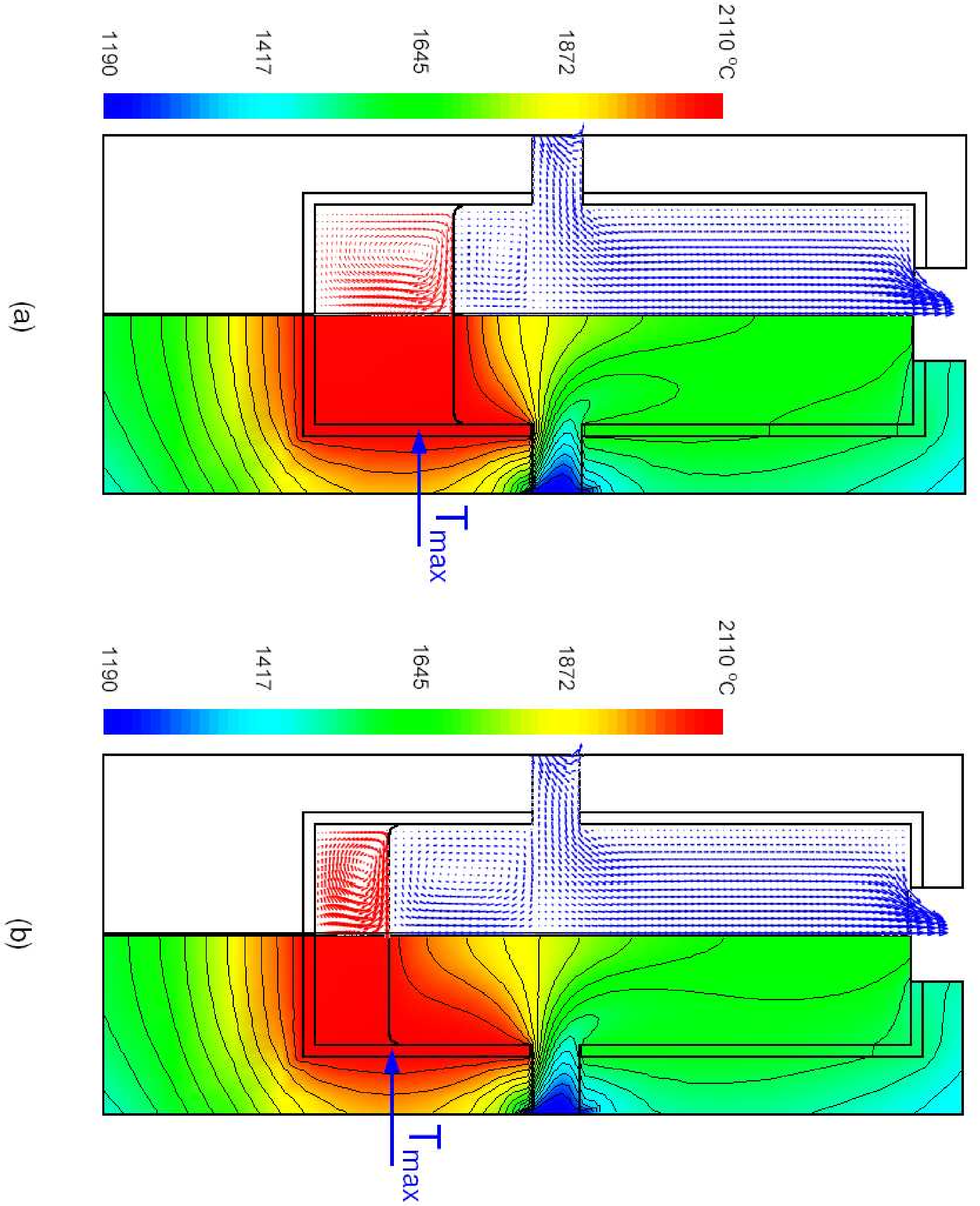

Fig. 4-b-3. Temperature distribution (right hand side) and fluid flow (left hand side) for different melt depth, (a) deep melt $d^1_{melt} = 26\ mm$ and (b) shallow melt $d^2_{melt} = 13\ mm$.

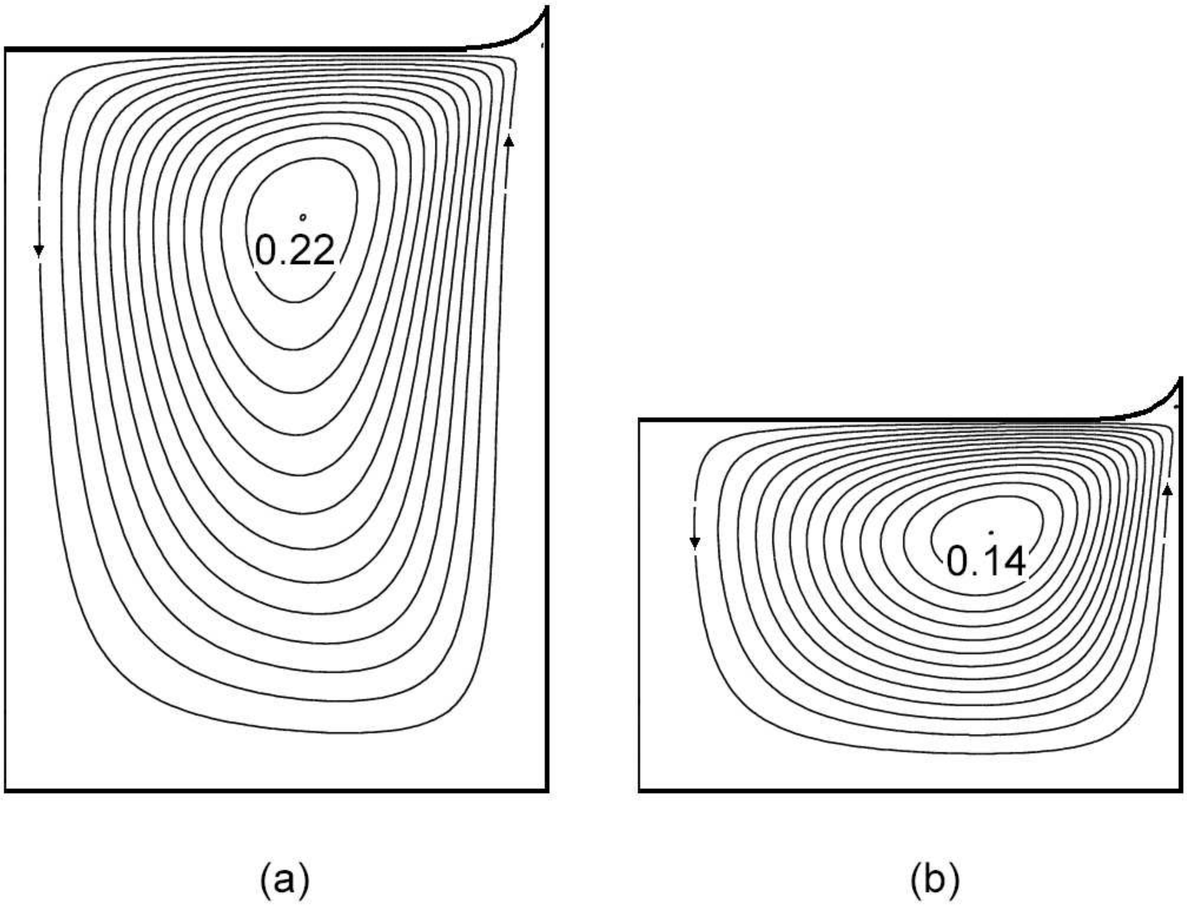

Fig. 4-b-4. Distribution of the streamfunction in the melt, (a) deep melt $d^1_{melt} = 26\ mm$ and (b) shallow melt $d^2_{melt} = 13\ mm$. In the shallow melt the location of the streamfunction center has been shifted towards the crucible meniscus.

shown in Fig. 4-b-5. These profiles demonstrate that the temperature gradient above the melt surface is high and non-linear in the case of $d^1_{melt} = 26\ mm$, but it is about linear in the case of $d^2_{melt} = 13\ mm$. As has already been mentioned,in the case of shallow melt the gas flow in the eddy above the melt is stronger than the case of deep melt and as result the temperature variation in the gas part of the deep melt is more smooth than the shallow melt. The tempearture at the crucible and afterheater side wall is approximately constant but the difference between their magnitude is really high ($\triangle T_{C\&A} \approx 480\ ^oC$), Fig. 4-b-6.

Using an open gap leads to cool the grown crystal effectively. This kind of cooling is suitable for the crystals that the surface evaporation occurs during their CZ growth. In the case of deep melt ($d^1_{melt} = 26\ mm$), a high thermal stress can be produced in the

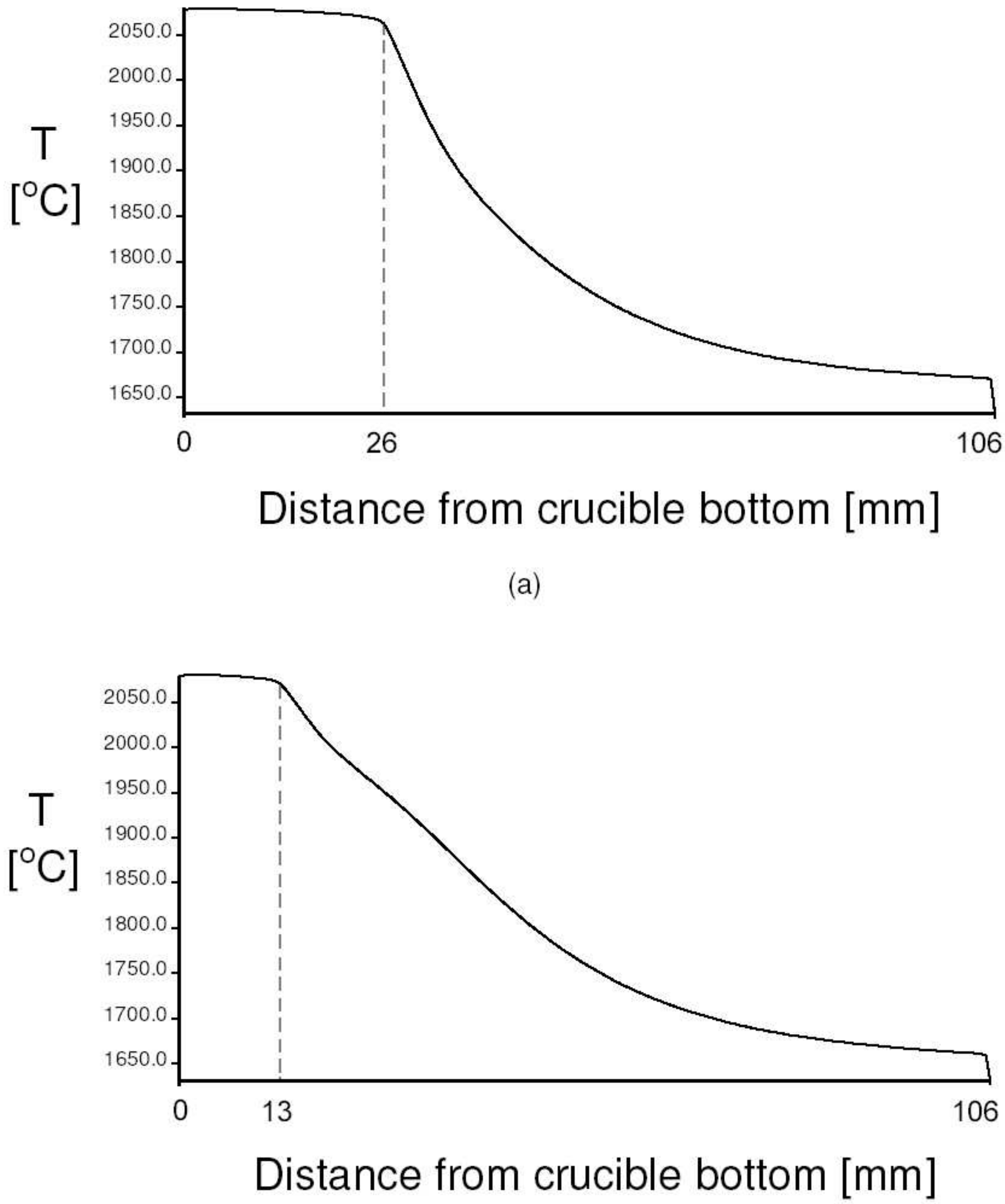

(a)

(b)

Fig. 4-b-5. Vertical temperature profiles along the axis of symmetry, (a) deep melt $d^1_{melt} = 26\ mm$ and (b) shallow melt $d^2_{melt} = 13\ mm$. A high thermal stress can be produced in (a) but it could be controlled in (b).

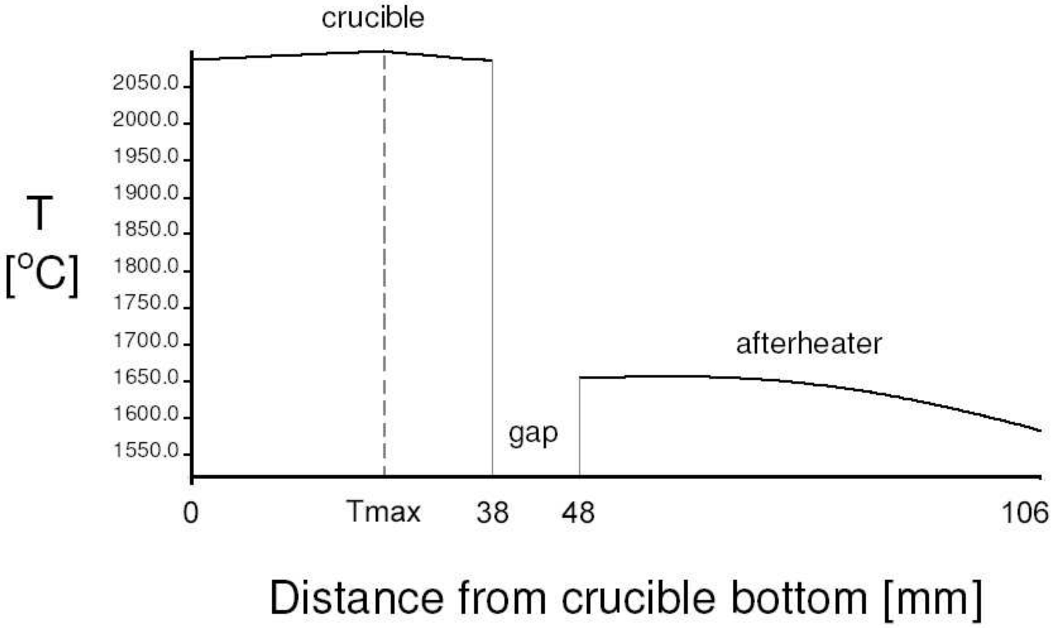

(a)

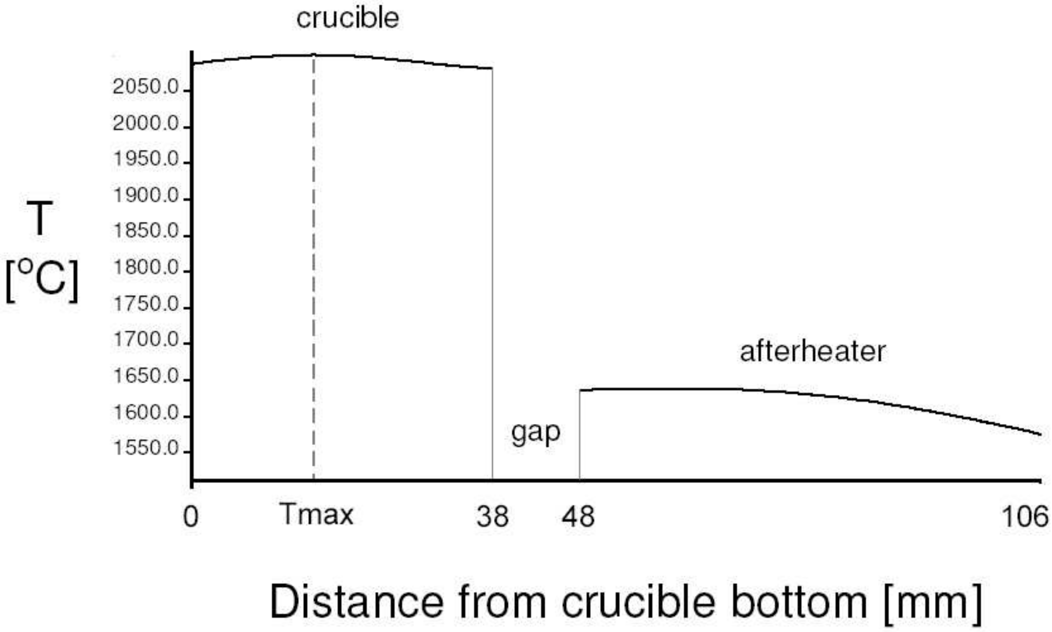

(b)

Fig. 4-a-6. Vertical temperature profiles along the crucible and afterheater side wall, (a) deep melt $d^1_{melt} = 26\ mm$ and (b) shallow melt $d^2_{melt} = 13\ mm$.

grown crystal since the secend derivation of temperature along the symmetry axis (i.e. $\partial^2 T/\partial z^2$) is not zero [6,8,10,28]. Accordingly, the thermal stress could be an important problem for the crystal. But in the shallow melt, $\partial^2 T/\partial z^2 \simeq 0$ and so the thermal stress could be controlled in the grown crystal such as $(La, Sr)(Al, Ta)O_3$.

Description (units)	Symbel	Value
Crucible inner radius (mm)	r_c	20
Crucible thickness (mm)	l_c	2
Crucible inner height (mm)	h_c	40
Crucible bottom radius (mm)	r_{cb}	0, 10
Afterheater inner height (mm)	h_{af}	70
Afterheater hole (mm)	r_{af}	9
Distance between crucible and afterheater (mm)	D_{ca}	0
Coil inner radius (mm)	r_{co}	60
Coil thickness (mm)	l_{co}	8
Height of coil turns (mm)	h_{co}	11
Distance between coil turns (mm)	d_{co}	2
Distance between the two coils (mm)	D_{co}	30
Thickness of crucible insulation at the bottom (mm)	h_{ci}	35
Thickness of crucible insulation at the wall (mm)	d_{ci}	10
Thickness of afterheater insulation (mm)	d_{ai}	10
Melt depth (mm)	d_{melt}	35
Ambient temperature (^oC)	T_a	25

Table 4-4. Operating parameters used for calculations of *case c*.

4.4.3 case c: crucible and afterheater, flat and rounded crucible bottom

Fig. 4-c-1 shows a sketch of these two systems and the operating parameters are listed in Table 4-4. The non-dimensional numbers are $Gr = 1.5 \times 10^4$, $Ma = 2340$, $Rad_l = 1.17$, $Rad_i = 1.27$ and $Bio_i = 0.09$. The temperature at the afterheater top cover hole is set to be 1600 ^oC, and the contact angle and deflection height is the same as *case b* for both configurations.

The aim of these calculations was to investigate the effect of a flat and a rounded crucible bottom on the fluid flow and temperature field of the system just before the seeding process. Accordingly, we have considered two different types of the crucible bottom: flat and rounded shape.

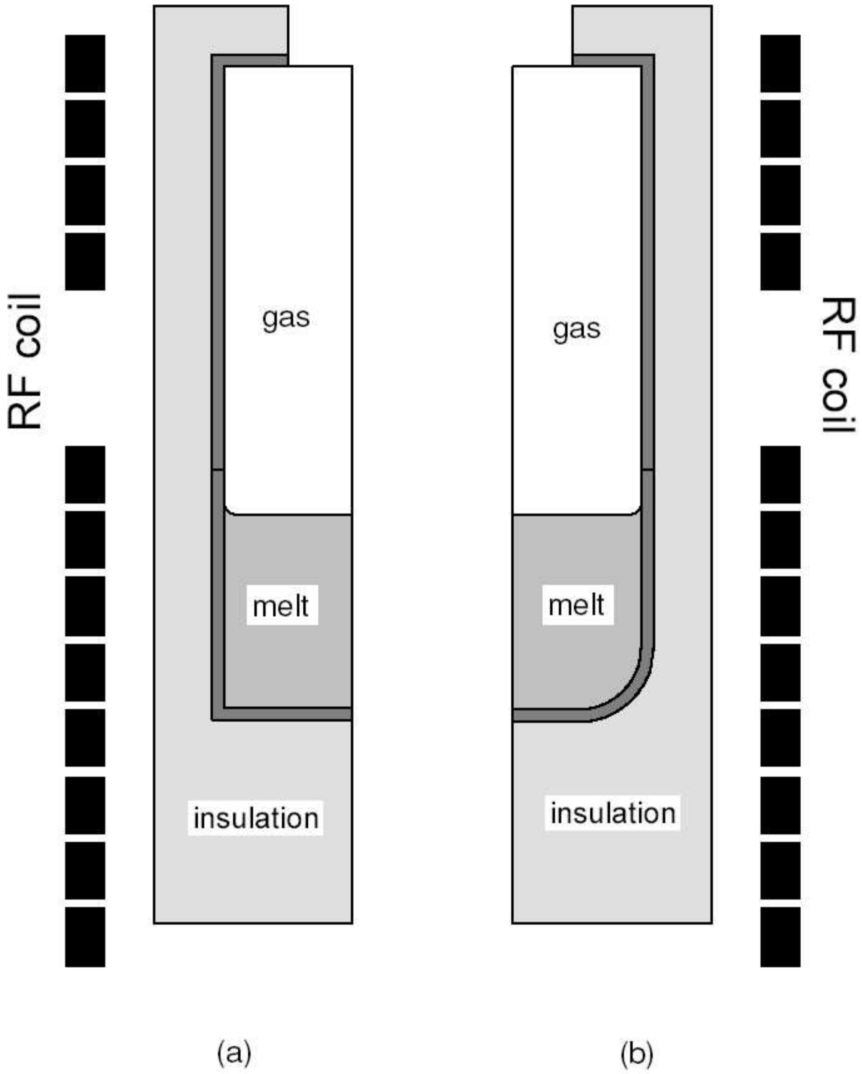

Fig. 4-c-1. A sketch of the configurations with different crucible bottom shape, (a)flat, and (b) rounded crucible bottom $r_{cb} = 10\ mm$.

Induction heating

Fig. 4-c-2 shows the volumetric distribution of heat generation in the crucible and afterheater for both configurations. The maximum of heat generation for both is $q_{max} \simeq 35\ W/cm^3$ at the crucible bottom corner where in the configuration with the rounded crucible bottom is $1\ cm \simeq r_{cb}$ distance above than the configuration with the flat crucible bottom. The total energy production is $Q^{flat}_{total} = 770\ W$ for the configuration of flat crucible bottom and $Q^{round}_{total} = 660\ W$ for the rounded bottom configuration.

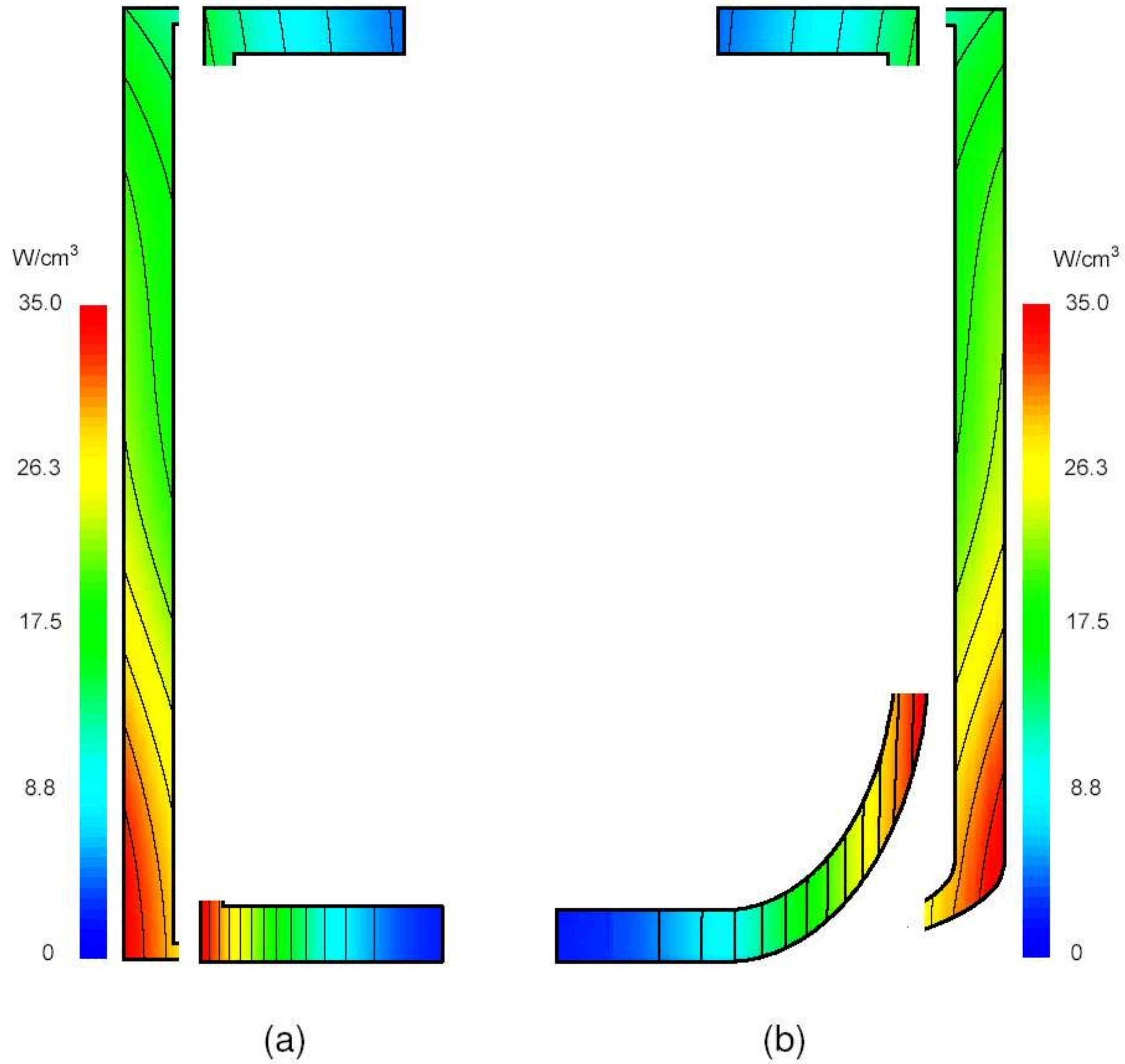

Fig. 4-c-2. Volumetric energy distribution (q) in the crucible and afterheater for configuration with the, (a)flat, and (b) rounded crucible bottom. In both configurations q_{max} is located at the bottom corner where in (b) is 1 $cm \simeq r_{cb}$ distance above than (a).

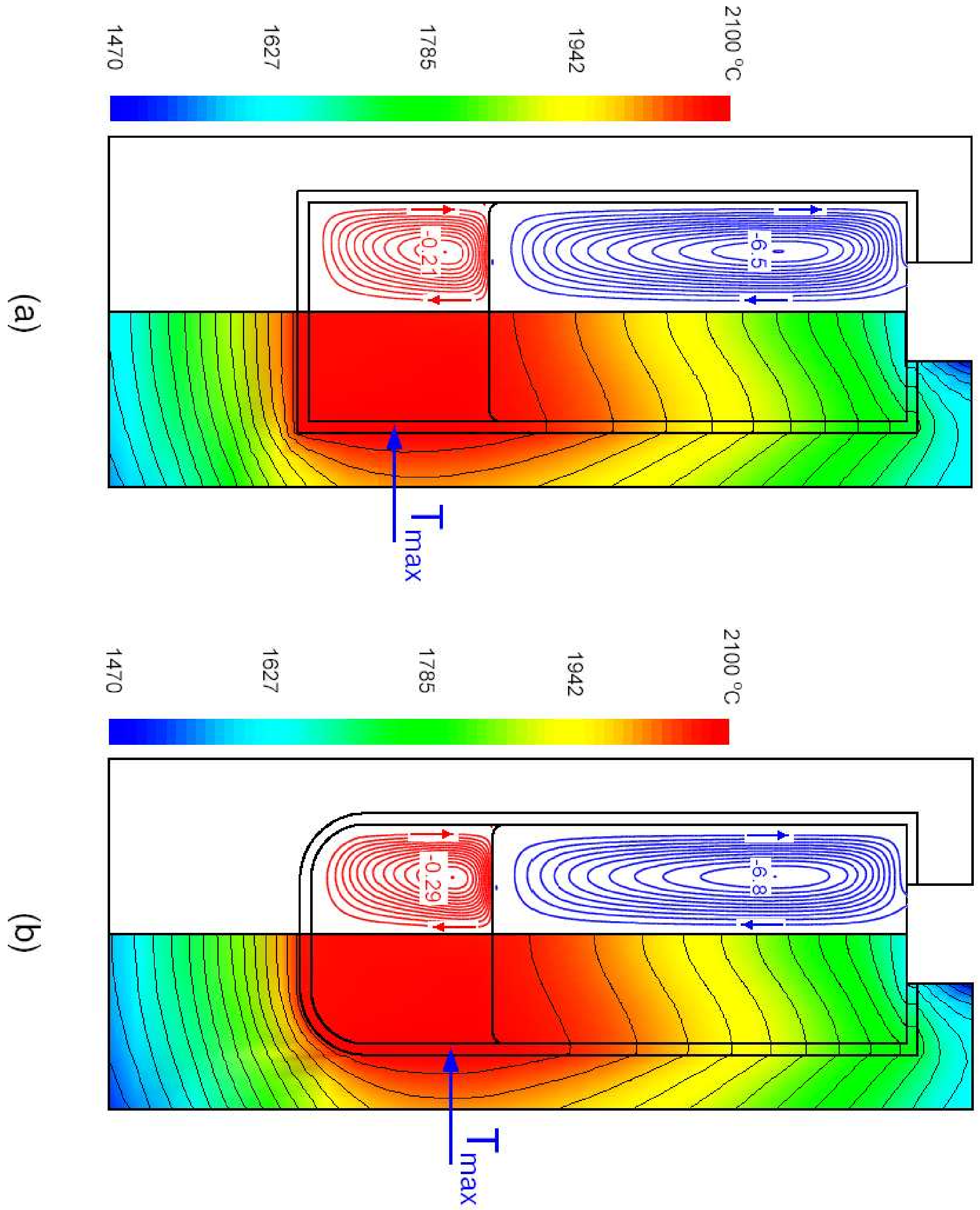

Fig. 4-c-3. Isotherms (right hand side) and streamlines (left hand side) for configuration with the (a) flat, and (b) rounded crucible bottom. Using the rounded crucible bottom lifts upwards the location of T_{max} and increases the thermal flow.

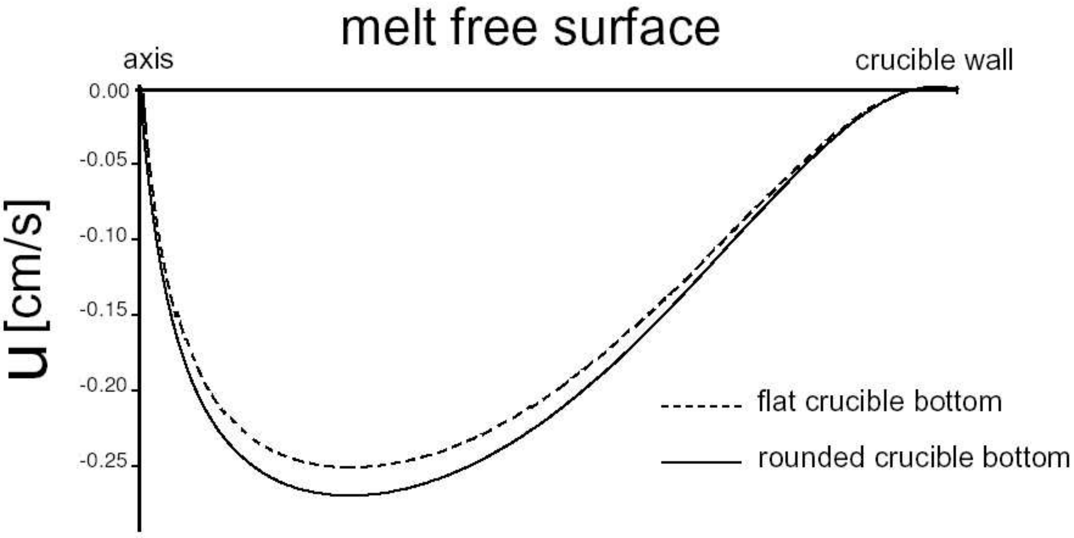

Fig. 4-c-4. Radial velocity profile at the melt surface for both configurations with the flat and rounded crucible bottom. The magnitude of $\mathrm{v}_{max}^{melt\ surface}$ in the configuration with the rounded crucible bottom is higher (0.27 cm/s) than in the case with flat bottom (0.24 cm/s).

Temperature and fluid flow

Fig. 4-c-3 represents the streamline pattern and isotherm distribution for both configurations of flat and rounded crucible bottom. In both configurations, there is a vortex in the melt which comes from buoyancy in the bulk and the Marangoni effect at the melt-gas interface with $\psi_{max(melt)}^{flat} = 0.21$ and $\psi_{max(melt)}^{round} = 0.29$. In the gas, there is a main and big vortex that goes upwards along the afterheater side wall and downwards along the symmetry axis with $\psi_{max(gas)}^{flat} = 6.5$ and $\psi_{max(gas)}^{round} = 6.8$. There is also a tiny and weak gas eddy just above the melt surface in the opposite rotation of the first one that arises from the continuous velocity at the melt-gas interface with $\psi_{second}^{gas} = -0.02$. The maximum value of velocity for the melt is $\mathrm{v}_{max(melt)}^{flat} = 0.27\ cm/s$ and $\mathrm{v}_{max(melt)}^{round} = 0.28\ cm/s$, and for the gas $\mathrm{v}_{max(gas)}^{flat} = 7.0\ cm/s$ and $\mathrm{v}_{max(gas)}^{round} = 7.5\ cm/s$, downwards and at the axis of symmetry.

The temperature maximum for both configurations is $T_{max} \simeq 2100\ {}^oC$ and the minimum is $T_{min} = 1470\ {}^oC$. While the location of T_{min} for both configurations is at the afterheater top cover insulation but the position of the T_{max} is different. In the configuration with a flat crucible bottom T_{max} is located at the middle of the crucible wall but in the configuration with a rounded crucible bottom is placed $\sim 1\ cm$ distance above the first configuration as is shown in Fig. 4-c-3. This lifting of T_{max} location increases the melt velocity (also gas velocity) and as a result thermal convection of the molten material becomes stronger, i.e. $\psi^{round}_{max(melt)} > \psi^{flat}_{max(melt)}$. Fig. 4-c-4 represents the velocity profile at the melt surface. It indicates that the magnitude of $\mathrm{v}^{melt\ surface}_{max}$ in the configuration with a rounded crucible bottom is higher ($\sim 0.03\ cm/s$) than configuration with a flat bottom shape.

Two reasons are responsible for the lifted upwards location of the T_{max}, heat generation and melt flow in the system. As has already been mentioned, the location of the q_{max} in both configuration is at the crucible bottom corner. In the configuration with a rounded crucible bottom, the location of the crucible bottom edge is 1 cm distance above than other configuration. On the other site, in the configuration with a rounded crucible bottom the streamlines in the melt and close to the bottom are displaced to a round shape proportional to the rounded bottom shape. But in the configuration with a flat bottom shape, they have been pushed towards the bottom corner. This difference between the melt streamline distribution close to the crucible wall and the bottom corner indicates that the melt velocity close to the crucible wall is higher in the configuration with a rounded crucible bottom.

As has already been explained, the difference between melt motion pattern in the vicinity of crucible bottom and side wall as well as the location of q_{max} lead to a relatively stronger thermal convection in the configuration with a rounded crucible bottom. This is a good advantage of using a crucible with rounded bottom shape. It is well known that during CZ growth of some oxide crystals such as $GdScO3$, $DyScO3$, $YVO4$ and $GdVO4$, the grown crystal tends to have a spiral shape (*spiral growth*)[7,18,20,41,58]. It seems that some instabilities and thermal interactions in the melt around the solidification front are responsible for the spiral growth. Using a rounded crucible bottom which results a relatively strong thermal convection leads to a reduction in these instabilities and thermal interactions. Consequently, the growth without spiral mode is increased and the spiral mode growth is delayed and so the corkscrew only appears at the crystal end. This yields the useful part of the grown crystal. Although the spiral growth phenomenon has not been fully understood yet, but using a rounded crucible bottom is a useful tool to inhibit the spiral growth.

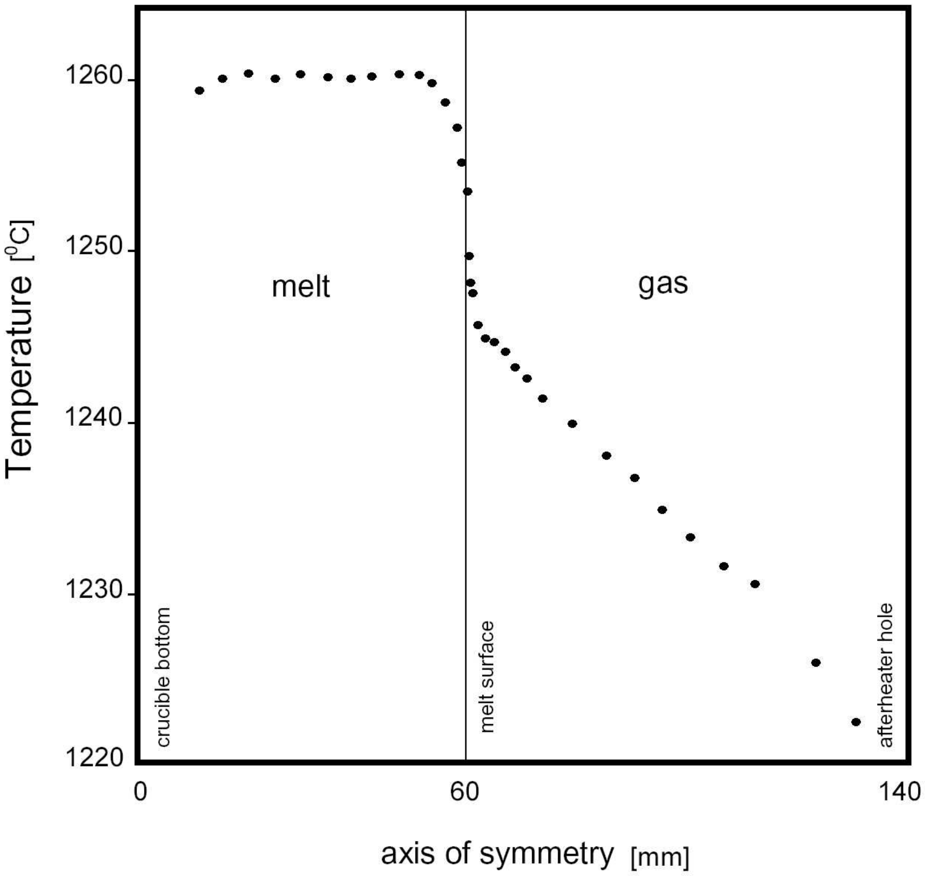

Fig. 4-d-1. Vertical temperature profile along the axis of symmetry measured in the lab for an oxide CZ furnace. The system contains Lithium niobate ($LiNbO_3$) melt and gas. Temperature variation is quite high close to the melt-gas interface.

4.5 Conclusions

In this chapter, an axisymmetric two-dimensional quasi-steady state modeling of the heat transport mechanism in some real Czochralski systems containing melt and gas have been performed. The aim of these calculations was to investigate and reveal the effect of several parameters such as the geometry and location of an active afterheater with respect to the crucible, arrangement and design of the thermal insulation, and crucible bottom shape on the flow and temperature field of the system.
From these calculations we can conclude:

1) Temperature variation along the axis of symmetry close to the melt-gas interface is markedly high and about linear, as has been shown by our results and measurements as well, Fig. 4-d-1 [33,38]. There are three reasons for it: (1) the melt is the hottest

part of the system since most of the heat generation occurs in the crucible wall while the gas domain is essentially a cold part which transfers the heat from the melt surface as well as afterheater wall outside, (2) the total heat capacity of the melt is much larger than that of the gas because of a large difference between mass and density ($\rho_{melt}/\rho_{gas} \sim 10^4$), (3) the melt motion is relatively slow ($v_{max}^{melt} \sim 10^{-1}\ cm/s$) contrary to the gas ($v_{max}^{gas} \sim 10^1\ cm/s$). This is not surprising because of the high density and high viscosity of the molten material and vise versa for the gas ($\nu^{melt}/\nu^{gas} \sim 10^{-2}$). In addition, both fluids (melt and gas) are approximately at rest close to the stagnation point (where the seed will be located) because of the rapid change in the motion direction (radial to axial or vise versa). So the conduction is more effective than convection in this area and as a result a linear change appears in the corresponding temperature profile.

2) The melt and gas flow caused by thermal gradients are essential in Czochralski crystal growth systems and are also one of the most important and difficult types of fluid flow to analyze, since they are strongly coupled with the temperature distribution [6,17].

3) Before seeding, the flow pattern in the system consist of a single circulation of slow moving fluid in the melt domain, and a fast fluid motion in the gaseous phase.

4) The temperature and fluid flow structure in the gas is strongly affected by the active afterheater and its position. The results indicate that a gap between crucible and afterheater significantly modifies the overall heat transfer through the gas phase and small changes in the melt are also observed.

5) Different location and orientation of an active afterheater and its insulation modifies the temperature gradient along the axis of symmetry in the gas domain. Accordingly, some crystal problems such as dislocation, defect, thermal stress and crack can be controlled in the grown crystal by using a suitable configuration of afterheater and insulation [6,33].

6) Using a lifted upwards afterheater results in increasing the heat dissipation from the melt surface. Therefore, the T_{max} position is shifted downwards and the thermal field of the melt is modified.

7) Using a closed gap between crucible and afterheater leads to a low temperature gradient along the symmetry axis in the gas part which can be useful to prevent dislocation, defect and thermal stress in the grown crystal.

8) A gas flow which enters the system through an open gap between crucible and afterheater markedly cools the grown crystal, but it could produce high thermal stress in the crystal.

9) Decreasing the level of the melt yields several interesting effects on the results such as:

- The temperature conditions and the structure of fluid flow in the system are modified. The location of T_{max} at the crucible side wall is shifted downwards while in the melt the position of T_{max}^{melt} is lifted upwards (compared to the melt level).
- The thermal convection becomes more intense close to the melt surface and crucible wall too. This produces a more stable thermal convection in the melt as well as increases the temperature gradient along the melt surface.
- The temperature gradient along the axis of symmetry in the gas part decreases and becomes linear. As a result the thermal stress can be better controlled in the grown crystal.

10) Using a crucible with a rounded bottom generates several special advantages such as:

- The location of T_{max} at the crucible side wall rises and as a result the tempearture gradient along the melt surface is increased.
- The melt streamlines close to the crucible bottom are parallel and have a curved shape similar to the rounded bottom shape.

These important features lead to increasing thermal convection and influences velocity field in the melt and gas domain.

Chapter 5

Configuration contains seed, melt and gas

5.1 Introduction

In this chapter, the temperature distribution and flow field are computed for some Czochralski systems containing *seed*, *melt* and *gas*, by application of the internal heat generation in the crucible and afterheater.

The aim of the work in this chapter is to develop a global analysis of an inductively heated CZ furnace for real oxide crystal growth systems during the seeding process, and to reveal the effect of an active afterheater and a crucible with different bottom shapes (flat and round) on the heat transport mechanism of the seed, melt and gas. In chapter 3 our attention was paid to the effect of thermal insulation, a gap between crucible and afterheater and different shapes of the crucible bottom on the melt and gas flow and temperature field of some CZ systems without any seed corresponding to the situation just before the seed touches the melt. But in the analysis presented here, the seed crystal is taken into account corresponding to the situations during seeding at the initial stages of the growth process.

One of the major benefits of this modeling is the ability to assign system responses to specific changes in growth parameters, thus yielding fundamental understanding of the interactions of heat transfer and interfacial phenomena. This information provides valuable insight into the effectiveness of design parameters and to the suitability of proposed strategies for process control.

We focus on different steps of the seeding process for CZ growth of oxide crystals. We do this by studying the response of a complete hydrodynamic and thermal model for oxide Czochralski growth systems with different configuration and orientation of crucible, afterheater and RF coil. A predictive model which accurately assessed the heat transfer in the system could be used to develop strategies for the control of seed-melt interface and other features of seeding and the growth procedure such as the stability of the process. The quasi-steady state model discussed in this chapter is well-suited for this task.

For a number of reasons, it is not sufficient to restrict our attention to the quasi-stationary state at the growing steps of the process, but it is also important to monitor and control the temperature field evolution during the seeding process itself. For example, thermal stresses can occur in the growing crystal due to temperature gradients in this step.

5.2 Mathematical model

The mathematical model described in the chapter 3, is valid here too. We only present the equations for the seed crystal here. As the seed is a dielectric solid part the equations of fluid flow (3.15), continuity (3.19) and stream function (3.33) are exactly the same. In addition to the BCs in chapter 3, there are some further BCs for the calculations.
a) at the seed surface:

$$v = r_s \omega_s \tag{5.1}$$

$$u = w = 0 \tag{5.2}$$

where ω_s is the seed rotation rate and r_s is the seed radius.
b) at the seed-melt interface:

$$v = r \omega_s \tag{5.3}$$

$$u = w = 0 \tag{5.4}$$

The non-dimensional form of the BC (5.3) is:

$$V = R \; Re \tag{5.5}$$

where $Re = \omega_s r_c^2 / \nu_l$ is the Reynolds number.

For the energy equation and conduction in the seed part,

$$\nabla^2 T_s = 0 \tag{5.6}$$

and also the BC at the seed-melt interface, i.e. the balance of heat fluxes between the melt and seed,

$$k_l \frac{\partial T_l}{\partial z} - k_s \frac{\partial T_s}{\partial z} = -\rho_s H_f V_g \tag{5.7}$$

should be added. In these equations, the subscripts l and s denote the melt and seed, respectively and T is temperature, k is conductivity, ρ is density, H_f is the latent heat of fusion and V_g is the growth rate. So the non-dimensional form for the weak form of the energy equations is:

$$\begin{aligned}
& \frac{k_{cl}}{Pr} \underset{crucible}{\iint} \left[\frac{\partial \Theta_c}{\partial R} \frac{\partial \Phi_{ce}}{\partial R} + \frac{\partial \Theta_c}{\partial Z} \frac{\partial \Phi_{ce}}{\partial Z} - \left(\frac{L_c^2}{T_c k_c} \right) q \Phi_{ce} \right] R \,\mathrm{d}R \,\mathrm{d}Z \\
+ \;& \frac{k_{il}}{Pr} \underset{insulation}{\iint} \left(\frac{\partial \Theta_i}{\partial R} \frac{\partial \Phi_{ie}}{\partial R} + \frac{\partial \Theta_i}{\partial Z} \frac{\partial \Phi_{ie}}{\partial Z} \right) R \,\mathrm{d}R \,\mathrm{d}Z \\
+ \;& \frac{k_{sl}}{Pr} \underset{seed}{\iint} \left(\frac{\partial \Theta_s}{\partial R} \frac{\partial \Phi_{se}}{\partial R} + \frac{\partial \Theta_s}{\partial Z} \frac{\partial \Phi_{se}}{\partial Z} \right) R \,\mathrm{d}R \,\mathrm{d}Z \\
+ \;& \frac{1}{Pr} \underset{melt}{\iint} \left(\frac{\partial \Theta_l}{\partial R} \frac{\partial \Phi_{le}}{\partial R} + \frac{\partial \Theta_l}{\partial Z} \frac{\partial \Phi_{le}}{\partial Z} \right) R \,\mathrm{d}R \,\mathrm{d}Z \\
+ \;& \underset{melt}{\iint} \left(U_l \frac{\partial \Theta_l}{\partial R} + W_l \frac{\partial \Theta_l}{\partial Z} \right) \Phi_{le} \; R \,\mathrm{d}R \,\mathrm{d}Z \qquad\qquad (5.8) \\
+ \;& \frac{k_{gl}}{Pr} \underset{gas}{\iint} \left(\frac{\partial \Theta_g}{\partial R} \frac{\partial \Phi_{ge}}{\partial R} + \frac{\partial \Theta_g}{\partial Z} \frac{\partial \Phi_{ge}}{\partial Z} \right) R \,\mathrm{d}R \,\mathrm{d}Z \\
+ \;& \frac{k_{gl}}{\alpha_{gl}} \underset{gas}{\iint} \left(U_g \frac{\partial \Theta_g}{\partial R} + W_g \frac{\partial \Theta_g}{\partial Z} \right) \Phi_{ge} \; R \,\mathrm{d}R \,\mathrm{d}Z \\
= \;& \frac{k_{il}}{Pr} \underset{\substack{outer\ surfaces \\ of\ insulation}}{\int} \frac{\partial \Theta_i}{\partial \hat{N}} \Phi_{ie} \; R \,\mathrm{d}R + \frac{1}{Pr} \underset{melt\ surface}{\int} \frac{\partial \Theta_l}{\partial Z} \Phi_{le} \; R \,\mathrm{d}R \\
+ \;& \frac{1}{Pr} \left(\underset{\substack{crystal\text{-}melt \\ interface}}{\int} \frac{\partial \Theta_l}{\partial \hat{N}} \Phi_{le} \; R\mathrm{d}R - k_{sl} \underset{\substack{crystal\text{-}melt \\ interface}}{\int} \frac{\partial \Theta_s}{\partial \hat{N}} \Phi_{se} \; R\mathrm{d}R \right)
\end{aligned}$$

where $k_{sl} = k_s/k_l$. The non-dimensional form of the BC (4.7) is as follow

$$\frac{\partial \Theta_l}{\partial Z} - k_{sl}\frac{\partial \Theta_s}{\partial Z} = -\rho_{sl}\ Pe\ S \tag{5.9}$$

where $\rho_{sl} = \rho_s/\rho_l$, $Pe = V_g L_c/\alpha_l$ is the Peclet number and $S = H_f/(c_{pl}T_c)$ is the Stefan number.

5.2.1 The calculation conditions

Values of physical properties of the melt and gas employed for our calculations have been presented in Table 4-1 (chapter 4) and for the seed crystal are shown in Table 5-1. Also the other conditions are the same as the chapter 4. The seed crystal geometry is assumed to be a straight cylinder with a flat top. But the seed bottom, i.e. the seed-melt interface can change depending on the heat transfer mode of the system. In other words, one approach in this chapter is finding the seed melt interface shape by using the moving boundary method. The melt-crystal interface shape is obtained by its iterative modification until it approaches the isotherm of the melting point. For this purpose, $\triangle H_{seed}$ denotes the deflection of the seed-melt interface measured from centerline to seed periphery. Positive values of $\triangle H_{seed}$ denote interfaces which are convex towards the melt. For simplicity we assume that the seed holder has been made of the seed crystal, i.e. there is no difference between the seed and the seed holder in our calculations.

Description (units)	Symbel	Value
Density (kg/m^3)	ρ_s	3955
Thermal conductivity ($W/m \cdot k$)	k_s	17.5
Latent heat (kJ/kg)	H_f	1100

Table 5-1. Physical properties of the seed crystal used for calculations; the subscript s denotes the seed crystal (*sapphire*).

Description (units)	Symbel	Value
Crucible inner radius (mm)	r_c	49
Crucible thickness (mm)	l_c	2
Crucible inner height (mm)	h_c	98
Afterheater inner height (mm)	h_{af}	100
Afterheater hole (mm)	r_{af}	10
Distance between crucible and afterheater (mm)	D_{ca}	0, 30
Coil inner radius (mm)	r_{co}	85
Coil thickness (mm)	l_{co}	13
Height of coil turns (mm)	h_{co}	27
Distance between coil turns (mm)	d_{co}	5
Distance between the two coils (mm)	D_{co}	25
Thickness of crucible insulation at the bottom (mm)	h_{ci}	50
Thickness of crucible insulation at the wall (mm)	d_{ci}	24
Thickness of afterheater insulation (mm)	d_{ai}	6
Melt depth (mm)	d_{melt}	93
Seed radius (mm)	r_s	5
Ambient temperature (^oC)	T_a	25
Temperature at the seed top (^oC)	T_{ah}	1650, 1600

Table 5-2. Operating parameters used for calculations of *case a*.

5.3 Results and discussion

For the *cases a-c*, the operating parameters are listed in Table 5-2 and the non-dimensional numbers are the same as the *case a* in chapter 4, i.e. $Gr = 2.6 \times 10^5$, $Ma = 6167$, $Rad_l = 3$, $Rad_i = 3.25$ and $Bio_i = 0.23$. The temperature at the seed top, i.e. at the afterheater top cover hole is set to be 1650 ^oC and 1600 ^oC for the configuration without and with a gap between crucible and afterheater, respectively.

The contact angle and deflection height of the crucible and the seed meniscus is set to be 18^0 (Table 4-1) and 4 mm, respectively, taken from observation in the lab during the seeding process of sapphire growth.

5.3.1 case a: Before touch and without seed rotation ($\omega_{seed} = 0$)

Fig. 5-a-1 shows a sketch of these two systems. There is a gap of 5 mm between the seed and the melt corresponding to the situation just before touching the seed. In this case the temperature at the center of the melt free surface (where the seed crystal will be placed, $r = 0$) is 2070 ^oC, i.e. 20 ^oC above the melting point of sapphire (corresponding to the real condition of the seeding process) similar to the configurations without a seed crystal (chapter 4). This is not a boundary condition but it should be a result from the calculations by changing the heat generation of the system.

The aim of these calculations is to find out the influence of the seed crystal before touching the melt on the fluid flow and temperature field of the system during the seeding process.

Induction heating

The geometry and orientation of the coil-crucible-afterheater is the same as *case a* in chapter 3 and chapter 4. So we do not discuss about the spatial distribution of the induction heating again. In the present case including the non-touched seed, melt and gas, the maximum value of energy deposition is $q_{max} \simeq 50\ W/cm^3$ for both cases and the total energy production in the crucible and afterheater is $Q^{without}_{total} = 2.95\ kW$ and $Q^{with}_{total} = 2.87\ kW$ for the configuration without and with a gap, respectively.

Temperature and flow field

Fig. 5-a-2 shows the contours of the stream function in the melt and gas (left hand side), and isotherms in all parts (right hand side) for both configurations. In the bulk melt, a clockwise circular flow caused by free convection (buoyancy force) and thermocapillary Marangoni convection exists and is directed from the crucible wall to the axis of symmetry, and from the crucible bottom to the melt surface (the same as configuration in chapter 4 but now including the detached seed). This thermal flow transfers the heat from the crucible wall (the hottest part of the system) to the melt surface and central part (where the seed crystal will be located). There is a more intense convection close to the melt surface which is a result of interaction between buoyancy and Marangoni effects. Fig. 5-a-3 shows the velocity profile along the melt-gas interface from the centerline to the crucible wall with $\mathrm{v}^{without}_{max(melt\ surface)} \simeq 0.28\ cm/s$ and $\mathrm{v}^{with}_{max(melt\ surface)} \simeq 0.27\ cm/s$ for the configuration without and with a gap, respectively, at the position $\sim 1.5\ cm$ distance off the symmetry axis. It demonstrates that this flow velocity has a very high gradient in the vicinity of the symmetry axis ($r = 0$), where the direction of the melt motion changes from the horizontal to the vertical direction, Fig. 5-a-4. Of course, the

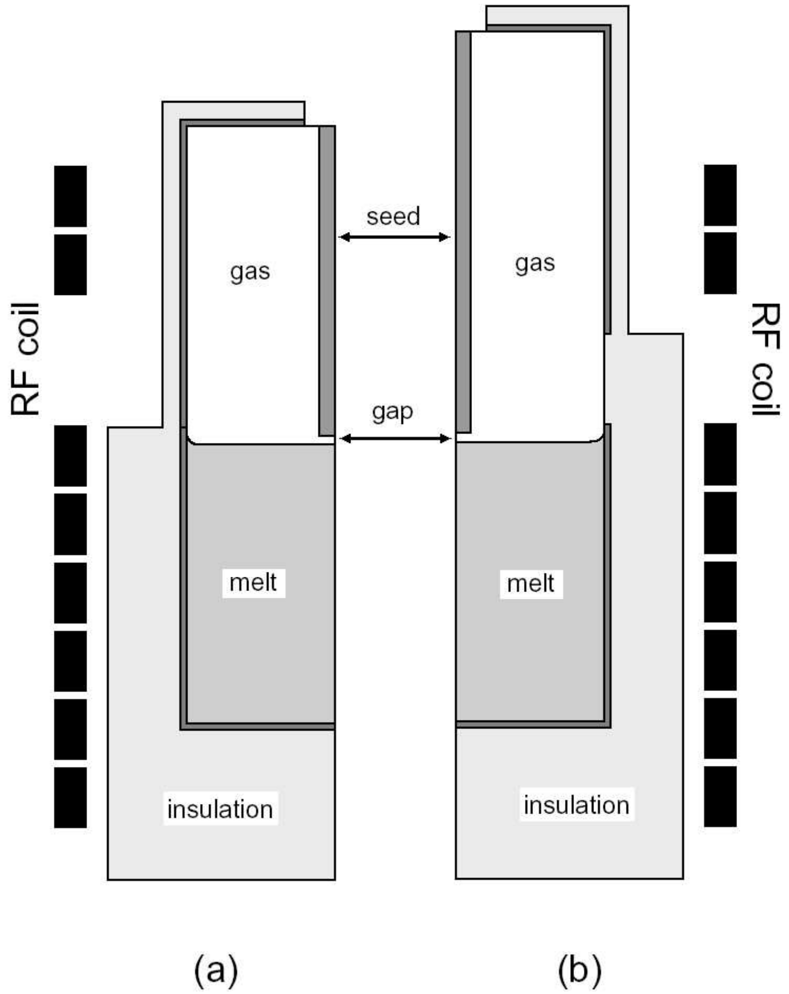

Fig. 5-a-1. Schematic diagram of two configurations of the Czochralski growth furnace containing the detached seed crystal, melt and gas, (a) without and (b) with a gap between crucible and afterheater. There is a gap of 5 mm between the seed crystal and the melt surface in both configurations.

presence of the thermal Marangoni effect at the malt-gas interface, which drags the melt towards the axis of symmetry, increases this velocity gradient. As has already been explained in chapter 1, in order to resolve and monitor this direction change of the molten material which is extremely high and important, a fine grid is required in that area. In the bulk melt, the maximum value of velocity is $\mathrm{v}_{max}^{melt} \simeq 0.71\ cm/s$, downwards, at the centerline and also markedly higher than elsewhere in the fluid part.

Although the results of the melt flow are approximately similar for both configurations, the gas flow pattern is considerably different. In the configuration without a gap, there are two separate gas vortices with opposite direction of rotation, a strong clockwise vortex and a weak counterclockwise one. The first is located above the melt surface and is extended to the afterheater hole while the second is placed close to the

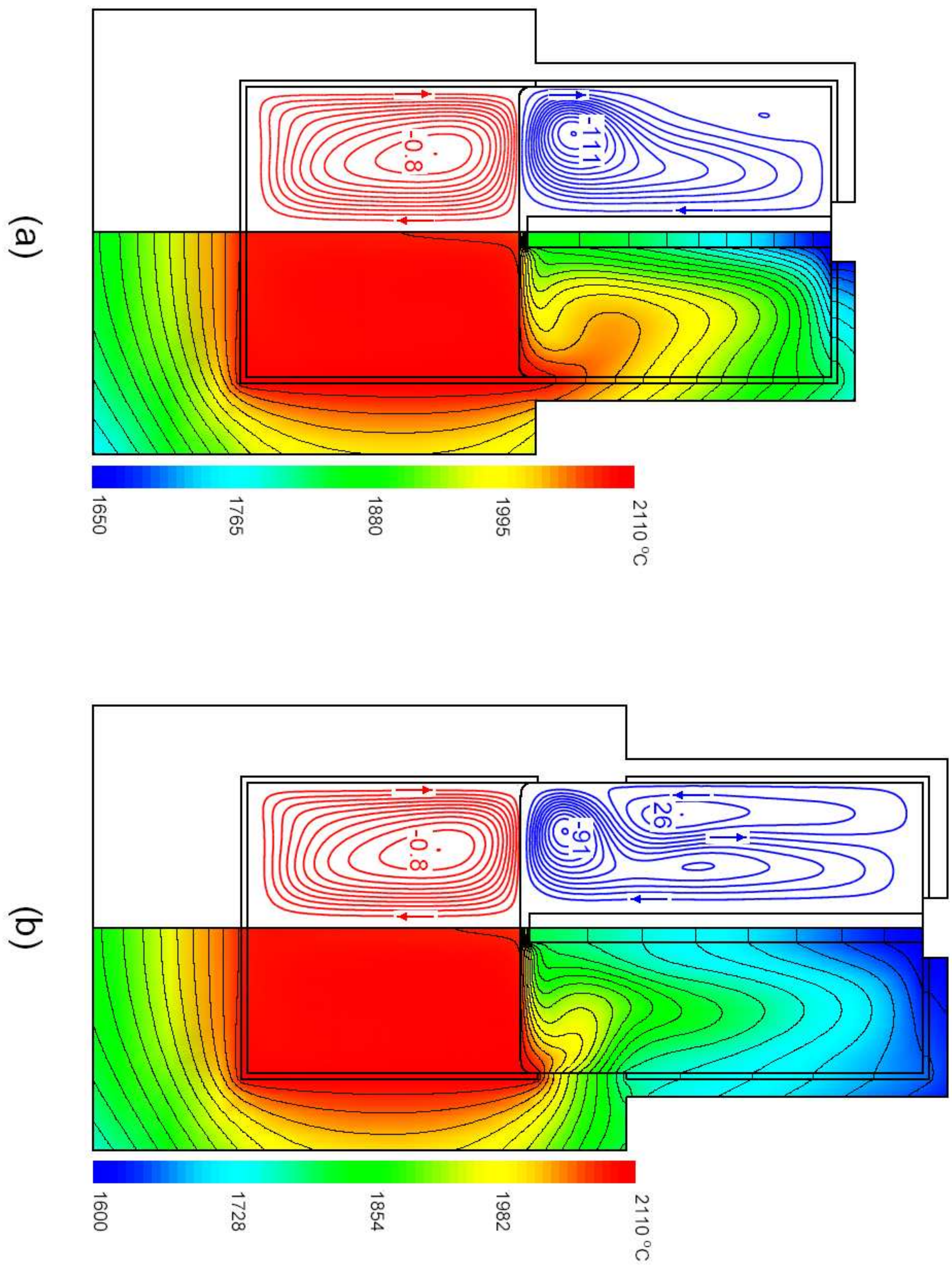

Fig. 5-a-2. Isotherms (right hand side) and streamlines (left hand side) for, (a) configuration without a gap and (b) configuration with a gap between crucible and afterheater in the case of detached seed.

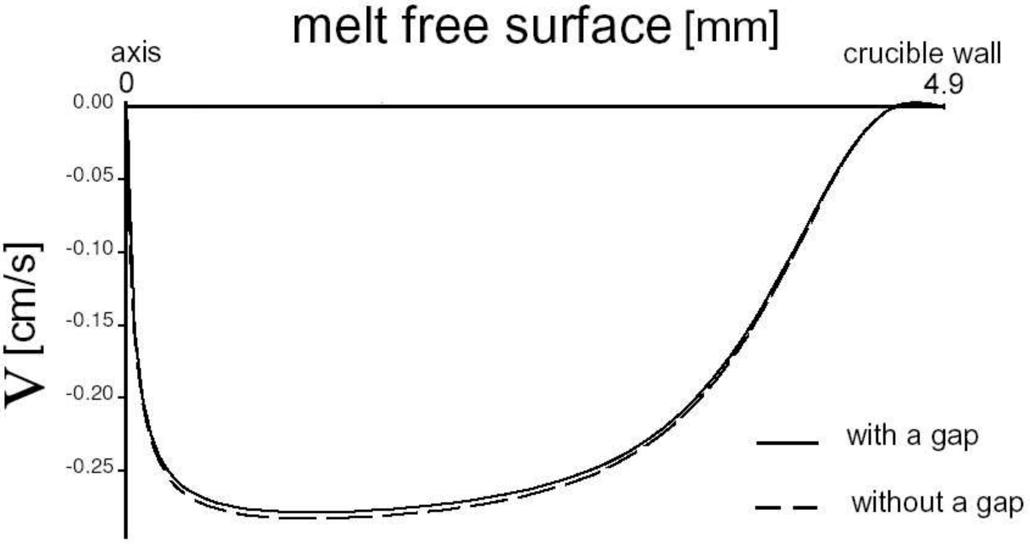

Fig. 5-a-3. Profile of the radial velocity along the melt-gas interface for both configurations in the case of detached seed. The maximum is $\mathrm{v}_{max}^{melt\ surface} \simeq 0.28$ and $0.27\ cm/s$ for the configuration without and with a gap, respectively and at the position $\sim 1.5\ cm$ distance from the centerline.

afterheater corner. In the configuration with a gap, there are also two separate gas eddies, similar to the previous configuration. But the first vortex is smaller and weaker, and the second located close to the afterheater wall is larger and stronger, and has been shifted downwards compared to the configuration without a gap.

It should be mentioned that in both configurations there is a very tiny and weak gas vortex just above the melt-gas interface (not visible), because of continuous condition for the velocity at the melt-gas interface which arises from the mechanical coupling between the melt and the gas phase. The maximum gas velocity is $\mathrm{v}_{max(gas)}^{without} = 36\ cm/s$ and $\mathrm{v}_{max(gas)}^{with} = 30\ cm/s$, downwards and close to the seed wall for the configuration without and with a gap, respectively.

It is noteworthy to compare these fluid flow results to those configurations before including the seed crystal, i.e. chapter 4, *case a*. For the configuration without a gap the gas convection results are similar but for the second configuration it is completely different. It means that in the configuration with a gap, the seed crystal has considerably modified the heat transfer mechanism in the gas domain because of its high thermal conductivity ($k_s/k_a \simeq 170$). In the configuration without a gap, the presence of the seed crystal has a secondary effect. The direct connection of the crucible and afterheater has the main influence on the temperature and flow field of the gas domain. In addition,

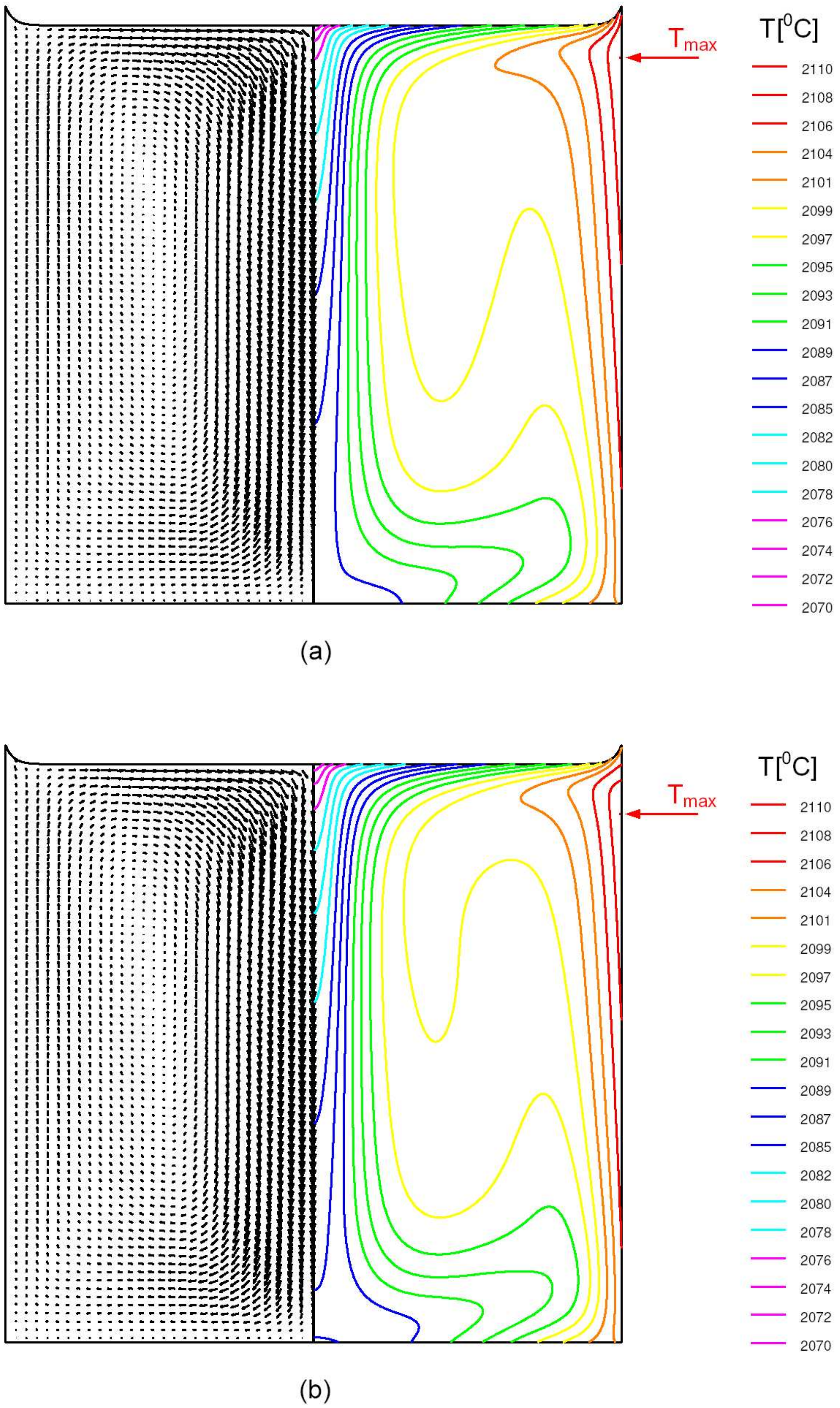

Fig. 5-a-4. Temperature and velocity field of the melt in the case of detached seed for (a) configuration without a gap and (b) configuration with a gap between crucible and afterheater.

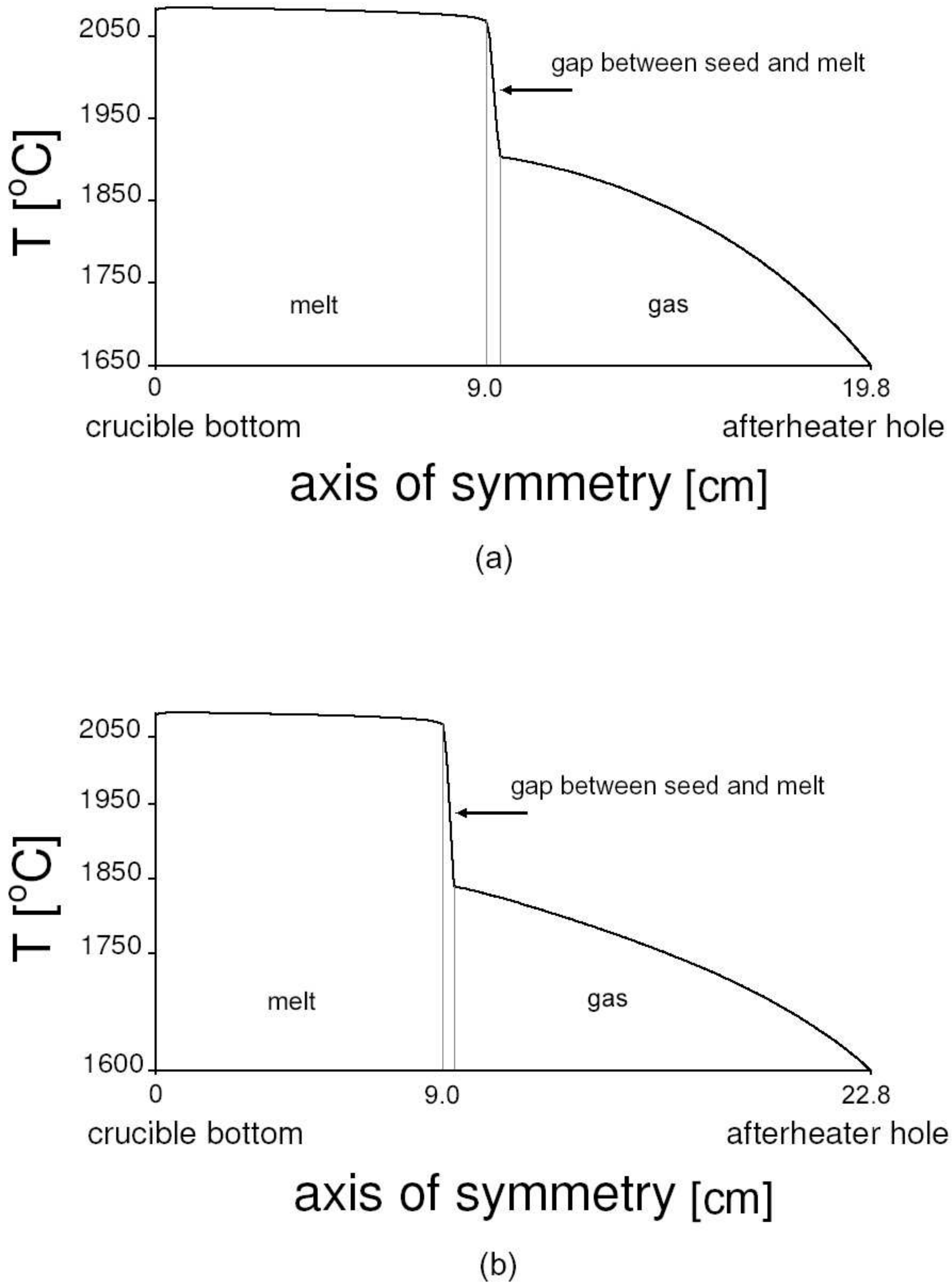

Fig. 5-a-5. Vertical temperature profiles along the axis of symmetry ($r = 0$) from crucible bottom to the afterheater hole in the case of detached seed, (a) configuration without a gap and (b) configuration with a gap between crucible and afterheater. Difference and gradient of temperature in the gap between the seed and the melt surface are: (a) $\triangle T_{gap}^{without} = 190\ ^{o}C$, $\delta T_{gap}^{without} = 38\ ^{o}C/mm$ and (b) $\triangle T_{gap}^{with} = 270\ ^{o}C$, $\delta T_{gap}^{with} = 54\ ^{o}C/mm$.

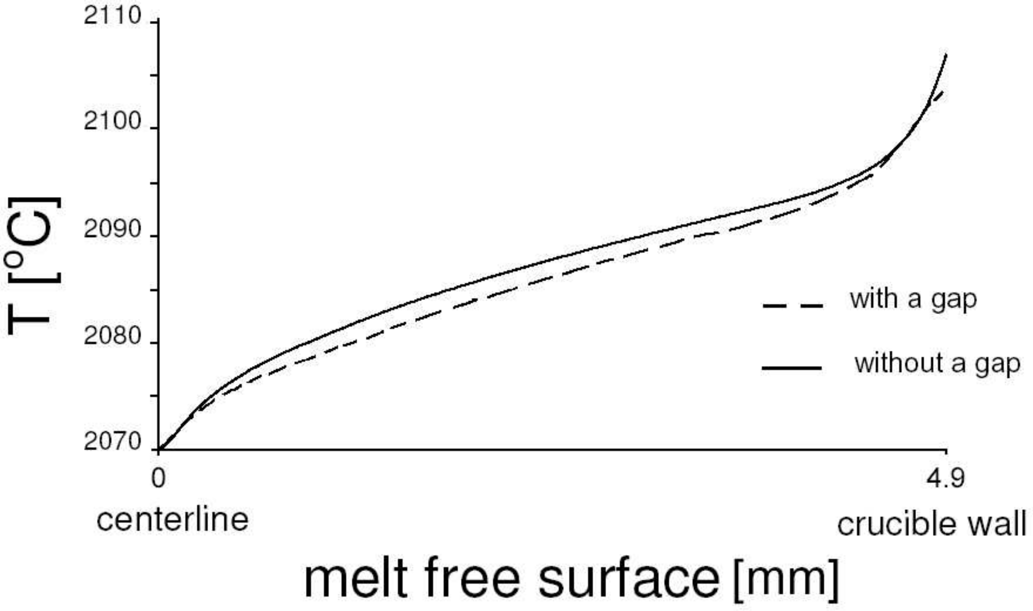

Fig. 5-a-6. Temperature profile along the melt surface for both configurations in the case of detached seed.

the distribution and total heat generation in the afterheater itself should be considered. In the configuration without a gap, the total heat generation in the afterheater is $Q_{afterheater}^{without} \simeq 530\ W$ while it is $Q_{afterheater}^{with} \simeq 450\ W$ (i.e. 15 % less) in the configuration with a gap.

The temperature field in the melt part of both configurations is considerably influenced by the strong thermal flow. The isotherms in the melt are deflected upwards along the crucible wall, pushed towards the symmetry axis close to the melt surface and deformed downwards in the vicinity of the centerline. There is a relatively considerable difference between the temperature field of both configurations which is a result of different heat radiation exchange from the melt surface and also differnet gas flow pattern especially above the melt-gas interface. The effect of the first parameter (i.e. heat dissipation from the melt surface) is more effective than the second (gas flow pattern). In the configuration with a gap the heat loss from the melt surface is stronger than other configuration since the temperature at the afterheater hole is 50 ^{o}C less than configuration without a gap between crucible and afterheater (Eq. 5-b-4).

In the gas domain, the isotherms are deflected upwards in the vicinity of the afterheater wall and downwards close to the seed sides in both configurations. Also there is a large concentration of isotherms in the gap between the melt surface and the seed bottom. It indicates that there is a strong heat flux from the melt surface to the lower surface of the seed crystal which is a result of the high thermal conductivity of the seed rod.

The maximum value of themperature is $T_{max} = 2110\ ^oC$ at the inner crucible wall for both configurations. It is located at 1 cm and 1.2 cm distance below the melt surface in the configuration without and with a gap, respectively. The maximum value of temperature difference for the melt is $\triangle T_{max}^{melt} \simeq 40\ ^oC$ for both configurations, and for the whole system $\triangle T_{max(system)}^{without} \simeq 440\ ^oC$ and $\triangle T_{max(system)}^{with} \simeq 510\ ^oC$.

Fig. 5-a-5 shows the temperature profile at the axis of symmetry ($r = 0$) for both configurations. It is plotted from the crucible bottom to the afterheater top cover. This figure represents that at the centerline, the temperature gradient is extremely high in the gap between the melt surface and the seed ($\delta T_{gap}^{without} \simeq 38\ ^oC/mm$ and $\delta T_{gap}^{with} \simeq 54\ ^oC/mm$), as has been already noted. Another interesting point which is shown in this figure is that the temperature profile in the seed crystal is not linear. Although the only conduction is present in the heat transfer mechanism of the seed part, but its temperature field is markedly influenced by the flow and tempearture field of the gas part. It arises from the existence of the gap between the seed bottom and the melt surface, i.e. it has no direct connection to the melt which is so hot and plays the main role on the formation of the fluid flow and temperature field of the system.

The temperature profile along the melt-gas interface is shown in Fig. 5-a-6. It indicates that the temperature variation is about uniform with $\delta \overline{T}_{melt\ surface} \sim 3\ ^oC/mm$, except in the vicinity of the crucible wall and centerline where the temperature gradient is somewhat higher. The temperature conditions at the melt surface are modified by the lifted upwards afterheater which increases ,in turn, the heat loss from this surface. As a result, the temperature at this interface is less (5 ^oC at the crucible wall) in the configuration with a gap.

5.3.2 case b: After touch and without seed rotation ($\omega_{seed} = 0$)

In this case we consider that a cylindrical rod of the seed crystal with no rotation rate ($\omega_{seed} = 0$) is touched on the melt, Fig. 5-b-1. The structure of the flow in the melt is more complicated than the cases previously considered. Because the melt surface is not planar since the seed supports a liquid meniscus of 4 mm height and also the seed-melt interface is usually not flat. The curved seed-melt interface and the seed-melt meniscus lead to different domain shapes for the flow field and consequently these affect the results. On the other hand, to resolve the fluid flow and to find accurate results close to the curved seed meniscus as well as the crucible meniscus, a very fine grid with special structure is necessary. Fortunately we could do it after careful studies of mesh refinement using the element bisect concept in the ENTWIFE package. In these calculations we intend to calculate the temperature and flow field of the system and also we try to compute the curved seed-melt interface shape.

Induction heating

In the present case including the non-rotating touched seed, the maximum value of energy deposition is $q_{max} \simeq 55\ W/cm^3$ for both configurations and the total energy production in the crucible and afterheater is $Q^{without}_{total} = 3.3\ kW$ and $Q^{with}_{total} = 3.19\ kW$ for the configuration without and with a gap, respectively.

Temperature and flow field

The temperature and flow field for both configurations are shown in Fig. 5-b-2. Similar to the previous case (i.e. detached seed), a clockwise vortex caused by the free convection superimposed with the Marangoni convection is present in the melt of both configurations. This vortex which is more intense close to the melt surface, is extended from the crucible wall to the centerline. The melt flows up along the crucible wall and down along the symmetry axis. In addition, there is a weak and small counterclockwise vortex in the crucible meniscus (not visible) which is a result of the melt meniscus with the crucible wall. Fig. 5-b-3 shows the velocity profile along the melt free surface from the seed to the crucible wall with a maximum value of $\mathrm{v}^{without}_{max(melt\ surface)} \simeq 0.32\ cm/s$ and $\mathrm{v}^{with}_{max(melt\ surface)} \simeq 0.30\ cm/s$ for the configuration without and with a gap, respectively, at a position $\sim$ 2 cm distance off the seed edge. In the melt, the velocity maximum value is $\mathrm{v}^{melt}_{max} \simeq 0.7\ cm/s$, downwards, at the centerline and also markedly higher than elsewhere in this fluid domain, Fig. 4-b-4. The seed-melt interface has a conic shape with a hight of $\triangle H^{without}_{seed} = 4.2\ mm$ and $\triangle H^{with}_{seed} = 3.9\ mm$ towards the melt for the configuration without and with a gap, respectively.

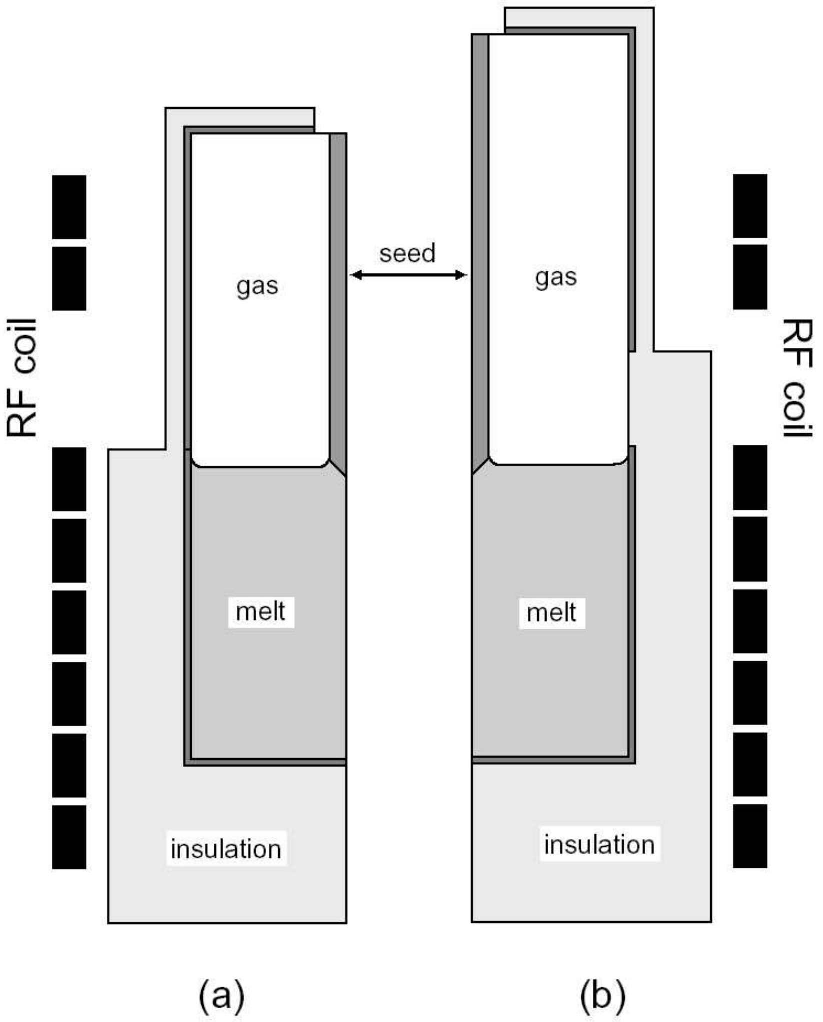

Fig. 5-b-1. Schematic diagram of two configurations of a Czochralski growth furnace containing the touched seed crystal, melt and gas, (a) without and (b) with a gap between crucible and afterheater.

In the gas domain the result for the configuration without a gap is mainly similar to the case of detached seed but for the second configuration it is completely different. In the configuration without a gap there are two separate eddies, a strong clockwise above the melt surface and a weak counterclockwise one in the afterheater corner. The first gas vortex which is extended from the melt surface to the afterheater top cover transfers the heat from the melt surface and hot lower part of the afterheater wall to the afterheater hole. In the configuration with a gap, there are three eddies of gas convection in the gap and afterheater region. The appearance of multiple eddies in the gas part indicates that the mechanism of heat transfer in this configuration is more complicated than the cases of without the seed or detached seed. Two strong vortices with opposite direction of rotation in the afterheater and the gap region close to the seed meniscus, and a weak

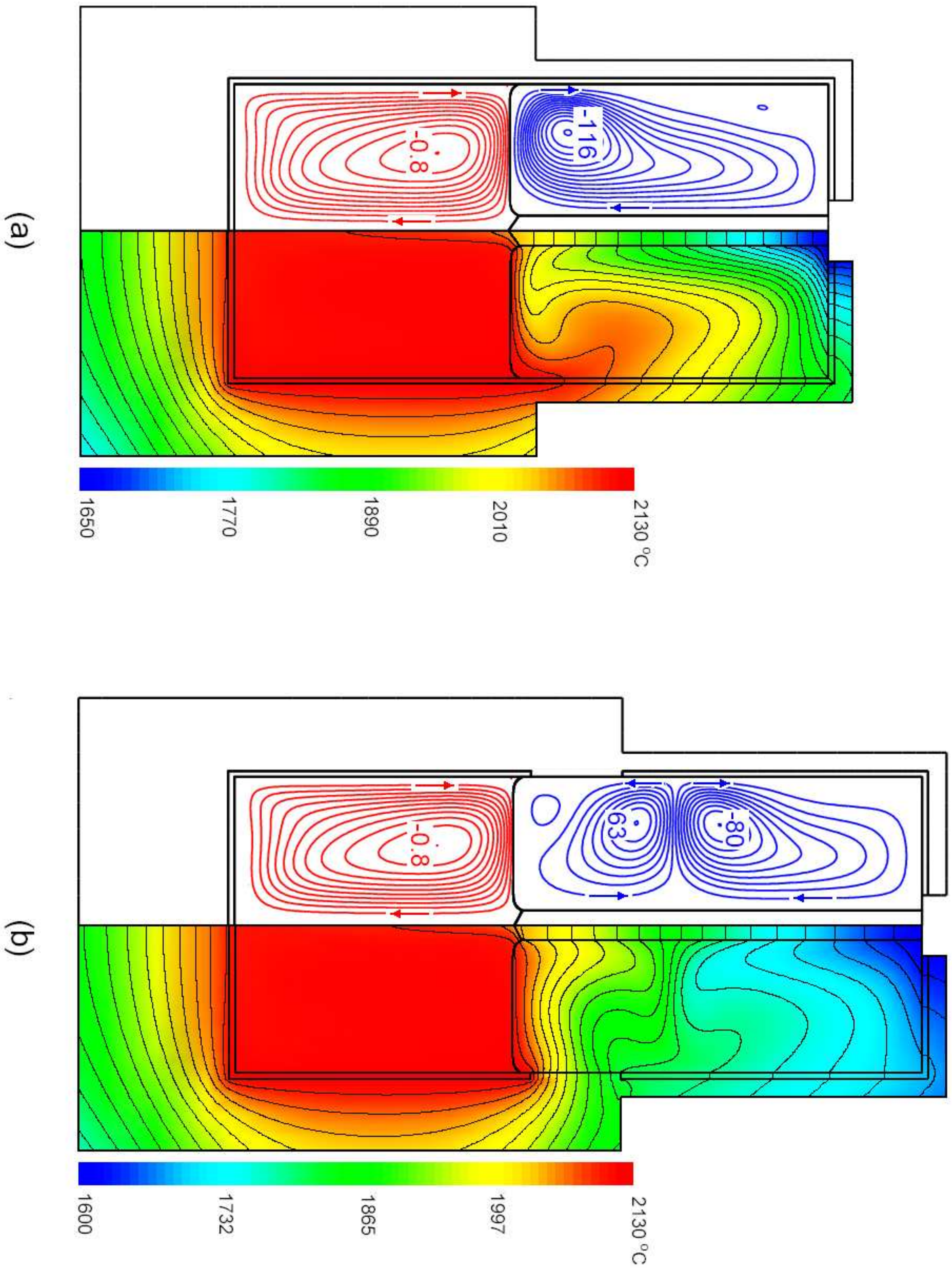

Fig. 5-b-2. Isotherms (right hand side) and streamlines (left hand side) for, (a) configuration without a gap and (b) configuration with a gap between crucible and afterheater ($\omega_{seed} = 0$).

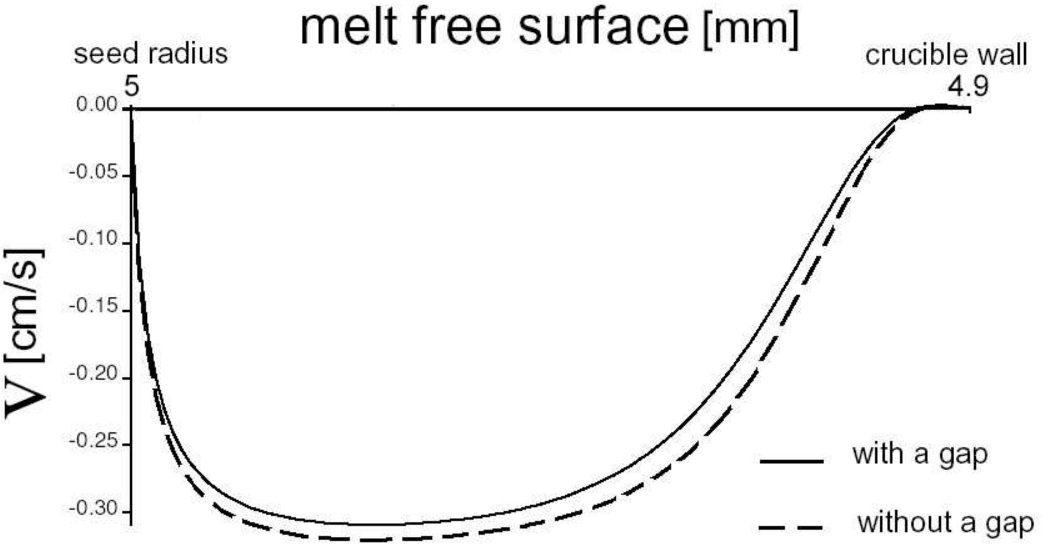

Fig. 5-b-3. Profile of the radial velocity along the melt-gas interface from axis to the crucible wall for both configurations. The maximum is $\mathrm{v}_{max}^{melt\ surface} \simeq 0.32$ and $0.30\ cm/s$ for the configuration without and with a gap, respectively and at the position $\sim 2\ cm$ distance to the centerline ($\omega_{seed} = 0$).

and small one in the vicinity of the crucible meniscus. The gas flow is upwards adjacent to the lower part of the seed side wall while it is flowing downwards in the upper part of it. The upwards gas convection brings the heat from the melt surface and lower part of the seed to the central part of the afterheater and then the second vortex (upper vortex) transfers this heat to the afterheater top cover. The maximum value of velocity in the gas is $\mathrm{v}_{max(gas)}^{without} = 36\ cm/s$ and $\mathrm{v}_{max(gas)}^{with} = 30\ cm/s$, downwards and close to the seed side wall for the configuration without and with a gap, respectively.

The melt temperature field of both configurations is relatively similar except close to the melt-gas interface as well as the seed-melt interface, Fig. 5-b-4 and Fig. 5-b-5. The largest temperature gradient of the melt is just under the seed which indicates a high flux of energy to the seed from the melt via the seed-melt interface. This effect is demonstrated by a smaller isotherm spacing in the melt adjacent the seed-melt interface. This high heat flux through the seed directly influences on the formation of the large deflection of the seed-melt interface towards the melt. Also noteworthy is that the temperature field in the melt domain of both configurations is considerably influenced by the strong buoyant and Marangoni flow. The isotherms in the melt are pushed up in the vicinity of crucible sides, convected towards the seed in the seed meniscus and deflected downwards along the centerline. In the gas domain of the configuration without

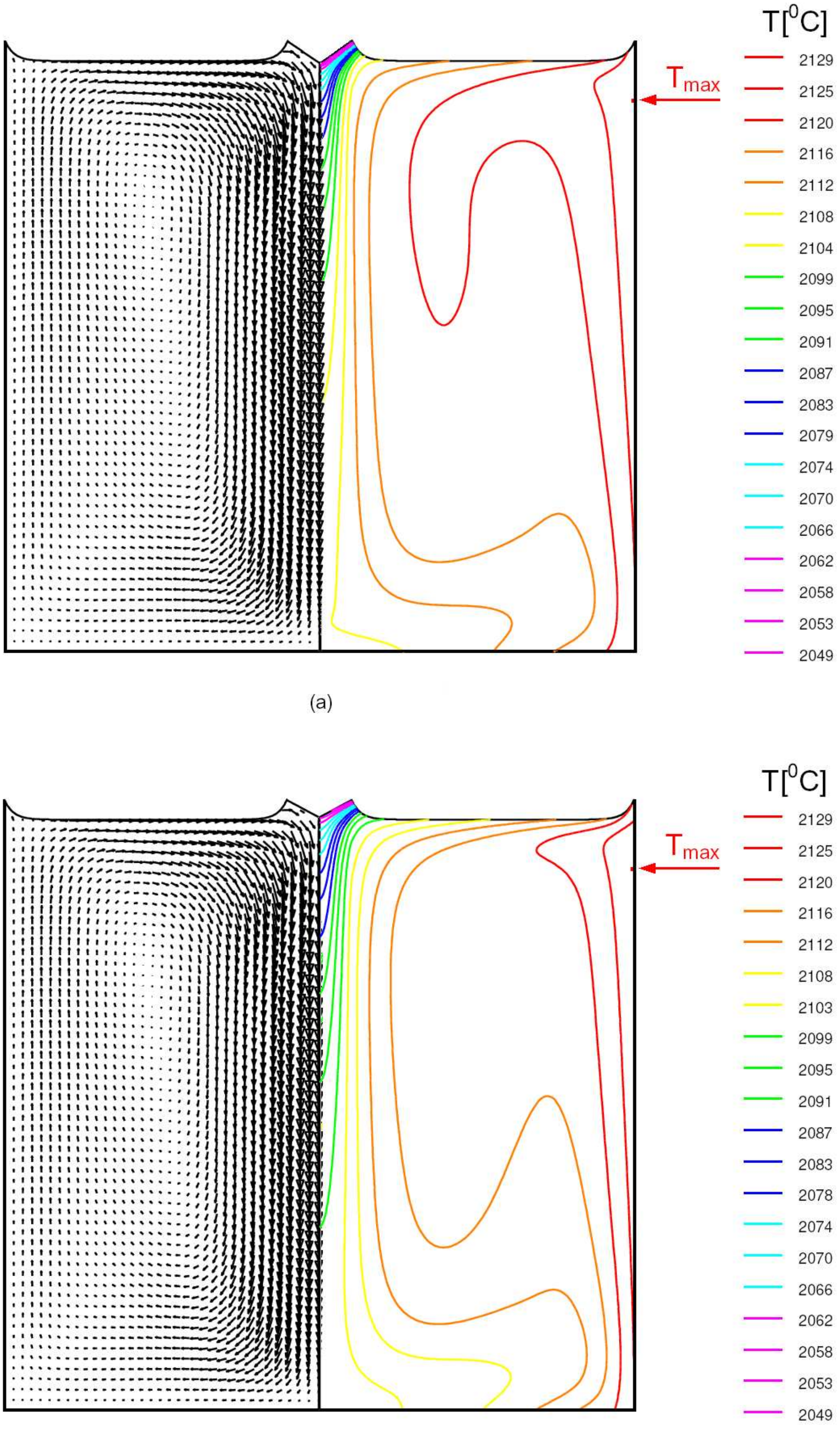

(a)

(b)

Fig. 5-b-4. Temperature and velocity field of the melt, (a) configuration without a gap and (b) configuration with a gap between crucible and afterheater ($\omega_{seed} = 0$).

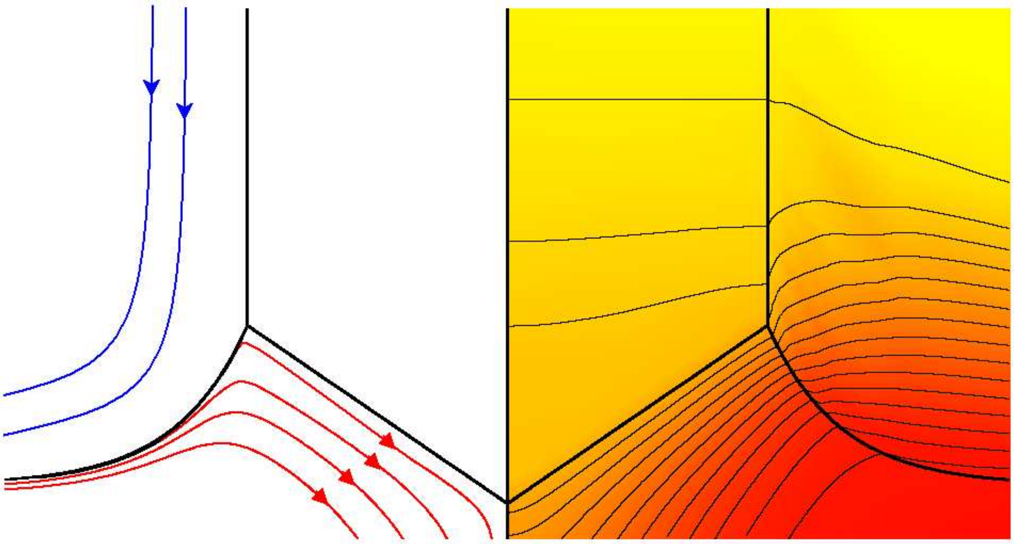

(a)

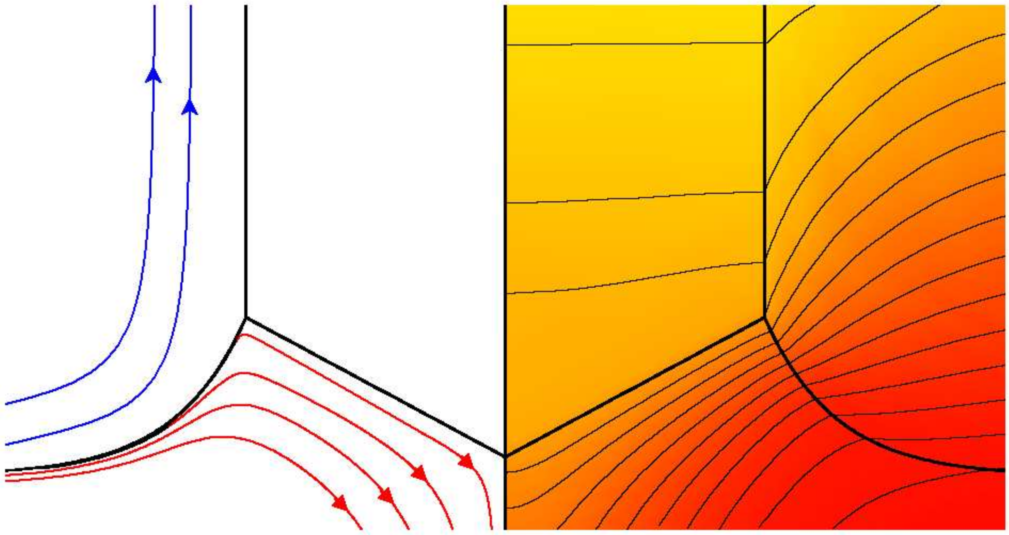

(b)

Fig. 5-b-5. Streamline and temperature distribution ($\triangle T_{isotherm} = 5\ ^{o}C$) in the vicinity of the crystal-melt interface, (a) configuration without a gap ($\triangle H_{seed}^{without} = 4.2\ mm$) and (b) configuration with a gap between crucible and afterheater ($\triangle H_{seed}^{without} = 3.9\ mm$) for the case of $\omega_{seed} = 0$.

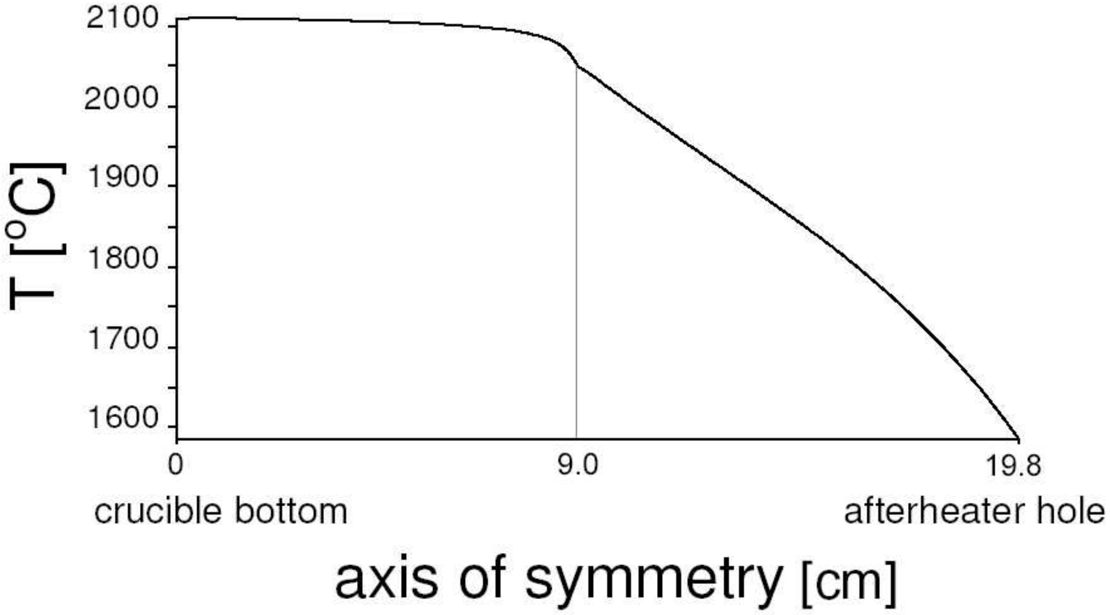

Fig. 5-b-6. Vertical temperature profile along the axis of symmetry ($r = 0$) from crucible bottom to the afterheater hole for the configuration without a gap between crucible and afterheater ($\omega_{seed} = 0$).

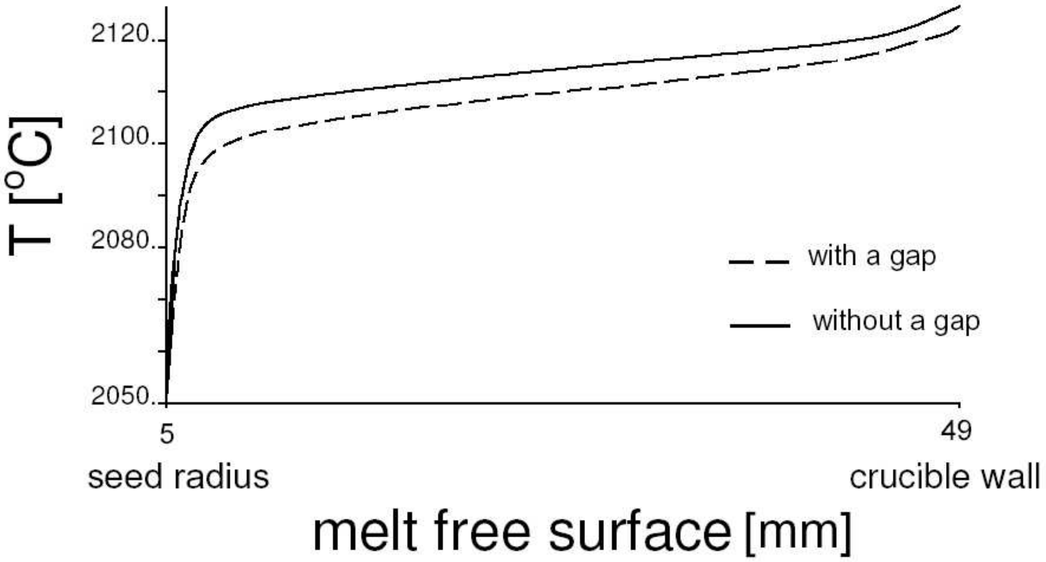

Fig. 5-b-7. Temperature profiles along the melt surface for both configurations. Average temperature gradient is $\delta\overline{T}_{melt\ surface} \sim 0.3\,^{o}C/mm$, except in the vicinity of the crucible wall and the seed meniscus ($\omega_{seed} = 0$).

a gap, the isotherms close to the afterheater wall are displaced upwards and towards the afterheater hole, and deflected downwards adjacent of the seed wall. Accordingly, there is a high temperature gradient in the vicinity of afterheater hole which indicates a high heat flux that is transfered out of the system via the afterheater hole. In the configuration with a gap the deflection of the isotherms is more complex corresponding to the structure of natural gas flow in this domain. They are deflected upwards close to the afterheater wall and vise versa in vicinity of the upper half part of seed crystal. In addition, the isotherms have a horizontal shape close to the gap between crucible and afterheater, and a upwards deflected shape adjacent of the lower part of the seed rod. In the gas domain of this configuration, there is a relatively high temperature gradient in the gap itself and the gas close to it. The temperature of the afterheater wall is higher than the seed in the configuration without a gap but it is approximately equal in the configuration with a gap between crucible and afterheater.

The temperature gradient along the seed meniscus for the configuration without a gap is $\delta T_{meniscus}^{without} \simeq 5.1\ ^oC/mm$ while it is $\delta T_{meniscus}^{with} \simeq 4.3\ ^oC/mm$ for the configuration with a gap. Two phenomena are responsible for the difference between this two temperature gradients. The first and main reason is the heat loss from the melt surface. It is stronger in the configuration with a gap than other one. The second reason is different gas convection around the seed meniscus. As has been already mentioned, in the vicinity of the seed meniscus there is a downwards gas flow in the configuration without a gap while in the other configuration the gas flow is upwards. The isotherm deflection in the gas domain just above the seed meniscus confirms the existence of this two oppositely gas convections in that area, Fig. 5-b-5. So, the gas convection introduces certain additional effects in the temperature field of the system and especially in the melt free surface, that can not be predicted from melt simulation alone.

The dynamics of the temperature gradient in all parts and fluid motion in the fluid domains (i.e. melt and gas) create the isotherm shapes of the system. In the seed the isotherms are horizontal lines with constant spacing which are a result of the high conductivity of this solid part except close to the non-flat seed-melt interface. Also, this high heat conduction within the touched seed crystal has significantly modified the overall heat transfer through the system. In the configuration without a gap the overall heat transfer in the afterheater is directed towards the afterheater hole but in the other one it is flowing towards the afterheater hole and afterheater top cover as well.

The maximum value of temperature is $T_{max} \simeq 2130\ ^oC$ at the crucible side wall below the melt surface (1 cm and 1.2 cm in the configuration without and with a gap, respectively), and the minimum $T_{min}^{without} = 1650\ ^oC$ and $T_{min}^{with} = 1600\ ^oC$ at the afterheater hole for the configuration without and with a gap, respectively. The maximum value of temperature difference across the melt is $\triangle T^{melt}_{max} \simeq 80\ ^{o}C$ for both configurations, and for the whole system $\triangle T^{without}_{max(system)} \simeq 460\ ^{o}C$ and $\triangle T^{with}_{max(system)} \simeq 530\ ^{o}C$ for the configuration without and with a gap, respectively and higher than in the situation before touching the seed. These results indicate that the melt is about isothermal compared to the seed and the gas domain (Fig. 5-b-2).

Fig. 5-b-6 shows the temperature profile along the symmetry axis ($r = 0$), from the crucible bottom to the afterheater hole for the configuration without a gap (This temperature profile is similar to the profile found for other configuration). This figure indicates that the axial temperature gradient in the seed is essentially linear ($\delta\overline{T}^{\,without}_{seed\ axis} \sim 3.9\ ^{o}C/mm$ and $\delta\overline{T}^{\,with}_{seed\ axis} \sim 3.4\ ^{o}C/mm$) except close to the seed-melt interface which is smaller than these values (Fig. 5-b-4). In the area just above the seed-melt interface, the temperature reaches a maximum at the surface of the seed in the section normal to the growth axis. Therefore, in this part of the seed, we will find the largest thermal expansion which gives rise to considerable thermoelastic stresses.

Fig. 5-b-7 shows the temperature variation at the melt-gas interface which is about uniform with $\delta\overline{T}_{melt\ surface} \sim 0.3\ ^{o}C/mm$, except in the vicinity of the crucible wall (a result of exitance of the invisible, weak and counterclockwise vortex in this area) and the seed meniscus where in the seed meniscus we have a typical temperature boundary layer and so the temperature gradient is markedly high, as has already been mentioned. This is a result of the interaction between the buoyancy force and the thermocapillary force which drag the hot melt from the crucible side wall towards the seed. In addition, this interaction makes the seed-melt interface more convex into the melt.

As has already been explained, the heat radiation from the melt surface is stronger in the configuration with a gap since the temperature at the afterheater hole (T_{ah}) is less than configuration without a gap. This results the different thermal field in the melt part (such as different melt velocity along the melt surface and different temperature gradient close to the seed-melt interface) which in turn, leads to a different deflection of the seed-melt interface.

5.3.3 case c: After touch and with seed rotation ($\omega_{seed} = 5 - 30\ rpm$)

In this case different values of the seed rotation rate are considered in the range of $\omega_{seed} = 5 - 30\ rpm$ for both configurations. In these set of calculations, we intend to calculate the temperature and flow field of the system as well as the curved seed-melt interface. Also we try to figure out the influence of the seed rotaion rate on the seed-melt interface inversion during the seeding process.

Induction heating

In this case including the rotating seed touched to the melt, the maximum value of energy generation in the system is in the range of $q_{max} \simeq 55.1 - 55.6\ W/cm^3$ for both configurations and different seed rotation rates. The total energy production in the crucible and afterheater is in the range of $Q_{total}^{without} = 3.31 - 3.34\ kW$, and $Q_{total}^{with} = 3.2 - 3.22\ kW$ for the configuration without and with a gap between crucible and afterheater, respectively.

Temperature and flow field

Temperature and flow field of both configurations are shown in Fig. 5-c-1 for $\omega_{seed} = 5\ rpm$, Fig. 5-c-2 for $\omega_{seed} = 20\ rpm$ and Fig. 5-c-3 for $\omega_{seed} = 30\ rpm$, respectively.

A clockwise vortex which arises from the natural convection superimposed with the thermal Marangoni convection exists in the melt of both configurations. This vortex is more intense close to the melt surface and has been extended from the crucible wall to the axis of symmetry. The melt thermal-buoyant flow is initiated along the heated crucible side wall which is the hottest part of the system and the melt surface where the temperature variation via the surface tension drives the flow.

In addition to this primary buoyancy-driven recirculation, a weak and small rotationally - driven convective cell which flows in the opposite direction is present below the seed. The rotation of the seed crystal results in the development of this forced convection loop which is located just under the seed rod, Fig. 5-c-4 and Fig. 5-c-5. The forced convection begins along the seed-melt interface since the rotating seed produces a centrifugal force which is spinning the melt up and moves it outwards radially. At a low rotation rate ($\omega_{seed} < 10\ rpm$), the rotational vortex occupies the corner adjacent to the seed edge and did not expand to the centerline. As the seed rotation rate is increased ($\omega_{seed} > 10\ rpm$), the forced convection vortex becomes larger and stronger to fill the space directly under the seed, i.e. the whole seed meniscus from the melt surface to the axis of symmetry. Further increase of the seed rotation rate (i.e. $\omega_{seed} > 20\ rpm$) will

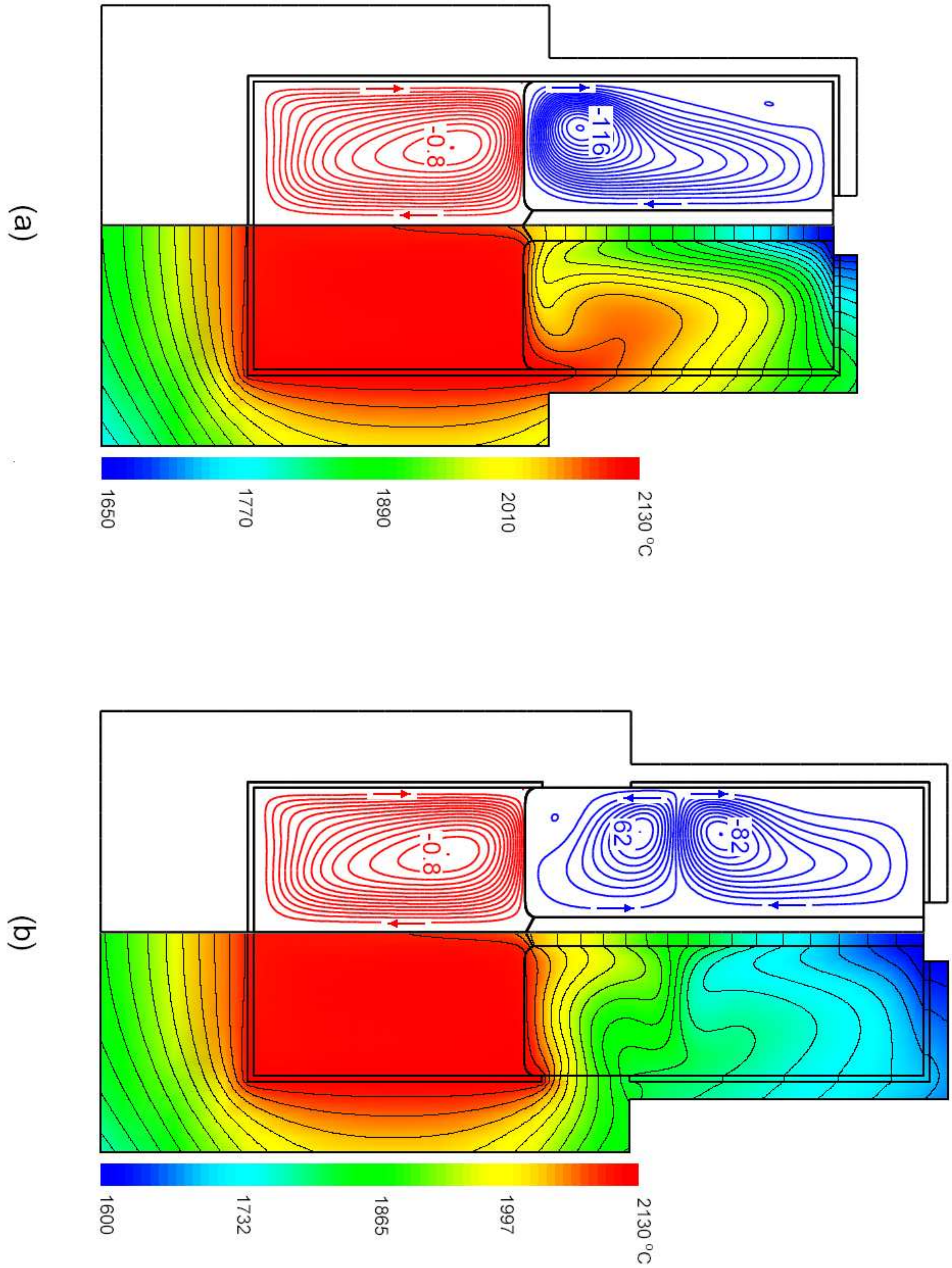

Fig. 5-c-1. Isotherms (right hand side) and streamlines (left hand side) for $\omega_{seed} = 5\,rpm$, (a) configuration without a gap and (b) configuration with a gap between crucible and afterheater.

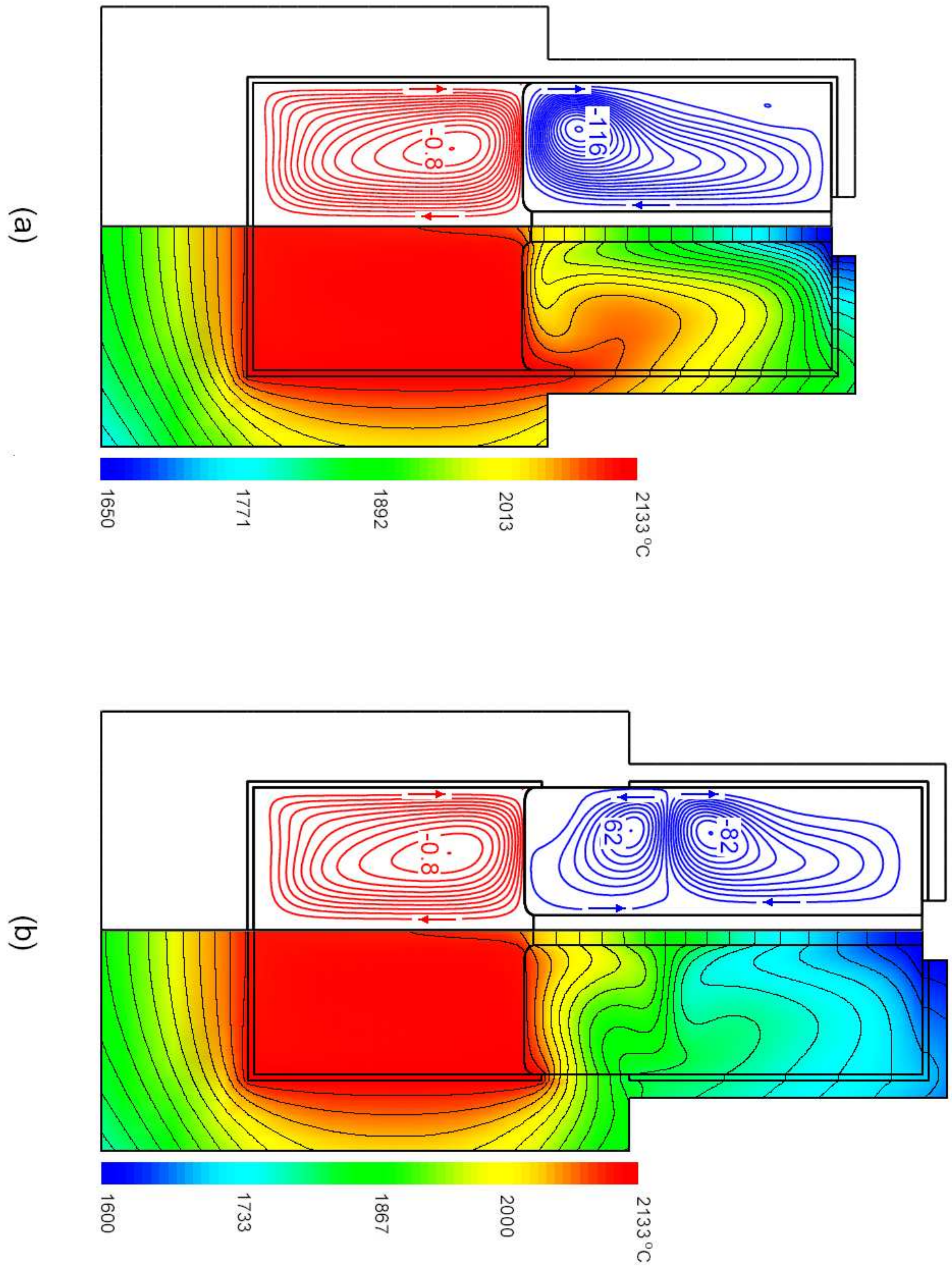

Fig. 5-c-2. Isotherms (right hand side) and streamlines (left hand side) for $\omega_{seed} = 20\ rpm$, (a) configuration without a gap and (b) configuration with a gap between crucible and afterheater.

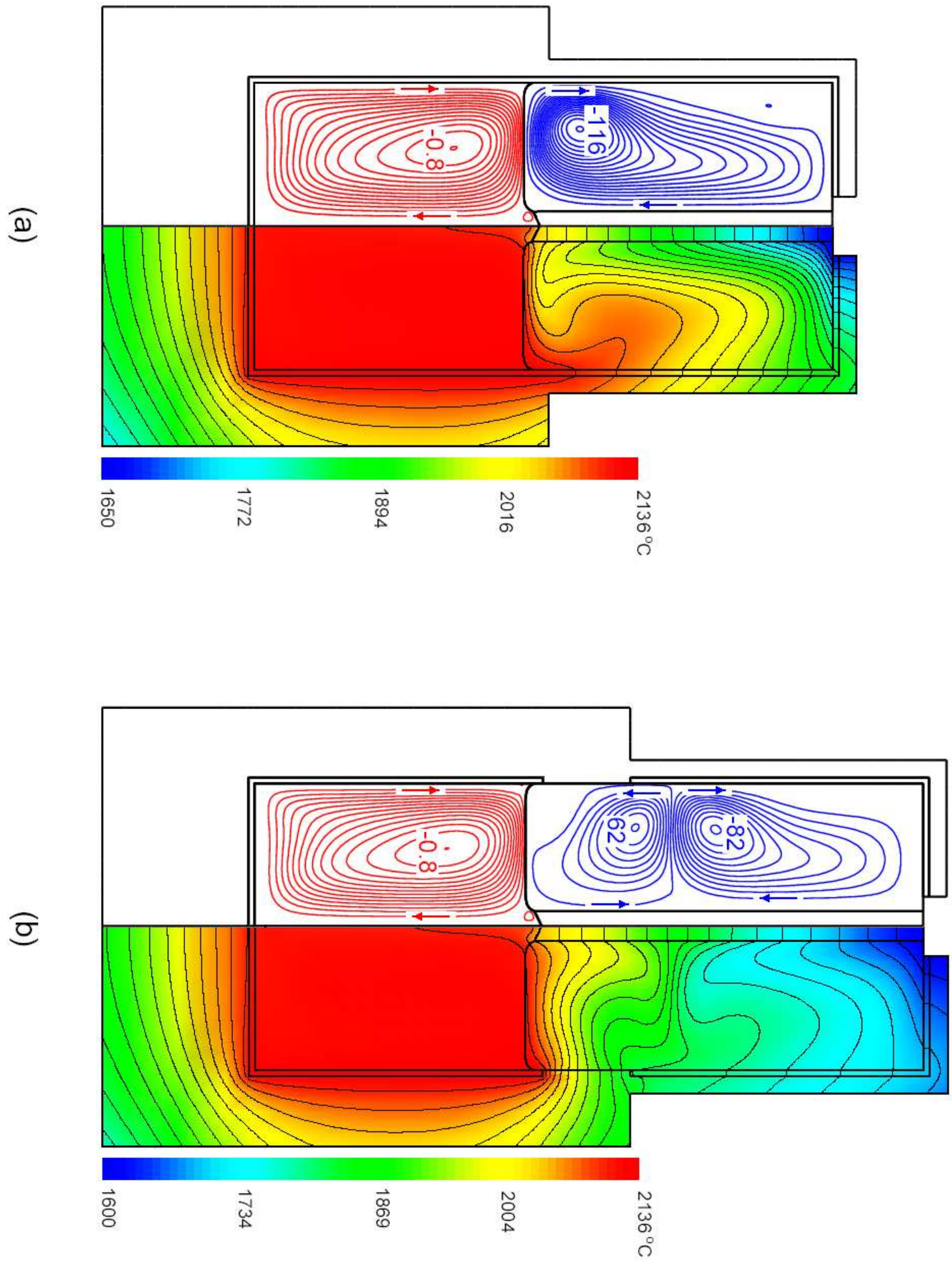

Fig. 5-c-3. Isotherms (right hand side) and streamlines (left hand side) for $\omega_{seed} = 30\ rpm$, (a) configuration without a gap and (b) configuration with a gap between crucible and afterheater.

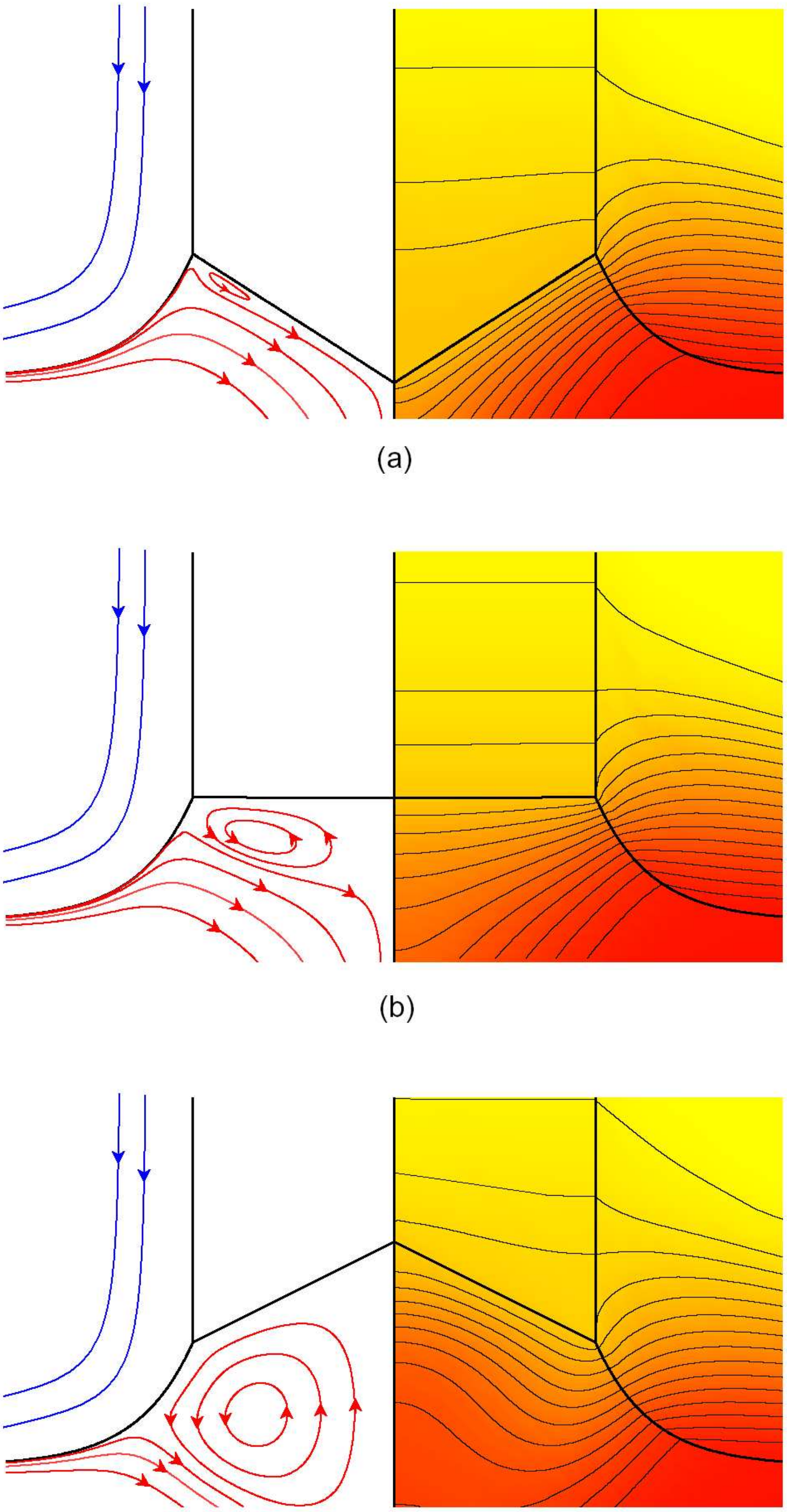
(a)

(b)

(c)

Fig. 5-c-4. Isotherms (right hand side) and streamlines (left hand side) close to the seed-melt interface for the configuration without a gap between crucible and afterheater, (a) $\omega_{seed} = 5\ rpm$, (b) $\omega_{seed} = 20\ rpm$ and (c) $\omega_{seed} = 30\ rpm$.

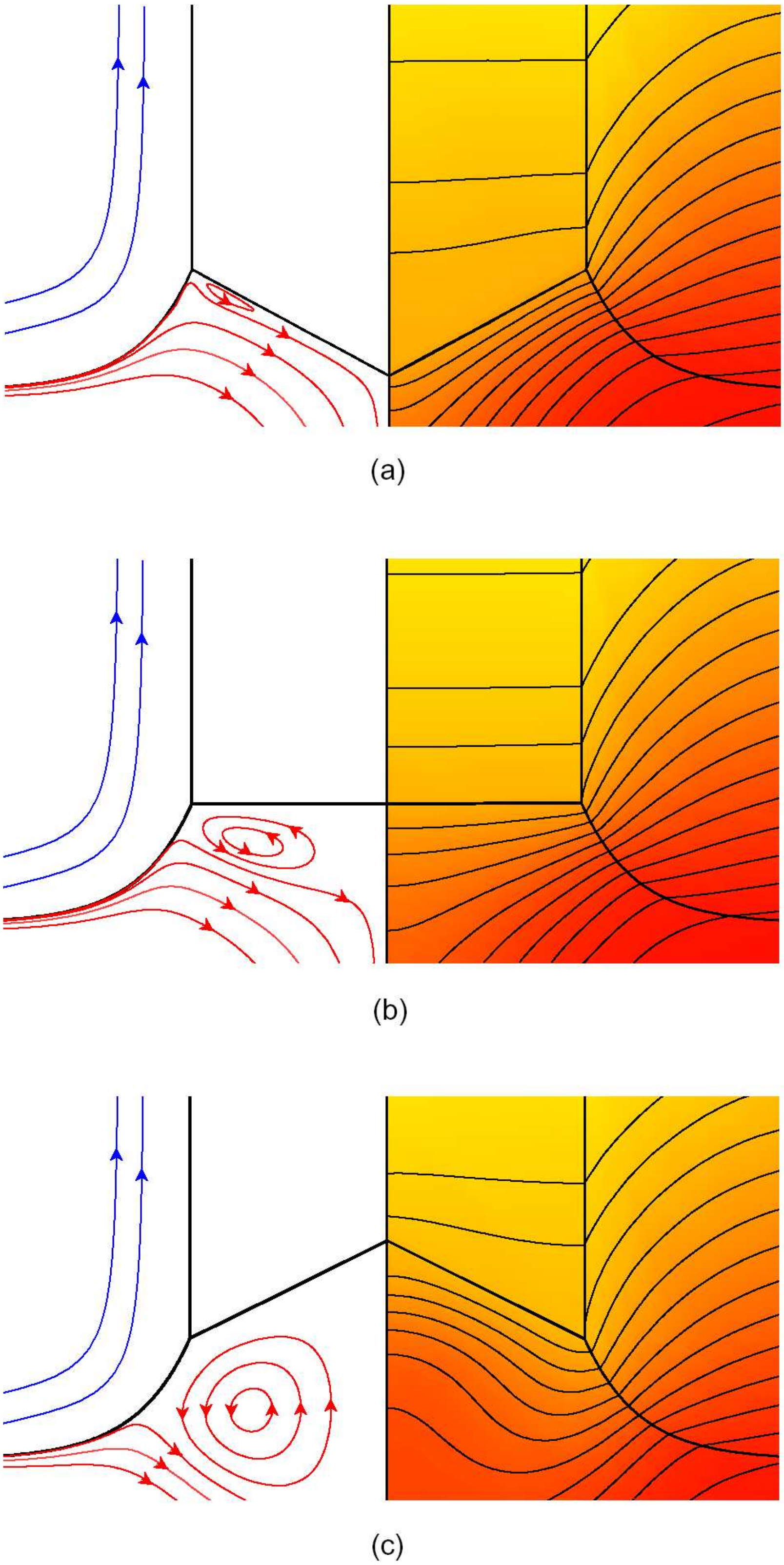

Fig. 5-c-5. Isotherms (right hand side) and streamlines (left hand side) close to the seed-melt interface for the configuration with a gap between crucible and afterheater, (a) $\omega_{seed} = 5\ rpm$, (b) $\omega_{seed} = 20\ rpm$ and (c) $\omega_{seed} = 30\ rpm$.

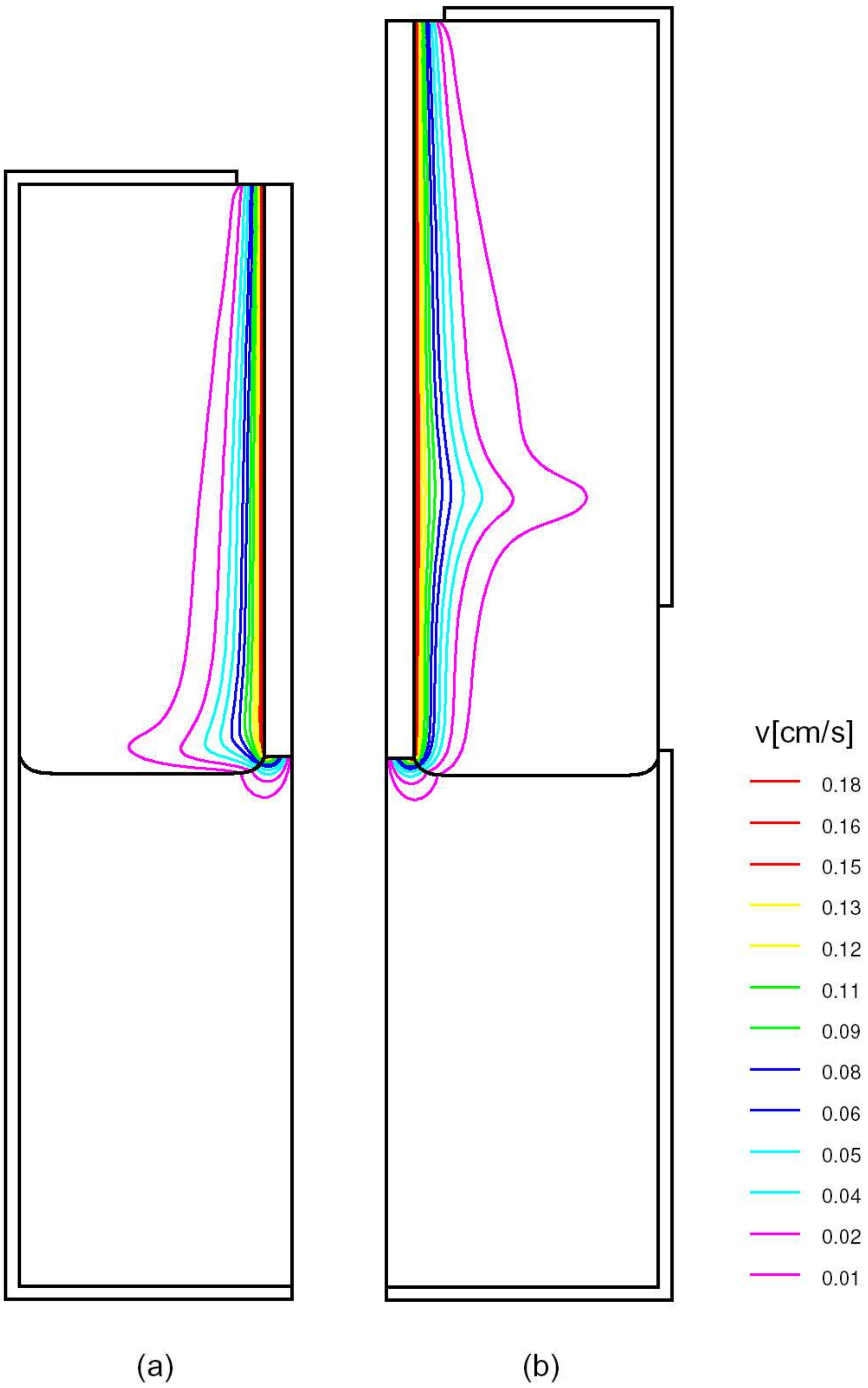

Fig. 5-c-6. Azimuthal velocity contours in the melt and gas domain for $\omega_{seed} = 20\ rpm$, (a) configuration without a gap and (b) configuration with a gap between crucible and afterheater.

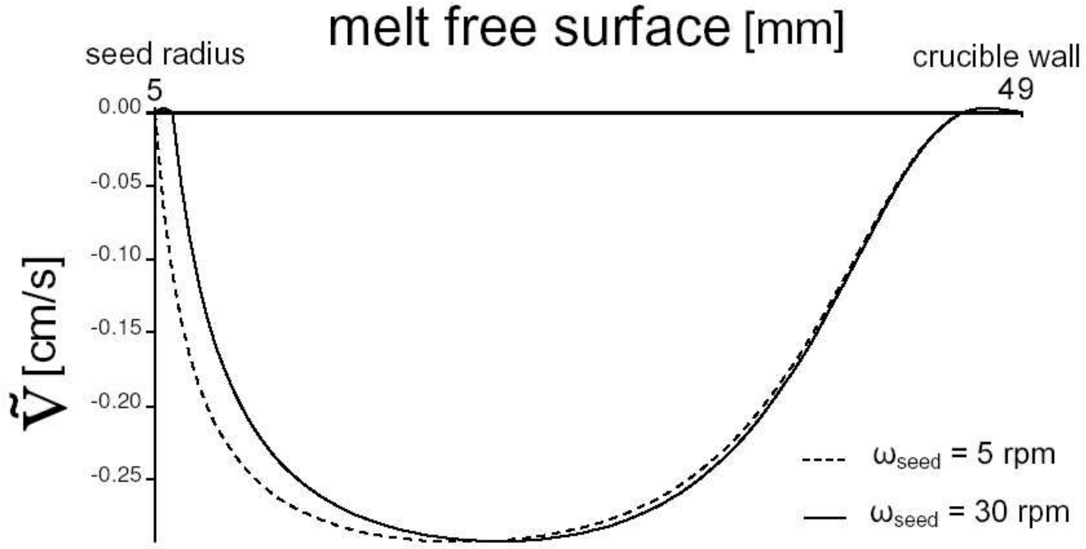

Fig. 5-c-7. Profiles of the radial velocity along the melt-gas interface from axis to the crucible wall for the configuration with a gap. The maximum is $v_{max}^{melt\ surface} \simeq 0.30\ cm/s$ and constant but its location is shifted towards the crucible wall as the seed rotation rate is increased.

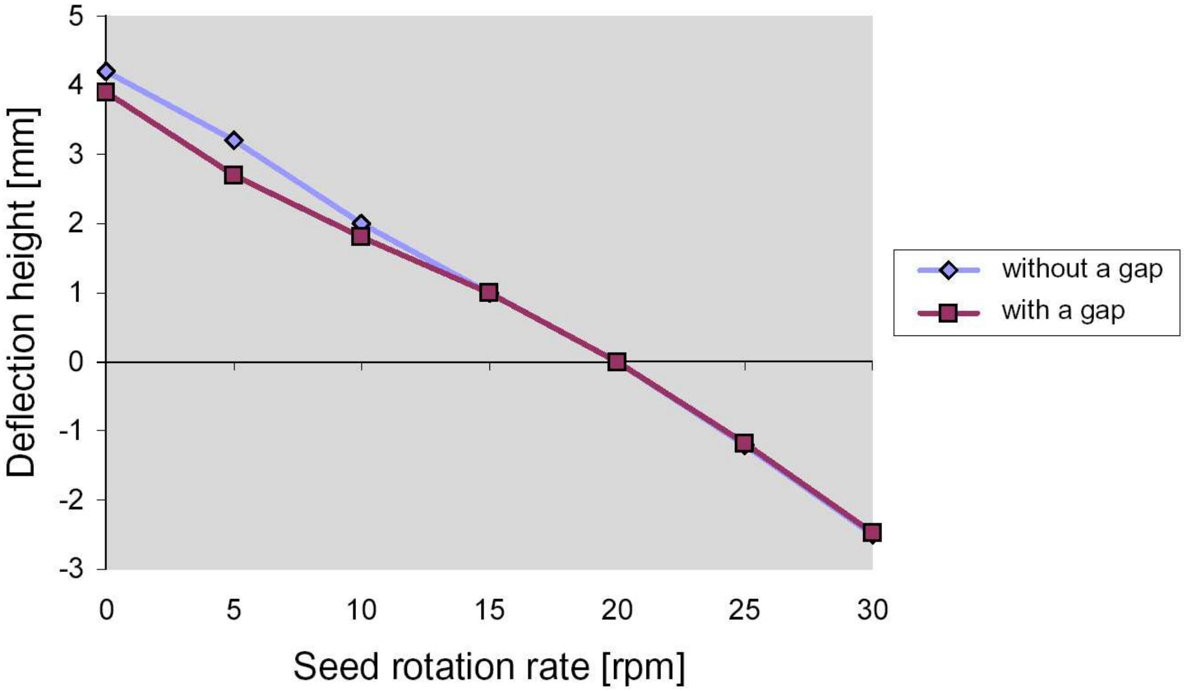

Fig. 5-c-8. Plot of the seed-melt interface deflection ($\triangle H_{seed}$) as a function of the seed rotation rate (ω_{seed}) for both configurations, resulting from our simulations. A linear variation of the interface deflection is clearly visible vs. the seed rotation rate.

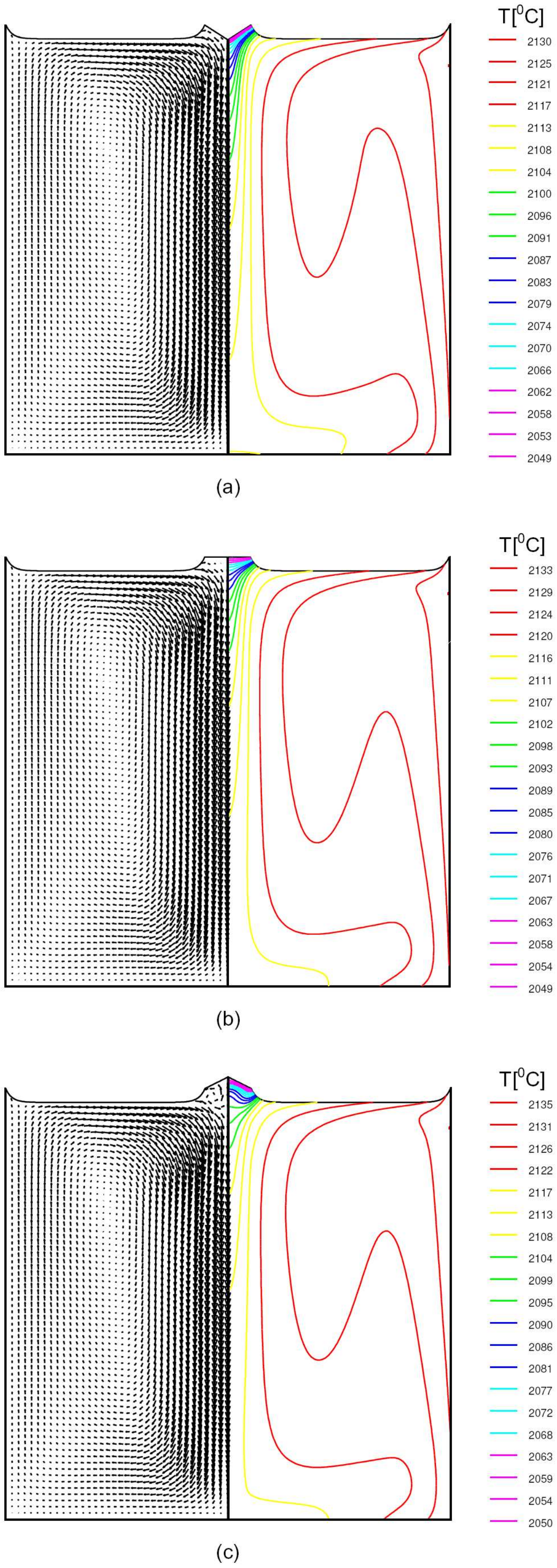

Fig. 5-c-9. Temperature and velocity field of the melt for the configuration without a gap between crucible and afterheater, (a) $\omega_{seed} = 5\ rpm$, (b) $\omega_{seed} = 20\ rpm$ and (c) $\omega_{seed} = 30\ rpm$.

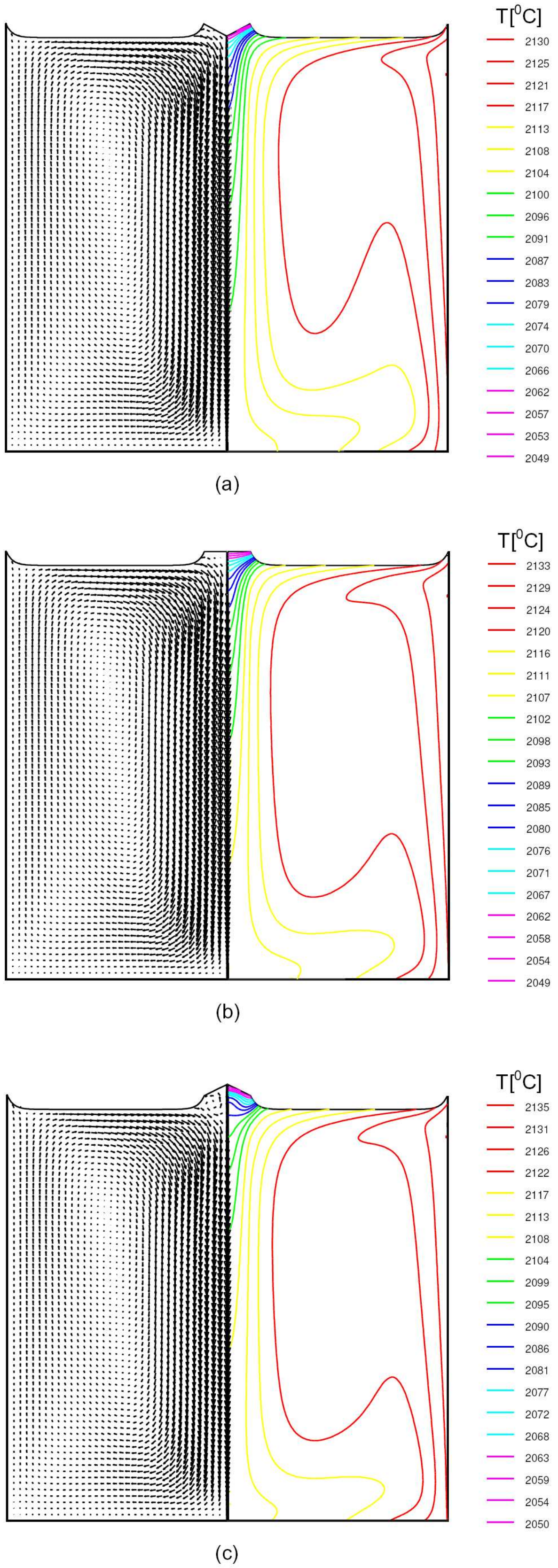

Fig. 5-c-10. Temperature and velocity field of the melt for the configuration with a gap between crucible and afterheater, (a) $\omega_{seed} = 5\ rpm$, (b) $\omega_{seed} = 20\ rpm$ and (c) $\omega_{seed} = 30\ rpm$.

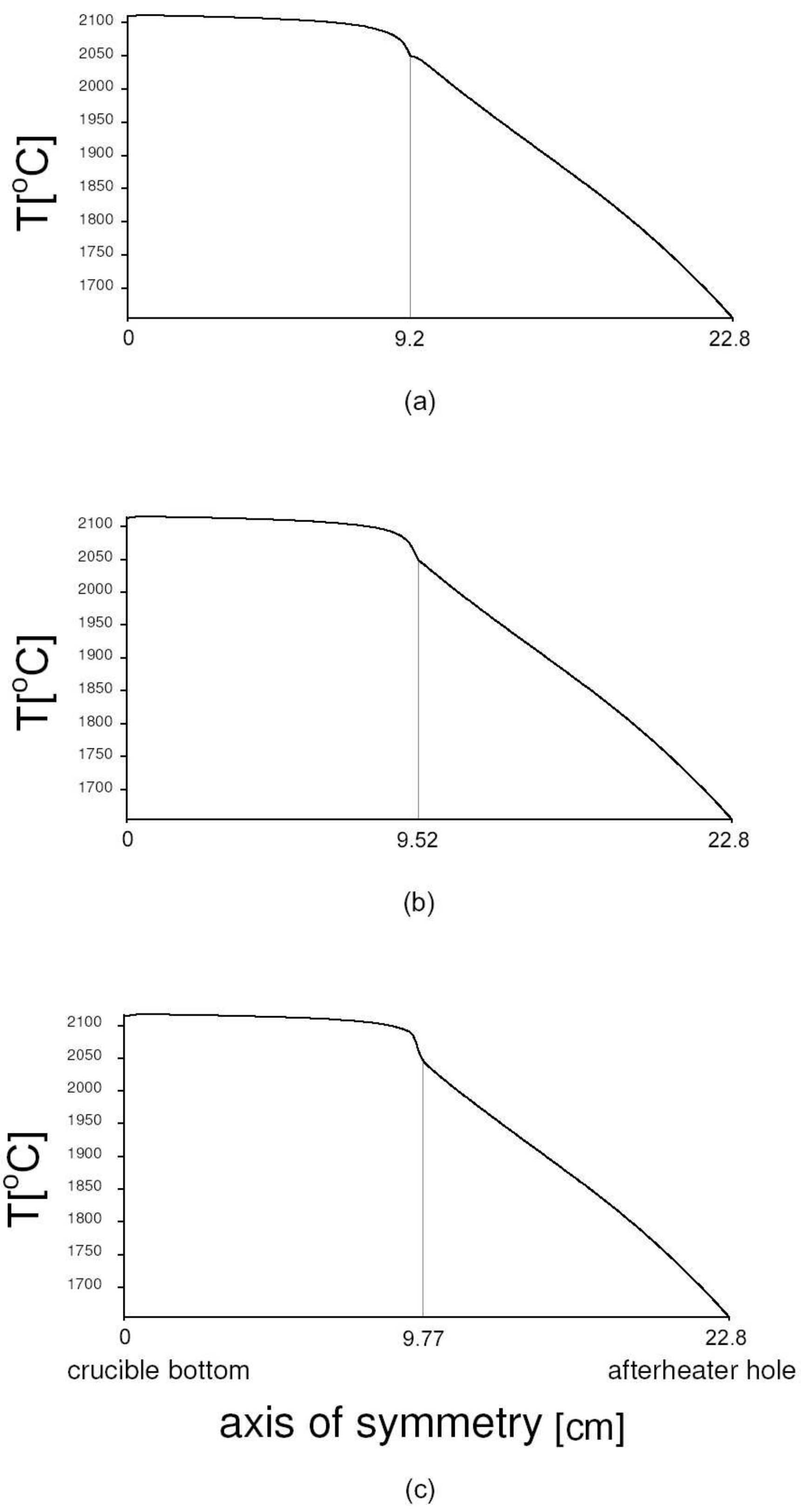

Fig. 5-c-11. Vertical temperature profiles along the axis of symmetry ($r = 0$) from crucible bottom to the afterheater hole for the configuration without a gap between crucible and afterheater, (a) $\omega_{seed} = 5\ rpm$, (b) $\omega_{seed} = 20\ rpm$ and (c) $\omega_{seed} = 30\ rpm$.

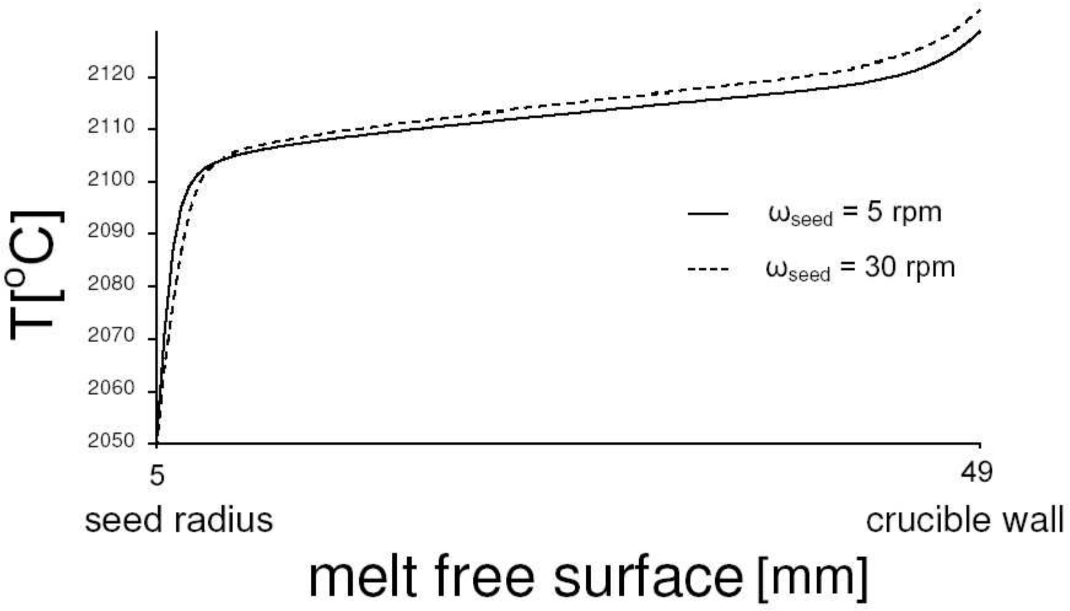

Fig. 5-c-12. Temperature profiles along the melt surface for the configuration without a gap. Average temperature gradient is $\delta\overline{T}_{melt\ surface} \sim 0.3\ ^{o}C/mm$, except in the vicinity of the crucible wall as well as the seed meniscus. Temperature gradient in the seed meniscus decreases as the seed rotation rate is increased.

result in a relatively strong rotating cell which expands outwards and downwards to occupying more space of the melt but remains still below the seed and can not spread more across the melt. It should be mentioned here that even for a high seed rotation rate, the forced convection is weaker and smaller than the thermal convection in the bulk melt ($\psi_{max}^{natural}/\psi_{max}^{forced} \sim 10^2$). The intensity of forced convection during the seeding process of CZ method depends on the seed radius (r_s) for a given seed rotation rate (ω_s). Therefore, during the initial stage the seed radius is too small ($r_{crucible}/r_{seed} \sim 10$) to produce a strong cell which can be comparably in size and intensity with the thermally-driven convection. Of course the effects of the centrifugal force due to the seed rotation are quite vigorous for the region just below the seed to build a forced convection vortex in that area. The establishment of this vortex under the seed influences markedly the mechanism of heat transfer in that portion and consequently modifies significantly the seed-melt interface shape. That we will discuss about it later.

It is noteworthy to mention that in addition to the thermally and rotationally drive vortices in the melt, there is another week and small counterclockwise vortex which is nested in the crucible meniscus (not visible). It is also generated by buoyancy and is a result of the sharp curved melt surface connected to the crucible wall.

The behavior and the effects of the azimuthal flow (v) in the melt and gas are quite different. Fig. 5-c-6 shows the distribution of azimuthal velocity contours in the melt and gas domain of both configurations for $\omega_{seed} = 20\ rpm$. The penetration of this flow component in the melt is low ($\sim 1\ cm$) but effective. It produces a forced convection cell which modifies considerably the heat transfer mechanism and temperature field in the vicinity of the crystallization front as well as the seed-melt interface shape. In the gas domain the penetration of this azimuthal flow is quite high and has been extended almost to the afterheater wall. Although it has a high penetration depth in the gas part but it can not produce any visible change of the temperature field and the heat transfer mechanism in the fluid region. This result is a consequence of the difference between the viscosity of melt and gas ($\nu_{melt}/\nu_{gas} \sim 10^3$).

Fig. 5-c-7 shows the radial velocity profiles along the melt surface from the seed side to the crucible wall for two different seed rotaion rates in the configuration with a gap. It indicates that the maximum value of the radial velocity in the melt surface is $\mathrm{v}_{max}^{melt\ surface} \simeq 0.30\ cm/s$ and about constant for different seed rotation rates. But its location is shifted towards the crucible wall if the seed rotation rate is increased. This is a result of the centrifugal force generated by the seed rotation.

In the gas domain the results are the same as case of absent seed rotation rate (*case b*). In the configuration without a gap two separate gas vortices exist, a strong and large clockwise cell above the melt surface and a weak and small counterclockwise one below the afterheater top cover. The first gas cell has been extended from the melt surface to the afterheater top cover and the second occupies only the afterheater corner. In the configuration with a gap, there are three gas convection cells in this fluid domain. There are two strong vortices with opposite direction of rotation which fill the entire afterheater as well as a part above the melt surface close to the seed meniscus. The third gas vortex which is weak and small is located in the vicinity of the gap close to the crucible wall. The gas flow is downwards along the upper half part of the seed side wall and is upwards along its lower half part. The presence of these multiple eddies in the gas part indicates a more complicated mechanism of heat transfer in this configuration than the configuration without a gap between crucible and afterheater.

In the melt, the velocity maximum is $\mathrm{v}_{max}^{melt} \simeq 0.7\ cm/s$, downwards, at the centerline for both configurations, and in the gas it is $\mathrm{v}_{max(gas)}^{without} = 36\ cm/s$ and $\mathrm{v}_{max(gas)}^{with} = 30\ cm/s$, downwards and close to the seed side wall for the configuration without and with a gap, respectively.

The increase of the seed rotation rate modifies the flow field structure in the melt domain. Consequently, the seed-melt interface shape is changed proportional to the modification of the melt flow field. As discussed previously (*case b*), in the case of no seed rotation, the flow field is of the free convection type and the interface shape is a deeply convex cone towards the melt ($\triangle H_{seed} \simeq 4\ mm$). When the rotation rate is small ($\omega_{seed} < 15\ rpm$), the free thermal convection is weakened and the interface becomes less convex. If the seed rotation rate is $\omega_{seed} = \omega_{seed}^{critical} \simeq 20\ rpm$, then the seed-melt interface has a almost flat shape. If the seed rotation rate is high ($\omega_{seed} > 20\ rpm$), then the interface shape is changed from the flat shape to the concave cone shape towards the melt. On the other hand if the seed rotation rate is increased, the seed-melt interface is deflected upwards from the changes in fluid motion which modifies the thermal gradient and heat transfer mode in the melt and gas close to the seed-melt interface. This trend agrees with the numerical [39-40,43,68,70] and experimental [25,40,64] findings for the interface shape inversion with the increase of the crystal rotation rate.

The seed-melt interface deflection ($\triangle H_{seed}$) is plotted in Fig. 5-c-8 as a function of the seed rotation rate (ω_{seed}) for both configurations resulting from our simulations. A linear variation of the interface deflection is clearly visible vs. the seed rotation rate. But the changing rate before and after the critical seed rotation rate ($\omega_{seed}^{critical} = 20\ rpm$) is somewhat different. For $\omega_{seed} < \omega_{seed}^{critical}$, $\delta H_{seed<} \sim 0.2\ mm/rpm$ and for $\omega_{seed} > \omega_{seed}^{critical}$, $\delta H_{seed>} \sim 0.25\ mm/rpm$.

The isotherm shapes are determined by the structure and dynamics of the fluid flow in the system. The temperature field in the melt domain is strongly affected by the fluid motion. The imposed seed rotation also influences the temperature field of the melt and seed, Fig. 5-c-9 and Fig. 5-c-10. In the case of absent seed rotation, the melt flow close to the seed-melt interface is of free convection type due to buoyancy and the Marangoni effect. This structure of flow in the melt leads to a deflection of the isotherms towards the seed-melt interface. In fact, the largest temperature variation of the melt is located just below the seed and indicates a high heat flux which going to the seed crystal from the melt through the seed-melt interface. As the seed rotation rate is increased from zero, the forced flow cell appears and becomes larger and stronger, and accordingly the isotherms in the melt become more deflected towards the seed. At high seed rotation rate (i.e. $\omega_{seed} > 20\ rpm$), the forced convection increases the temperature of the melt below the seed and so the isotherms are pushed up (towards the seed) especially in this part of the melt. Thus, there is a high temperature melt motion along the seed-melt interface. In this portion of melt, the isotherms are parallel unlike to the conditions of a low seed rotation rate (i.e. $\omega_{seed} < 10\ rpm$). In fact, the strength and position of the forced rotationally-driven cell allows additional heat to be convected towards the seed-melt interface, hence effectively melting it away. As has already been explained, the shape of the crystallization front is strongly affected by this flow and the seed-melt interface cone considerably deflected to the seed region.

It is important to mention that there is a dividing streamline between the thermal and forced flow. It is a stagnant surface ($\psi = 0$) and separates the free surface of the melt at the seed meniscus. This streamline forms a boundary within the fluid that separates the flow inwards from the crucible wall (thermal convection) and the moving outwards flow from the seed crystal (forced convection). The power supplied to the system, which directly produces the temperature difference across the melt and system, must compensate the additional heat transfer resistance caused by this stagnant surface between the two counter-rotating vortices. The power supplied to the crucible and afterheater is increased uniformally to maintain a constant seed diameter if the convective heat transfer in the fluid domains (i.e. melt and gas) is modified. On the other hand the temperature difference across the melt also increases linearly (increasing of T_{max}) proportional to the increasing of the seed rotation rate.

It should be noted here that the seed rotation has not any visible influence on the temperature field of the gas domain except close to the seed meniscus. Because it can not produce any resolved forced convection mode in this fluid part, as it has already been mentioned.

The isotherms are deflected upwards and towards the afterheater hole along the afterheater wall and displaced downwards in the vicinity of the seed crystal in the configuration without a gap. In the configuration with a gap, the isotherms are pushed upwards along the afterheater wall and downwards adjacent to the upper half part of the seed. The isotherms have a horizontal and parallel shape close to the gap between crucible and afterheater while they are deflected upwards along the lower half part of the seed. In the configuration without a gap, the temperature of the afterheater wall is higher than the seed when compared to the configuration with a gap between crucible and afterheater which is relatively equal. On the other hand, the temperature gradient in the afterheater of the configuration without a gap is quite high contrary to the other configuration. It means that the heat radiation exchange (i.e. wall to wall radiation) could be an important factor for the grown crystal in the configuration without a gap.

The results of the temperature calculations show that the temperature distribution in the seed crystal does not markedly depend on the flow field structure of the melt except close to the seed-melt interface, since it has a higher thermal conductivity than gas and melt. The isotherms are parallel and have a horizontal shape in this solid part except in the vicinity of the seed-melt interface. From our point of view, the formation of a thermoelastic stress (related to $|\partial^2 T/\partial z^2| > 0$) can be initiated during growth crystal with a convex or concave solidification front in the seed. In the case of low seed-rotation rate, the seed-melt interface has a convex cone shape towards the melt and the seed isotherms are not parallel close to the crystallization surface. In the part just above the seed-melt interface, the distance between isotherms in the seed core is higher than of the seed side and as a result the variation of the axial temperature gradient at the centerline is negative ($\partial^2 T/\partial z^2 < 0$). In the case of high seed-rotation rate when the seed-melt has a concave cone shape towards the melt, the distance between seed isotherms in the core is smaller than of the sides. So the variation of the axial temperature gradient at the symmetry axis of this seed part is positive ($\partial^2 T/\partial z^2 > 0$).

The maximum value of temperature is in the range of $T_{max} \simeq 2130-2136\ ^oC$ at the crucible side wall below the melt surface (1 cm and 1.2 cm in the configuration without and with a gap, respectively), and the minimum $T_{min}^{without} = 1650\ ^oC$ and $T_{min}^{with} = 1600\ ^oC$ at the afterheater hole for the configuration without and with a gap, respectively. The maximum value of temperature difference across the melt is in the range of $\triangle T_{max}^{melt} \simeq 80-86\ ^oC$ for both configurations, and for the whole system $\triangle T_{max(system)}^{without} \simeq 460-466\ ^oC$ and $\triangle T_{max(system)}^{with} \simeq 530-536\ ^oC$ for the configuration without and with a gap, respectively. These results indicate that the melt is about isothermal compared with the seed and gas domain (Fig. 5-c-1 - Fig. 5-c-3).

Temperature profiles along the symmetry axis ($r = 0$) for different seed rotation rates plotted from the crucible bottom to the afterheater hole are shown in Fig. 5-c-11 for the configuration without a gap between crucible and afterheater (similar results for the other configuration). These figure indicates that the axial temperature gradient in the seed is about linear and approximately independent on the seed rotation rate ($\delta\overline{T}_{seed\ axis}^{without} \sim 3.9\ ^oC/mm$ and $\delta\overline{T}_{seed\ axis}^{with} \sim 3.4\ ^oC/mm$) because of the high thermal conductivity of the seed and also its small diameter. This behavior of the temperature gradient is not valid close to the seed-melt interface. As it has already been discussed, the temperature variation is smaller (concave seed-melt interface) or higher (convex seed-melt interface) than these values in the cases of deflected seed-melt interface shapes.

Fig. 5-c-12 shows the temperature variation at the melt-gas interface in the configuration without a gap. This temperature gradient is about uniform with $\delta\overline{T}_{melt\ surface} \sim 0.3\ ^oC/mm$, except in the vicinity of the crucible wall (a result of the existence of the invisible, weak and counterclockwise rotating vortex in this area) as well as the seed meniscus. In the seed meniscus the temperature gradient is considerably high and is also a function of the flow pattern mode in the melt and gas, as has already been mentioned. This is a result of the interaction between the thermocapillary-buoyancy force and the centrifugal force which creates the temperature gradient in that part. As the seed rotation rate is increased and the flow is rearranged, differences in convective heat transfer in the melt and gas cause the temperature gradient in the seed meniscus to decrease as indicated by this Figure.

A different position of the afterheater with respect to the crucible alters the thermal gradients in the system and also heat radiation exchange between the imposed surfaces.

They result in a different temperature and velocity field in the melt as well as in the gas domain. The melt velocities are higher close to the melt-gas interface in the configuration without a gap compared to the other configuration. In addition, the temperature difference along the melt-gas interface and especially the temperature gradient at the seed meniscus is increased. This condition is meaningful for some materials such as scandates (spiral growth) in order to produce strong thermal convection in the melt. During Czochralski growth of some oxide materials, spiral growth is a serious problem. Instabilities in the melt temperature and flow field close to the crystal-melt interface produce a corkscrew shape of the grown crystal. This kind of acentric growth was also observed in many gallium garnet crystals such as Gadolinium gallium garnet $Gd_3Ga_5O_{12}$ (GGG), $Li_6Gd(BO_3)_3$ and Substituted gadolinium gallium garnet (SGGG). It is generally accepted that a small temperature gradient at the growth interface can result in spiral growth. Therefore, increasing temperature gradients should reduce this tendency. In order to inhibit or delay the spiral growth, increasing thermal fluid flow in the melt is required. In the gaseous phase different convection modes and temperature fields are advantageous because of the lifted upwards afterheater for preventing evaporation from seed surface.

5.3.4 case d: Flat and rounded crucible bottom

Fig. 5-d-1 shows a sketch of these two systems and the operating parameters are listed in Table 5-3. Then the non-dimensional numbers are $Gr = 1.5 \times 10^4$, $Ma = 2340$, $Rad_l = 1.17$, $Rad_i = 1.27$ and $Bio_i = 0.09$. The contact angle and deflection height of the meniscus with the crucible side wall and the seed are set to be 18^0 and 2 mm, respectively.

The aim of these calculations is to investigate the effect of a flat and a rounded crucible bottom on the fluid flow and temperature field of the system during the seeding process of CZ growth. For this two different types of the crucible: flat and rounded bottom are considered. The temperature at the afterheater top cover hole is set to be 1600 ^oC and the seed rotation rate $\omega_{seed} = 15$ rpm, for both configurations.

Induction heating

Volumetric distribution of the heat generation in the crucible and afterheater has been shown in Fig. 4-c-2 (chapter 4, *case c*) for both configurations. The maximum of heat generation for both configurations is $q_{max} \simeq 39$ W/cm^3 at the crucible bottom corner where in the configuration with the rounded crucible bottom it is $\simeq 1$ $cm \simeq r_{cb}$ distance above the position of the configuration with the flat crucible bottom. The total energy production in the crucible and afterheater is $Q^{flat}_{total} = 860$ W for the configuration of flat crucible bottom and $Q^{round}_{total} = 740$ W for the rounded bottom configuration.

Temperature and fluid flow

Fig. 5-d-2 shows the streamline pattern and isotherm distribution for both configurations. There is a strong and large vortex in the melt which comes from buoyancy in the bulk and the Marangoni effect at the melt-gas interface with $\psi^{flat}_{max(melt)} = -0.24$ and $\psi^{round}_{max(melt)} = -0.30$ for the configuration with a flat and rounded crucible bottom, respectively. In addition, a small and weak rotationally-driven convective cell also exists below the seed. The melt flows in this cell in opposite direction to the buoyancy-driven vortex.

It should be mentioned that in addition to these two types of vortices in the melt, there is another week and small counterclockwise vortex which is nested in the crucible meniscus (not visible). It is produced by the buoyancy force too and is a result of the presence of a sharp curved gas-melt interface connected to the crucible wall.

In the gas, there is a main and large vortex that flows upwards along the afterheater side wall and downwards along the seed sides with $\psi^{flat}_{max(gas)} = -6.5$ and $\psi^{round}_{max(gas)} = -8.5$, for the configuration of flat and rounded crucible bottom, respectively. There is

Description (units)	Symbel	Value
Crucible inner radius (mm)	r_c	20
Crucible thickness (mm)	l_c	2
Crucible inner height (mm)	h_c	40
Crucible bottom radius (mm)	r_{cb}	0, 10
Afterheater inner height (mm)	h_{af}	70
Afterheater hole (mm)	r_{af}	9
Distance between crucible and afterheater (mm)	D_{ca}	0
Coil inner radius (mm)	r_{co}	60
Coil thickness (mm)	l_{co}	8
Height of coil turns (mm)	h_{co}	11
Distance between coil turns (mm)	d_{co}	2
Distance between the two coils (mm)	D_{co}	30
Thickness of crucible insulation at the bottom (mm)	h_{ci}	35
Thickness of crucible insulation at the wall (mm)	d_{ci}	10
Thickness of afterheater insulation (mm)	d_{ai}	10
Melt depth (mm)	d_{melt}	35
Seed radius (mm)	r_s	5
Seed rotation rate (rpm)	ω_{seed}	15
Ambient temperature (^oC)	T_a	25

Table 5-3. Operating parameters used for calculations of *case d*.

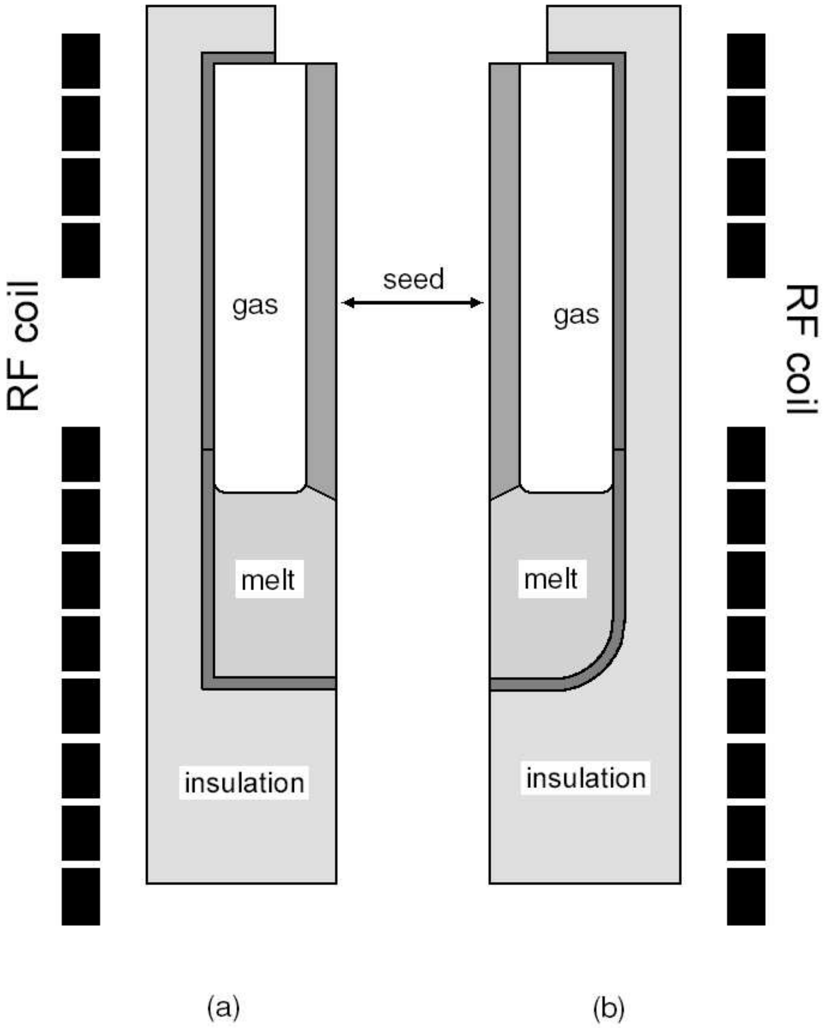

Fig. 5-d-1. A sketch of the configurations with different crucible bottom shape, (a)flat, and (b) rounded crucible bottom $r_{cb} = 10\ mm$.

also a small and weak gas eddy just above the melt surface in the opposite rotation of the first one with $\psi^{gas}_{second} = 0.02$ (Fig. 5-d-4). It arises from the mechanical coupling of melt and gas at the melt-gas interface. The maximum value of velocity for the melt is $\mathrm{v}^{flat}_{max(melt)} = 0.28\ cm/s$ and $\mathrm{v}^{round}_{max(melt)} = 0.29\ cm/s$, for the configuration of flat and rounded crucible bottom, respectively. In the gas $\mathrm{v}^{flat}_{max(gas)} = 4.0\ cm/s$ and $\mathrm{v}^{round}_{max(gas)} = 4.2\ cm/s$, downwards and close to the seed crystal.

The temperature maximum for both configurations is $T_{max} \simeq 2128\ ^oC$ and the minimum is $T_{min} = 1450\ ^oC$. Although the location of T_{min} for both configurations is at the crucible bottom insulation the position of T_{max} is different. In the configuration with a flat crucible bottom T_{max} is located in the middle of the crucible wall but in the configuration with a rounded crucible bottom is placed $\sim 1\ cm$ distance above

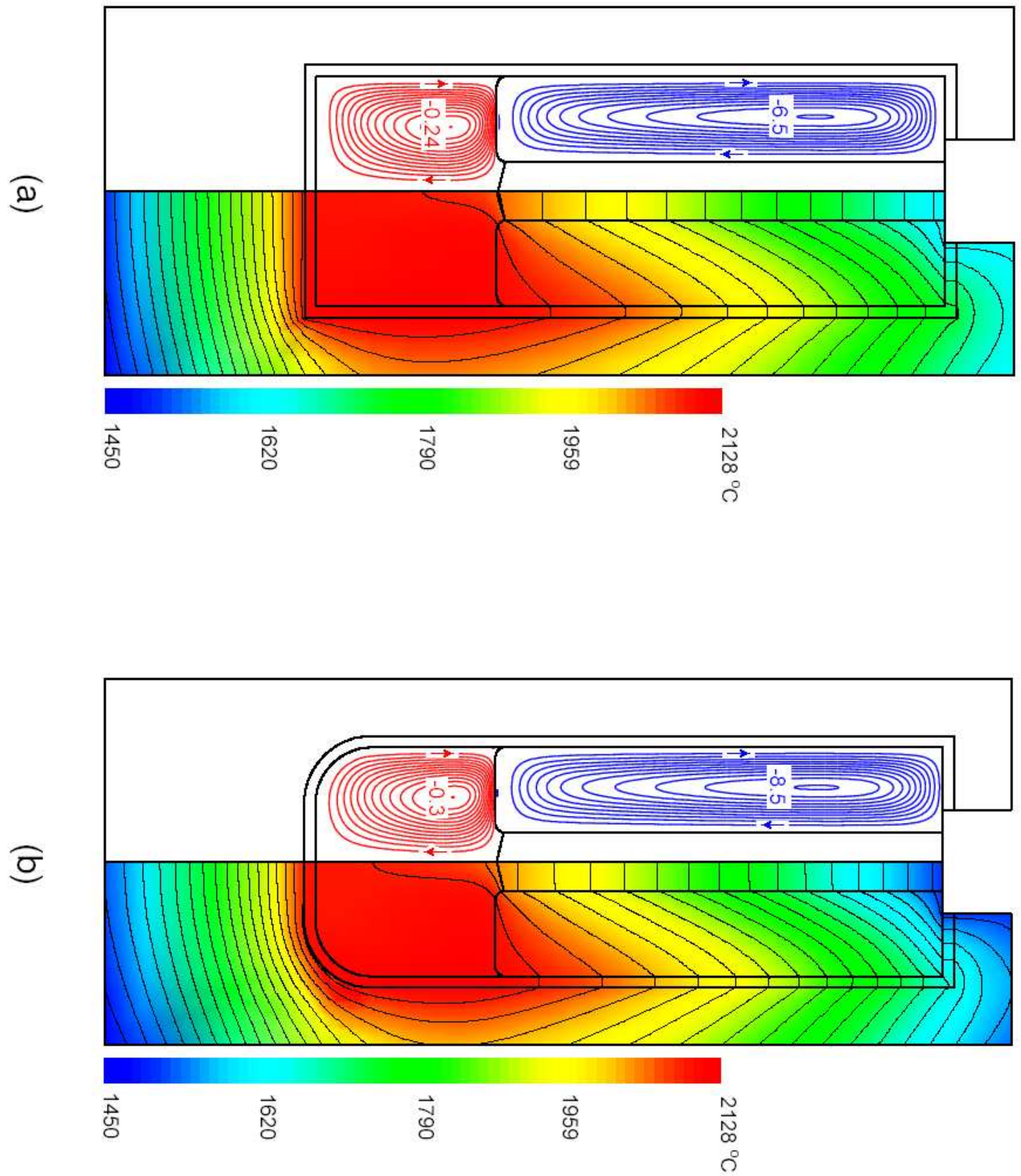

Fig. 5-d-2. Isotherms (right hand side) and stream function distribution (left hand side) for configuration with the (a) flat, and (b) rounded crucible bottom.

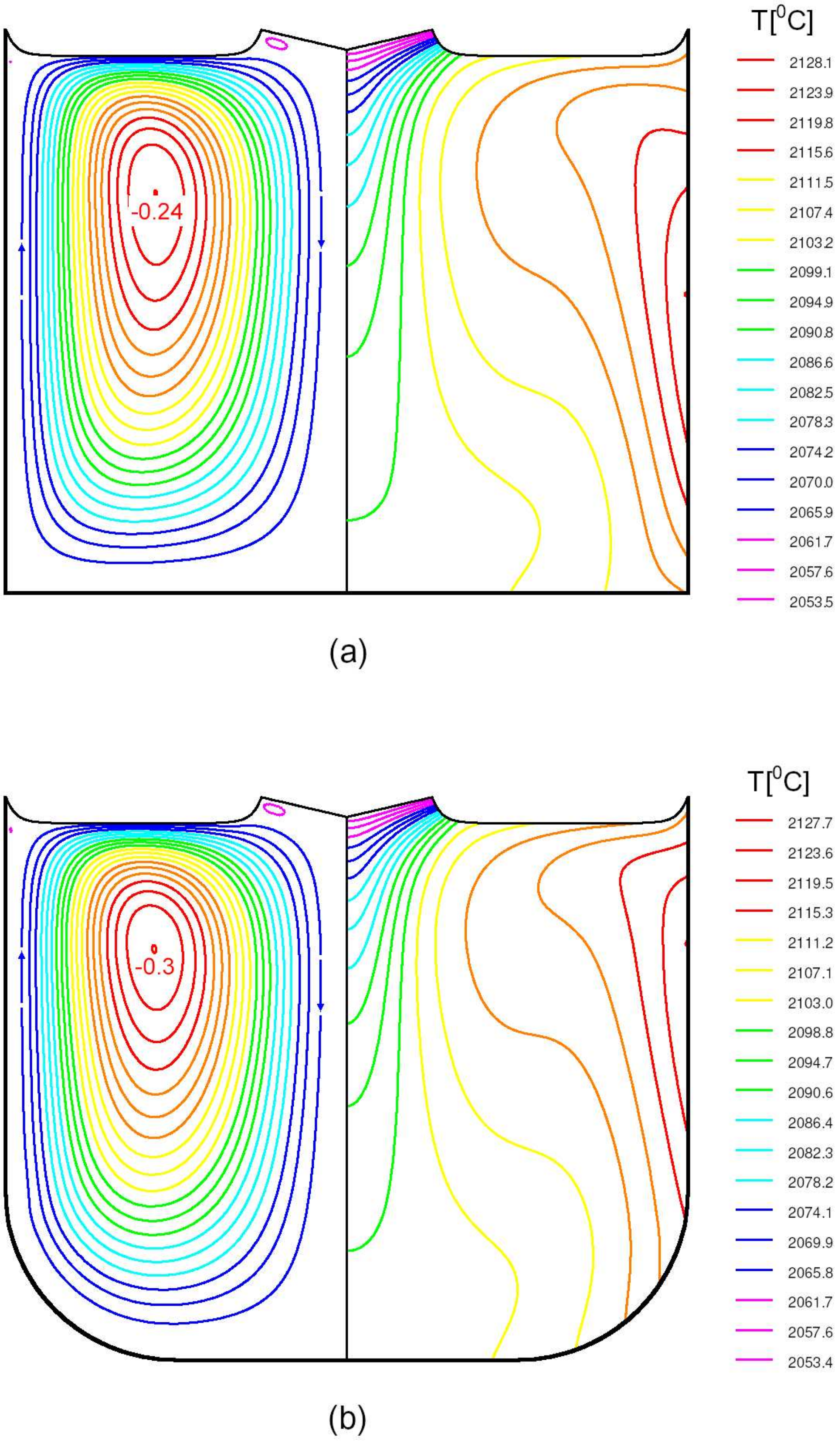

Fig. 5-d-3. Temperature (right hand side) and streamlines (left hand side) of the melt for configuration with the (a) flat, and (b) rounded crucible bottom.

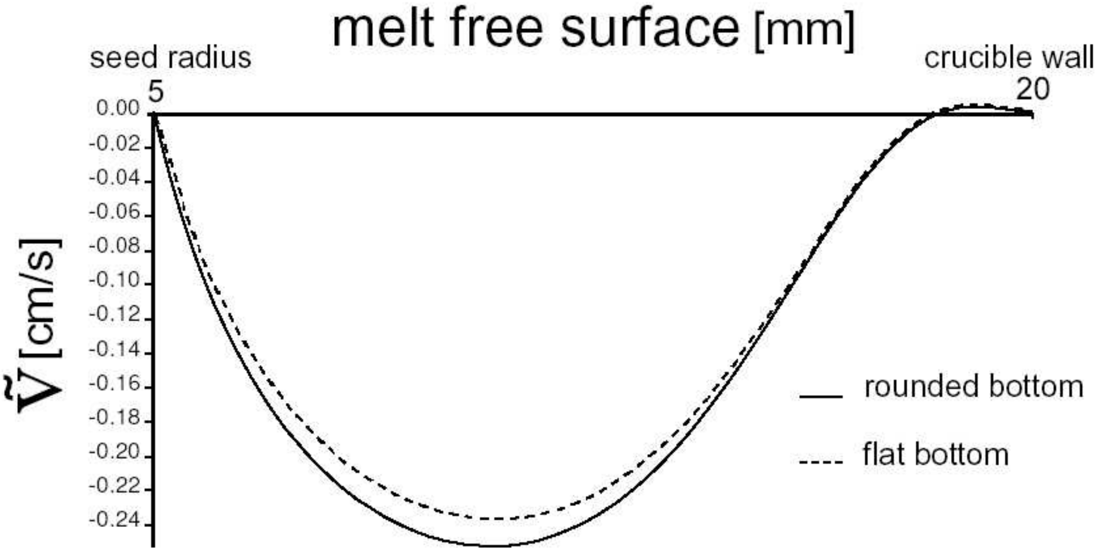

Fig. 5-d-4. Radial velocity profile at the melt surface for both configurations with the flat and rounded crucible bottom. The magnitude of $v_{max}^{melt\ surface}$ in the configuration with the rounded crucible bottom is higher (0.25 cm/s) than configuration with the flat bottom shape (0.23 cm/s).

the first configuration, as is shown in Fig. 5-d-3. There are two reasons for the lifted upwards location of the T_{max}, heat generation and fluid flow in the system. As has already been mentioned, the location of q_{max} in both configuration is at the crucible bottom corner. On the configuration with a rounded crucible bottom, the location of the crucible bottom edge is 1 cm distance above than other configuration. In the other site, in the configuration with a rounded crucible bottom the streamlines in the melt close to the bottom are aligned to the rounded bottom shape. But in the configuration with a flat bottom shape, they have been pushed towards the bottom corner. This difference between the streamline patterns in the melt indicates that the melt velocity close to the crucible wall is higher in the configuration with a rounded crucible bottom. As a result, the difference between melt motion pattern in the vicinity of the crucible bottom and side wall as well as the location of q_{max} lead to a relatively stronger thermal convection in the configuration with a rounded crucible bottom.

This lifting of T_{max} location increases the melt velocity and as a result thermal convection of the molten material, i.e. $\psi_{max(melt)}^{round} > \psi_{max(melt)}^{flat}$. Fig. 5-d-4 represents the radial velocity (v) at the melt surface. It indicates that the magnitude of $v_{max}^{melt\ surface}$ in the configuration with a rounded crucible bottom is higher ($\sim$ 0.02 cm/s) than at the configuration with a flat bottom shape.

In Czochralski growth of various kinds of oxide single crystals such as scandates ($DyScO_3$ and $SmScO_3$), peculiar growth morphology so-called "spiral" or "footing" growth sometimes appears, even when the growth parameters are well controlled. Particularly, it has been observed that the spiral growth started at early stages of the pulling, when the melt level in a crucible decreased. The spiral growth is detrimental not only for the shape of the crystal but also for its crystal quality. Therefore, this morphology should be avoided in order to grow large and long single crystals in practical applications. Small radial temperature gradient beneath the melt surface is one of the main factors that can cause this unstable growth. Therefore, the radial temperature gradient must be as large as possible so as to enhance the thermal convection in the melt, which must limit the initial growth of spiral at the meniscus part. Changing the crucible bottom to a rounded shape creates a larger temperature gradient difference between the radial and vertical direction in the crucible, which has a more positive effect in preventing this serious growth problem.

The seed-melt interface has a conic shape with a height of $\triangle H_{seed}^{flat} = 1.1\ mm$ and $\triangle H_{seed}^{round} = 1.4\ mm$ towards the melt for the configuration with a flat and rounded crucible bottom, respectively. This $0.3\ mm$ difference between the seed-melt interface deflections represents a stronger thermal convection in the configuration with a rounded crucible bottom than the configuration of a flat crucible bottom, as has already been explained.

The maximum value of the temperature difference across the melt is $\triangle T_{max}^{melt} \simeq 80\ {}^oC$ and for the whole system $\triangle T_{max}^{system} \simeq 680\ {}^oC$, for both configurations,.

5.4 Conclusions

We have performed an axisymmetric two-dimensional quasi-steady-state modeling and numerical simulations for the seeding process of some real Czochralski systems in particular sapphire growth. Our modeling includes the induction heating in the metallic parts, heat conduction in the solid parts (i.e. crucible, afterheater, thermal insulation and seed), and heat conduction and convection in the fluid parts (melt and gas).

In an oxide Czochralski crystal growth system, the melt flow is relatively slow ($\mathrm{v}_{max}^{melt} \sim 10^{-1}\ cm/s$) and the gas velocity is high ($\mathrm{v}_{max}^{gas} \sim 10\ cm/s$). This is not surprising because of the high density and high viscosity of the molten material and vise versa for the gas. Although the melt motion is slow compared to the gas flow it is one of the hottest part in the system and its circulation is a substantial source of heat transfer in the system. The maximum temperature (T_{max}) in the system occurs along the crucible sidewall and some times close to the melt surface. This temperature of the sidewall decreases gradually and linearly towards the crucible bottom. Thermal convection in the melt cools significant portions of the heated crucible wall, thus decreasing the temperature at the lower part of it and as a result it lifts the location of T_{max} upwards with respect to the position of q_{max}. On the other hand, thermal convection in the gas considerably cools the melt surface, seed and afterheater wall. Especially the temperature gradient within and around the crystal is very important because of thermoelastic stresses, dislocation and other structural defects, cracks and evaporation. Consequently, the melt and gas of an oxide CZ system do not behave as passive fluid domains with simple boundary conditions. There is a strong coupling between the melt and gas flow and the overall heat transfer of the oxide CZ system. In the melt, temperature decreases as one approaches the symmetry axis ($r = 0$) and the seed-melt interface. But in the seed crystal the temperature is uniform as one approaches the centerline except close to the seed-melt interface. This is obvious by the horizontal isotherms in the seed domain and indicates that heat is essentially flowing out of the seed in axial direction but within the melt in the radial direction and towards the seed-melt interface.

If there is no seed rotation, the melt flow close to the seed-melt interface is of thermal convection type due to buoyancy and the Marangoni effect. As the seed rotation rate is increased from zero, initially the thermal convection becomes weaker and simultaneously a small and weak forced convection vortex will be present just under the seed-melt interface and close to the edge of the seed. Further increase of the seed rotation rate will result in a relatively strong forced convection just under the seed-melt interface, but this forced flow is still weaker and smaller than that arising from the thermally induced convection even for a high seed rotation rate. This vortex flows upwards at the melt symmetry axis, outwards along the seed-melt interface and opposite with respect to the

Fig. 5-e-1. A photo of a sapphire seed with a conic interface shape, which is predicted by our calculations.

flow circulation driven by buoyancy.

The calculations also show the effect of melt and gas convection on the shape of the seed-melt interface. If the seed rotation rate (ω_{seed}) increases, the seed-melt interface changes from convex to concave looking from the melt. According to these changes, the temperature difference across the melt ($\triangle T_{max}^{melt}$) also increases as indicated by increasing T_{max} (and q_{max}). This is caused by the increased forced convection across the melt especially close to the seed-melt interface, the heat generation has to be increased to maintain the seed radius.

So far, we have discussed the effects of the operating conditions on the interface shape based on the numerical predictions obtained in this chapter. These numerical predictions agree at least qualitatively with the experimental results obtained in our Czochralski-dielectric lab in IKZ, Fig. 5-e-1. These numerical studies enable us to understand better the physics underlying the deformation of the seed-melt interface shape.

Observations of the melt flow structure in our results support this point that as heat leaves the melt through the crucible bottom insulation (crucible bottom cooling), the pure buoyancy driven convection in the melt becomes slow and more stratified.

From these calculations, we also obtained the following conclusions:

1) The calculations reported here surely can aid working out the equipment and control strategies.

2) Natural and thermal Marangoni convection are important factors in the heat transfer of the molten material. Although the melt motion is relatively slow there is a strong coupling between the melt flow and the overall heat transfer of the oxide CZ system.

3) The temperature and flow field in the afterheater strongly depends on its position. The temperature at the afterheater hole becomes smaller when the afterheater is lifted upwards with respect to the crucible. As a result the heat radiation loss from the melt surface is stronger and therefore the temperature gradient in the melt is modified. Shifted downwards the T_{max} location, causes reduction of the temperature gradient at the seed meniscus and so a weaker thermal convection in the melt is the main result of this modification.

4) Any change in the heating facilities of the high-temperature Czochralski puller can strongly affect the thermal conditions of the system. On the other hand, the overall heat transfer in the CZ system is quite sensitive to any change in the configuration, which is well-known in practice.

5) Any change in the insulation modifies the total amount of heat loss and also the temperature distribution in the crucible and afterheater. The corresponding temperature profile of the crucible and afterheater influences the heat transfer mechanism through the system.

6) In oxide CZ growth, the flows driven by thermal gradients and the temperature distribution are strongly coupled to each other.

7) In the case of no seed rotation ($\omega_{seed} = 0$), the flow pattern in the melt domain consists of a single circulation of slow fluid flow.

8) During the seeding process, the thermal convection dominates in the melt flow. In the cases of seed rotation only a small and weak rotational vortex is present under the seed.

9) The results presented here demonstrate the important role played by seed rotation in forming the shape of the seed-melt interface during the seeding process of CZ growth.

10) The seed-melt interface shape is quite sensitive to the convective heat transfer in the melt and gas domain.

11) When the local flow close to the seed-melt interface is formed mainly by natural convection and the Marangoni effect, the interface becomes convex towards the melt.

12) When the local flow under the seed-melt interface is of the forced convection flow type generated by seed rotation, the interface becomes more concave towards the melt as the intensity of the forced convection increases (i.e. increasing of the seed rotation rate).

13) Using a crucible with a rounded bottom shape leads to lifting upward the T_{max} location and a relatively stronger thermal convection in the system exists compared to a flat crucible bottom. This modification of geometrical conditions has a positive effect in preventing or delaying the spiral growth and allowes growing large and long single crystal.

Chapter 6

Towards the three-dimensional calculation

6.1 Introduction

In previous chapters, we successfully simulated the seeding process of the oxide Czochralski crystal growth systems with the assumptions of axisymmetric (two-dimensional) and steady state conditions using the induction heating as the source for temperature and fluid flow calculation. The influences of some items such as afterheater position, seed rotation rate and crucible bottom shape on the temperature and flow field of some real systems, were explained via extensive numerical studies. The employed mathematical model and numerical method (Galerkin finite element method), proved to be robust and efficient.

Although axisymmetric steady-state conditions represent much of the phenomena in the Czochralski crystal growth, three-dimensional flows are common during the real growth processes [18,20]. As we observed in the axisymmetric steady-state calculations, flow patterns in the melt and gas domains strongly affect the heat transfer mechanism through the entire system. So three-dimensional flows and temperature gradients are expected to make the global heat transfer different from that of the axisymmetric cases, especially when the CZ system has not axisymmetric conditions and/or geometry. In several real CZ systems the non-axisymmetric conditions dominate with respect to temperature and flow pattern. The non-axisymmetric conditions lead to non-axisymmetric flows and temperature distribution and consequently modify the convective heat transfer through the system, which in turn, affect the quality of a grown crystal. For example, high-melting oxide and spiral growth are well known non-axisymmetric conditions during the growth process. Prediction of non-axisymmetric phenomena and understanding their physical mechanisms are necessary to find means of growth control, which is required to growth a single crystal. In numerical studies on the oxide CZ growth, most investigations were limited to three-dimensional melt flow in an axisymmetric geometry of the system [47,49,52,53,57,62,63,65]. But, since the real shape of the growth furnace is sometimes not completely axisymmetric, three-dimensional (3D) global modeling is essential and also of great interest.

Having an observation window in the oxide CZ growth is common for observation and controlling the crystal diameter and the growth process, Fig. 6-1. Using this small observation window in the afterheater breaks the axisymmetric conditions. The observation window in the CZ furnace produces a complicated three-dimensional gas flow in the system and represents one of the most interesting problems of numerical modeling. We choose this configuration of a CZ system containing only gas as a benchmark for our initial three-dimensional simulation because it is widely used in the CZ furnaces for oxide crystals in our lab. In addition, three-dimensional simulation of the full CZ system including gas, melt and crystal would be possible, using our knowledge and experience from this initial three-dimensional calculation.

Simulating three-dimensional flows using previous computation algorithms, which have been successfully used for axisymmetric simulations, has generally failed because of the limits of computer capacities. Adding another dimension to the axisymmetric steady-state simulations means significantly increasing the size of data and number of computational operations. This consumes much more computer memory and a certain amount of CPU time for calculation.

In this chapter, we employ a finite element methodology using the ENTWIFE package on a PC-cluster for simulating three-dimensional, steady-state incompressible flow in a CZ growth system containing only gas. Therefore the gas flow is driven only by buoyancy. Clearly, this is a simplified model which does not account for melt and seed (crystal) and so for many important phenomena in these parts of the setup. But it allows us to study some main features raising from a non-axisymmetric geometry of the system and its influences on the gas flow pattern inside the CZ apparatus.

6.2 Mathematical model

In axisymmetric calculations, the axis of symmetry ($r = 0$ in the cylindrical coordinate system) is considered as a boundary of the mathematical domain where the symmetry conditions are imposed. But in non-axisymmetric cases, it is not a boundary and no symmetry conditions exist.

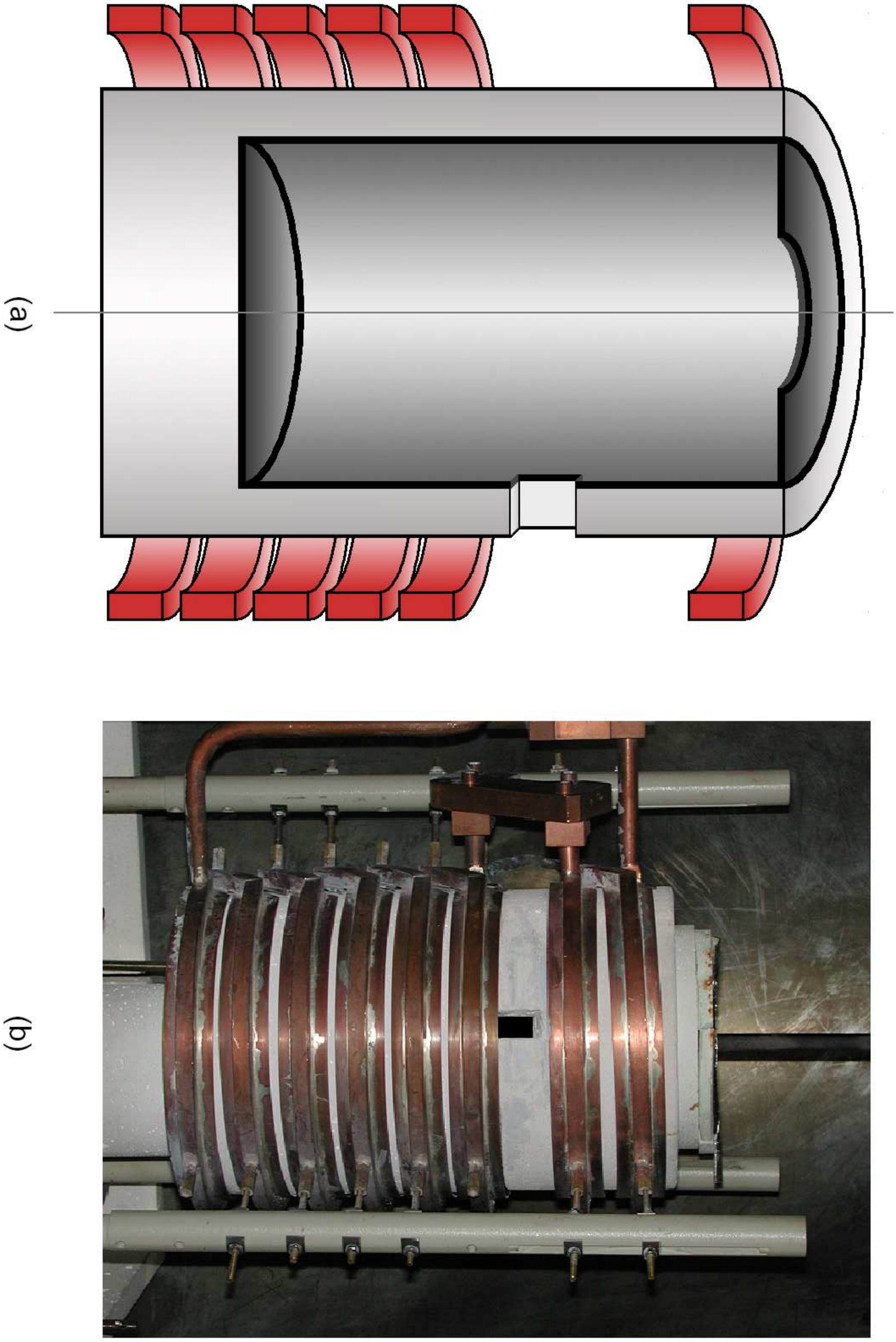

Fig. 6-1. Czochralski crystal growth system with an observation window, (a) a schematic diagram and (b) a photo (from our Czochralski-dielectrics lab in *IKZ*).

6.2.1 Induction heating

As we have described in chapter 2, it is physically reasonable and computationally very cost-effective to ignore the helicity (pitch) of the heater coils and thus assume that $\mathbf{J} = \mathbf{e}_\phi J_\phi$; i.e., the current flows only in the azimuthal direction - both in the coil and (via induction) in the conductors. This easily leads to the simplification that the (scalar) governing equation is now

$$\frac{\partial}{\partial r}\left[\frac{1}{r}\frac{\partial}{\partial r}\left(rA_\phi\right)\right] + \frac{1}{r^2}\frac{\partial^2 A_\phi}{\partial \varphi^2} + \frac{\partial^2 A_\phi}{\partial z^2} = -\mu J_\phi \tag{6.1}$$

where $A_\phi = A_\phi(r,\phi,z)$. For $\psi_B\left(r,\phi,z,t\right) \equiv rA_\phi\left(r,\phi,z,t\right)$ (i.e. *magnetic stream function*),

$$\frac{\partial}{\partial r}\left(\frac{1}{r}\frac{\partial \psi_B}{\partial r}\right) + \frac{1}{r^3}\frac{\partial^2 \psi_B}{\partial \varphi^2} + \frac{\partial}{\partial z}\left(\frac{1}{r}\frac{\partial \psi_B}{\partial z}\right) = -\mu J_\phi \tag{6.2}$$

which is the equation that will be solved numerically - once J_ϕ and boundary conditions are specified.

If we assume the driving current in the coil as

$$J_\phi = J_0 \cos \omega t$$

we can find a solution of the form

$$\psi_B\left(r,\varphi,z,t\right) = C\left(r,\varphi,z\right)\cos\omega t + S\left(r,\varphi,z\right)\sin\omega t \tag{6.3}$$

where $C\left(r,\varphi,z\right)$ is the in-phase component and $S\left(r,\varphi,z\right)$ is the out-of-phase component of the solution. The final coupled linear second-order equations are thus

$$\frac{\partial}{\partial r}\left(\frac{1}{r}\frac{\partial C}{\partial r}\right) + \frac{1}{r^3}\frac{\partial^2 C}{\partial \varphi^2} + \frac{\partial}{\partial z}\left(\frac{1}{r}\frac{\partial C}{\partial z}\right) = \begin{cases} -\mu J_0 & \text{in the coil} \\ \dfrac{\mu\sigma_e\omega}{r}S & \text{in the conductors} \\ 0 & \text{elsewhere} \end{cases} \tag{6.4}$$

$$\frac{\partial}{\partial r}\left(\frac{1}{r}\frac{\partial S}{\partial r}\right)+\frac{1}{r^3}\frac{\partial^2 S}{\partial \varphi^2}+\frac{\partial}{\partial z}\left(\frac{1}{r}\frac{\partial S}{\partial z}\right)=\begin{cases}0 & \text{in the coil}\\ -\dfrac{\mu\sigma_e\omega}{r}C & \text{in the conductors}\\ 0 & \text{elsewhere}\end{cases} \tag{6.5}$$

For the volumetric heat generation rate,

$$q\left(r,\varphi,z\right) \;=\; \frac{\sigma_e\omega^2}{2r^2}\left(C^2+S^2\right) \tag{6.6}$$

This is the function that will be used as a source term in the heat transport equation.

Weak form calculation

The weak form of the equations (6.4) and (6.5) for $C\left(r,\varphi,z\right)$ and $S\left(r,\varphi,z\right)$ are

$$\iiint\left(\frac{\partial C}{\partial r}\frac{\Phi_c}{r}+\frac{\partial C}{\partial r}\frac{\partial \Phi_c}{\partial r}+\frac{1}{r^3}\frac{\partial C}{\partial \varphi}\frac{\partial \Phi}{\partial \varphi}+\frac{\partial C}{\partial z}\frac{\partial \Phi_c}{\partial z}\right)\,\mathrm{d}r\,\mathrm{d}\varphi\,\mathrm{d}z$$

$$=\begin{cases}-\mu J_0\displaystyle\iiint \Phi_c\; r\,\mathrm{d}r\,\mathrm{d}\varphi\,\mathrm{d}z & \text{in the coil}\\ \mu\sigma_e\omega\displaystyle\iiint S\Phi_c\; r\,\mathrm{d}r\,\mathrm{d}\varphi\,\mathrm{d}z & \text{in the conductors}\\ 0 & \text{elsewhere}\end{cases} \tag{6.7}$$

$$\iiint\left(\frac{\partial S}{\partial r}\frac{\Phi_s}{r}+\frac{\partial S}{\partial r}\frac{\partial \Phi_s}{\partial r}+\frac{1}{r^3}\frac{\partial S}{\partial \varphi}\frac{\partial \Phi}{\partial \varphi}+\frac{\partial S}{\partial z}\frac{\partial \Phi_s}{\partial z}\right)\,\mathrm{d}r\,\mathrm{d}\varphi\,\mathrm{d}z$$

$$=\begin{cases}0 & \text{in the coil}\\ -\mu\sigma_e\omega\displaystyle\iiint C\Phi_s\; r\,\mathrm{d}r\,\mathrm{d}\varphi\,\mathrm{d}z & \text{in the conductors}\\ 0 & \text{elsewhere}\end{cases} \tag{6.8}$$

For the volumetric heat generation rate $q\left(r,\varphi,z\right)$, the weak form is

$$\iiint\left[q-\frac{\sigma_e\omega^2}{2r^2}\left(C^2+S^2\right)\right]\Phi_q\; r\,\mathrm{d}r\,\mathrm{d}\varphi\,\mathrm{d}z=0 \tag{6.9}$$

6.2.2 Temperature and flow field

Our model for three-dimensional calculation involves the following basic assumptions: (1) The system is in the steady state, (2) Internal radiation is not included, (3) There is no melt and crystal in the system. (5) The gas is an incompressible Newtonian fluid satisfying the Boussinesq approximation. Thus the fundamental equations are,
(a) Fluid flow in gas:

$$\rho \mathbf{v} \cdot \nabla \mathbf{v} = -\nabla p + \mu \nabla^2 \mathbf{v} + \rho \beta g (T - T_0) \vec{e}_z \tag{6.10}$$

which is the Navier-Stokes equation with Boussinesq approximation.
(b) continuity equation:

$$\nabla \cdot \mathbf{v} = 0 \tag{6.11}$$

(c) Heat transport by conduction and convection (energy equation):

$$\alpha \nabla^2 T_g - \mathbf{v} \cdot \nabla T_g = 0 \qquad \text{convection and conduction in the gas} \tag{6.12}$$

$$\nabla^2 T_c + q = 0 \qquad \text{conduction in the crucible and afterheater} \tag{6.13}$$

$$\nabla^2 T_i = 0 \qquad \text{conduction in the insulation} \tag{6.14}$$

where the subscripts g, c and i denote gas, conductors (crucible and afterheater) and insulation, respectively. The boundary conditions are,
a) at bottom and wall of the crucible, afterheater wall and top cover:

$$\mathbf{v} = 0 \tag{6.15}$$

b) at the outer surfaces of insulation:

$$-k_i \frac{\partial T_i}{\partial \hat{n}} = h_i \left(T_i - T_a\right) + \sigma \varepsilon_i \left(T_i^4 - T_a^4\right) \tag{6.16}$$

which denotes the heat dissipation via radiation and convection from those surfaces.
c) at the afterheater hole:

$$T = T_{ah} \tag{6.17}$$

where $\mathbf{v} = (u, v, w)$ is the fluid velocity vector, p the pressure, T the temperature, $\vec{e}_z$ the z-directional unit vector, g the acceleration due to gravity, β the thermal expansion coefficient, μ the dynamic viscosity, α the thermal diffusivity, q the heat source density, ε

the emissivity, k the thermal conductivity, ρ the density, h the Newtonian heat transfer coefficient, $\hat{n}$ the unit normal vector, σ the Stefan-Boltzmann constant, T_a the ambient temperature and T_{ah} the temperature at the afterheater hole.

Weak form calculation

To solve the equations which are appropriate for numerical computation using the finite element method, similar to the previous chapters at first we write the components of the governing equations and BCs in cylindrical coordinates (r, ϕ, z), then we calculate their weak form and finally the non-dimensional form of the weak form.

(a) Fluid flow

Components of the Navier-Stokes equation with Boussinesq approximation (Eq. 6.10) in the cylindrical coordinates are as:

$$\begin{cases} u\dfrac{\partial u}{\partial r} + \dfrac{v}{r}\dfrac{\partial u}{\partial \varphi} + w\dfrac{\partial u}{\partial z} - \dfrac{v^2}{r} = -\dfrac{1}{\rho}\dfrac{\partial p}{\partial r} + \nu\left[\left(\nabla^2 u - \dfrac{u}{r^2}\right) - \dfrac{2}{r^2}\dfrac{\partial v}{\partial \varphi}\right] \\ u\dfrac{\partial v}{\partial r} + \dfrac{v}{r}\dfrac{\partial v}{\partial \varphi} + w\dfrac{\partial v}{\partial z} + \dfrac{uv}{r} = -\dfrac{1}{\rho r}\dfrac{\partial p}{\partial \varphi} + \nu\left[\left(\nabla^2 v - \dfrac{v}{r^2}\right) + \dfrac{2}{r^2}\dfrac{\partial u}{\partial \varphi}\right] \\ u\dfrac{\partial w}{\partial r} + \dfrac{v}{r}\dfrac{\partial w}{\partial \varphi} + w\dfrac{\partial w}{\partial z} = -\dfrac{1}{\rho}\dfrac{\partial p}{\partial z} + \nu\nabla^2 w + g\beta\left(T - T_0\right) \end{cases} \tag{6.18}$$

where $\nabla^2 \equiv \frac{1}{r}\frac{\partial}{\partial r}\left(r\frac{\partial}{\partial r}\right) + \frac{1}{r^2}\frac{\partial^2}{\partial \varphi^2} + \frac{\partial}{\partial z^2}$ is the *Laplacian operator.* We have $\nu = \mu/\rho$ where ν is the kinematic viscosity and assume $T_0 = 0$.

Weak form

The weak form of the set of equations (6.18) is as:

$$
\begin{aligned}
&\iiint \left\{ \left[u\frac{\partial u}{\partial r} + \frac{v}{r}\frac{\partial u}{\partial \varphi} + w\frac{\partial u}{\partial z} - \frac{v^2}{r} + \nu\left(\frac{u}{r^2} + \frac{2}{r^2}\frac{\partial v}{\partial \varphi}\right)\right]\Phi_u - \frac{p}{\rho}\left(\frac{\partial \Phi_u}{\partial r} + \frac{\Phi_u}{r}\right) \right. \\
&\left. + \nu\left(\frac{\partial u}{\partial r}\frac{\partial \Phi_u}{\partial r} + \frac{1}{r^2}\frac{\partial u}{\partial \varphi}\frac{\partial \Phi_u}{\partial \varphi} + \frac{\partial u}{\partial z}\frac{\partial \Phi_u}{\partial z}\right)\right\} r\,\mathrm{d}r\,\mathrm{d}\varphi\,\mathrm{d}z \\
+ &\iiint \left\{ \left[u\frac{\partial v}{\partial r} + \frac{v}{r}\frac{\partial v}{\partial \varphi} + w\frac{\partial v}{\partial z} + \frac{uv}{r} + \nu\left(\frac{v}{r^2} - \frac{2}{r^2}\frac{\partial u}{\partial \varphi}\right)\right]\Phi_v - \frac{p}{\rho}\frac{\partial \Phi_v}{\partial \varphi} \right. \\
&\left. + \nu\left(\frac{\partial v}{\partial r}\frac{\partial \Phi_v}{\partial r} + \frac{1}{r^2}\frac{\partial v}{\partial \varphi}\frac{\partial \Phi_v}{\partial \varphi} + \frac{\partial v}{\partial z}\frac{\partial \Phi_v}{\partial z}\right)\right\} r\,\mathrm{d}r\,\mathrm{d}\varphi\,\mathrm{d}z \qquad (6.19) \\
+ &\iiint \left[\left(u\frac{\partial w}{\partial r} + \frac{v}{r}\frac{\partial w}{\partial \varphi} + w\frac{\partial w}{\partial z} - g\beta T\right)\Phi_w - \frac{p}{\rho}\frac{\partial \Phi_w}{\partial z} \right. \\
&\left. + \nu\left(\frac{\partial w}{\partial r}\frac{\partial \Phi_w}{\partial r} + \frac{1}{r^2}\frac{\partial w}{\partial \varphi}\frac{\partial \Phi_w}{\partial \varphi} + \frac{\partial w}{\partial z}\frac{\partial \Phi_w}{\partial z}\right)\right] r\,\mathrm{d}r\,\mathrm{d}\varphi\,\mathrm{d}z = 0
\end{aligned}
$$

where Φ is the weighting function.

Non-dimensional form

By using $(R, Z) = (r, z)/L_c$, $(U, V, W) = (u, v, w)/U_c$, $\Theta = T/T_c$, $P = p/\rho U_c^2$ and $U_c = \nu/L_c$, where L_c is the characteristic length, U_c the characteristic velocity and T_c the characteristic temperature, the non-dimensional form is,

$$\iiint \Bigg[\left(U\frac{\partial U}{\partial R}+\frac{V}{R}\frac{\partial U}{\partial \varphi}+W\frac{\partial U}{\partial Z}-\frac{V^2}{R}+\frac{U}{R^2}+\frac{2}{R^2}\frac{\partial V}{\partial \varphi}\right)\Phi_u - P\left(\frac{\partial \Phi_u}{\partial R}+\frac{\Phi_u}{R}\right)$$

$$+\frac{\partial U}{\partial R}\frac{\partial \Phi_u}{\partial R}+\frac{1}{R^2}\frac{\partial U}{\partial \varphi}\frac{\partial \Phi_u}{\partial \varphi}+\frac{\partial U}{\partial Z}\frac{\partial \Phi_u}{\partial Z}\Bigg]\; R\,\mathrm{d}R\,\mathrm{d}\varphi\,\mathrm{d}Z$$

$$+\quad \iiint \Bigg[\left(U\frac{\partial V}{\partial R}+\frac{V}{R}\frac{\partial V}{\partial \varphi}+W\frac{\partial V}{\partial Z}+\frac{UV}{R}+\frac{V}{R^2}-\frac{2}{R^2}\frac{\partial U}{\partial \varphi}\right)\Phi_v - P\frac{\partial \Phi_v}{\partial \varphi}$$

$$+\frac{\partial V}{\partial R}\frac{\partial \Phi_v}{\partial R}+\frac{1}{R^2}\frac{\partial V}{\partial \varphi}\frac{\partial \Phi_v}{\partial \varphi}+\frac{\partial V}{\partial Z}\frac{\partial \Phi_v}{\partial Z}\Bigg]\; R\,\mathrm{d}R\,\mathrm{d}\varphi\,\mathrm{d}Z$$

$$+\quad \iiint \Bigg[\left(U\frac{\partial W}{\partial R}+\frac{V}{R}\frac{\partial W}{\partial \varphi}+W\frac{\partial W}{\partial Z}-Gr\cdot\Theta\right)\Phi_w$$

$$+\frac{\partial W}{\partial R}\frac{\partial \Phi_w}{\partial R}+\frac{1}{R^2}\frac{\partial W}{\partial \varphi}\frac{\partial \Phi_w}{\partial \varphi}+\left(\frac{\partial W}{\partial Z}-P\right)\frac{\partial \Phi_w}{\partial Z}\Bigg]\; R\,\mathrm{d}R\,\mathrm{d}\varphi\,\mathrm{d}Z = 0 \qquad (6.20)$$

where $Gr = g\beta T_c L_c^3/\nu^2$ is the *Grashof number.*

(b) Continuity equation

From Eq. (6-11) we have

$$\nabla.\mathbf{v} = 0 \;\longrightarrow\; \frac{\partial u}{\partial r}+\frac{1}{r}\frac{\partial v}{\partial \varphi}+\frac{u}{r}+\frac{\partial w}{\partial z} = 0 \qquad (6.21)$$

So the weak form is as:

$$\iiint \left(\frac{\partial u}{\partial r}+\frac{1}{r}\frac{\partial v}{\partial \varphi}+\frac{u}{r}+\frac{\partial w}{\partial z}\right)\Phi_c\; r\,\mathrm{d}r\,\mathrm{d}\varphi\,\mathrm{d}z = 0 \qquad (6.22)$$

and the non-dimensional form:

$$\iiint \left(\frac{\partial U}{\partial R}+\frac{1}{R}\frac{\partial V}{\partial \varphi}+\frac{U}{R}+\frac{\partial W}{\partial Z}\right)\Phi_c\; R\,\mathrm{d}R\,\mathrm{d}\varphi\,\mathrm{d}Z = 0 \qquad (6.23)$$

(c) Energy equation

From Eq.s (6-12)-(6-14) and $\alpha = k/\rho c_p$, where α is the thermal diffusivity and c_p the specific heat at constant pressure, we can calculate the weak form of the energy equations.

Weak form

$$
\begin{aligned}
& k_c \iint\limits_{crucible} \int \left(\nabla T_c \cdot \nabla \Phi_{ce} - \frac{q}{k_c} \Phi_{ce} \right) \, r \, \mathrm{d}r \, \mathrm{d}\varphi \, \mathrm{d}z \\
+ \quad & k_i \iint\limits_{insulation} \int \nabla T_i \cdot \nabla \Phi_{ie} \, r \, \mathrm{d}r \, \mathrm{d}\varphi \, \mathrm{d}z \; + \; k_i \int\limits_{\substack{outer\ surfaces \\ of\ insulation}} \int \frac{\partial T_i}{\partial \hat{n}} \Phi_{ie} \, r \, \mathrm{d}r \, \mathrm{d}\varphi \\
+ \quad & \iiint\limits_{gas} \left[k_g \left(\nabla T_g \cdot \nabla \Phi_{ge} \right) + \rho_g c_p \mathbf{v} \cdot \nabla T_g \Phi_{ge} \right] \, r \, \mathrm{d}r \, \mathrm{d}\varphi \, \mathrm{d}z = 0 \qquad (6.24)
\end{aligned}
$$

and dividing by k_g, we will find

$$
\begin{aligned}
& k_{cg} \iint\limits_{crucible} \int \left(\frac{\partial T_c}{\partial r} \frac{\partial \Phi_{ce}}{\partial r} + \frac{1}{r^2} \frac{\partial T}{\partial \varphi} \frac{\partial \Phi_{ce}}{\partial \varphi} + \frac{\partial T_c}{\partial z} \frac{\partial \Phi_{ce}}{\partial z} \; - \; \frac{q}{k_c} \Phi_{ce} \right) \, r \, \mathrm{d}r \, \mathrm{d}\varphi \, \mathrm{d}z \\
+ \quad & k_{ig} \iint\limits_{insulation} \int \left(\frac{\partial T_i}{\partial r} \frac{\partial \Phi_{ie}}{\partial r} + \frac{1}{r^2} \frac{\partial T}{\partial \varphi} \frac{\partial \Phi_{ie}}{\partial \varphi} + \frac{\partial T_i}{\partial z} \frac{\partial \Phi_{ie}}{\partial z} \right) \, r \, \mathrm{d}r \, \mathrm{d}\varphi \, \mathrm{d}z \\
& + k_{ig} \int\limits_{\substack{outer\ surfaces \\ of\ insulation}} \int \frac{\partial T_i}{\partial \hat{n}} \Phi_{ie} \, r \, \mathrm{d}r \, \mathrm{d}\varphi \\
+ \quad & \iiint\limits_{gas} \left(\frac{\partial T_g}{\partial r} \frac{\partial \Phi_{ge}}{\partial r} + \frac{1}{r^2} \frac{\partial T}{\partial \varphi} \frac{\partial \Phi_{ge}}{\partial \varphi} + \frac{\partial T_g}{\partial z} \frac{\partial \Phi_{ge}}{\partial z} \right) \, r \, \mathrm{d}r \, \mathrm{d}\varphi \, \mathrm{d}z \\
& + \frac{1}{\alpha} \iiint\limits_{gas} \left(u \frac{\partial T_g}{\partial r} + \frac{v}{r} \frac{\partial T_g}{\partial \varphi} + w \frac{\partial T_g}{\partial z} \right) \Phi_{ge} \, r \, \mathrm{d}r \, \mathrm{d}\varphi \, \mathrm{d}z = 0 \qquad (6.25)
\end{aligned}
$$

where $k_{cg} = k_c / k_g$ and, $k_{ig} = k_i / k_g$.

Non-dimensional form

The non-dimensional form is

$$\frac{k_{cg}}{Pr}\iint\int\limits_{crucible}\left[\frac{\partial\Theta_c}{\partial R}\frac{\partial\Phi_{ce}}{\partial R}+\frac{1}{R^2}\frac{\partial\Theta_c}{\partial\varphi}\frac{\partial\Phi_{ce}}{\partial\varphi}+\frac{\partial\Theta_c}{\partial Z}\frac{\partial\Phi_{ce}}{\partial Z}-\left(\frac{L_c^2}{T_c k_c}\right)q\Phi_{ce}\right]\,R\,\mathrm{d}R\,\mathrm{d}\varphi\,\mathrm{d}Z$$

$$+\quad\frac{k_{ig}}{Pr}\iint\int\limits_{insulation}\left(\frac{\partial\Theta_i}{\partial R}\frac{\partial\Phi_{ie}}{\partial R}+\frac{1}{R^2}\frac{\partial\Theta_i}{\partial\varphi}\frac{\partial\Phi_{ie}}{\partial\varphi}+\frac{\partial\Theta_i}{\partial Z}\frac{\partial\Phi_{ie}}{\partial Z}\right)\,R\,\mathrm{d}R\,\mathrm{d}Z$$

$$+\frac{k_{ig}}{Pr}\int\int\limits_{\substack{outer\ surfaces\\ of\ insulation}}\frac{\partial\Theta_i}{\partial\hat{N}}\Phi_{ie}\,R\,\mathrm{d}R\,\mathrm{d}\varphi$$

$$+\quad\frac{1}{Pr}\iiint\limits_{gas}\left(\frac{\partial\Theta_g}{\partial R}\frac{\partial\Phi_{ge}}{\partial R}+\frac{1}{R^2}\frac{\partial\Theta_g}{\partial\varphi}\frac{\partial\Phi_{ge}}{\partial\varphi}+\frac{\partial\Theta_g}{\partial Z}\frac{\partial\Phi_{ge}}{\partial Z}\right)\,R\,\mathrm{d}R\,\mathrm{d}Z$$

$$+\iiint\limits_{gas}\left(U\frac{\partial\Theta_g}{\partial R}+\frac{V}{R}\frac{\partial\Theta_g}{\partial\varphi}+W\frac{\partial\Theta_g}{\partial Z}\right)\Phi_{ge}\,R\,\mathrm{d}R\,\mathrm{d}Z=0 \qquad (6.26)$$

where $Pr=\nu/\alpha$ is the *Prandtl number.*

6.2.3 Calculation procedure

The design and structure of the implemented grid (mesh) is a relatively easy task for regular two-dimensional geometries. But for complicated three-dimensional geometries, the design of an appropriate grid is not so easy. Fortunately, the ENTWIFE package could be used successfully to carry out our grid structure for the three-dimensional calculation of heat generation as well as the heat transfer in the calculation domains.

The three-dimensional finite element discretization of fluid flow problems such as Czochralski systems, typically result in structured matrices characterized by extremely large bandwidths. The direct solution of such matrices requires a great amount of memory and, more importantly, an enormous number of computational operations. In our three-dimensional calculation of flow and temperature field, more than 20000 QC elements are used which need $\simeq$ 100 *GBytes* memory for calculation. It means, the three-dimensional simulation of fluid flow is in principle an extremely large computation even using the currently faster direct solver MUMPS [23].

In this chapter, our solutions are calculated for three different configurations of a CZ system, Fig. 6-2:

Description (units)	Symbel	Value
Crucible inner radius (mm)	r_c	50
Crucible thickness (mm)	l_c	2
Crucible inner height (mm)	h_c	100
Afterheater inner height (mm)	h_{af}	100, 80
Afterheater top cover hole (mm)	r_{af}	25
Distance between crucible and afterheater (mm)	D_{ca}	0, 20
Height and width of the observation window (mm)	h_w	20
Coil inner radius (mm)	r_{co}	92.5
Coil thickness (mm)	l_{co}	10
Height of coil turns (mm)	h_{co}	32
Distance between coil turns (mm)	d_{co}	3
Distance between two coils (mm)	D_{co}	70
Thickness of crucible insulation at the bottom (mm)	h_{ci}	50
Thickness of insulation at the wall (mm)	d_{ci}	35.2
Temperature at the afterheater hole (^oC)	T_{ah}	310
Ambient temperature (^oC)	T_a	25

Table 6-1. Operating parameters used for the calculations.

(a) configuration without any gap or window,

(b) configuration with an open gap between crucible and afterheater,

(c) configuration with an open observation window.

For both configurations (a) and (b), a two-dimensional calculation is necessary because of the axisymmetric geometry of the system. But for the configuration (c), a three-dimensional computation is required since it has non-axisymmetric geometry and conditions. From these calculations we intend to compare the results of two-dimensional and three-dimensional calculations and to figure out the influences of the open observation window on the gas flow structure and heat transfer mechanism in a CZ system. For this purpose the following points are considered:

(1) We consider a certain maximum temperature difference across the gas part ($\triangle T_{max}^{gas}$) for all configurations, since the buoyant force in the system is created by this temperature gradient. It means that the magnitude of T_{max}^{gas} as well as the temperature at the afterheater hole is the same for all configurations. We can change and control the T_{max}^{gas} magnitude during the calculations. This can be done by changing in the induction heating which occurs in the metallic crucible and afterheater.

(2) The temperature at the afterheater hole as well as the open gap or the window, is the same and fixed at 310 ^0C obtained from the measurement in the lab. On the other hand, a comparison between the results of calculations and measurement is possible.

(3) Height and width of the window and the gap height is the same and equal to 20 mm.

(4) The height of all configurations is the same. On the other hand, the height of the afterheater in the configurations of no gap is equal to the height of the gap plus afterheater height in the configuration with a gap, and equal to 10 cm.

In order to save computer memory and reduce computation time of the three-dimensional problem, the calculation of the configuration with an observation window, is done only for a half vertical part of the system. Because our simulation is a steady state calculation it can be assumed that there is a vertical symmetry plane in the configuration, Fig. 6-3. It should be mentioned that for a transient problem, the assumption of this vertical symmetry plane as well as taking only half of the vertical part may fail. In a three-dimensional transient calculation, all governing equations should be solved for the whole system because oscillatory calculations are possible.

Values of physical properties employed for our calculations are presented in Table 3-1 (chapter 3) and the operating parameters are listed in Table 6-1. The results of the two-dimensional and three-dimensional computations of induction heating, temperature and flow fields will be presented in the next section of this chapter.

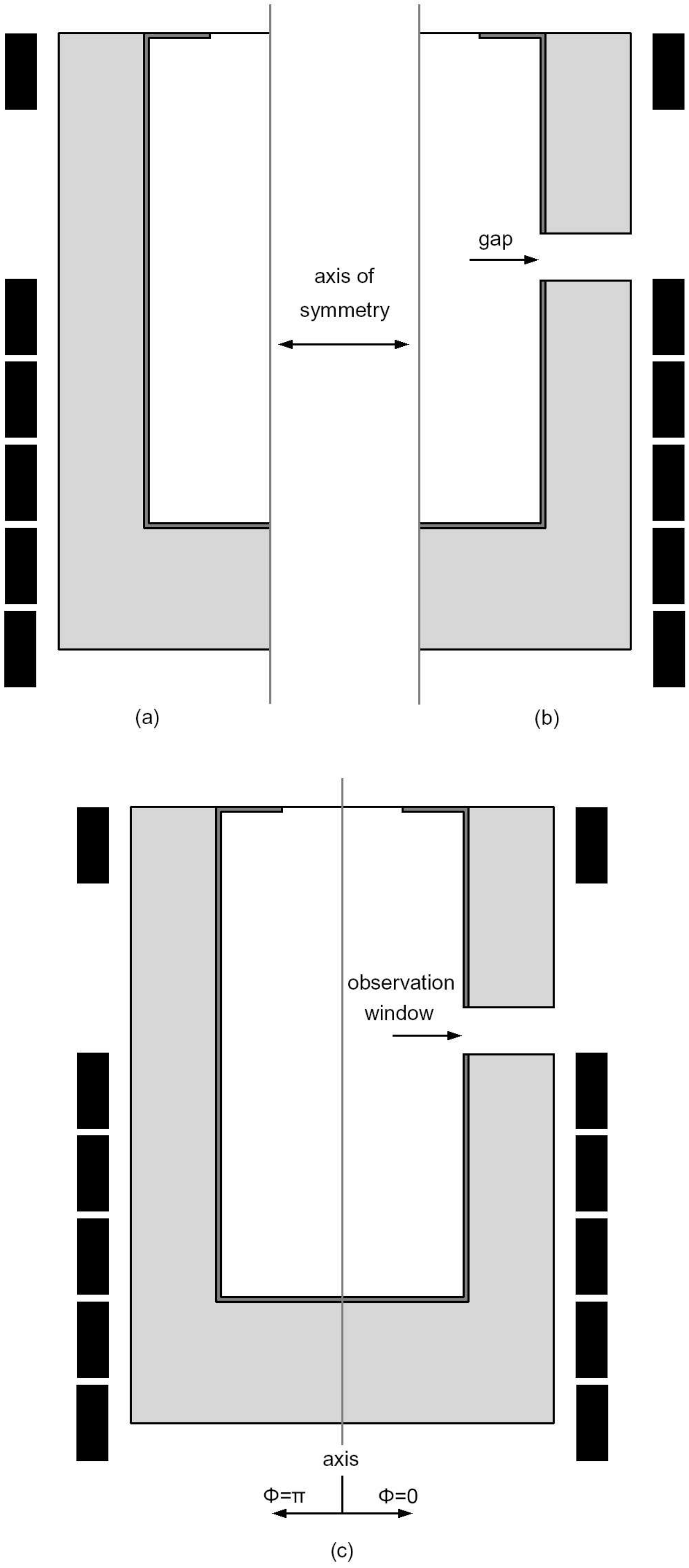

Fig. 6-2. Schematic diagram of three configurations of a Czochralski growth furnace containing only gas, (a) without any gap or window, (b) with an open gap between crucible and afterheater, and (c) with an open observation window.

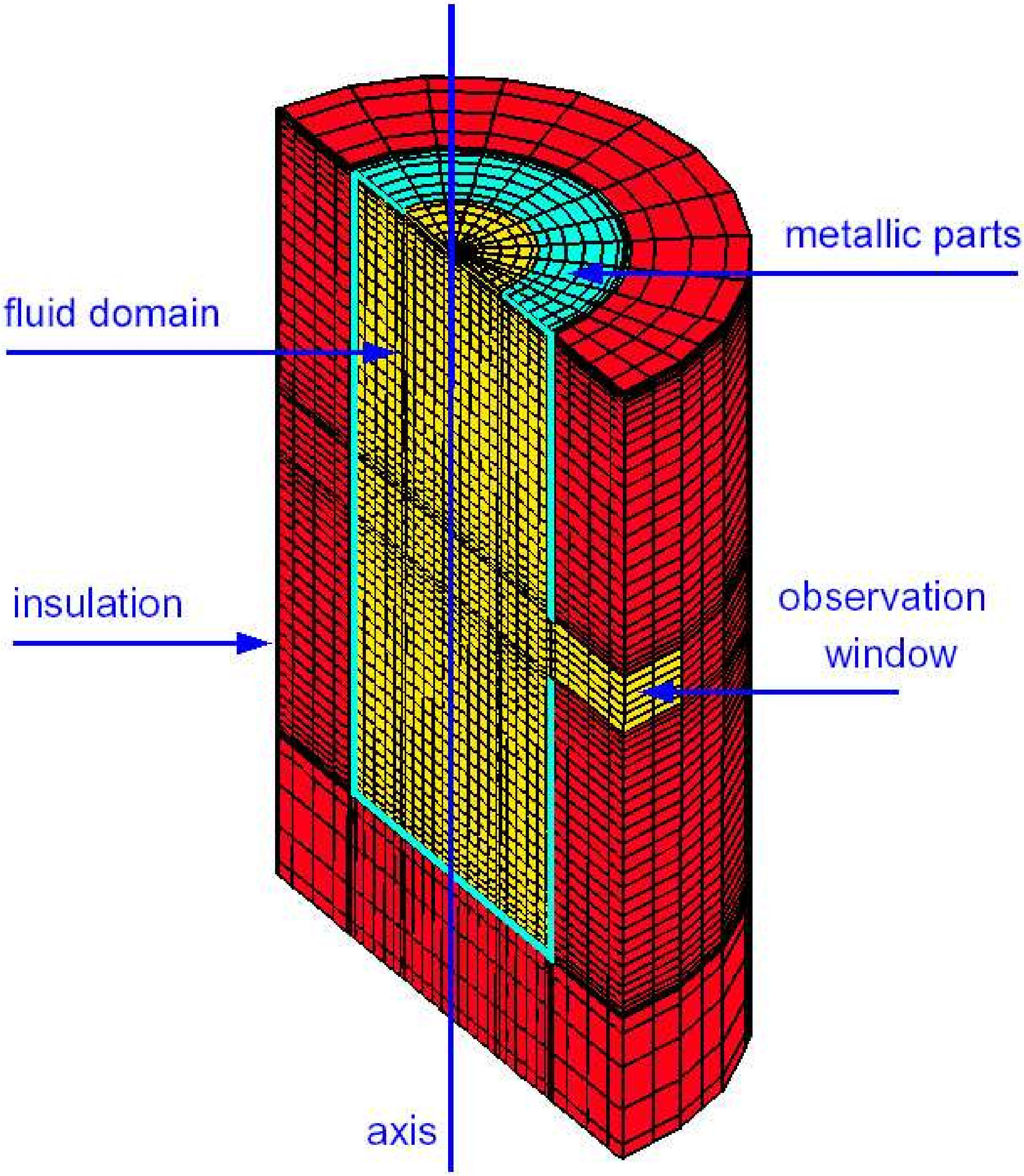

Fig. 6-3. Finite element mesh used for the three-dimensional calculation of the configuration with an observation window.

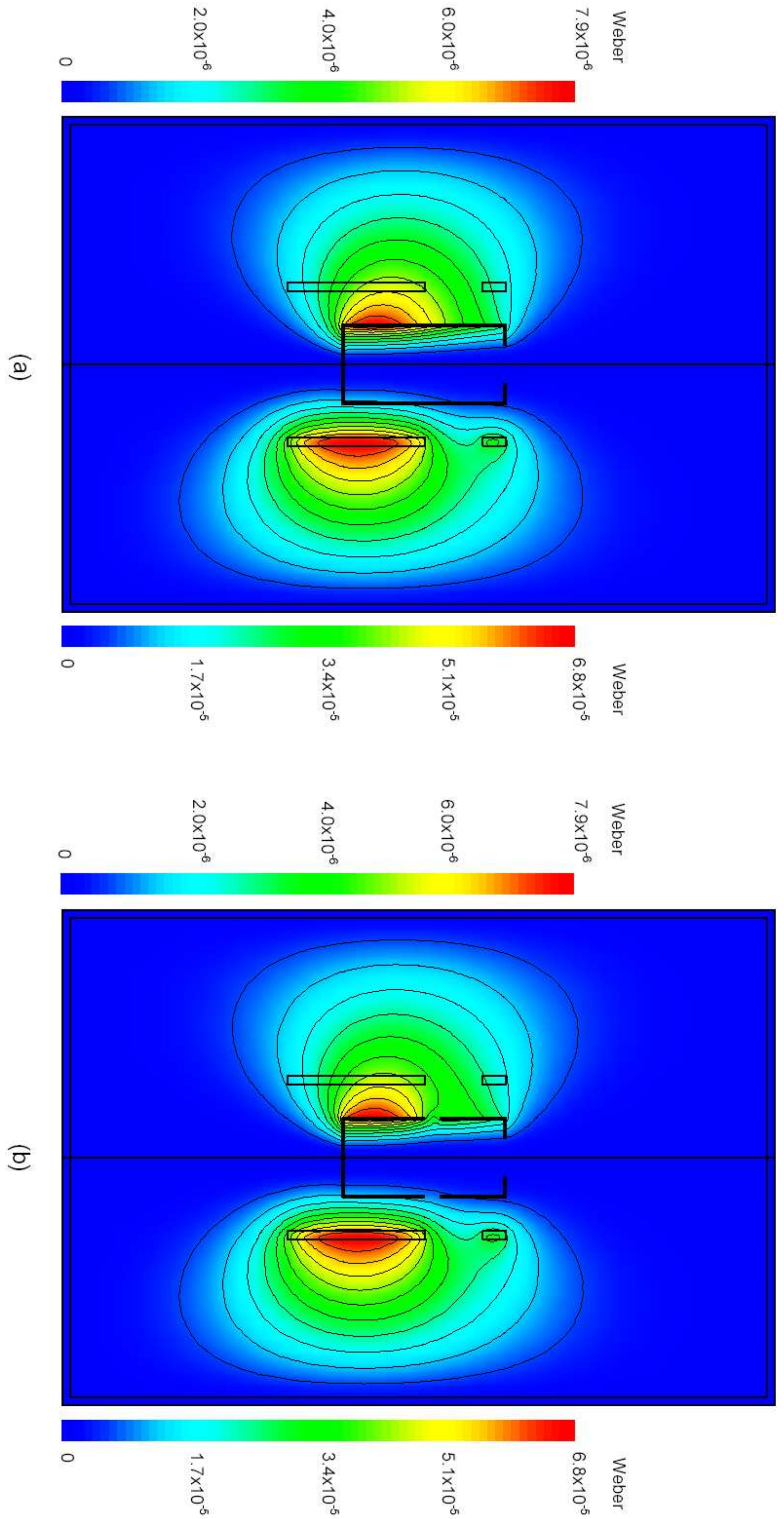

Fig. 6-4. Components of the magnetic stream function (ψ_B) calculated for configuration (a) without any gap or window, (b) with an open gap between crucible and afterheater. The right hand side shows the in-phase component (C) and the left hand side represents the out-of-phase component (S).

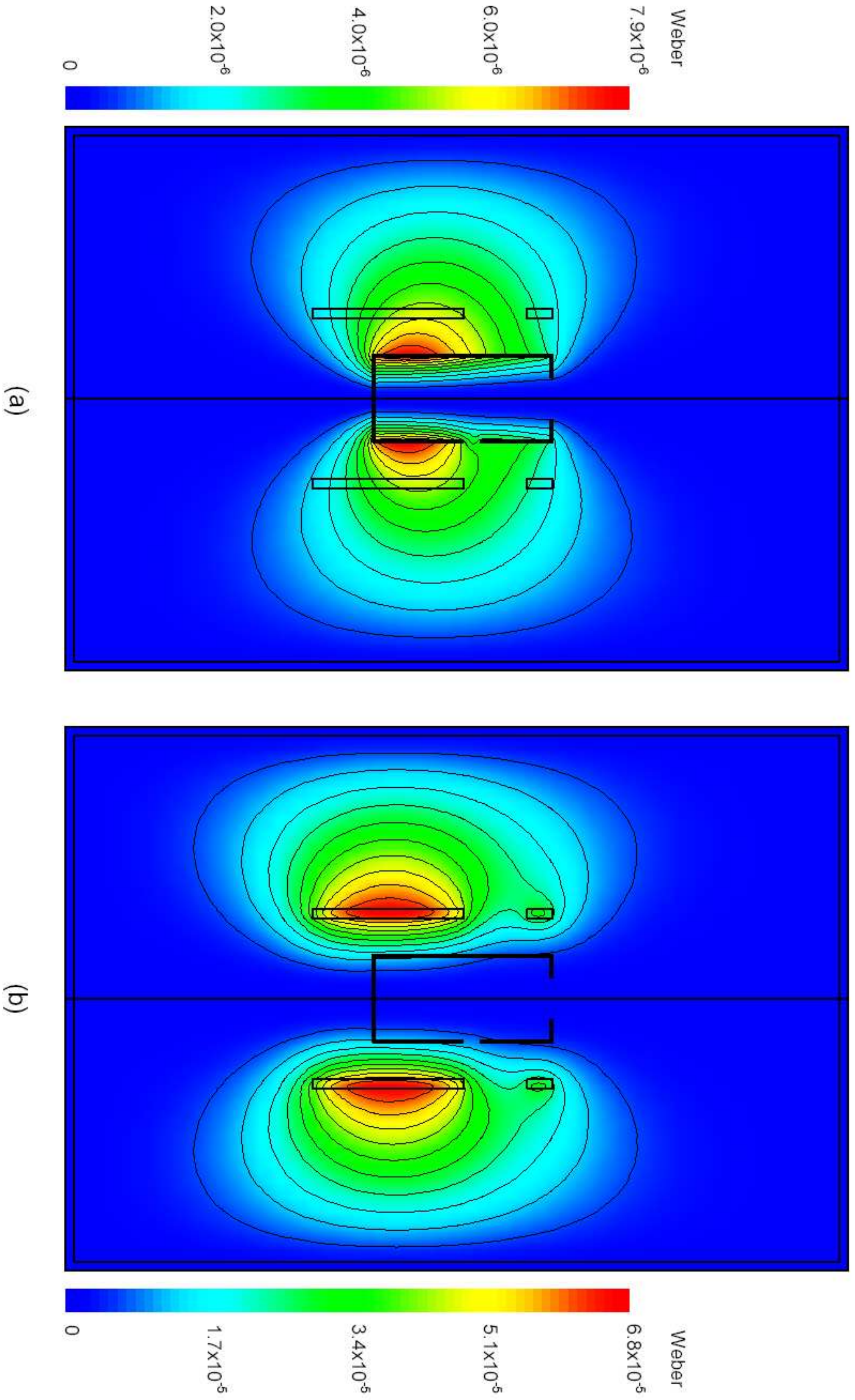

Fig. 6-5. Components of the magnetic stream function (ψ_B) calculated for configuration with an observation window, (a) the out-of-phase component (S) and (b) the in-phase component (C).

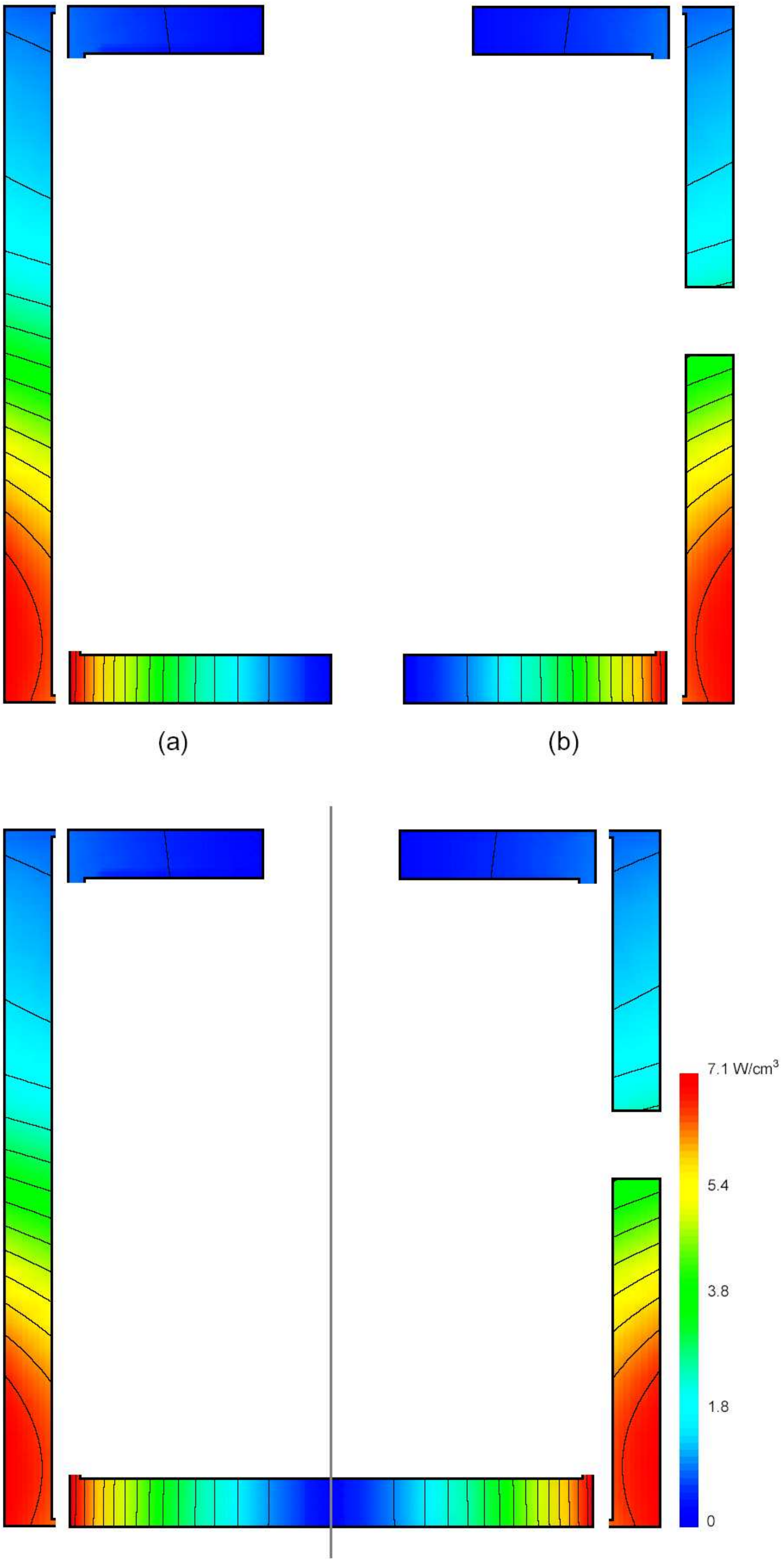

(a) (b)

(c)

Fig. 6-6. Contours of the volumetric power distribution (q) in the crucible and afterheater, computed for configuration (a) without any gap or window, (b) with an open gap between crucible and afterheater, and (c) with an observation window. The maximum value of energy deposition is located at the outer surface of the crucible wall.

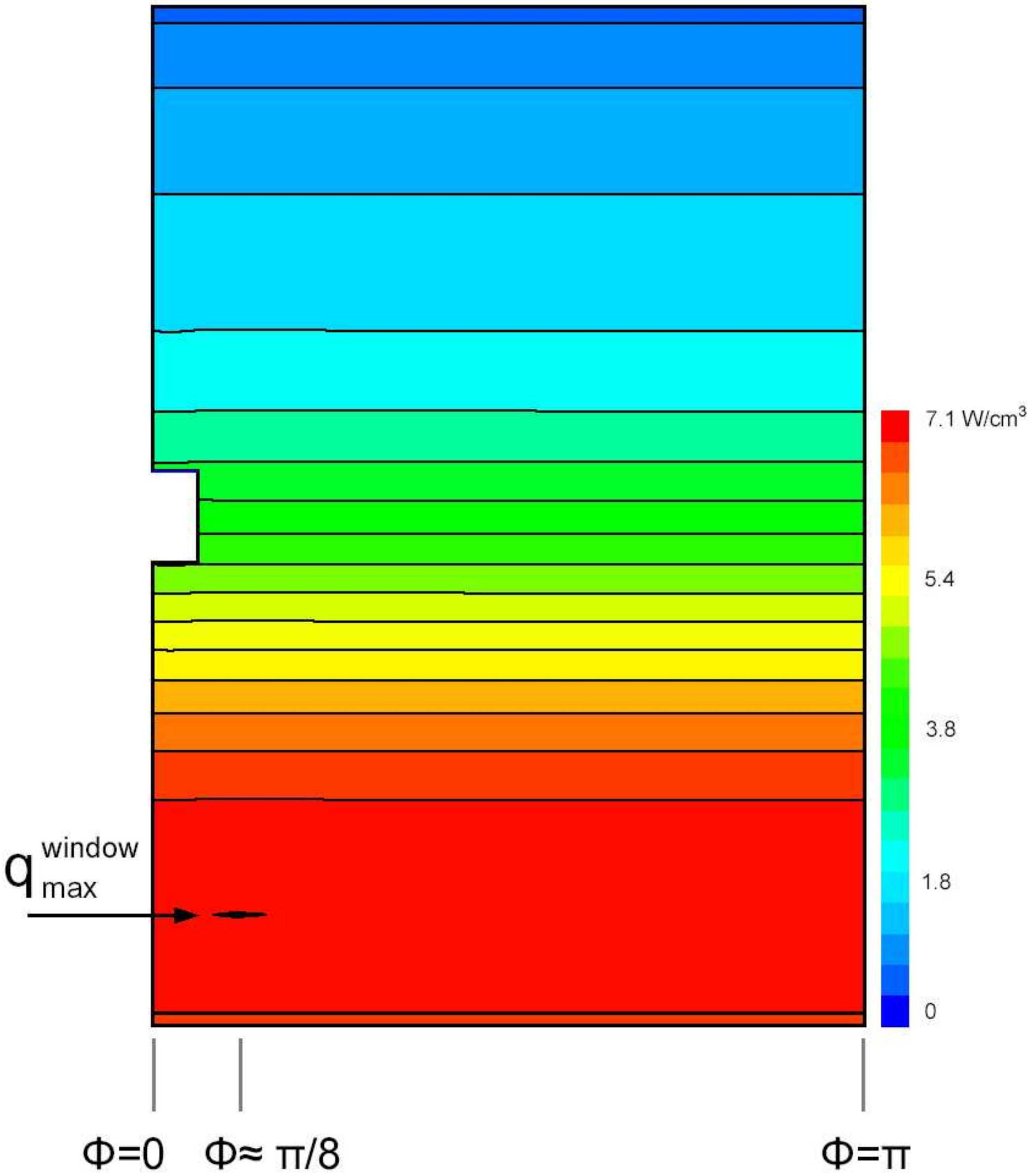

Fig. 6-7. Contours of the volumetric power distribution (q) in the side wall of the crucible and afterheater (outer surface) computed for the configuration with an observation window. The maximum value of energy deposition is located in the vertical plane $\phi \simeq \pi/8$.

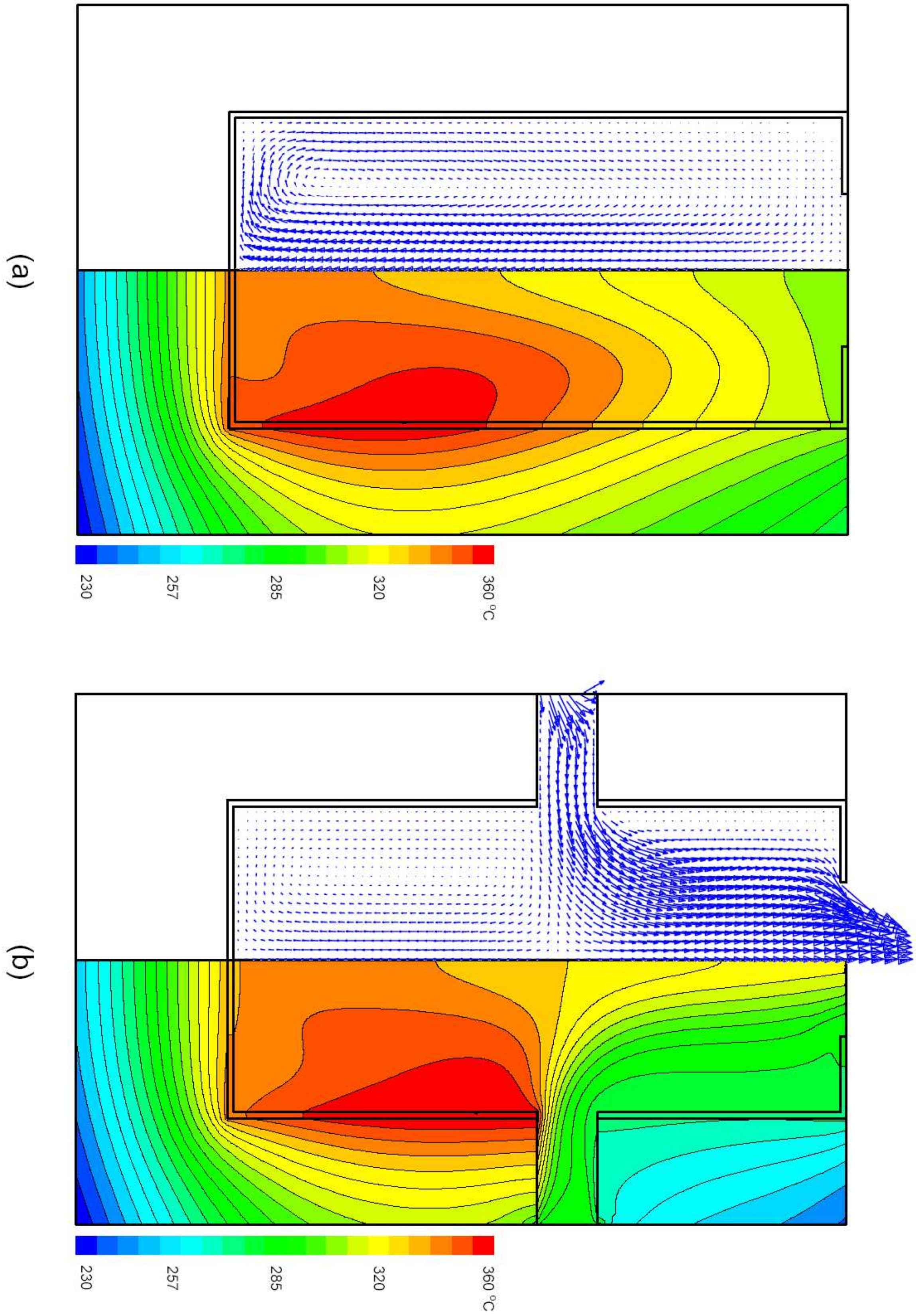

Fig. 6-8. Temperature (right hand side) and velocity field (left hand side) for the axisymmetric configurations, (a) configuration without a gap or window and (b) configuration with a gap between crucible and afterheater.

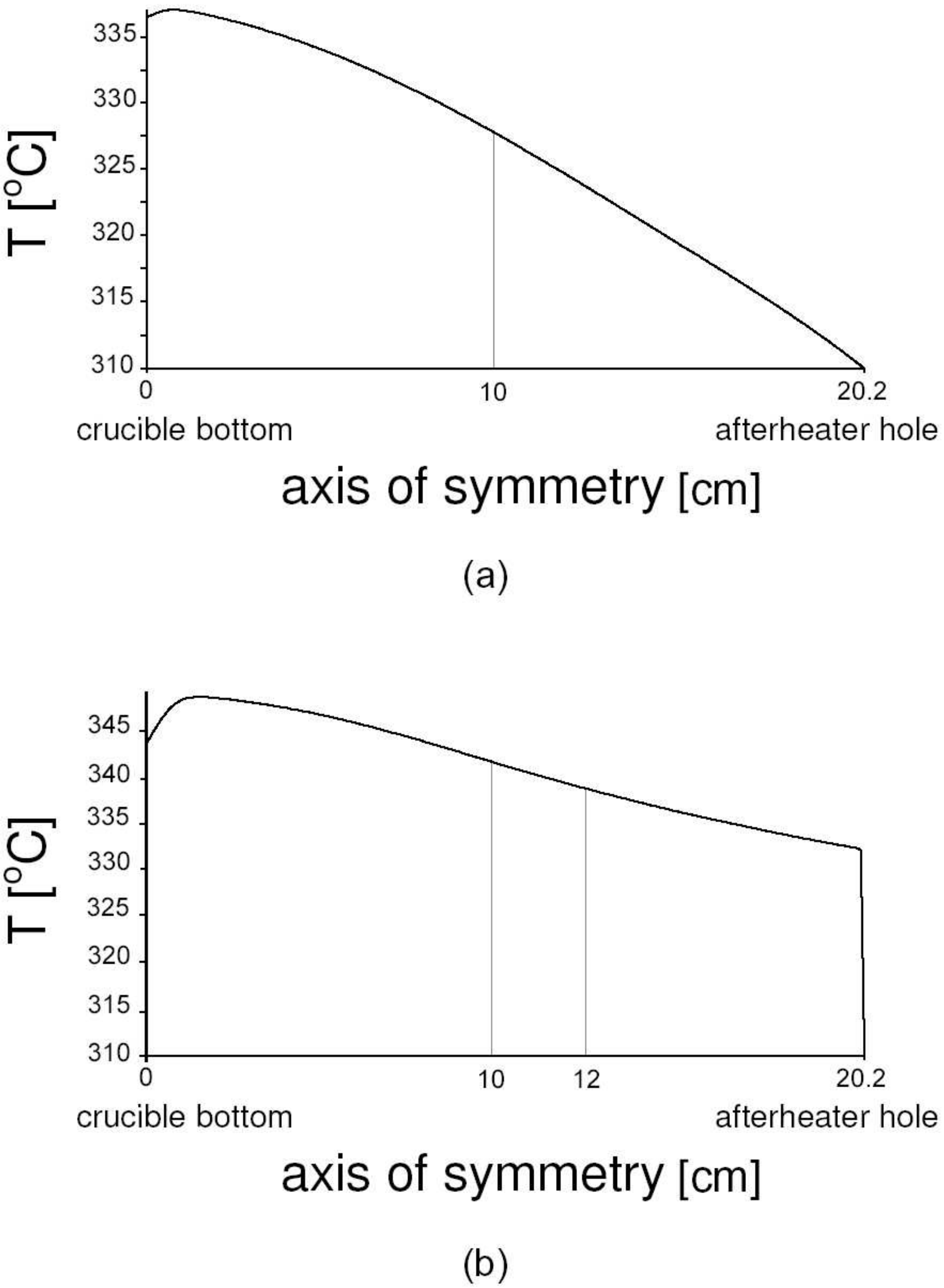

Fig. 6-9. Vertical temperature profiles along the axis of symmetry ($r = 0$) from the crucible bottom to the afterheater hole for the axisymmetric configurations, (a) configuration without a gap or window and (b) configuration with a gap between crucible and afterheater.

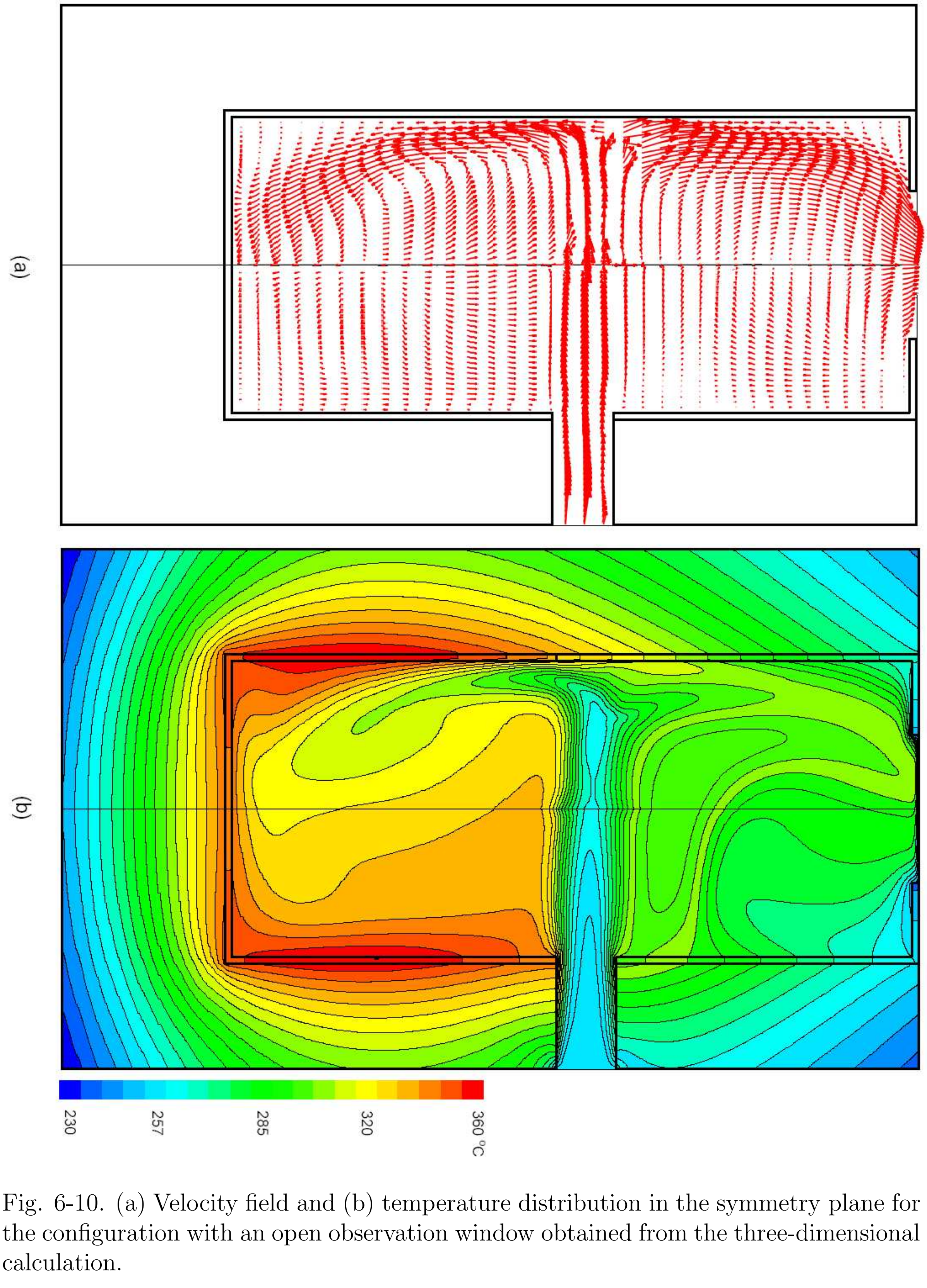

Fig. 6-10. (a) Velocity field and (b) temperature distribution in the symmetry plane for the configuration with an open observation window obtained from the three-dimensional calculation.

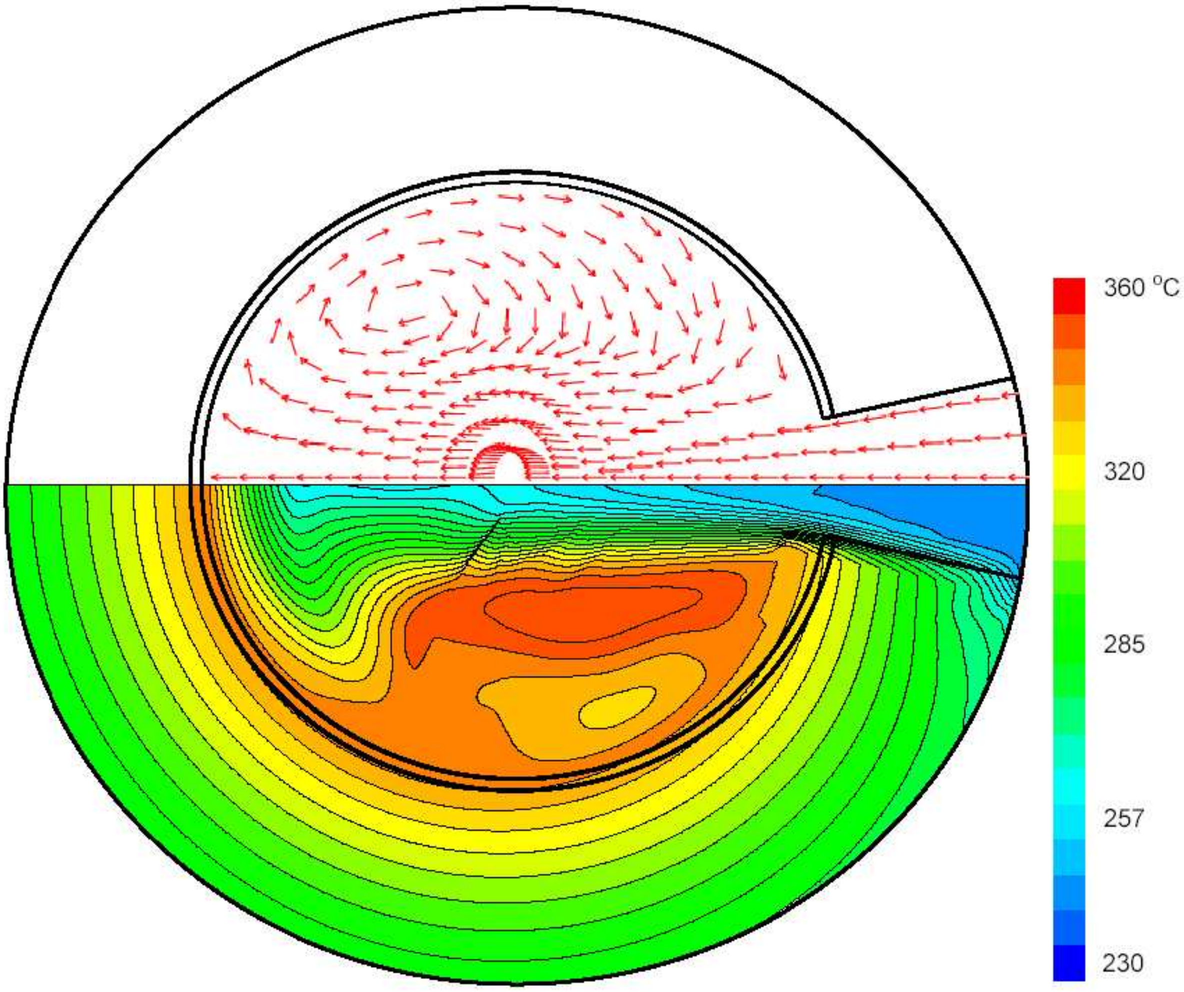

Fig. 6-11. Velocity field and temperature distribution in the horizontal plane crossing the middle height of the gap for the configuration with an observation window obtained from the three-dimensional calculation.

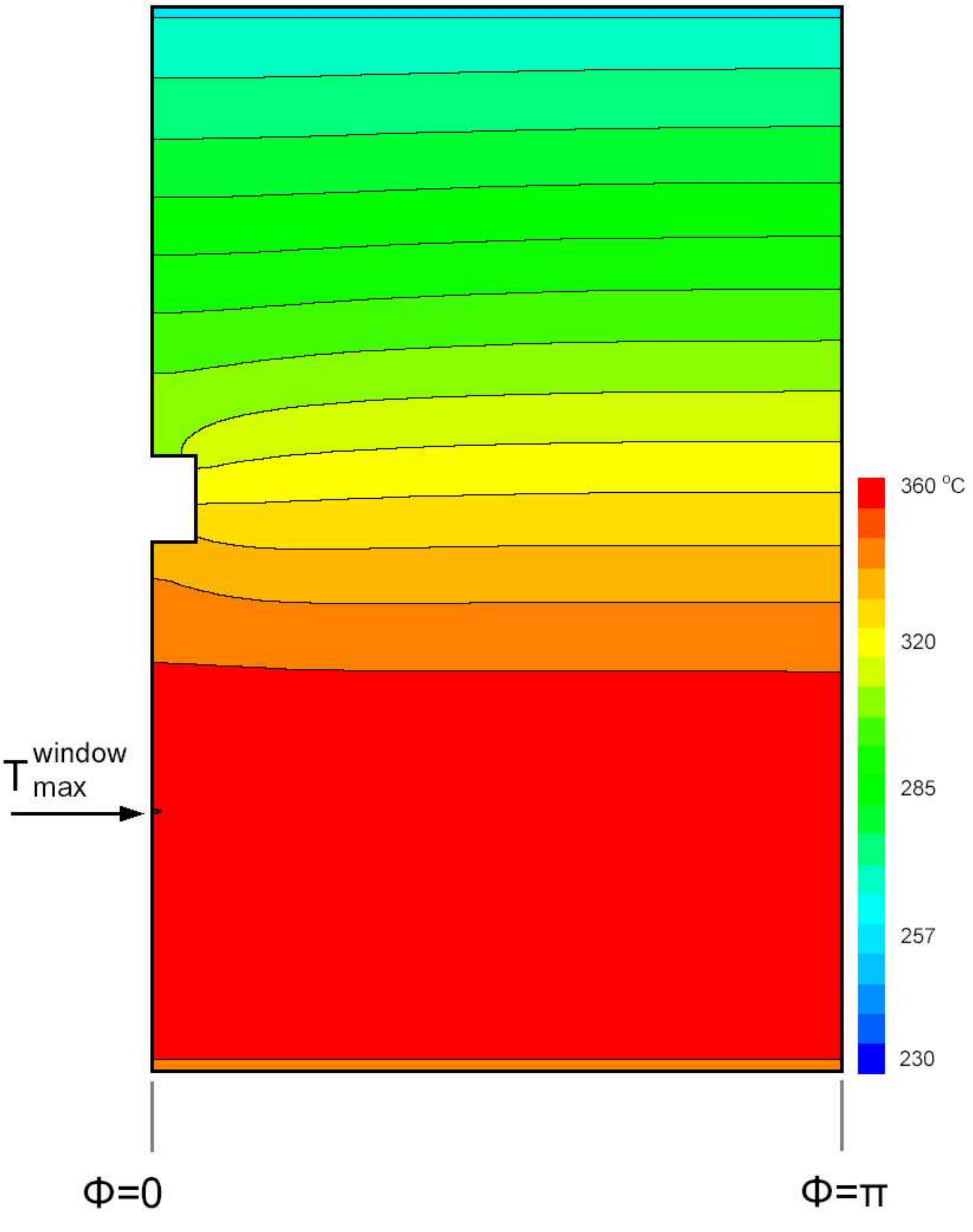

Fig. 6-12. Isotherm distribution at the inner surface of the crucible and afterheater for the configuration with an observation window obtained from the three-dimensional calculation. The T_{max}^{window} is located in the vertical plane $\phi = 0$ and the middle part of the crucible wall.

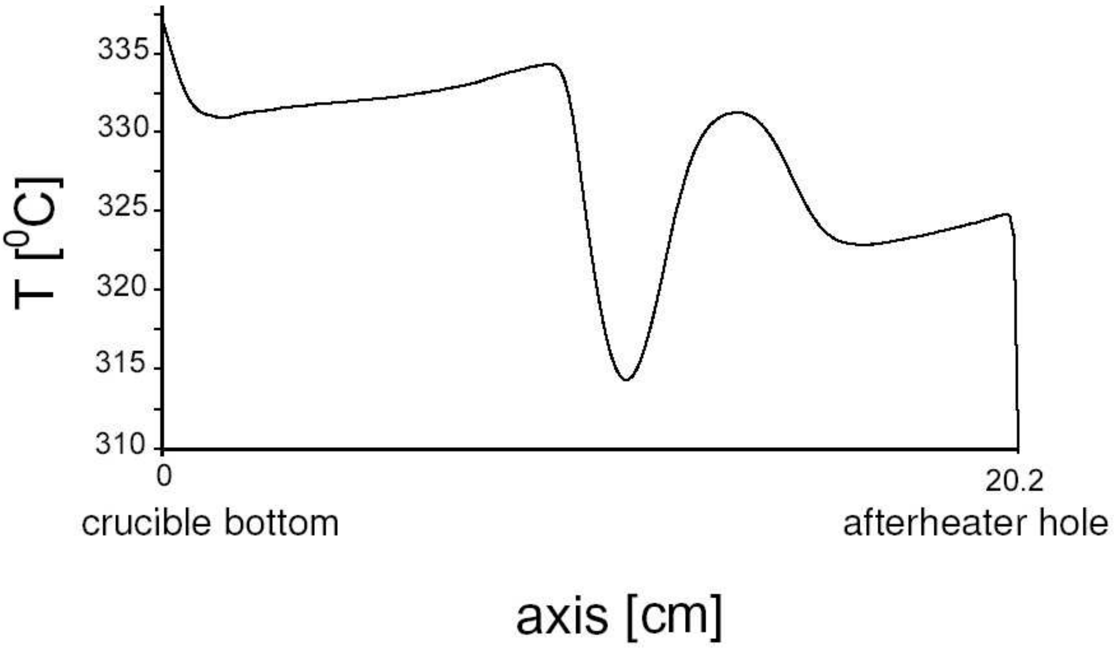

(a)

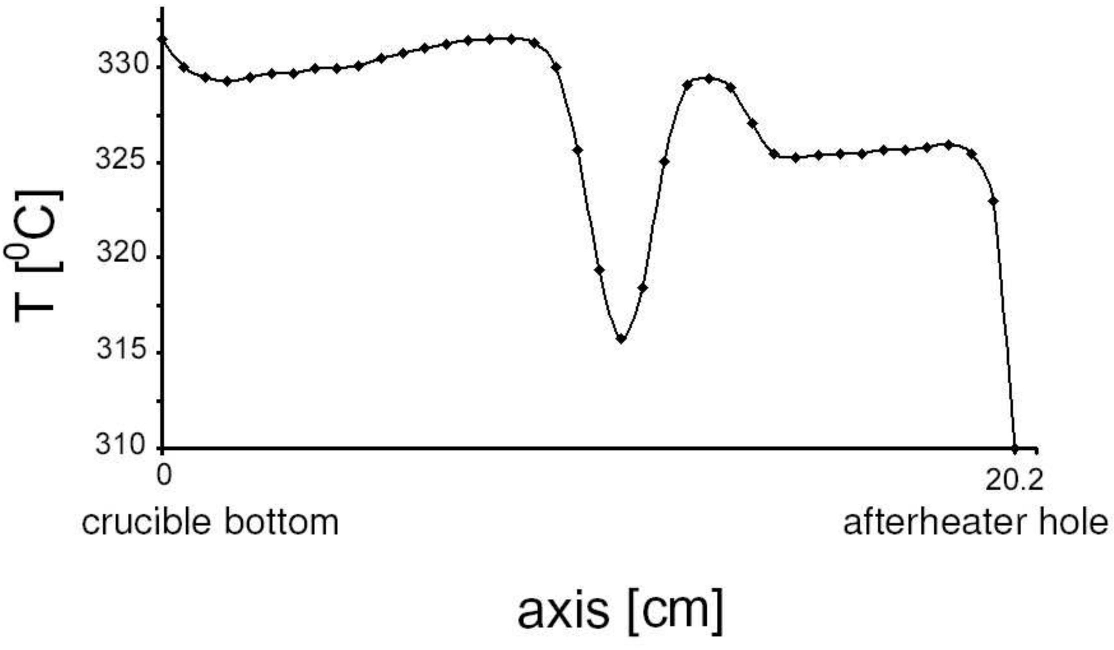

(b)

Fig. 6-13. Vertical temperature profiles along the axis ($r = 0$) from the crucible bottom to the afterheater hole for the configuration with an observation window obtained from (a) the three-dimensional calculation and (b) the measurement in the lab, the temperature scale is different because of slightly different configuration of the CZ setup.

6.3 Results and discussion

6.3.1 Induction heating

The in-phase and out-of-phase components of the magnetic stream function (ψ_B) computed for the configurations without and with a gap are presented in Fig. 6-4. The distribution of the in-phase component (C) is approximately the same for both configurations while the distribution of out-of-phase component (S) is different particularly in the gap between crucible and afterheater. As has already been explained in chapter 2, the spatial distribution of the in-phase component depends strongly on the geometry of the RF-coil itself and also its orientation with respect to the crucible and afterheater. For this reason the distribution of the C component does not change considerably by the gap between the crucible and afterheater. But for the out-of-phase component, it is determined markedly by the design and arrangement of the crucible and afterheater. Accordingly, the presence of a gap has changed the distribution of the S component in the chamber. The location of C_{max} is in the middle part of the main coil and S_{max} is positioned in the crucible side wall, in both configurations. In addition, there is a local maximum of the in-phase component in the upper coil, which is a result of the distance between two separate parts of the induction coil. The concentration of the in-phase contours is quite high between the coil and the crucible which indicates a high gradient in that area. For the out-of-phase component, the distances between isolines are small in the inner space of the crucible and afterheater. It means that there is a high variation of this component between the inner crucible side wall and the axis of symmetry. In addition, the S isolines have a deflection outwards in the gap with respect to the crucible and afterheater which is a direct result of the gap itself.

Fig. 6-5 represents the distribution of both components of the magnetic stream function (ψ_B) for the configuration with an observation window in the symmetry plane, obtained from the three-dimensional calculation. Obviously, the results in the vertical plane $\phi = 0$ (i.e. including the window) is quite similar to the configuration with a gap while in the vertical plane $\phi = \pi$, they are the same as configuration without a gap. The distribution of the in-phase component (C) is about axisymmetric because of the rotational symmetric orientation of the RF-coil turns. The distribution of the out-of-phase component (S) is also approximately axisymmetric except in the window and the area close to it. In the window, the out-of-phase isolines have deflected outwards with respect to the crucible and afterheater similar to the configuration with a gap, as has already been explained.

The volumetric distribution of heat generation in the crucible and afterheater is shown in Fig. 6-6 for all configurations (in the symmetry plane for the configuration with an observation window). Although q_{max} is located in the lower part of the crucible side wall (outer surface) and at the same height from the crucible bottom for all configurations, in the configuration with a window q^{window}_{max} is not placed in the symmetry plane, Fig. 6-7. It is located in the vertical plane $\phi \simeq \pi/8$, i.e. a short distance along the azimuthal plane of the window side wall. This non-uniform distribution of heat generation is a result of the presence of the window in the afterheater which has modified the distribution of the components C and especially S in the system. As a result the distribution of energy production in this system is altered compared to the axisymmetric configurations. It is noteworthy to mention that besides of the q^{window}_{max} location in the configuration with the window, the other q isolines have a parallel horizontal line shape as it has been shown in Fig. 6-7. It indicates that the volumetric distribution of delivered energy to this system is about rotationally symmetric except for q^{window}_{max}.

6.3.2 Temperature and flow field

For this set of calculations, the temperature at the afterheater hole, the gap between crucible and afterheater as well as the window is set to be 310 ^0C. Accordingly, the Grashof number is $Gr = 2.1 \times 4$ for all configurations. The temperature maximum is $T_{max} = 360\ ^0C$ for all configurations, obtained from the computations. Accordingly, the total heat generation in the system is $Q^{without}_{total} = 310\ Watt$, $Q^{gap}_{total} = 240\ Watt$ and $Q^{window}_{total} = 300\ Watt$ for the configuration without and with a gap, and with an observation window, respectively.

Fig. 6-8 demonstrates the temperature distribution in the whole system and the velocity map in the gas phase obtained from the two-dimensional heat transfer simulations for the configurations without and with a gap. In the configuration without a gap or window, there is a single vortex of gas convection in the crucible and afterheater which occupies the entire volume of the setup. In this vortex, the gas flow is directed upwards along the crucible and afterheater side wall and downwards along the symmetry axis. The gas flow is stronger in the crucible than in the afterheater. In fact, the gas is approximately at rest close to the afterheater top cover. The center of this gas eddy is located close to the crucible bottom which is a result of high heat loss from the afterheater top cover. The maximum value of the gas velocity is $\mathrm{v}^{without}_{max} \simeq 3.7\ cm/s$ at the axis of symmetry, downwards and in the crucible. The structure of this single gas eddy reflects the heat transfer mode in the system which transfers the energy from the crucible wall to the afterheater top cover and its hole.

In the temperature field, the isotherms are deflected upwards along the crucible and afterhear sides, and downwards in the vicinity of centerline proportional to the related gas flow. The isotherms deflection is high in the crucible compared to the afterheater space which is a result of different gas velocity in these areas. It is noteworthy to mention that the distance between the isolines in the gas part is about equal and constant which represents a linear variation of the temperature in this part of the system. The location of $T_{max}^{without}$ is in the middle part of the crucible wall, as has been shown in the Fig. 6-8(a). Fig. 6-9(a) represents the temperature profile along the axis of symmetry for this configuration, which is plotted from the crucible bottom to the afterheater hole. It shows an approximately linear variation for the temperature, as has already been mentioned.

In the configuration with an open gap, there is a gas flow which enters the system through the gap ($\mathrm{v}_{max}^{in\ the\ gap} = 10\ cm/s$) and the outflow is via the afterheater top cover hole. Its velocity is increased gradually and becomes extremely high in the afterheater hole with $\mathrm{v}_{max}^{gap} \simeq 22\ cm/s$, which is the maximum gas velocity in this configuration. In addition, there is a vortex in the crucible which is directed upwards in the vicinity of its sides and downwards along the symmetry axis. This gas eddy has its center in the middle part of the crucible and occupies it completely. Also there is a weak and small gas vortex adjacent to the afterheater wall in which the gas motion is directed downwards along the afterheater side wall. In addition, a small part of the gas flow exits immediately from the upper part of the gap since it becomes relatively hot over a short distance.

In this configuration the deflection of the isotherms is more complicated than in the configuration without a gap because of the presence of an external gas influx. The isotherm shapes have a deflection upwards in the vicinity of the crucible wall and downwards along the axis of symmetry. In the gap, the isotherms are strongly pushed towards the symmetry axis and in the afterheater towards the afterheater hole. The temperature gradient in the gap space in the radial as well as the axial direction is high especially close to the crucible insulation. Also the temperature variation is quite high in the vicinity of the afterheater hole in axial direction. In this configuration, the temperature maximum T_{max}^{gap} is located in the upper part of the crucible wall and $\simeq 1\ cm$ distance above the location of $T_{max}^{without}$ in the configuration without a gap. The temperature variation in the afterheater part is very low and so it is about isothermal compared to the other parts of the setup.

Fig 6-9(b) represents the temperature profile along the axis of symmetry from the crucible bottom to the afterheater hole for the configuration with a gap. It shows a linear variation of temperature (less than in the configuration without a gap) except near the afterheater hole. The temperature gradient is extremely high close to the afterheater hole which indicates a strong heat flux in that area. This is a direct result of the high external gas flow which transfers efficiently the heat from the crucible to the afterheater.

For the configuration with a small observation window, the flow and thermal field are very complex under the influences of the open window. It was observed that the flow and temperature field of the system are obviously three-dimensional and non-axisymmetric. Fig. 6-10 represents the temperature and velocity field in the symmetry plane ($\phi = 0, \pi$) of this configuration. As has been shown in this figure, the gas enters the system through the open window with a relatively high velocity ($\mathrm{v}_{max}^{in\ the\ window} = 10\ cm/s$) and goes outside via the afterheater hole. This gas flow is strong and about horizontal directed from the window to the symmetry axis. The gas flow is directed towards the opposite side wall ($\phi = \pi$), where it is divided into two parts of vertical direction. One part flows downwards and returns to the crucible of the vertical plane $\phi = 0$, and another part moves upwards along the afterheater wall towards the afterheater top cover hole. As a result in the crucible there are two vortices in the vertical plane $\phi = \pi$ and a strong upwards gas motion in the vertical plane $\phi = 0$. In the plane $\phi = \pi$, the first eddy which is originated from the hot crucible wall (buoyancy) is nested in the crucible bottom edge. The second circulation which is a result of the incoming gas flow via the window is located in the upper part of the crucible. In the plane $\phi = 0$, the upwards gas flow is a superposition of the returned flow from the plane $\phi = \pi$ and that one raised from buoyancy along the crucible wall.

In the afterheater symmetry plane, there is an upwards directed gas flow in the vertical plane $\phi = \pi$. But in the vertical plane $\phi = 0$, in addition to the outwards gas flow via the afterheater hole, there is a small upwards directed gas motion just above the window and a downwards flow below the afterheater top cover. The latter is a result of the horizontal circulation of the gas in the setup. The gas velocities in the afterheater are quite high and larger than in the crucible. Interestingly, the outflowing gas in the afterheater hole is not axisymmetric, which is a result of the non-axisymmetric flow pattern in the system. In the hole, the gas velocities in the vertical plane $\phi = \pi$ are larger than in the plane $\phi = 0$, because of a strong upwards gas convection in the plane $\phi = \pi$ of the afterheater. It should be mentioned that the axial velocity (v) along the axis ($r = 0$) is smaller than in the axisymmetric configurations, except close to the afterheater hole where it is high similar to the configuration with a gap. The maximum gas velocity is $\mathrm{v}_{max}^{window} = 8\ cm/s$ located in the vertical plane $\phi = \pi$ and in the afterheater hole.

Fig. 6-11 illustrates the temperature and flow patterns in a horizontal plane crossing the middle height of the window. This figure shows that the incoming gas flow expands in the horizontal direction and returns towards the window. Consequently, a flow circulation occurs in the horizontal plane. The combination of the horizontal and vertical gas motion produces a very complicated spiral gas flow in the crucible and afterheater which rotates in the horizontal direction along the side walls.

The appearance of a three-dimensional structure of gas convection influences the temperature field of the system and generates a very complicated isotherm distribution in the gas part. The isotherm shapes are deflected from the gap towards the opposite side wall of the afterheater with a high concentration in axial and radial direction, Fig. 6-10 and Fig. 6-11. It indicates that the temperature in the middle portion of the system is much lower than in the crucible and afterheater space. Consequently, the temperature variation around this area is quite high in the vertical as well as the horizontal direction. In the crucible, the isotherm shapes in the vertical plane $\phi = \pi$ are deflected downwards, and in its lower portion towards the plane $\phi = 0$. In the vertical plane $\phi = 0$ of the crucible, they are deflected upwards, and in the upper part towards the axis. In the afterheater of the plane $\phi = \pi$, the isotherms are strongly displaced upwards and towards its hole which is a result of the high velocities of gas motion in that area. But in the vertical plane $\phi = 0$, the isotherm displacements are downwards and towards the axis ($r = 0$), except close to the afterheater top cover where they are strongly directed upwards. As a result, the temperature variation is extremely high close to the afterheater hole, similar to the configuration with a gap.

The non-uniform temperature distribution in the azimuthal direction is shown in Fig. 6-11. This figure confirms the complexity of the temperature distribution in the gas part under the influence of the incoming gas flow through the window and the spiral flow in this part, by observing the different isoline shapes in the azimuthal direction at the middle height of the window.

Fig. 6-12 shows the temperature distribution at the inner surface of the crucible and afterheater side wall. It indicates that T_{max}^{window} is located at the symmetry plane unlike to the position of q_{max}^{window}. It is placed below the window at the middle part of the crucible wall. This is a result of spiral gas flow in the system since its circulation in the crucible is towards the vertical plane $\phi = 0$ along the crucible side wall. This figure also illustrates that the temperature distribution is about symmetric at the crucible and afterheater side wall except close to the window and the vertical plane $\phi = 0$, where the T_{max}^{window} is located.

Fig. 6-13 represents the temperature profiles along the axis ($r = 0$), obtained from the three-dimensional calculation and the measurement in the lab. They are plotted from the crucible bottom to the afterheater hole. It shows some interesting and important features: (a) There is a good qualitative agreement between our calculation result and the measurement. (b) There are three local temperature minimums in this profile, a low close to the crucible bottom, a high one which is located in the window plane and a relatively high located in the afterheater. As has already been explained, there is a gas motion at the symmetry plane from the plane $\phi = \pi$ to the vertical plane $\phi = 0$ close to the crucible bottom. For this reason, the first and small local temperature minimum appears in that area. In fact, the incoming cold gas through the observation window, acts to cool significant portions of gas in the crucible adjacent to the symmetry plane, thus decreasing the temperature above the crucible bottom. The second and high temperature minimum arises also from the cold gas inflow. It affects markedly the temperature distribution in the middle part of the gas domain and directly cools this area, as has already been noted. The third local minimum located in the middle of the afterheater is a result of the spiral gas flow in that part of the system. In principle, these three local minimums at the axis, occur where the axial component of velocity is $v \simeq 0$, i.e. the spiral gas flow has a horizontal component only in those areas. It is noteworthy to mention that this behavior of the axial temperature profile is distinctly different from the axisymmetric configurations. It indicates that the open observation window has effectively changed the temperature and flow field of the system which has been observed in the lab too.

There are two mechanisms of heat transfer which influence effectively the temperature and flow field of the configurations: (i) Heat radiation from the afterheater top cover where there is no insulation, and (ii) incoming gas flow through the open gap or window. In the configuration without a gap or window, the heat dissipation from the afterheater top cover leads to cool efficiently the setup, push downwards the single gas vortex as well as the $T_{max}^{without}$ location and increases the internal heat generation in the system. In the configuration with an open gap, both mechanisms mentioned are present. Although the metal afterheater is about isothermal under the influence of the heat radiation, the open gap separates this part from the crucible. The gap acts as a good insulation and therefore the heat loss from the afterheater top cover can not affect the temperature field of the crucible markedly. In fact, the strong gas inflow via the gap plays the major role for the heat transfer mechanism in the system. For this reason, the T_{max}^{gap} is located about 1 cm distance above the $T_{max}^{without}$ position in the configuration without a gap. In the third configuration, i.e. configuration with an observation window, the importance of both mechanisms is approximately equal on the temperature and flow field of the system. The heat radiation from the afterheater top cover produces some results such as: push downwards the position of T_{max}^{window} and increase the energy production in the system, similar to the configuration without a gap. The incoming cold gas flow via the open window generates several features as: deflection of the isotherm shapes in the window towards the axis, modification of the gas temperature field and a high temperature gradient close to the afterheater hole, similar to the configuration with a gap between the crucible and afterheater. On the other hand, the roles of both factors are quite important and effective on the heat transfer structure of the system.

The fact that we could calculate the three-dimensional heat generation, temperature and flow field in a real Czochralski system containing only gas is specially encouraging. This initial successes show the flexibility of our model and demonstrate the great potential of the applied software. The consistency of our results and experimental finding is an initial success of our effort to solve three-dimensional fluid flows in CZ growth. Since a non-axisymmetric geometry is one of the factors which determines the three-dimensional flows in a CZ crystal growth, this success bring us one step closer towards the computations of three-dimensional, time-dependent flows and temperature fields in Czochralski systems.

6.4 Conclusions

In this chapter we reported on a set of two-dimensional and three-dimensional numerical calculations for three different Czochralski configurations in order to compare the results of the induction heating and the hydrodynamic model in these configurations. Two configurations without and with a gap between crucible and afterheater have axisymmetric conditions while the configuration with an open observation window is characterized by a non-axisymmetric geometry. The computational procedure included a preliminary computation of the global heat generation in the metallic parts and then a simulation of the heat transfer in the whole setup containing only gas, with taking into account heat exchange modes like convective, radiative and conductive-performed by using a steady state model. Further development of the numerical approach described would include the heat transfer calculation in a CZ system containing melt and crystal together with the calculation of the nonflat crystal-melt and melt-gas interface. The present numerical approach can be easily extended to the study of full CZ growth.

There are significant differences between the results of the axisymmetric configurations and configuration with an observation window for all flows which are driven by a temperature field. The coupling of incoming gas flow through the window and buoyancy also leads to a very complicated results. The results demonstrate an essential non-axisymmetrical temperature field and flow structure with multi-scale vortices in different areas of the computational domain. The most intensive three-dimensional convection and temperature field is observed in the window plane and the middle part of the growth setup. The differences in the two-dimensional and three-dimensional model predictions with respect to flows influenced by an open gap and an open observation window, are not surprising and also lead to an extremely important point about Czochralski gas hydrodynamics. The strong coupling of the extremely nonlinear gas flow process with the overall heat transfer in the configuration with an observation window leads to a behavior which can not be predicted by two-dimensional models.

In the configuration without any gap or window, the temperature gradient is approximately uniform in the gas domain and the isotherm shapes have been deformed proportional to the related gas flow pattern. In the configuration with a gap, the isotherms are strongly deformed following the gap geometry towards the centerline and in the afterheater towards the afterheater top cover hole. As a result the temperature variation is markedly high in the vicinity of the afterheater hole.

In the non-axisymmetric configuration under the influence of the observation window, q_{max}^{window} is not placed in the symmetry plane but it is located at the crucible side wall close to the window. Besides q_{max}^{window}, the volumetric distribution of heat generation in the system is about symmetric. In this setup, the gas flow is strong and about horizontal from the open window to the axis but after crossing the axis it becomes weak and expands in horizontal as well as vertical direction. Consequently, there is a spiral gas flow in the half crucible and afterheater which rotates upwards in azimuthal direction along the walls.

It has been found that gas flow raised from the observation window, greatly influences the axial temperature gradient along the axis, furthermore, it produces a high local temperature minimum between the crucible and afterheater (window area). This findings indicate an importance of the account of an open observation window on the gas convection in the CZ system. It is important for an analysis of defect formation or when making growth optimization procedures. This can include some modifications of the growth set-up design, and building in various constructive elements in the gas region.

Our calculations show that there is a reasonably good agreement between three-dimensional results and that from the measurement. This is, of course, encouraging and also not surprising since our mathematical model involves several important and real factors such as induction heating, real dimensions and geometries, and also the calculations are save because of using the Galerkin finite element method.

The interaction between natural gas convection and window driven gas flow is of great importance in the CZ crystal growth process, since the observation window is commonly employed to control the growth process. The nonlinear interaction of these driving forces produces gas flows which are much more complicated than those obtained from two-dimensional calculations in previous chapters. In addition, these interactions modify the heat transfer mechanism through the system and especially in the gas part, thereby changing overall heat transfer of the system. This makes direct influences on the quality of the grown crystal, since the crystal problems strongly depend on the growth conditions.

The observation window problem studied in this chapter, was chosen as a benchmark because its spatial complexity is essential and comparable to those exhibited for Czochralski crystal growth system. The non-axisymmetric geometry and orientation of the setup is one of the mechanisms which produces the non-axisymmetric temperature and flow fields during CZ growth. The other mechanisms are that under certain conditions, the axisymmetric thermal condition in a rotating fluid annulus becomes unstable and gives way to non-axisymmetric wavy flow, which resembles some flow patterns in Czochralski crystal growth system [47,52,53,57,62,63,65].

The Czochralski crystal growth systems are enormously complex. While the two-dimensional approach greatly simplifies the mathematical modeling of these system, the three-dimensional calculations are essential and can produce more qualitatively and quantitatively reliable results.

Our results demonstrate the great importance of a three-dimensional simulation for the Czochralski oxide crystal growth. But this does not invalidate our two-dimensional simulations in previous chapters. Our former simulations deal with the interactions between flow in the melt and gas, thermal radiation and seed rotation rate, while the three-dimensional simulations in this chapter is to study the effects of non-axisymmetric conditions (a small open observation window in the afterheater) on the temperature field and fluid flow in the system containing only gas. Clearly, this is a simplified model, which does not account for many important phenomena such as melt flow and crystal-melt interface, but allows us to study the main features of the gas flow structure in the system. Three-dimensional flow which arises from non-axisymmetry conditions, will quantitatively and qualititatively change the two-dimensional results which are related to axisymmetry condition in the CZ systems.

The transition from a two-dimensional quasi-steady state to a three-dimensional approach affects the temperature gradient in the Czochralski system, which may influence the temperature field in the melt and seed (or crystal) and seed (crystal)-melt interface shape. Currently, the seed crystal and melt are absent in our calculations. Any attempt to take into account these domains with moving boundaries in calculations, will be difficult because of the size of the problem. We probably have to wait for development of the software and parallel computers before we can solve very large moving boundary problems. But this is not frustrating at all, considering the fast advancement of the software as well as the hardware technologies.

Another difficulty we face is how to visualize three-dimensional solutions so that the physics of the solutions can be readily perceived. The two-dimensional isotherms, streamlines and velocity vectors in previous chapters provide some informations of the temperature and flow patterns in the setup, but they are not enough to show all of the important details in a three-dimensional calculation. The colored three-dimensional temperature iso-surfaces generated by advanced visualization tools can be used to describe temperature distributions, but how to properly visualize the velocity field is the system? This is an important challenge visualizing three-dimensional simulations and it should be solved in a good manner.

Conclusions and outlook

Conclusions

For the first time a set of two-dimensional and three-dimensional quasi-steady state numerical simulations have been performed for the initial stages (seeding process) of the Czochralski growth of oxide crystals. We have employed a finite element method (ENTWIFE package) using the standard Galerkin formulation. The distribution and number of elements used was chosen after careful studies of mesh refinement. The discrete equations were solved using a Newton-Raphson method combined with the frontal solver MUMPS (*MUltifrontal Massively Parallel sparse direct Solver*) for the linear system arising from this method. We have considered different cases and configurations with respect to the real systems in our Czochralski-dielectrics lab in *IKZ* and special steps of the seeding process.

At first (chapter 2) the spatial distribution of electromagnetic field in the system and volumetric distribution of heat generation inside the metal parts inducted by the RF coil were carefully analyzed for different geometries and orientations of crucible-afterheater-coil. Using this heat generation as a source the fluid flow and temperature field were determined in the whole system (chapter 3-6).

In chapters 3-5, an axisymmetric two-dimensional quasi-steady state modeling and numerical simulation of the heat transport mechanism in some real Czochralski systems containing only gas (chapter 3), melt and gas (chapter 4); seed, melt and gas (chapter 5) have been performed. The aim of these calculations was to investigate and reveal the effect of several parameters such as the geometry and location of an active afterheater with respect to the crucible, arrangement and design of thermal insulation, crucible bottom shape, and seed rotation rate on the flow and temperature field of the system and the seed-melt interface shape.

In chapter 6, a non-axisymmetric three-dimensional quasi-steady state analysis of the induction heating, temperature and flow field were carried out for a real Czochralski crystal growth furnace containing only gas in order to investigate the effect of a small open observation window on the heat transfer mechanism of the system. It was observed that the flow and thermal fields of the system are obviously three-dimensional, non-axisymmetric and very complex under the influence of this window.

These simulations show the importance of an active afterheater and its insulation as well as their geometry and position with respect to the crucible on the global heat transfer in a CZ growth and in particular during the seeding process. The results of heat transfer computation demonstrate that the temperature and fluid flow in the gas domain is strongly affected while in the melt part it is especially influenced close to its surface, by orientation and arrangement of these solid parts.

The properties of a Czochralski-grown crystal depend not only on the conditions prevailing at the point of growth (such as crystal-melt interface) but also on the processes which occur as that crystal cools from the melting point down to room temperature (such as gas convection and thermal field in the afterheater). On the other hand, the temperature gradient in the gas is critically important. Different thermal fields in the gas domain due to special orientation of the afterheater provide a possibility to control the grown crystal problems such as thermal stress, crack and evaporation. The required temperature gradient in the gaseous phase especially along the axis of symmetry can be established by an optimum design of the afterheater and its insulation.

It was also observed that in the case of absent seed as well as including the seed with no rotation ($\omega_{seed} = 0$), the flow pattern in the bulk melt consists of a single circulation of slow moving flow. In the gas domain, there are different types of flow motion related to different positions of the seed crystal. In the case of non-rotating touched seed, the seed-melt interface has a deep conic shape towards the melt.

The results presented here demonstrate the important role played by the seed rotation rate (ω_{seed}) in setting the shape of the seed-melt interface during the seeding process. The seed-melt interface shape is quite sensitive to the convective heat transfer in the melt and gaseous domain. When the local flow close to the seed-melt interface is formed mainly due to the natural convection and the Marangoni effect, the interface becomes convex towards the melt. When the local flow under the seed-melt interface is of the forced convection type from the seed rotation, the interface becomes more concave towards the melt as the seed rotation rate is increased. A linear variation of the interface deflection with respect to the seed rotation rate has been found too.

Using a mathematical model - developed in the present work - one can predict the heat generation in metallic parts, the flow pattern in the melt and gas, and the temperature distribution in the whole system. Doing these calculations we intend to investigate the influence of some parameters such as crucible-afterheater-coil orientation, thermal insulation and gas flow on the heat transport mechanisms of CZ growth and we try to find out an optional temperature distribution for the seeding process.

Outlook

The model of induction heating used in this work contains a relatively simple form of the *coil physics*. On the other hand, effects of the induced eddy current in the RF coil itself (i.e. self-inductance effect), has not been included. But it seems the coil physics is an important factor and can change the results considerably [61]. Thus, in order to find better quantitative and qualitative results and to correctly describe the phenomena, it is necessary to take into account the coil physics.

Another important point (especially in three-dimensional calculation) is the assumption of the vector potential components (A_r, A_φ, A_z). We have assumed that $A_r = A_z = 0$, because of the cylindrical shape of the RF coil and the metallic parts. To find more accurate results all componenets of the vector potential field should be included in the modeling. This could be especially more important in the case of configuration with an observation window because of non-axisymmetric conditions in the system.

The form of the Navier-Stokes equation given in this work is suitable for conditions of laminar flow. But turbulence is common in the big crucible of Czochralski systems. The crudest approach to incorporating turbulent effect in a big crucible is to use enhanced transport properties (e.g. viscosity, thermal conduction) in a laminar-flow model. A more accurate picture of transport can be obtained using a turbulent model.

Internal radiation [18,20,41,70] and wall to wall radiation [18,20,37,54] are also important parameters in the Czochralski crystal growth process and so they should be taken into account in the numerical calculations in order to find more realistic results. But radiative heat transfer is too difficult to simulate numerically because of the amount of computational time required, in particular in the three-dimensional case.

Due to the temperature fluctuations and transition behavior in the system [42,67], a time-dependent calculation may be required. In order to investigate some special aspects such as spiral growth and spoke patterns on the melt surface, a three-dimensional computation should be performed. Modeling of three-dimensional radiation heat transfer in a crystal growth furnace is a daunting problem, but in many cases it appears to be unnecessary since furnaces are usually designed to be nearly axisymmetric. So our conclusions may or may not be true in a three-dimensional transient simulation since the convective heat transfer in the system will be significantly changed. Any attempt to take into account all domains and parameters with moving boundaries in a transient calculation, will be difficult because of the computational size of the problem. We probably have to wait for the development of the software and parallel supercomputers before we can solve very large transient moving boundary problems. But this is not disappointing at all, considering the fast advancement of the software as well as the hardware technologies.

References

[1] A.F. Leatherman and D.E. Stutz, *Induction heating advances*, National Aeronautics and Space Administration, 1969.

[2] A.W.A. Hart, *Czochralski Crystal Growth*, Leiden Univ. Diss. 1978.

[3] F.E. Rosenberger, *Fundamentals of Crystal Growth*, Springer 1979.

[4] J.C. Brice, *Crystal Growth Processes*, Blackie 1986.

[5] H. Arend, *Crystal Growth in Science and Technology*, Plenum Press 1989.

[6] W.A. Tiller, *The Science of Crystallization*, Cambridge University Press 1991.

[7] D.T.J. Hurle, *Crystal Pulling from the Melt*, Springer-Verlag 1993.

[8] D.T.J. Hurle, *Handbook of Crystal Growth vol. A-B*, North-Holland 1993-1994.

[9] A.F. Mills, *Heat and Mass Transfer*, IRWIN 1995.

[10] S. Kou, *Transport Phenomena and Materials Processing*, John Wiley & Sons 1996.

[11] P.G. Ciarlet, *Handbook of Numerical Analysis*, Elsevier, 1998.

[12] R. Fornari, *Theoretical and Technological Aspects of Crystal Growth*, Trans. Tech. Publ. 1998.

[13] J.D. Jackson, *Classical Electrodynamics*, Wiley 1999.

[14] D.R. Lide, *Handbook of Chemistry and Physics*, CRC Press 1999.

[15] J.F. Shackel and W. Alexander, *Materials Science and Engineering Handbook*, CRC Press 2001.

[16] E.L. Allgower and K. Georg, *Introduction to Numerical Continuation Methods*, SIAM 2003.

[17] M. Rappaz, M. Bellet and M. Deville, *Numerical Modeling in Materials Science and Engineering*, Springer-Verlag 2003.

[18] H.J. Scheel and T. Fukuda, *Crystal Growth Technology*, Wiley 2003.

[19] V. Rudnev, D. Loveles, R. Cook and M. Black, *Handbook of induction heating*, New York NY 2003.

[20] P. Capper, *Bulk Crystal Growth of Electronic, Optical and Optoelectronic Materials*, John Wiley & Sons 2005.

[21] K.A. Cliffe, SERCO Ltd., http://www.sercoassurance.com/entwife.

[22] K.H. Winters, ENTWIFE - User Manual, Harwell Laboratory 1991.

[23] http://www.enseeiht.fr/lima/apo/MUMPS.

[25] K. Takagi, T. Fukazawa and M. Ishii, *Inversion of the direction of the solid-liquid interface on the Czochralski growth of GGG crystals*, Journal of Crystal Growth 32 (1976) 89.

[26] C.D. Brandle, *Simulation of fluid flow in Gd3Ga5O12 melts*, Journal of Crystal Growth 42 (1977) 400.

[27] N. Kobayashi, *Computational simulation of the melt flow during Czochralski growth*, Journal of Crystal Growth 43 (1978) 357.

[28] V.A. Borodin, L.B. Davidova, V.N. Erofeev, A.V. Shdanov, S.A. Startsev and V.A. Tatarchenko, *The effect of the solidification front shape on the temperature distribution in the crystal*, Journal of Crystal Growth 46 (1979) 757.

[29] N. Kobayashi and T. Arizumi, *Computational studies on the convection caused by crystal rotation in a crucible*, Journal of Crystal Growth 49 (1980) 419.

[30] N. Kobayashi, *Hydrodynamics in Czochralski growth-computer analysis and experiments*, Journal of Crystal Growth 52 (1981) 425.

[31] C.D. Brandle, *Flow transitions in Czochralski oxide melts*, Journal of Crystal Growth 57 (1982) 65.

[32] D.T.J. Hurle, *Analytical representation of the shape of the meniscus in Czochralski growth*, Journal of Crystal Growth 63 (1983) 13.

[33] P. Reiche, B. Hermoneit and D. Schultze, *A modified Heater system for RF-Czochralski Equipments*, Crystal Research and Technology 20 (1985) 845.

[34] M. Berkowski, K. Iliev, V. Nikolov, P. Peshev and W. Piekarczyk, *On the conditions of formation of a flat crystal/melt interface during Czochralski growth of single crystals*, Journal of Crystal Growth 83 (1987) 507.

[35] P.M. Gresho and J.J. Derby, *A finite element model for induction heating of a metal crucible*, Journal of Crystal Growth 85 (1987) 40.

[36] A.D.W. Jones, *Scaling analysis of the flow of a low Prandtl number Czochralski melt*, Journal of Crystal Growth 88 (1988) 465.

[37] T. Tsukada, N. Imaishi and M. Hozawa, *Theoretical study of the flow and temperature fields in CZ single crystal growth*, Journal of Chemical Engineering of Japan 21 (1988) 2.

[38] J.J. Derby, L.J. Atherton and P.M. Gresho, *An integrated process model for the growth of oxide crystals by the Czochralski method*, Journal of Crystal Growth 97 (1989) 792.

[39] H. Kopetsch, *Numerical simulation of the interface inversion in Czochralski growth of oxide crystals*, Journal of Crystal Growth 102 (1990) 505.

[40] J. Trauth and B.C. Grabmaier, *The shape of the crystal/melt interface during the growth of lithium niobate crystals by the Czochralski technique*, Journal of Crystal Growth 112 (1991) 451.

[41] J.J. Derby and Q. Xiao, *The role of internal radiation and melt convection in Czochralski oxide growth: deep interfaces, interface inversion, and spiraling*, Journal of Crystal Growth 113 (1991) 575.

[42] G. Müller, *Convective instabilities in melt growth configurations*, Journal of Crystal Growth 128 (1993) 26.

[43] J.J. Derby and Q. Xiao, *Heat transfer and interface inversion during the Czochralski growth of yttrium aluminum garnet and gadolinium gallium garnet*, Journal of Crystal Growth 139 (1994) 147.

[44] T. Tsukada, M. Hozawa and N. Imaishi, *Global Analysis of Heat Transfer in CZ Crystal Growth of Oxide*, Journal of Chemical Engineering of Japan 27 (1994) 25.

[45] T. Tsukada, K. Kakinoki, M. Hozawa, N. Imaishi, K. Shimamura and T. Fukuda, *Numerical and experimental studies on crack formation in LiNbO3 single crystal*, Journal of Crystal Growth 180 (1997) 543.

[46] C. Shu, Y.T. Chew, Y. Liu, *An efficient approach for numerical simulation of flows in Czochralski crystal growth*, Journal of Crystal Growth 181 (1997) 427.

[47] C.J. Jing, N. Imaishi, S. Yasuhiro and Y. Miyazawa, *Three-dimensional numerical simulation of spoke pattern in oxide melt*, Journal of Crystal Growth 200 (1999) 204.

[48] W. Miller, U. Rehse and K. Böttcher, *Melt Convection in a Czochralski Crucible*, Crystal Research and Technology 34 (1999) 481.

[49] C.J. Jing, N. Imaishi, T. Sato and Y. Miyazawa, *Three-dimensional numerical simulation of oxide melt flow in Czochralski configuration*, Journal of Crystal Growth 216 (2000) 372.

[50] Z. Galazka and H. Wilke, *Influence of Marangoni convection on the flow pattern in the melt during growth of Y3Al5O12 single crystals by the Czochralski method*, Journal of Crystal Growth 216 (2000) 389.

[51] J.H. Jeong and I.S. Kang, *Analytical studies on the crystal-melt interface shape in the Czochralski process for oxide single crystals*, Journal of Crystal Growth 218 (2000) 294.

[52] B. Basu, S. Enger, M. Breuer and F. Durst, *Three-dimensional simulation of flow and thermal field in a Czochralski melt using a block-structured finite-volume method*, Journal of Crystal Growth 219 (2000) 123.

[53] S. Enger, B. Basu, M. Breuer and F. Durst, *Numerical study of three-dimensional mixed convection due to buoyancy and centrifugal force in an oxide melt for Czochralski growth*, Journal of Crystal Growth 219 (2000) 144.

[54] Z. Galazka and H. Wilke, *Heat Transfer and Fluid Flow during Growth of Y3Al5O12 Single Crystals using the Czochralski Method*, Crystal Research and Technology 35 (2000) 1263.

[55] P. Hintz, D. Schwabe and H. Wilke, *Convection in a Czochralski crucible - Part 1: non-rotating crystal*, Journal of Crystal Growth 222 (2001) 343.

[56] P. Hintz, D. Schwabe and H. Wilke, *Convection in a Czochralski crucible - Part 2: rotating crystal*, Journal of Crystal Growth 222 (2001) 356.

[57] B. Basu, S. Enger, M. Breuer and F. Durst, *Effect of crystal rotation on the three-dimensional mixed convection in the oxide melt for Czochralski growth*, Journal of Crystal Growth 230 (2001) 148.

[58] J-P. Chaminade, O. Viraphong and S. Miyazawa, *One possible mechanism of spiral/footing growth of Cz-grown Li6Gd(BO3)3*, Journal of Crystal Growth 237-239 (2002) 864.

[59] G. Müller, *Experimental analysis and modeling of melt growth processes*, Journal of Crystal Growth 237-239 (2002) 1628.

[60] Y. Fei, M.M.C. Chou and B.H.T. Chai, *Crystal growth and morphology of substituted gadolinium gallium garnet*, Journal of Crystal Growth 240 (2002) 185.

[61] O. Klein and P. Philip, *Transient numerical investigation of induction heating during sublimation growth of silicon carbide single crystals*, Journal of Crystal Growth 247 (2003) 219.

[62] C.J. Jing, M. Kobayashi, T. Tsukada, M. Hozawa, T. Fukuda, N. Imaishi, K. Shimamura and N. Ichinose, *Effect of RF coil position on spoke pattern on oxide melt surface in Czochralski crystal growth*, Journal of Crystal Growth 252 (2003) 550.

[63] V. Kumar, B. Basu, S. Enger, G. Brenner and F. Durst, *Role of Marangoni convection in Si-Czochralski melts, part I: 3D predictions without crystal*, Journal of Crystal Growth 253 (2001) 142.

[64] V.S. Yuferev, O.N. Budenkova, M.G. Vasiliev, S.A. Rukolaine, V.N. Shlegel, Ya.V. Vasiliev and A.I. Zhmakin, *Variations of solid-liquid interface in the BGO low thermal gradients Cz growth for diffuse and specular crystal side surface*, Journal of Crystal Growth 253 (2003) 383.

[65] V. Kumar, B. Basu, S. Enger, G. Brenner and F. Durst, *Role of Marangoni convection in Si-Czochralski melts-Part II: 3D predictions with crystal rotation*, Journal of Crystal Growth 255 (2001) 27.

[66] S. Ganschow, P. Reiche, M. Ziem and R. Uecker, *Controlling the axial temperature gradient in inductively heated Czochralski systems*, Crystal Research and Technology 38 (2003) 42.

[67] C.D. Brandle, *Czochralski growth of oxides*, Journal of Crystal Growth 264 (2004) 593.

[68] D. Schwabe, R. R. Sumathi, and H. Wilke, *The interface inversion process during the Czochralski growth of high melting point oxides*, Journal of Crystal Growth 265 (2004) 494.

[69] O.A. Louchev, S. Kumaragurubaran, S. Takekawa and K. Kitamura, *Thermally induced effects during initial stage of crystal growth from melts*, Journal of Crystal Growth 273 (2004) 320.

[70] J. Banerjee and K. Muralidhar, *Simulation of transport processes during Czochralski growth of YAG crystals*, Journal of Crystal Growth 286 (2006) 350.